U.PORTO

FEUP FACULDADE DE ENGENHARIA
UNIVERSIDADE DO PORTO

ASSESSMENT OF OVERTOPPING RISK REDUCTION SOLUTIONS ON URBANIZED COASTAL AREAS SUPPORTED BY MACHINE LEARNING

MOEKETSI LAWRENCE DUIKER

Dissertation submitted in partial fulfilment of the requirements for the degree of

MASTER'S IN CIVIL ENGINEERING - SPECIALIZATION IN HYDRAULICS

Advisor: Professor Paulo Jorge Rosa Santos

Co-Supervisor: Doctor Jose Victor Ramos Castro

Doctor Ivan Mira Pombo

JULY 2023

MASTER'S IN CIVIL ENGINEERING 2022/2023

DEPARTMENT OF CIVIL ENGINEERING

Tel. +351-22-508 1901

Fax +351-22-508 1446

✉ m.ec@fe.up.pt

Edited by

FACULTY OF ENGINEERING OF THE UNIVERSITY OF PORTO

Rua Dr. Roberto Frias

4200-465 PORTO

Portugal

Tel. +351-22-508 1400

Fax +351-22-508 1440

✉ feup@fe.up.pt

http://www.fe.up.pt

Future is for those who mastered the present, because when you get to the future you will realize that it is the present.

ACKNOWLEDGEMENTS

I would like to express my deepest gratitude to God for enabling the completion of this work. I am also deeply appreciative of all those who have accompanied and supported me throughout my academic path, contributing to both my personal and intellectual growth.

I extend my sincere appreciation to the University of Porto, the Faculty of Engineering in particular, including its administrative services and academic staff, for their warm welcome, continuous support, and constant encouragement. I am likewise grateful to all professors and researchers of the Section of Hydraulics, Water Resources, and Environment for their guidance, expertise, and valuable insights.

I extend my heartfelt appreciation to Professors Francisco Taveira Pinto and Luciana das Neves for their assistance throughout my academic career. I am especially grateful to Professor Paulo Rosa Santos for his confidence in my abilities, for encouraging me to recognize my own potential, for his sustained availability, and for his dedication to the successful completion of this dissertation.

My sincere thanks also go to Dr. Victor Ramos Castro for his exceptional support, from helping me with MATLAB, SWASH, and Delft3D, to offering encouragement and availability from the very beginning to the final stages of this work. His contributions were fundamental to the completion of this dissertation.

I am deeply thankful to my family for their unconditional belief in me.

Finally, I would like to acknowledge myself for the dedication, perseverance, and resilience shown throughout this journey.

This work was developed in partnership with Inductiva Research Labs from January 2023 to July 2023. I would like to thank Inductiva for the continuous support with simulation, both via Inductiva API and computational resources provided during the collaboration. I further thank Ivan Pombo and Dr. Luis Sarmento for their constructive comments and insightful feedback on multiple versions of this manuscript.

This Master's dissertation was supported by the Free State Provincial Government-International Scholarship Programme (2017/2023). I would like to express my sincere gratitude to the Free State Provincial Government for its generous support, without which the completion of this work would not have been possible.

RESUMO

Devido aos efeitos das alterações climáticas, as zonas costeiras estão a ser expostas a ações do ambiente marinho de magnitude crescente, que se prevê resultem em riscos costeiros acrescidos, como a erosão, os galgamentos, as inundações e a subida do nível médio do mar. Dada a importância das zonas costeiras, com um interesse económico e social elevado e diversificado, torna-se cada vez mais importante avaliar com precisão esses riscos e conceber estruturas de defesa costeira otimizadas para minimizar esses riscos.

Esta dissertação utiliza como caso de estudo uma praia da costa portuguesa – a Praia do Furadouro, Ovar, que tem sido afetada ao longo dos anos por inundações, erosão e recuo da linha de costa. Os principais objetivos deste trabalho de investigação são analisar as condições atuais dessa praia, mapear o galgamento no espaço e no tempo para diferentes cenários e avaliar a eficácia de novas medidas destinadas a reduzir o galgamento nesse troço costeiro, usando um modelo numérico CFD – SWASH (acrónimo de *Simulating Waves till Shore*). Este trabalho envolve a utilização de aprendizagem automática (*machine learning*) que permite acelerar o processo de otimização das soluções de proteção costeira, ao permitir explorar espaços de projeto grandes e muito complexos num tempo razoável, reduzindo a utilização de modelos numéricos computacionalmente exigentes que discretizam as dimensões espaciais e temporais em grelhas muito finas no tempo e no espaço.

Inicialmente, é feita uma breve introdução aos impactes das alterações climáticas, riscos costeiros e galgamentos, seguindo-se a análise comparativa de eventos semelhantes aos ocorridos na frente costeira do Furadouro. Posteriormente, é apresentada a área de estudo e a descrição dos problemas de galgamentos ocorridos anteriormente na proximidade e as suas consequências na malha urbana. Depois da descrição do modelo numérico SWASH, é feita a sua aplicação ao caso de estudo juntamente com a sua validação utilizando os dados do evento de inundação que ocorreu em fevereiro de 2014. Por último, é feitas uma descrição das ferramentas de aprendizagem automática e da sua aplicação na resolução dos problemas da área de estudo.

Finalmente, conclui-se que o modelo numérico selecionado é capaz de mapear a extensão da inundação que resulta do galgamento do muro da frente costeira da Praia do Furadouro. Por outro lado, os modelos de aprendizagem automática que foram gerados e treinados são capazes de prever a área inundada com uma precisão razoável (suficientemente boa) quando lhes são fornecidos dados de entrada em quantidade suficiente. No entanto, concluiu-se que para melhorar a precisão desses modelos é necessária a utilização de mais dados.

PALAVRAS-CHAVE: Riscos costeiros, modelação numérica, aprendizagem automática, galgamento costeiro, medidas de adaptação.

ABSTRACT

Due to the effects of ongoing climate change, coastal zones are being exposed to the actions from the marine environment which are expected to increase in the future and result in increased coastal risks, such as erosion, overtopping, flooding and mean sea level rise. Given the importance of coastal zones, with high and diversified economic and social interest, it becomes increasingly important to accurately assess those risks and to design optimized coastal defence structures in order to mitigate those risks.

This dissertation uses as case-study a beach on the Portuguese coast – Praia do Furadouro, Ovar, which has been impacted over the years by flooding, erosion, and retreat of the coastline. The main goals of this research work are to analyse the current conditions of that beach, to map overtopping in space and time for different scenarios and to evaluate the effectiveness of new measures aimed at reducing overtopping in this coastal stretch using a CFD numerical model – SWASH (an acronym of *Simulating Waves till Shore*). This work involves the use of machine learning which allows to speed-up the optimization process of the coastal protection solutions, by allowing to explore large and very complex design spaces at a reasonable time, reducing the use of computationally demanding numerical models discretizing the space and time dimensions in very fine grids over time and space.

Initially, a brief introduction of the impacts of climate change, coastal risks and overtopping is made, followed by the comparative analysis of similar events to the ones occurred in Furadouro coastal front. Subsequently, the study area is presented and the problems of overtopping that occurred previously in the vicinity of the urban seafront as well as their consequences are discussed. Later, a SWASH numerical model description is made together with its validation using the data from the flood event that occurred in February 2014. Lastly, a description of the machine learning tools used and their application to the study area are given.

Finally, it is concluded that the selected numerical model is capable to map the extension of the flood that resulted from the overtopping of the coastal front sea wall. In the other hand, the machine learning models that were generated and trained are able to predict the flooded area with a reasonable accuracy (sufficiently good) when sufficient input data are used. However, it was concluded that to improve the accuracy of the machine learning models the use of larger input datasets is required.

KEYWORDS: Coastal risks, Numerical modelling, Machine Learning, Coastal overtopping, Adaptation measures.

GENERAL INDEX

INDEX OF FIGURES

LIST OF TABLES

SYMBOLS

q - average overtopping flow per linear meter [$m^3 /s/m$]

H_s - significant wave height [m]

H_{m0} - spectral significant wave height [m]

T_p - peak period [s]

R_c - crest freeboard [m]

A_c - armour crest freeboard of the structure [m]

G_c - width of structure crest [m]

B_t - width of the berm [m]

s, - slope angle of the armour layer [-]

h - water depth [m]

$T_{m-1,0}$ - spectral wave period [s]

Cr - roughness coefficient [$m^{-1/3}s$]

D - flow distribution [θ]

ΔH - heat difference [m]

μ - wind speed [m/s]

v̄ - wind direction [°]

β - turbulent friction loss [$kg/m^2/s^2$]

R_c/H_{mo} - relative crest freeboard [-]

S_{op} - wave steepness [-]

m - number of weights [-]

y_i - true values [-]

$\hat{y}_i$ - predicted values [-]

a - penalty parameter [-]

w – weight [-]

b – bias [-]

g - gravitational acceleration [m/s^2]

u_b - velocity distribution [m/s]

c_f - coefficient of bottom friction [-]

n - manning roughness coefficient [$m^{-1/3}s$]

ζ_b - incident wave surface elevation signal [-]

τ_b - bottom friction [-]

p_h - hydrostatic pressure [m^2/s^2]

p_{nh} - non-hydrostatic pressure [m^2/s^2]

τ - turbulence term [-]

ω - angular frequency [rad/s]

β - direction of propagation of the sea disturbance [º]

ACRONYMS

AI - Artificial intelligence

ANN - Artificial Neural Network

API - Application Programming Interface

ARH - Hydrographic Regional Administration

ASR - Artificial Surf Reef

CC - Climate Change

CD - Chart Datum

CDF - Computational Fluid Dynamics

CDW - Coastal Defence Works

CERA - Code-Expanded Random-Access technique

CMA - China Meteorological Administration

DD - Dune System Destruction

DEC - Civil Engineering Department

DI - Damage to Infrastructure

ELU - Exponential Linear Unit

GDP - Gross Domestic Product

HKO - Hong Kong Observatory

IH - Hydrographic Institute

INE - Instituto Nacional de Estatística (National Institute of Statistics)

IPCC - Intergovernmental Panel on Climate Change

ISO - International Organization for Standardization

LR - Linear Regression

LTC - Long-Term Configuration numerical model

LTH - Topographic Hydrographic Survey

ML - Machine Learning

MSE - Mean Square Error

MSL - Mean Sea Level

NAO - North Atlantic Oscillation

NN_Overtopping - Overtopping Neural Network

OV - Overtopping

PTO - Power Take Off

QGIS - Quantum Geographic Information System

RANS - Reynolds Averaged Navier-Stokes

RELU - Rectified Linear Unit

RF - Random Forest

RMSE - Root Mean Square Error

SELU - Scaled Exponential Linear Unit

SLR - Sea Level Rise

SPH - Smooth Particle Hydrodynamics

SR - Shoreline Retreat

SVM - Support Vector Machine

SWASH - Simulating WAves till SHore

TKO - Tseung Kwan O

WNW - West Northwest

1
INTRODUCTION

1.1. MOTIVATION

Over the years, there has been a significant development in coastal areas, increasing human occupation through the construction of residential buildings and commerce closer and closer to the shoreline due to the fact that the coastline has significant advantage from the commercial, leisure and economic point of view. However, these areas are exposed to the actions of the maritime environment, which are expected to increase in the future due, for instance, to an increase in the mean sea level led by the ongoing effects of climate change, resulting naturally in an increase of coastal risks such as erosion, retreat, overtopping and floodings.

In terms of leisure, economic and environmental aspects, the Portuguese coast has gained a great relevance for tourism and there is an increase of population in these areas, some coming from the inner cities of the mainland moving towards the coastline, Figure 1.1. Because the mainland of Portugal stretches along the Atlantic Ocean, an extensive coastline is available and it is still used as a primary sector for economic, environmental, political, social and scientific activities. Because of the type of existing infrastructures, activities and associated costs, it is usually not feasible to implement solutions such as accommodation or retreat. In fact, most of the time, the only solution that can be adopted is to protect the coastline through interventions such as the used of artificial beach and/or dune nourishment, seawalls, sea dykes and storm barriers.

Since the nineteenth century (Lamy and Rodrigues, 2001), there have been records of issues and damages at Furadouro beach due to the energetic wave climate. These records show that existing coastal defense structures are not efficient enough. Hence, there are events of landslides, overtopping and damage of properties behind the coastal protection structures. Those structures have undergone several alterations over the years and have had to be rebuilt several times due to the extensive damage caused by wave action. These modifications are frequently designed and built as an emergency response. Therefore, there are not thorough studies supporting the execution and positioning of the coastal defense structures. Even when those design studies are conducted, only a handful of alternatives are analyzed and compared due to time and budget constraints. This is because studies with advanced numerical models are computationally demanding and time-consuming, and the use of physical model testing is frequently considered to be expensive. This context creates an opportunity for the application of machine learning tools, which, if properly implemented, can provide engineers with the optimal solution in terms of the scale and placement of those coastal structures at a reasonable cost and in time.

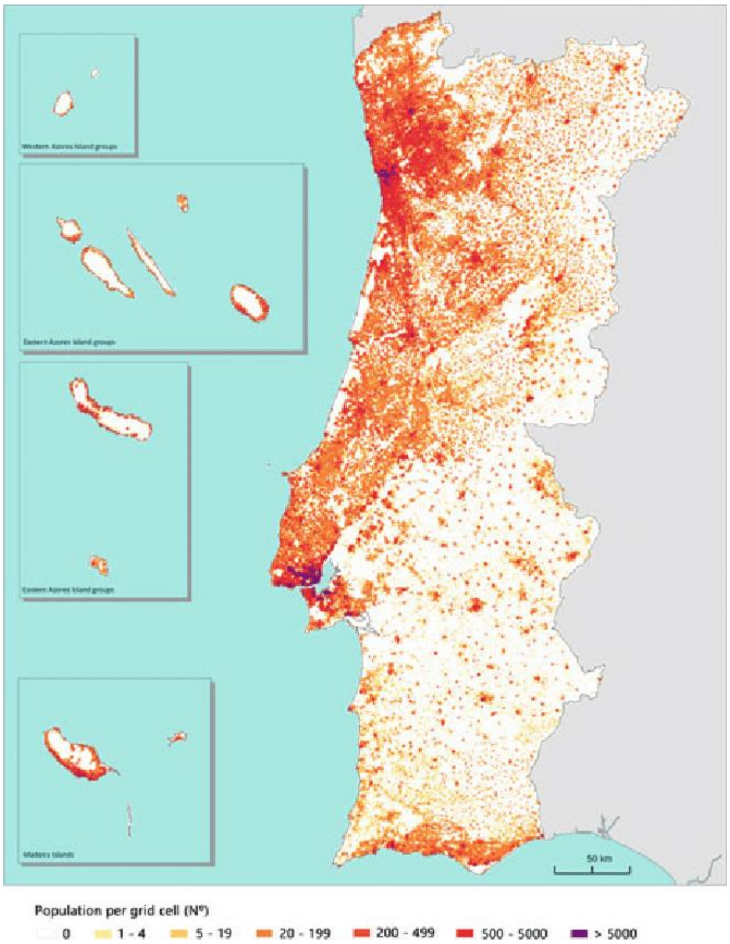

Figure 1.1 – Population density in Portugal (INE, 2011).

1.2. Objective

The aim of this dissertation is to analyse the overtopping and flooding risk in urbanized coastal areas by means of reviewing and critically analyzing experimental and numerical studies performed for similar cases to Furadouro (nationally and internationally), highlighting the most relevant conclusions for the present work as well as the consequences of climate change on coastal risk, economy and the solutions to mitigate problems.

Furthermore, the CFD numerical model SWASH is used to characterize and assess overtopping in space and time for the current situation of the case study coastal stretch and also to evaluate the effectiveness of new measures that will be proposed for the study area aiming at reducing overtopping, using different hydrodynamic boundary conditions. Finally, the use of machine learning tools aims to support the optimization process of the coastal protection solutions designed for the selected case study.

1.3. Dissertation Structure

This master dissertation is divided into 5 chapters. It begins with this brief introduction of the dissertation topic, the aim and the morphologies used and finally the structure of the dissertation.

In the second chapter, overtopping and flooding risk assessment in urbanized coastal areas are discussed. It starts by addressing the consequences of climate change on coastal risks together with the impacts on economy and the solutions that can be used to minimize those risks. Moreover, assessment methodologies are described and a comparative analysis of similar cases to Furadouro are presented to highlight the most relevant conclusions for the current work.

The case study of the dissertation is described in chapter 3, namely in terms of location, topo-hydrography, sedimentary dynamics, tide regime and wave conditions. This chapter also describes the solutions studied in previous works and, finally, presents the development and definition of the new solutions to be studied in the present dissertation.

Chapter 4, entitled *numerical study,* presents the general description of the numerical models used and their practical application to different scenarios, *i.e*., the analysis of different combination of water levels and wave conditions for: (i) the current situation of the Furadouro coastal stretch and (ii) the different intervention alternatives. In addition, it also includes the integrated critical analysis of obtained results and the improvements proposed to the tested solutions by the application of machine learning tools and optimization algorithms.

Lastly, Chapter 5, *conclusions and future developments,* presents the synthesis of the results obtained covering the mapping of coastal overtopping in space and time for different scenarios using advanced CFD numerical models, the evaluation of the effectiveness of new measures aimed at reducing overtopping and the use of machine learning tools.

2

OVERTOPPING AND FLOODING RISK ASSESSMENT IN URBANIZED COASTAL AREAS

2.1. CONSEQUENCES OF CLIMATE CHANGE

2.1.1. COASTAL RISKS

Climate change is one of the greatest threats faced by the planet and humanity (environmental, social, and economic). It results from a statistically significant change in climate directly or indirectly attributed to anthropogenic activities that alter the overall composition of the atmosphere over more than 3 decades in the average state of the climate or its variability, without absolute identification of the causes of the change, according to the Intergovernmental Panel on Climate Change (IPCC, 2014).

These changes are mainly due to the increase in global temperature which results in an increase in the mean sea level (MSL) due to the melting glaciers and thermal expansion of the ocean. Future changes will occur at a faster rate and on a larger scale than in the past, making adaptation decisions more difficult (Hallegatte, 2009). Figure 2.1 shows the rise in average annual temperature between 1850 and 2020. By 2100, regardless of the selected emission scenario, extreme sea level rise events will become more frequent (IPCC, 2019), and more regions are projected to become vulnerable to coastal flooding and inundation (Almar *et al.*, 2021). Thermal variations between the oceans and continents will create a high-pressure zone along the coast, resulting in an increase in wind intensity and a consequent increase in wave intensity along the coast. In coastal environments there are three main consequences of climate change:

- The rise in the average sea level,
- The change in the storm regime, and
- The intensification of the winter storms.

This phenomenon can result in different hazards, such as erosion due to high waves and tides, shoreline retreat, run-ups that are higher than the coastal defense structures (which result in overtopping and damaging of properties behind the structure), and flooding of urbanized coastal areas caused by the rupture or overtopping of natural or artificial means of protection by waves. The climate exerts an influence on ecosystems and presents a risk when basic elements for life, such as water supply, health, or safety, are threatened (ANCORIM, 2010).

While parallels can be derived in the interpretation of risk, between impacts and consequences, and between hazards and events, ISO 31000 (2018) disregards exposure and vulnerability as stand-alone components but rather incorporates them within the consequences. Exposure is a necessary but insufficient factor in determining risk, as it is possible to be exposed without being vulnerable., such as by residing in a floodplain but having the resources to modify a building or structure and mitigate potential losses (IPCC, 2012). To be vulnerable and susceptible to adverse effects (such as inundation), however, it is necessary to be exposed. In some densely populated coastal areas, vulnerability variations may become the primary source of risk.

Risk analysis combines hazard, exposure, and vulnerability in diverse ways. This ranges from index-based approaches that detect clusters at large scales or in areas with limited quantitative data to more advanced methodologies that consider multiple sectors, multiple impacts, multiple hazards and vulnerability attributes, or the evolution of risk over time. All these risk analysis types are reliable in that they evaluate one or two risk attributes, but none of them is exhaustive. This dilemma is brought into prominence by CC's expansion of uncertainty (Toimil *et al.*, 2020).

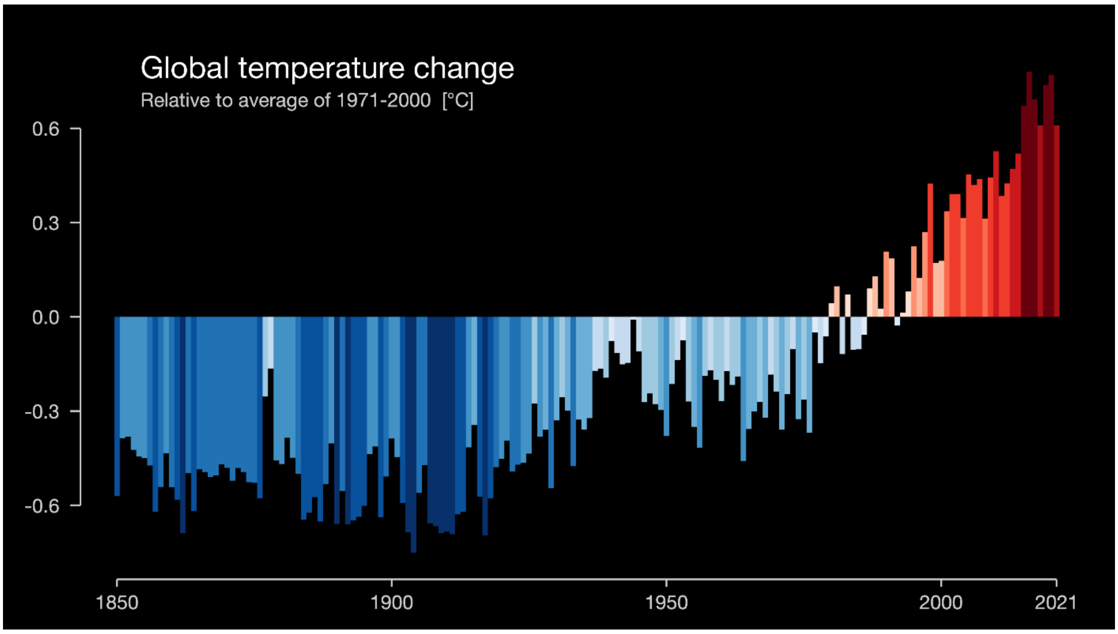

Figure 2.1- Global annual average temperature between 1850-2020 (https://showyourstripes.info/).

2.1.2. Economic impacts

Although it is common practice to reduce exposure to physical assets such as buildings and infrastructures, information regarding indirect effects (e.g., sectoral GDP, income) cannot be ignored. For instance, when an industrial facility is flooded, the repercussions are not limited to damage to the structure and contents but can also include revenue loss due to business interruption or delay.

When addressing coastal hazards through land use planning, typically only small groups of affected citizens are engaged, as opposed to the larger impacted community, which may also contribute to the funding of coastal adaptation (Anguelovski *et al.*, 2016). For instance, inland communities that utilize beaches and protected coastal ecosystems should be concerned with the financing of adaptation to coastal conditions. Additionally, they may be affected by migrants fleeing coastal regions. To obtain public funding or to gain access to national and international funding sources, it is necessary to contemplate the correct fiscal scale. Improving the coordination of responses across all levels of government and policy domains, which has proved to be an effective response (IPCC, 2019), continues to be a significant challenge.

Lastly, coastal adaptation raises issues of equity and requires ensuring that responses do not further marginalize the most vulnerable populations, particularly in fast-growing cities in developing countries (See and Wilmsen, 2020) and also in areas with large existing wealth and resource gaps, and do not trigger or exacerbate social conflicts (McGinlay *et al*., 2021). Efforts should be made to promote climate resilience alongside sustainable, just, and equitable development. Otherwise, SLR is likely to bring about or aggravate social conflicts over time, making them more difficult to resolve; this is why Bongarts Lebbe *et al.* (2021) emphasize the importance of contemplating larger dimensions and adjacent jurisdictions. The significance of contemplating multiple temporal scales is now emphasized.

2.1.3. Adaptation measures and solutions

The strategy to be implemented is influenced by the socio-economic conditions of the site. Decision-making should be based on cost-benefit analyses in order to assess the best strategy and measures for the site. The cost of the adaptation strategy is the sum of the costs associated with its implementation and the residual impacts to be eliminated. In this sense, the following are 3 strategies that can be implemented for coastal adaptation:

1. The accommodation strategy: This type of strategy consists of adapting people's livelihoods so that they can continue to live in areas vulnerable to coastal erosion and coastal flooding and it should be integrated with a long-term retreat approach. There are measures used to implement the accommodation approach such as the ones presented in Table 2.1. However, uses below flood risk levels should be conditioned and more resilient urban solutions should be created (PROCIV, 2010).
2. The protection strategy: The intention is to maintain the coastline or even advance over the sea, protecting the coastline from the effects of coastal erosion. For this reason, there are two types of interventions that can be used as shown in Table 2. 2.
3. The strategy of relocation consists in the removal of properties from areas vulnerable to coastal risks. Relocation should be the last strategy to be adopted and only when it is the only option because the vulnerability is too high. The measures to be taken should always be followed by a natural strengthening in the areas that were previously occupied, in order to reduce vulnerability, acting as a buffer zone between the new occupied areas and the sea (Veloso-Gomes and Oliveira, 2013). These measures can be relocation, withdrawal, and retrofitting (Oliveira, 2013).

Table 2.1 - Measures used to implement an accommodation approach (Mesuras, 2018).

Strategies	Measures	Goals
Urban planning resilient (more resilient and functional urban fronts)	Permanent barrier and walls	Decrease the risk of overflow
	Permeable sidewalks	Promote the infiltration of water and flooding
	Green Infrastructure	Decrease the risk of flooding
	Drainage System	Rerouting water to areas plug-in
	Building Accommodation	Decrease the risk of flooding
	Seasonal Uses	Intelligent land occupation
Prevention	Elaboration of risk maps	Provide information on coastal risk
	Adverse condition alert system	Warns the community in time to take the necessary precautions

Table 2. 2 - Different works for coastal zone protection (Mesuras, 2018).

Intervention type	Name	Definition
Light	Artificial beach nourishment	Carried out periodically with the objective of maintaining the desired beach profile and minimizing the sediment deficit
Heavy	Groin	Structure perpendicular to the coastline with the intention of retaining sediments
	Detached and floating structures	Structure without grounding with the objective to reduce wave energy near the shoreline
	Adherent defense structure	Structure located on the shoreline to prevent coastal overtopping and erosion

Since heavy works are costly, these structures should be built only when the decision is supported by in-depth analysis of the processes that cause erosion, as well as the evolution of the coastline in the past and estimated in the future, so that the measure to be taken is as effective as possible. The following are methods that can be used to protect the coastline:

Artificial beach nourishment permits the coastline to adapt dynamically to change. Despite the fact that soft adaptation is a short-term response to sea level rise, optimal beach and shore nourishment responses offer economic and social benefits and may minimize forced migration, according to (Hinkel *et al.*, 2013). The sands may be dredged in front of the coast or borrowed from an inland site with comparable qualities to the beach to be fed; if the borrowed sand is too fine, it will cause rapid erosion, but if it is too coarse, it may increase the slope of the beach face. Feeding using dune sand is very seldom possible and invariably has negative environmental effects.

Groins are lengthy, perpendicular to the beach, constructions that extend into the surf zone and may reach at least 300 m into the surf zone. They are often constructed of concrete blocks or rock and may have many designs, including straight, "L", "T", and "Y", among others. Since their primary purpose is to hold sediments as mud, they should be implemented in places where sediment movement occurs. This retention causes sediment loss downstream of the structure, hence increasing the erosive process, as shown in Figure 2.2. Groins serve mostly to stabilize sediments generated by artificial feeding on natural or manmade beaches. Hold coastal drift and limit coastal erosion by preventing sediment flow between sediment cells where sinkholes are found (Cardona, 2015).

Figure 2.3 depicts detached breakwaters, which resemble groins but are parallel to the shore. Like groins, breakwaters may be constructed singly or in a field, and they can be emersed or submerged. Its cross-section is usually trapezoidal, and they may be constructed from concrete and rocky blocks. As much as they increase biodiversity and promote sediment deposition, reducing the need for artificial feeding, they are expensive (construction and maintenance), can generate conflict in the management of maritime space, and have a negative effect on the landscape when emersed breakwaters are utilized (van Rijn, 2013).

The main functions of detached breakwaters are:

- To reduce the action of the waves on the coast,
- To reduce erosion and retain sediments which can create tombola (Figure 2.3).

As seen in Figure 2.4, longitudinal adherent coastal defense structures are erected along a marginal or along the length of the coastline. They are used for beach protection. Often, they are sprayed in locations affected by or formerly affected by storm surges and erosion, which have caused damage to housing projects. The primary objective of these structures is to protect the coastline from the effects of the water. Its downsides include expensive installation and maintenance costs, loss of biodiversity, and sediment loss, which results in the wintertime lowering of the beach profile in regions next to the structures enhancing the seasonal variation of sediment volume (Mesuras, 2018).

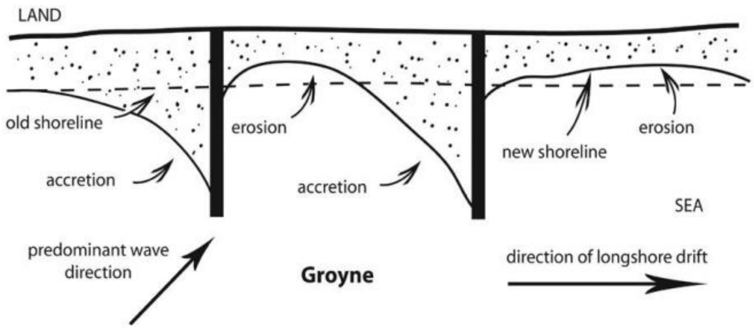

Figure 2.2 - Groyne field and its effects (O'Keefee, 1978).

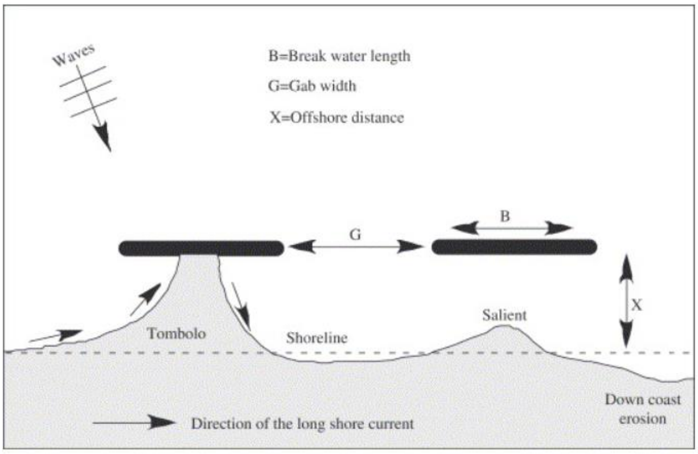

Figure 2.3 - Detached breakwaters [130].

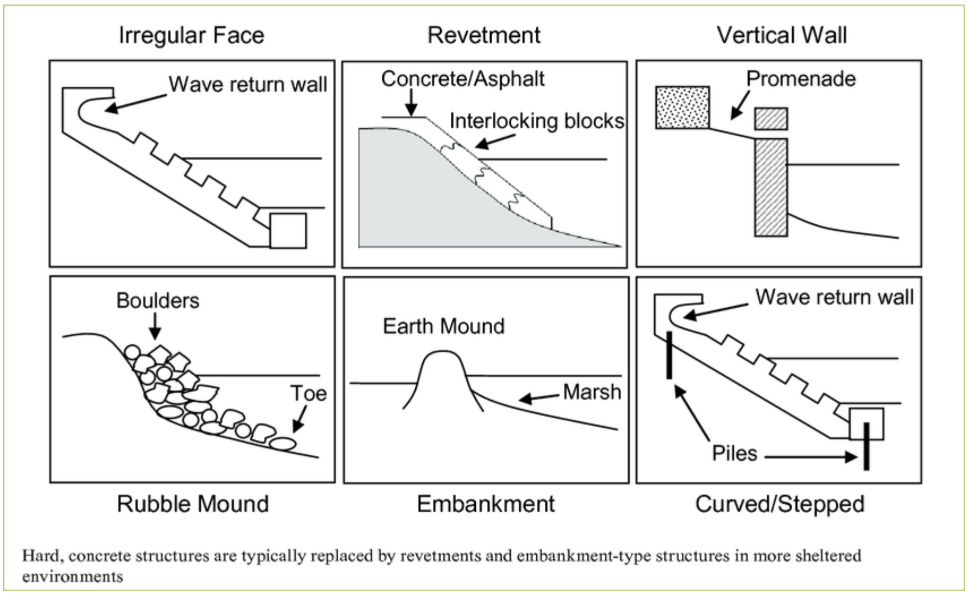

Figure 2.4 - Longitudinal adhering coastal defense structures [131].

Retreat

The retreat response can occur at various scales and degrees of complexity, including the relocation of a few particularly vulnerable homes, entire communities, large cities, and entire island populations to new host nations. Moreover, if this appears to be the most effective response of protecting people and property from coastal hazards, then it should be implemented. In fact, managed retreat raises a variety of social, cultural, psychological, and economic issues (Abel *et al.*, 2011). To prevent current economic losses, regulations may allow temporary construction in vulnerable areas for more than thirty years. Innovative planning concepts include buy-out programs to prevent future value loss (André *et al.*, 2016), and other scientific research investigates innovations in compensation arrangements to reduce the cost of compensation, although this cannot be the only source of funding for relocation strategies.

2.1.4. Governance archetypes for responding to sea level rise

Based on this typology of responses, (Bongarts *et al.*, 2021) proposed four governance archetypes for responding to SLR, which enables ranking the complexity of implementing the various approaches to coastal adaptation. Using an integrated, systems-based approach, the design of a new coastal model archetype encourages adaptation to new climatic conditions. In order to overcome the complexity of implementing responses that correspond to this archetype, a high level of stakeholder engagement in the decision-making process and extensive spatial planning are required.

On the vertical axis of the synthesis table (Figure 2.5), archetypes are categorized according to two contrasting paradigms. The initial paradigm is Protect against coastal hazards. It comprises of battling against the sea's advance in order to safeguard threatened infrastructure and population. Adapt to coastal hazards by embracing the mobility of coastlines is the second paradigm. If certain areas must be surrendered to the sea, this paradigm suggests planning upfront for the relocation of communities and activities to secure areas. Concerning governance modalities, (Bongarts *et al.*, 2021) hypothesize that the level of stakeholder engagement in the decision-making process is presently low for responses that fit the first paradigm and high for responses that suit the second paradigm.

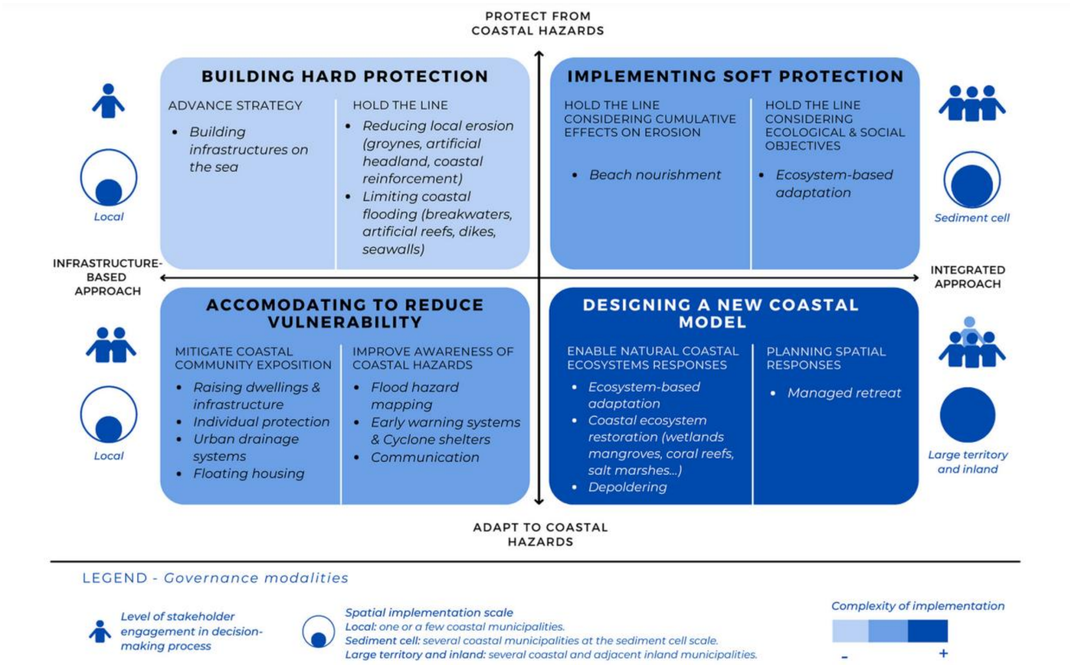

Figure 2.5 - Governance archetypes of adaptation strategies to sea level rise (Bongarts *et al.*, 2021).

The horizontal axis of the synthesis table also refers to how adaptation responses are planned and implemented, depending on whether they favour an Infrastructure-based approach, i.e., technological or technical solutions, or an integrated approach that takes into account broader societal objectives. Governance-wise, (Bongarts *et al*., 2021) hypothesize that the more integrated a response to coastal hazards is, the larger the spatial implementation scale must be.

2.2. OVERTOPPING

Wave overtopping problems at coastal areas occur when waves meet an emerged reef or structure with a lower crest elevation than the run-up level. During wave overtopping events, there are two main phenomena that should be considered which are wave transmission through the structure and the crossing water over the crest of the structure.

The main methods to predict wave overtopping and estimate overtopping volumes are:

- Empirical methods based on observation and comparison of structures. These methods use simplified representation of the physics of the process with dimensionless equations to allow establishments of relationships between structures and parameters and therefore the estimation or prediction of wave overtopping volumes and discharges (Van der Meer *et al*., 2018).
- The PC-Overtopping is used when empirical test data does not already exist, or when other methods don't give clear conclusions, but presents some practical limitations (Van der Meer *et al*., 2018).
- Numerical models, which simulate wave overtopping using a set of boundary conditions and flow equations in the process. There are several numerical models that can be used to predict wave overtopping, such as the non-linear shallow water equation models, Reynolds Averaged Navier-Stokes (RANS) and Smooth Particle Hydrodynamics (SPH) models. The model SWASH is based on nonlinear shallow water equations. The DualSPHysics and the FLOW-3D models are based on the Navier-Stokes equations and can be used, for instance, for sea walls design, because they provide reliable estimates of the wave impacts on the sea wall (Vanneste, 2014). The CFD (Computational Fluid Dynamics) numerical models simulate run-up, wave breaking and overtopping.
- Physical modelling is used to predict overtopping by laboratory experiments and involves the reproduction of the real structure at an appropriate scale (Van der Meer *et al*., 2018).
- NN Overtopping – The Neural Network tool is used for overtopping prediction, based on artificial intelligence, and supported by an extensive database of measured wave overtopping discharges and volumes (Van der Meer, 2018).

2.3. MACHINE LEARNING

Many years ago, humans endeavoured to comprehend the numerous phenomena that occur in the ocean. Complicated interactions involving physical, chemical, and biological processes make it difficult, even after centuries, to explain these phenomena (Dawarakish *et al*., 2013). Through statistical analysis, spectrum analysis, time series analysis, empirical formulas based on mathematical model experiments, and other mathematical and physical analyses, numerous methods have been developed. However, precise results are limited due to the complex interrelationships between numerous natural parameters (Goldstein *et al*., 2019).

Machine Learning (ML) models that identify and predict statistical structures from input and output data using computers to solve a variety of engineering problems in the natural world are attracting considerable interest. In the field of artificial intelligence (AI), ML is an inductive method that identifies rules through learning using data and results, as opposed to the conventional program method that derives results from rules and data. It employs a specific algorithm that can learn from the input data and provides accurate Network's Learning Process.

Machine learning algorithms

General ML algorithms consist of supervised learning, unsupervised learning, and reinforcement learning (Figure 2.6). Regression and classification are the two supervised learning models. Artificial neural network (ANN), support vector machine (SVM), and random forest (RF) are examples of supervised learning algorithms. Unsupervised learning is a technique for predicting the outcomes of new data by clustering patterns or characteristics from unlabelled data.

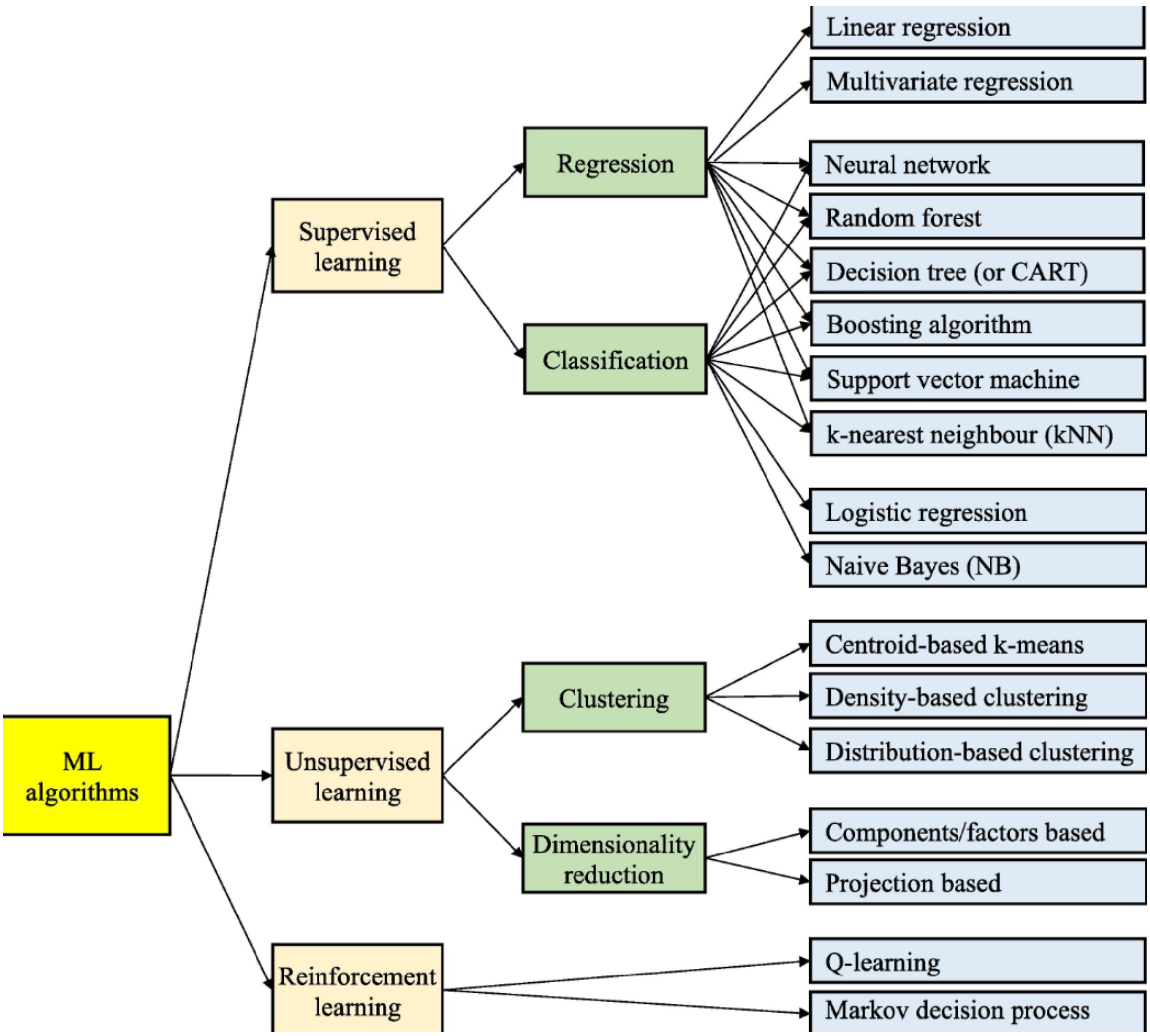

Figure 2.6 - Machine learning algorithms (Thai, H-T., 2022).

The **Linear Regression (LR) model** employs linear parameters and gives simple and rapid analyses. It generates a regression model using one or more features and derives parameters that minimize the mean squared error (MSE) between the experimental value (y) and the predicted value ($\hat{y}$) (Equations (1) and (2)).

$$\hat{y} = w[0] \times x[0] + w[1] \times x[1] + \cdots + w[p] \times x[p] + b \quad (1)$$

$$MSE = \frac{1}{n} \sum_{i=1}^{n} (y_i - \hat{y}_i)^2 \quad (2)$$

In some instances, the conventional LR method results in overfitting, i.e., when new data are provided, the predictive performance is subpar. As a result, lasso regression was created, which restricts models by force using the L1 regulation as follows (Equation 3):

$$E = MSE + penalty = \frac{1}{n} \sum_{i=1}^{n} (y_i - \hat{y}_i)^2 + a \sum_{j=1}^{m} |m_j| \quad (3)$$

where *m* is the number of weights, and a is the penalty parameter. This equation obtains *w* and *b* that minimize the sum of the MSE and penalty.

In **lasso regression**, the weights are zero, whereas in **ridge regression**, the weights are not precisely zero but are close to zero. Consequently, the lasso regression provides high accuracy only if some of the input variables are significant, whereas the ridge model provides high accuracy if the significance of the input variables is comparable in general (Kim, T., & Lee, W., 2022). The equation of lasso regression is given by:

$$E = MSE + penalty = \frac{1}{n} \sum_{i=1}^{n} (y_i - \hat{y}_i)^2 + a \frac{1}{2} \sum_{j=1}^{m} |m_j|^2 \quad (4)$$

An **Artificial Neural Network (ANN)** is a network-based information processing structure modelled after the human nervous system, in which basic functional processors are interconnected on a massive scale. In a feedforward method, the values are transmitted from the input layer to all nodes of the hidden layer. In addition, the coupling and activation functions transmit the output values of all nodes in the hidden layer to all nodes. The backpropagation algorithm redistributes weights between neurons so that they converge in a direction in which the errors are minimized, to minimize the difference between predicted and experimental values (Figure 2.7). This is done by using optimizers. Optimizers are algorithms used to change the attributes of the NN, such as weights and learning rate, in order to reduce the losses. There are numerous types of optimizers, including Gradient descent, Stochastic Gradient descent, Minibatch Stochastic Gradient descent, Adam, RMSProp, AdaDelta, and Adagrad.

In the neural network's data processing procedure (Figure 2.8), each node multiplies the input value by a weight and then passes the output value through the activation function before outputting the result, as shown in Equation (5).

$$N_j = \sum_{i=1}^{N_i} w_{ij} x_i + b_j \quad (5)$$

where *w* is the weight, *b* the bias, and *x* the input value.

Adjusting the gradient during activation training hinges on the activation function. Activation functions are functions that activate neurons in a network, similar to what happens in the brain, which contains touch, taste, vision, hearing, and scent neutrons. When a body is contacted, a signal is sent to the touch neutron, which then becomes active. In neural networks, various activation functions, such as the linear, sigmoid, tanh, exponential, softmax, ReLU (rectified linear unit), ELU (Exponential Linear Unit), and SELU (Scaled Exponential Linear Unit) are utilized (Kim, T., & Lee, W., 2022).

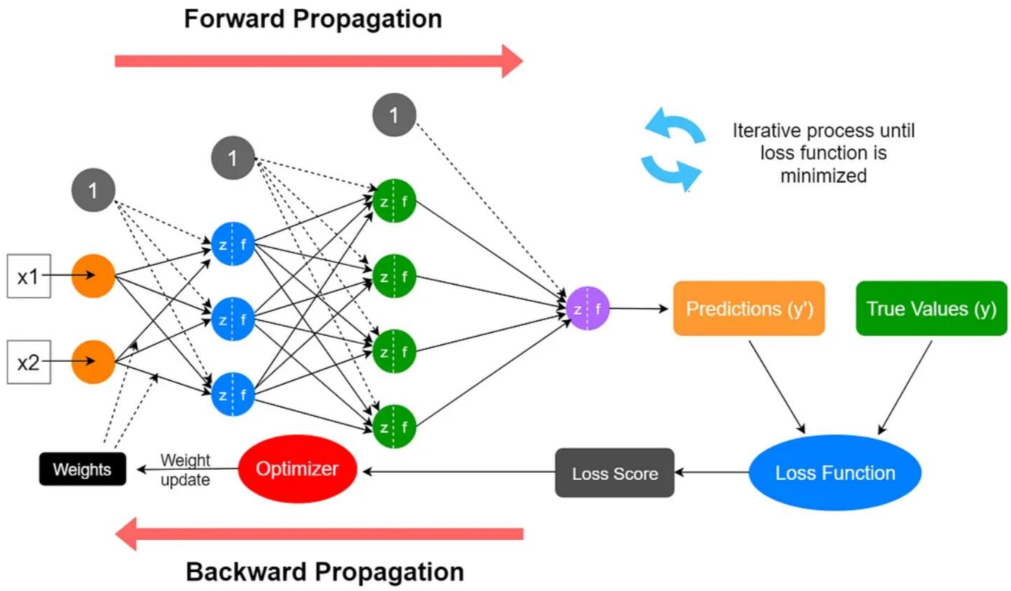

Figure 2.7 - Overview of a Neural Network's Learning Process [132].

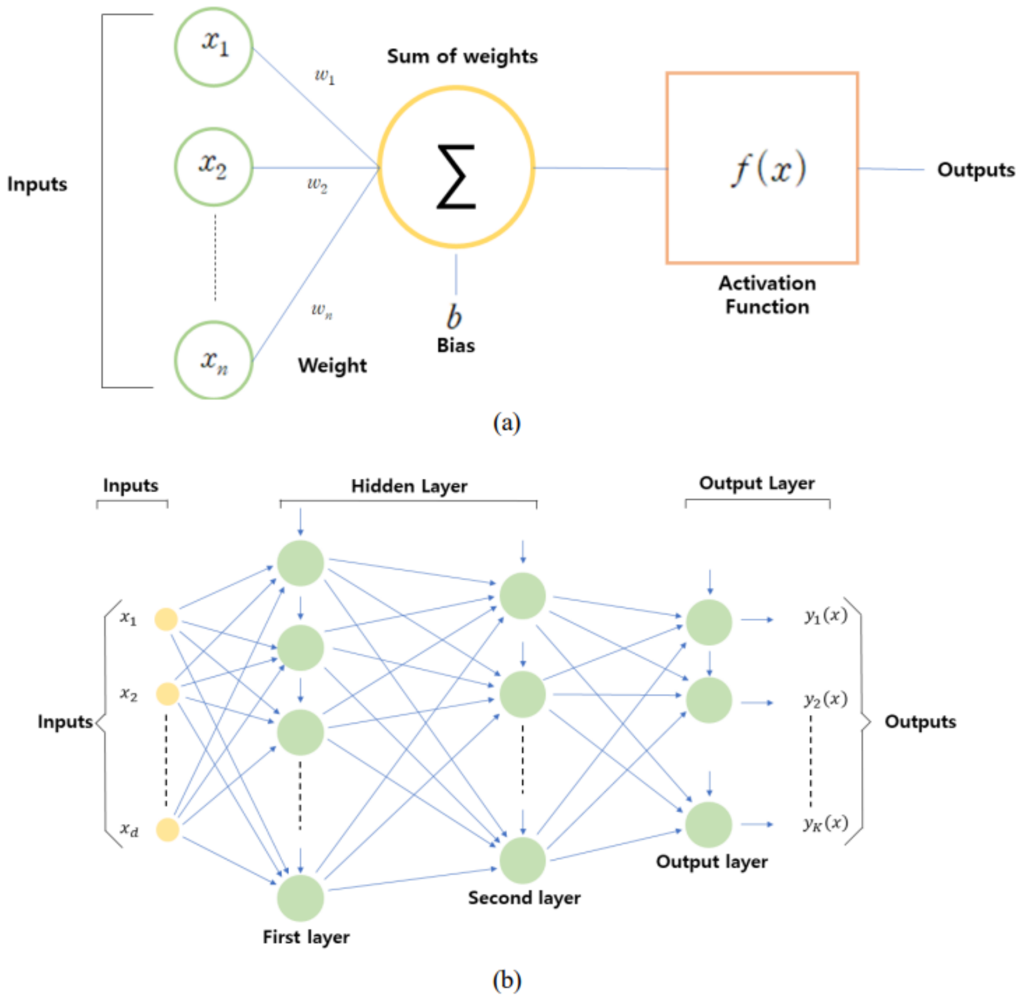

Figure 2.8 - Artificial neural network: (a) Neural network diagram of element; (b) typical layout of neural network (Liu *et al.*, 2021).

Support Vector Machine (SVM) regression training includes as many data points as possible within the specified margin error limit line. The limit line modifies the margin's breadth based on the hyperparameter. The first introduction of this approach was conducted by Boser *et al.* (1992) with the purpose of addressing classification problems, specifically in the context of support vector clustering (SVC), using non-linear classifiers. Support vector regression (SVR) was further extended to address regression problems, as documented by Vapnik (1995). The principles and methodologies used in Support Vector Machines (SVM) are also applicable to Support Vector Regression (SVR). The core principle of Support Vector Machines (SVM) is to discern dissimilarities across sets of data attributes, commonly known as vectors, in order to ascertain an optimal separation hyperplane that maximizes the margin (Figure 2.9). In this instance, the margin refers to the distance between the particle boundary and the support vector. It uses the following functions:

$$f(x) = \sum_{j=1}^{nsv} (\alpha_i - \alpha_i^*) K(x_i, x_j) + b \tag{6}$$

$$k(x_i, x_j) = exp\left(-\frac{\|x_i - x_j\|^2}{2\sigma^2}\right) \tag{7}$$

where α_i and α_i^* are Lagrangian coefficients, and $K(x_i, x_j)$ represents the kernel function. In general, homogeneous polynomials, polynomial kernels, Gaussian radial basis functions and hyperbolic tangent functions are used as the kernel function.

The kernel parameters operate by calculating the distance between data points in the enlarged feature representation, without explicitly performing the expansion itself (Müller, A. C., & Guido, S., 2016). There are two kernel techniques that are often used in Support Vector Machines (SVM). The **Radial Basis Function (RBF)**, commonly referred to as the Gaussian kernel, encompasses all potential polynomials of varying degrees. The **Polynomial** kernel is responsible for identifying all potential polynomials up to a certain degree based on the original features.

Support Vector Machines (SVMs) are capable of effectively handling datasets with intricate decision boundaries, irrespective of the number of features included in the data. The algorithm performs well on datasets of varying dimensions, including both low-dimensional and high-dimensional data. However, its scalability is limited as the number of samples increases. In order to achieve optimal performance, it is necessary to engage in meticulous hyperparameter tuning and thorough data pre-processing.

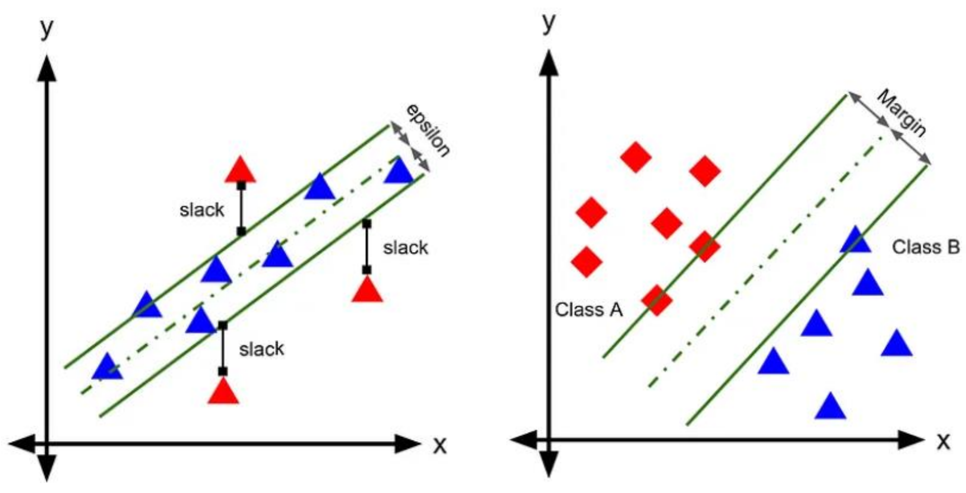

Figure 2.9 - Support Vector Machine for: regression (a) and classification (b) [135].

Decision trees are a kind of model that is built on a tree structure and is often used for classification and regression tasks. They acquire knowledge of the sequential implementation of if/else questions in order to construct a tree-based model that visually represents the decision-making process. Figure 2.10 illustrates a graphical representation consisting of four key components: the root node, branches, decision nodes, and leaf (terminal) nodes. The leaf node serves as an indicator of the ultimate choice to be taken (Thai, H. T., 2022). The procedure of constructing and analysing a decision tree classifier is identical to that of a decision tree regressor, with the exception that the regressor is unable to make predictions beyond the range of the training data.

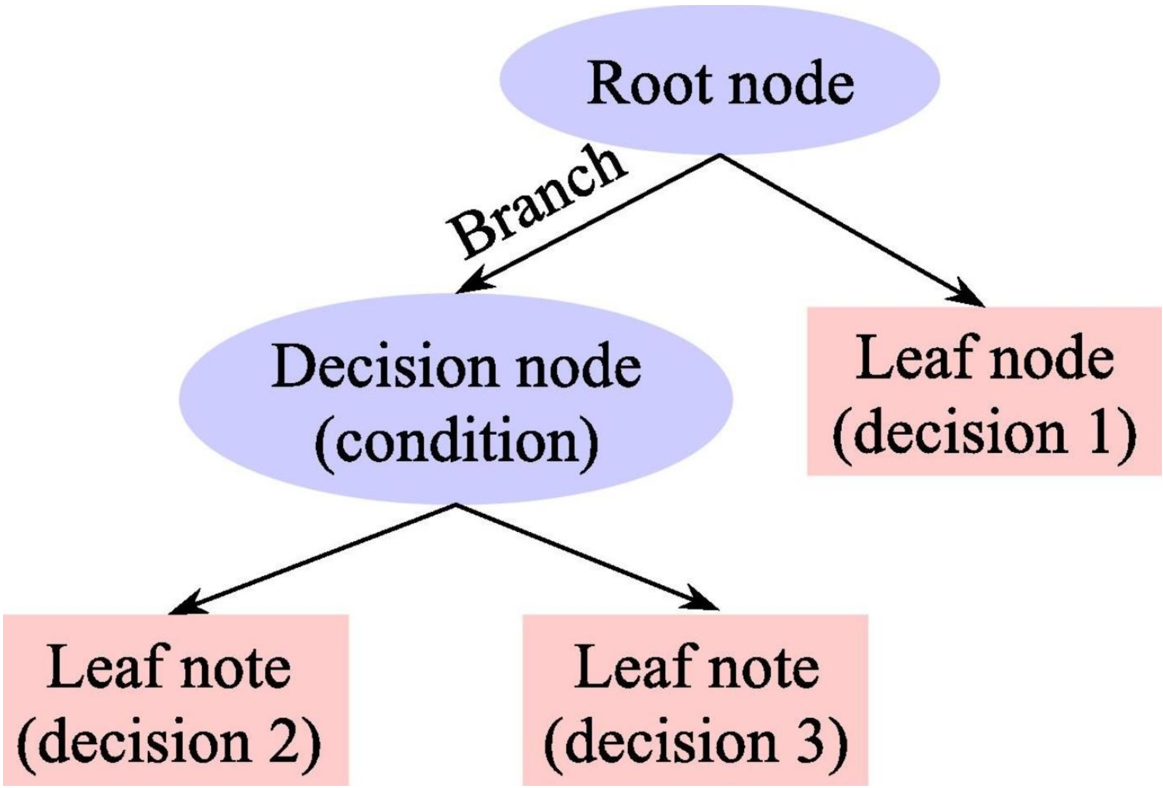

Figure 2.10 - Decision Tree algorithm (Thai, H-T., 2022).

One benefit of this approach is its ease of visualization and interpretation when the number of trees is small, without the need for data scaling. Hence, there is no need for any preprocessing of features as it effectively operates with characteristics that have varying scales (Müller, A. C., & Guido, S., 2016). One limitation of this approach is its tendency to overfit, resulting in suboptimal generalization performance even when pre-pruning techniques are used.

The **ensemble method** was developed to enhance the classification and regression tree's performance. By creating multiple classifiers and integrating their predictions, an accurate prediction model is generated. The ensemble models can be classified predominantly as bagging or boosting models. Bagging is a technique for reducing variance by averaging or voting on the results predicted by multiple models, whereas boosting is a technique for generating robust classifiers by combining weak classifiers.

Random Forest (RF) is a machine learning technique that belongs to the category of ensemble methods. It is based on the use of several Decision Trees. Ensemble learning refers to the methodology of using many models that have been trained on identical datasets, with the objective of aggregating their outcomes to provide predictions that are more precise or robust. Random Forest (RF) addresses the issue of overfitting by using an ensemble of diverse Decision Trees (DT). This is achieved by computing the average of the outcomes generated by all the individual trees inside the forest (refer to Figure 2.11). The algorithm employs bootstrapping as a method for constructing its decision tree. The process of bootstrapping entails the random selection of subsets of data over a predefined number of rounds and variables. Data scaling and parameter adjustment are not required for its implementation (Müller, A. C., & Guido, S., 2016). It is a method of improving the large variance of the decision tree and the large fluctuation range of performance. It integrates the concept and properties of bagging with randomized node optimization to surmount the shortcomings of existing decision trees and enhance generalization. Random Forest (RF) is a very effective machine learning technique that has the capability to operate on data without the need for extensive parameter adjustment or data scaling. One limitation of RF models is their suboptimal performance when applied to datasets with a large number of dimensions and sparse data.

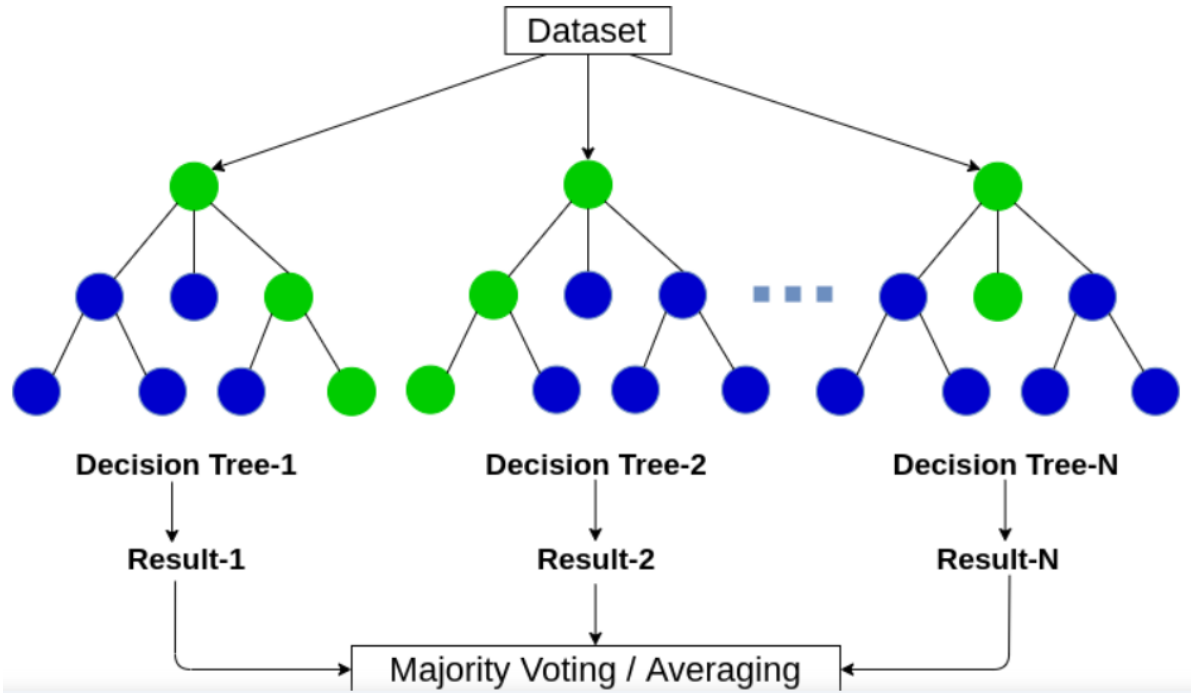

Figure 2.11 - Random Forest algorithm [136].

The **Gradient Boosting** Machine Learning algorithm is an additional ensemble technique that leverages the combination of decision trees. This tool has the capability to be used for both regression and classification tasks. In contrast to the random forest (RF) algorithm, the gradient boost algorithm constructs trees with the objective of rectifying the errors made by the preceding trees (Müller, A. C., & Guido, S., 2016). Randomization is not necessary for this method, however, it does need the implementation of robust pre-pruning techniques. Additionally, the usage of shallow trees in this approach facilitates speedier prediction. The sensitivity of this technique to parameter choices is greater in comparison to RF, however, it has the potential to provide accurate results when the parameters are well selected. The learning rate is a significant parameter that governs the pace at which each tree attempts to rectify the preceding one (Müller, A. C., & Guido, S., 2016). In order to make significant adjustments, complex models need a high learning rate. The selection of the number of trees, denoted as "n_estimators," for ensemble learning is a crucial parameter that governs the complexity of the model. An augmentation in the parameter "n_estimators" results in an elevation of the model's complexity, hence affording the model an increased capacity to rectify errors present in the training data. One of the primary limitations associated with this algorithm is that it requires careful tuning of the parameters, which might potentially result in a high computational cost.

Ahmad (2019) conducted research giving a summary about ML applications in oceanographically different areas as shown in Table 2.3.

Table 2.3 - Machine learning algorithms and scope of application in oceanography (Ahmad, 2019).

Types	Major machine learning algorithms	Scope and potential of application
Supervised	Linear regression	
	Support vector machine Support vector regression	1.Oil spill mapping and detection 2.Satellite image processing for land use 3.Retrieve Ocean surface chorophy11 concentration 4.Habitat modeling
	Decision tree	1.Resources management 2.Sediment properties
	Random forest	Mapping of marine substrates
	Naïve Bayes	
Unsupervised	k-means	Clustering ocean biomes
	PCA	
Reinforcement	Markov decision process	1.Quickly detect hazardous weathers 2.Detection of whale acoustics
Deep learning	Artificial neural network Recurrent neural network	1.Wave modelling 2.Coastal water monitoring 3.Prediction of coastal morphologic properties

ML-based algorithms are increasingly used in coastal engineering to predict wave generation, wave breaking, tidal changes, hydraulic properties around structures, and changes in shore profiles (Kankal and Yuksek, 2012). Some examples of the application of ML are provided in the following sections.

Wave prediction

James *et al*. (2018) created an ML model for predicting the characteristics of wave distributions, using Monterey Bay in California as the case study area. Using a physics-based model known as the simulating waves nearshore (SWAN) model, data were generated via several thousand cycles of iterative learning. Using a multilayer perceptron and a support vector machine, a model for predicting the significant wave height and peak period was also proposed.

Consideration was given to 741 input variables, including wave conditions at the interface (H_s, T_p, D), flow distribution within the grid (u, v), wind speed, and wind direction. In the meantime, 11,078 data points were used for training, where two output variables (the significant wave height and peak period) were calculated using the SWAN model.

The outcome demonstrated that the ML model regenerated more than 90% of the wave characteristics of the physics-based model with a mean squared error (MSE) of 9 cm. In addition, the computation time was much lesser than that of the SWAN model; consequently, it was anticipated that it will be a viable alternative to the physics-based model. Figure 2.12 is a heat map displaying the difference (ΔH) between the value predicted by the representative ML model and the value calculated using the SWAN model for the result of the ML model based on data derived from the SWAN model calculations of 11,078 cases. The image on the left displays the consequence of underestimating the significant wave height to a maximum of 15 cm near the estuary, despite the fact that the root mean square error (RMSE) is 6 cm. Nonetheless, the image on the right indicates an RMSE of 14 cm, although the error near the bay is reduced, and a distinct location-based trend is not displayed. Despite the significance of statistical values such as the RMSE, the application context may affect the model's reliability. Therefore, it was concluded that additional data analysis was necessary to enhance the precision.

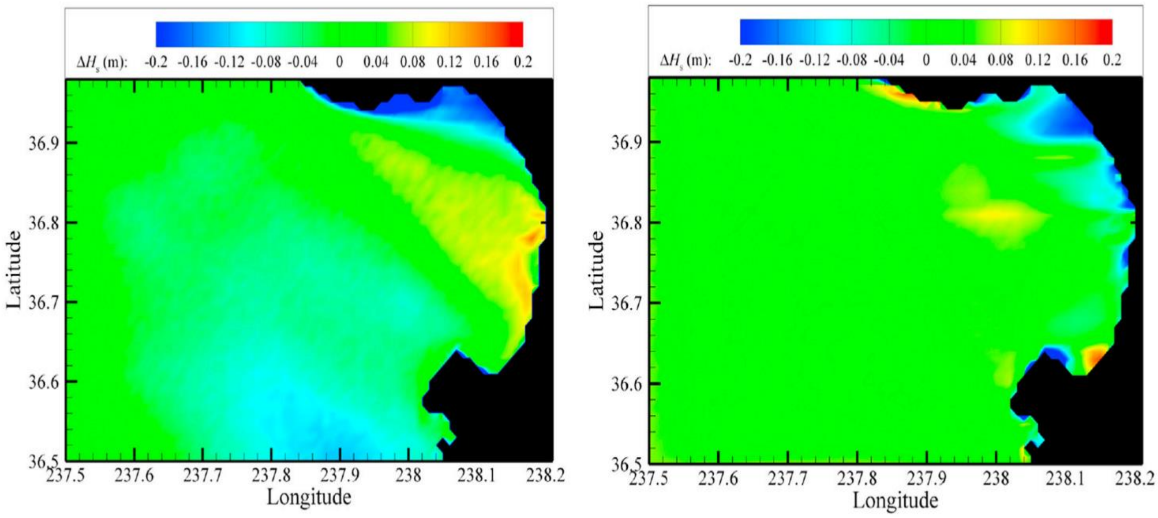

Figure 2.12 - Heat map displaying the difference (delta H) between the value predicted by the representative ML model (James *et al*., 2018).

Prediction of morphological changes

The seasonal variation characteristics of beach profiles were predicted by Hashemi *et al*. (2010) using an artificial neural network (ANN) model based on seven years of data from 19 stations near Tremadoc Bay, eastern Irish Sea, Since wave buoy data were not available near the study area, a SWAN numerical model was used to determine the effect of wind speed and direction on wave characteristics. The input variables for the model included nine parameters: the minimum wind speed, wind direction, continuous storm frequency, storm frequency, significant wave height, significant period, wave, beach slope, and wind duration. In addition, they developed a model with 12 output variables, including the elevation of 10 points of each cross-sectional profile, the area under each profile curve, and the length of each profile. In comparison to the observed value, the MSE converged to 0.0007, demonstrating the model's high predictive accuracy in estimating the characteristics of beach variability. Due to the complexity and uncertainty associated with the physical comprehension of morphological dynamics at the shore, the ML model may be a more effective instrument than the mathematical model for predicting changes in the beach profile at the same sites. However, the ML model is only applicable to previous measurement data; it cannot be readily applied to climates or structures not depicted in the training data. Therefore, a study incorporating mathematical models and machine learning is required.

Definition of used terms

- The word "**generalization**" pertains to the capacity of a model to effectively adjust and provide appropriate responses to novel, unobserved data that is derived from the same dataset used in constructing the model. The evaluation assesses the efficacy of a model in assimilating new data and generating precise predictions subsequent to its training on a designated training dataset.

- **Overfitting** refers to the phenomenon in which a model achieves high accuracy while making predictions on the training dataset, but fails to generalize well when presented with new, unseen data. This phenomenon occurs when a sophisticated model attempts to include all training data, even incorrect information within the dataset, therefore compromising its learning process. When evaluating the test dataset, it yields outcomes characterized by high variance and low bias.
- **Regularization** refers to the deliberate imposition of constraints on a model to prevent overfitting, hence enhancing the ability of the model to make accurate predictions on unseen data. One possible approach to achieve this objective is to reduce the magnitudes of the coefficients. L1 and L2 regularization techniques are often used in linear models, whereas dropout is a regularization approach commonly used in neural networks.
- **Underfitting** refers to the phenomenon in which a model exhibits poor performance on both its training and testing datasets. This phenomenon occurs when a model exhibits excessive simplicity, is trained on a substantial amount of unprocessed data, and thus struggles to adequately capture its underlying patterns and relationships. When subjected to testing, this will provide outcomes characterized by a significant bias and low variation.

2.4. COMPARATIVE ANALYSIS OF SIMILAR CASES

Many human activities have weakened sediment supplies to coastal regions, reducing the quantity of sediments accessible on beaches and causing a general and periodic retreat of the coastline position. In recent decades, several coastal defence measures, often longitudinal revetments, have been implemented in regions with significant erosion rates. However, the lack of monitoring of these coastal defence structures, coupled with the high exposure of urban areas to erosion, has resulted in an increase in the frequency of damage events in multiple locations and overtopping, causing damage to infrastructures, commercial establishments, and residential properties. In this section, a comparative analysis is made from studies and works that were conducted to improve the safety in coastal areas by means of implementing strategies that would reduce overtopping.

2.4.1. FIRST CASE STUDY

This case study consists of two research works, one developed by (Pereira *et al.*, 2013) and the second one by (Ferreira *et al.*, 2021).

The Portuguese northwest coast faces the Atlantic Ocean, is orientated around N218E and mostly composed of sand. The study area is situated in the central part of Portugal, inside the districts of Aveiro and Coimbra, and comprises four coastal municipalities: Aveiro, Ílhavo, Vagos, and Mira. This section of coastline is around 35 km in length (Figure 2.13). The topography of the examined stretch is determined by its closeness to the Ria de Aveiro lagoon and by the barrier of sand dunes that separated the lagoon from the sea between the eleventh and nineteenth centuries. This kind of morphology is generally linked with substantial sediment deposition from rivers that carry enormous quantities of sediments, particularly during flood seasons. Douro River, situated to the north of the study region, provided the most sediments to the system under study (Coelho *et al.*, 2009a).

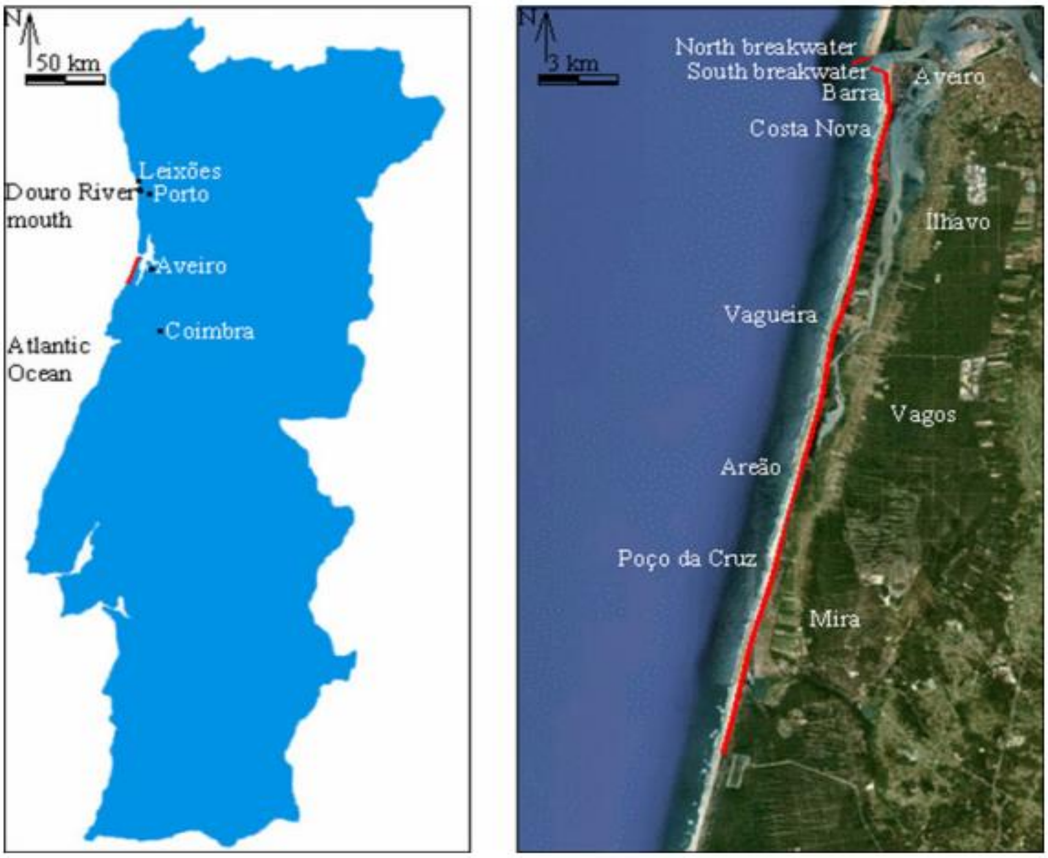

Figure 2.13 - Study area: Location in Portugal (left); Main urban areas in the Barra-Mira coastal stretch (right) (Pereira *et al*., 2013).

2.4.1.1. Section 1

This section aims to examine three of the most significant climate change occurrences over a length of the Portuguese west coast (at Aveiro region)

Figure 2.14 shows the number of coastal defence interventions in the study area over the last few decades, given that Coastal interventions encompass all measures made to safeguard land from the effects of sea waves, including the construction of new structures, maintenance of existing structures, nourishment of beaches, and reinforcement of dunes systems. According to Pereira *et al*. (2013), the metropolitan areas with the highest artificialization (Barra, Costa Nova, and Vagueira) are the most vulnerable to the sea wave action and also where most interventions are located.

Up to 2011, 66 events with energetic wave actions were reported, 30 of these incidents corresponded to overtopping, 16 to dunes destruction, 15 to infrastructures' destruction and damages to coastal defences, and 5 to coastline retreat, (Pereira *et al*., 2013). Costa Nova (22 incidents) and Vagueira were the most impacted beaches (20 events). In the 1990s, an average of two incidents per year were recorded, however in the 2000s, the average increased to three. Table 2.4 present, the number of reported events related with energetic wave conditions. Other figures related with the wave climatic conditions described by the frequency of occurrence of wave direction and wave height classes to be considered for the LTC numerical model simulation, including the description of the numerical model can be found from (Pereira *et al*., 2013).

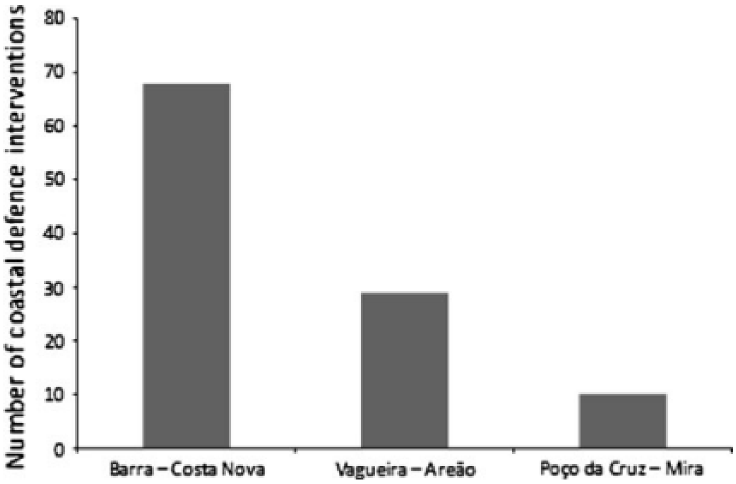

Figure 2.14 - Number of coastal defense interventions performed until 2011 in different coastal stretches of the study area.

Table 2.4 - Number of reported events (until 2011) related with energetic wave conditions, in the study area (Coelho *et al*., 2013).

Events	Areão	Barra	Costa Nova	Mira	Poço da Cruz	Vagueira
Overtopping	8	5	10	1	0	6
Dune's destruction	2	0	8	2	0	4
Infrastructure damages	0	0	0	1	0	2
Coastal defences damages	0	0	4	1	0	7
Shoreline retreat	1	1	0	1	1	1

In consideration of the above, eight simulation runs were conducted for each scenario to provide a range of likely outcomes using shoreline evolution numerical model LTC, the model was developed to support coastal zone planning and management in relation to coastal erosion problems (Coelho, 2005; Coelho et al., 2004, 2007, 2013). During the preliminary phase of this investigation, it was determined that eight simulations were sufficient to illustrate the amplitude range of the shoreline location, taking into account the optimization of resources and simulation procedures. The link between resources and quality outcomes depends on the processing time of each run. Each wave effect is accounted for using a 1-h time step, and 50-year calculations need 438,000-time steps (for each run, in each scenario). Figure 2.15a) illustrates a brief segment of a coastal zone in the vicinity of a groin as an example of the eight shoreline positions produced (eight simulation runs) while always using the identical wave spectrum circumstances for each simulation scenario. For the purposes of risk assessment and map display, the area lost in all eight simulations was deemed a high-risk region for erosion. These classification criteria are shown in red in Figure 2.15b), which depicts this region. The orange region, which represents the area that was lost in at least one of the simulations, is rated as having a moderate risk of erosion during the time of study. Lastly, regions of accretion are denoted by the colour green and have a minimal danger of erosion.

In this first part of the work, it was concluded that shoreline evolution projections are now required for the development of more effective planning strategies for coastal zones. Thus, the study of vulnerability and risk in coastal regions is essential to the formulation of effective planning and management strategies, allowing for improved decision-making in places where the risk is already present. Adaptation plans must be undertaken, taking into account the assessment of repercussions and options for mitigating social and economic costs and benefits of potential scenarios. Long-term (decades to centuries) time horizons should be emphasized for the completion of these important activities.

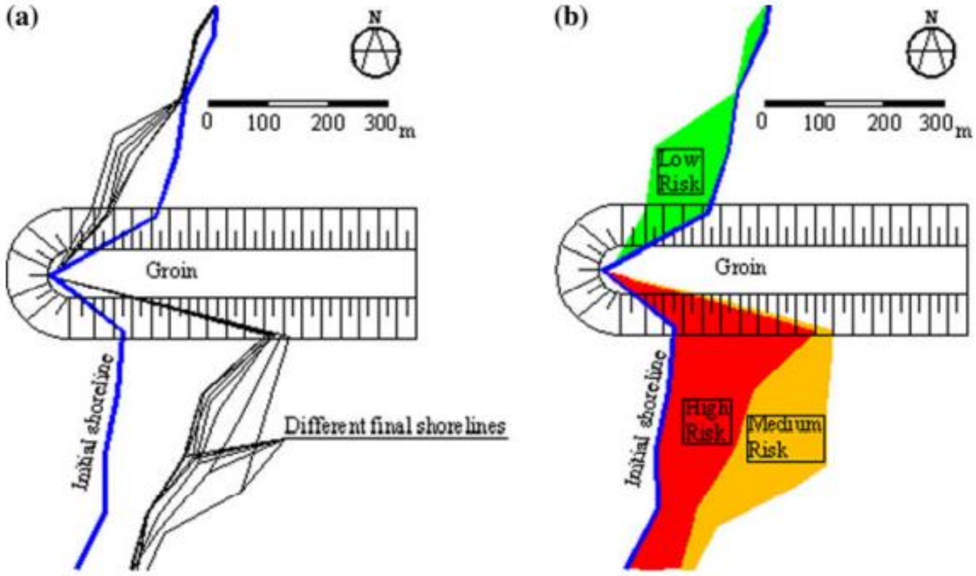

Figure 2.15 - Representation of shoreline evolution modelling: a) position of shoreline in eight runs; b) representation of the risk (Coelho *et al*., 2013).

2.4.1.2. Section 2

As already mentioned, the second study was conducted to examine and analyze coastal management options based on the use of a technique of coastal erosion risk classification, allowing for straightforward scenario comparison. The research was conducted for the Barra-Vagueira length of the Portuguese coast. CERA technique and its plugin for the QGIS program were used to evaluate the erosion risk of the Barra-Vagueira stretch under several coastal erosion mitigation scenarios.

Developed by Narra (2018), the CERA methodology permits the assessment of coastal erosion risk based on the source-pathway-receptors-consequences (SPRC) conceptual model. This model considers the various system components in order to determine how risk is dispersed. In the CERA methodology, the wave climate action capable of causing erosion (waves, cyclones, and sea-level trend) is the source of hazard. The distance between the study location and the coast is represented by the path. The territory and the people are the receptors, and the result is the loss of territory (Narra 2018; Narra et al. 2019). The propagation of the coastal erosion risk is evaluated using four modules: susceptibility, value, exposure, and coastal erosion. The modules are then combined to produce vulnerability, consequence, and risk results. The application requires a total of 12 parameters for the entire territory where the coastal erosion risk is to be assessed, including geomorphology, coastal defence structures, infrastructures, population density, ecology, distance to the coastline, topography, storm surge, wave height (m), number of storms per year, shoreline change rates (m/year), and sea-level trend (mm). In order to facilitate the application of CERA, Narra (2018) developed a QGIS plugin.

This coastal stretch has experienced erosion rates of 8 m per year over the last 50 years (Lira *et al*., 2016) and has a sediment deficit of the scale of 10^5 m^3/year (Santos *et al*., 2014).

Mitigation strategies

Guidelines for coastal management and planning were derived from the work of the Portuguese Littoral Working Group (Santos *et al*., 2014). The studied coastal defence methods included both new coastal defence structures and longer lengths of the existing groins. Table 2.5 highlights the various examined defence scenarios.

The following constant shoreline change rates were examined for the Nourishment strategies: +0.5 m/year; 0.5 m/year; 1.5 m/year; 2.5 m/year; and 3.0 m/year. According to CERA methodology, these values were chosen to impose distinct classes for the metric "shoreline change rate". In addition, the figures reported by Fernández *et al*. (2019) for coastline position change for the period between 2013 and 2018 along the Barra-Vagueira stretch were examined (Table 2.6).

Table 2.5 - Description of the defense scenarios (adapted from Ferreira *et al*., 2021).

Scenario	Description
Scenario D.1	Increased length of the existing groins: +100 m to +500 m in increments of 100 m
Scenario D.2	Detached breakwater at south of Barra, considering different structures length: from 120 to 480 m in increments of 120 m
Scenario D.3	Detached breakwater at front of the urban area of Vagueira, considering different structures length: from 120 to 480 m in increments of 120 m
Scenario D.4	Detached breakwater at the south of Vagueira, considering different structures length: from 120 to 480 m in increments of 120 m
Scenario D.5	Longitudinal rocky revetment at the south of Barra with 940 m of length
Scenario D.6	Longitudinal rocky revetment at the south of Vagueira with 365 m of length

Table 2.6 - Shoreline change rate in Barra-Vagueira (m/year), from 2013 to 2018, (Fernández *et al*., 2019).

Barra – Costa Nova	Costa Nova - Vagueira	Vagueira - Areão
+0.16	-2.46	-0.01

Climate change

The analysis of long-term changes in coastal regions should not be limited just to the examination of their reaction to sea level rise (SLR), but rather should be conducted within a broader framework that encompasses all elements of coastal climatology. Indeed, climate change will have an impact not only on the relative sea water surface level, but also on several climatic elements such as storm characteristics (including strength, duration, and frequency), temperature, rainfall, and evaporation rates. Modifications in these variables will also have a significant impact on the enduring coastal transformation. Hence, it is vital to establish a clear definition of the current climatic conditions, trace their historical progression, and anticipate future climate change in order to cultivate a full comprehension of their impacts on coastal regions. The climate change effect scenarios that were deemed most pertinent for this investigation included the rise in seawater levels, the augmentation of wave heights, and the rotation of wave directions towards the north. In order to assess the influence of sea level rise (SLR) on the research area, a consistent and uniform rate of 1.5 mm/year was used across the whole of the numerical modelling simulation periods. Table 2.7 presents wave characteristics for climate change scenarios that were determined by analysing three numerical model-generated series of wave data: historical, RCP4.5, and RCP8.5. Other relevant information regarding climate change effects considered can be found in (Pereira *et al*., 2013).

Table 2.7 - Wave climate characteristics for the different wave series.

Series	H_s [m]	No. of storms [per year]	Sea-level trend [mm/year]
Baseline Scenario	2.16	10	+1.27
Historical (1960 – 2005)	2.67	25	+1.41
RCP4.5 (2026 – 2045)	2.61	25	+4.89
RCP4.5 (2081 – 2100)	2.50	21	+6.58
RCP8.5 (2026 – 2045)	2.58	25	+6.11
RCP8.5 (2081 – 2100)	2.47	19	+13.84

Results and discussion

Compared to the Baseline Scenario, in which about 36% of the Aveiro region is classified with class 5 erosion risk, in the accretion of sediments scenario (shoreline change rate equal to+0.5 m/year), 38% of the territory presents a coastal erosion risk classification of class 3 and 62% of class 4 (no class 5 is observed). More than half of the coast is at high danger of erosion, and 88% of it is classed as level 5 on the coastal erosion module's scale, see (Pereira *et al*., 2013).

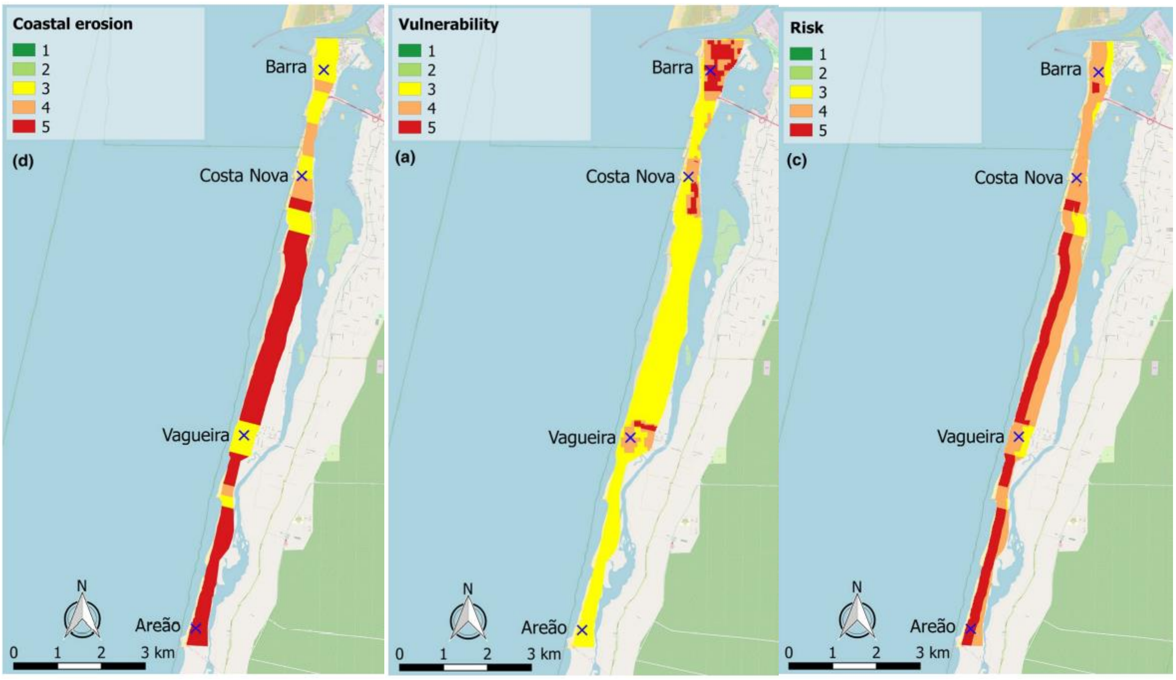

Figure 2.16 – Present the mapping of coastal erosion ranging between class 3 and 4 and most of the area shows the highest class or erosion, the area shows class 3 of vulnerability as the highest percent and lastly the risk range between 3 and 5.

The CERA methodology does not combine the simultaneous effect of multiple coastal defence structures located in the same area of the stretch, and it has been determined that there is no advantage in lowering the susceptibility of the stretch through the deployment of a detached breakwater on the urban waterfront of Vagueira, as the territory maintains the same susceptibility classification as in the current situation due to the presence of a rocky revetment. Similarly, a detached breakwater with a length more than 360 m south of Vagueira, where there are already other structures, would not reduce the stretch's vulnerability.

The findings of the research indicate that the pace of coastline retreat is a significant element in the risk evolution of the study region, with a decrease in shoreline retreat reducing the risk of erosion along the length. Hence, initiatives that allow for the replacement of the sand shortfall along the Barra-Vagueira coastline may be effective techniques for mitigating the existing coastal erosion issues. This finding is consistent with the approach outlined by Santos *et al*. (2014).

The results indicate that strategies aimed at reducing the sediment deficit and constraining the regressive trend of the coast are the solutions that result in a more substantial decrease in coastal erosion risk, resulting in the conclusion that significant advantages can be obtained from artificial beach nourishments or avoid solutions to reduce coastal erosion risk. Building coastal defence systems or extending the length of existing ones contribute to lowering a territory's vulnerability to coastal erosion, but do not considerably lessen the danger of coastal erosion.

2.4.2. Second case study

In this section, the town of Tseung Kwan O in Hong Kong, China, is taken as a case study. The objective of the research carried out was to construct a flood analysis model that integrates the impacts of numerous flooding triggers, such as precipitation, high sea levels, and wave overtopping during intense tropical storms, and to explore coastal flood risks in an urban region at the street scale (Qiang *et al*., 2021).

In 2018, Typhoon Mangkhut was one of the most powerful tropical cyclones to strike the Pearl River Delta in recent decades. The ten-hour duration of the tenth hurricane warning issued by the Hong Kong Observatory on September 16 was the second-longest since 1946 (HKO, 2020a). Figure 2.17 depicts Typhoon Mangkhut's route. It formed over the western North Pacific and intensified into a super typhoon on September 11. It weakened after traversing the northern portion of Luzon, Philippines, but rebuilt its eye before making landfall in Jiangmen, Guangdong Province, on September 16; and it weakened again after making landfall in Jiangmen, Guangdong Province, on September 16.

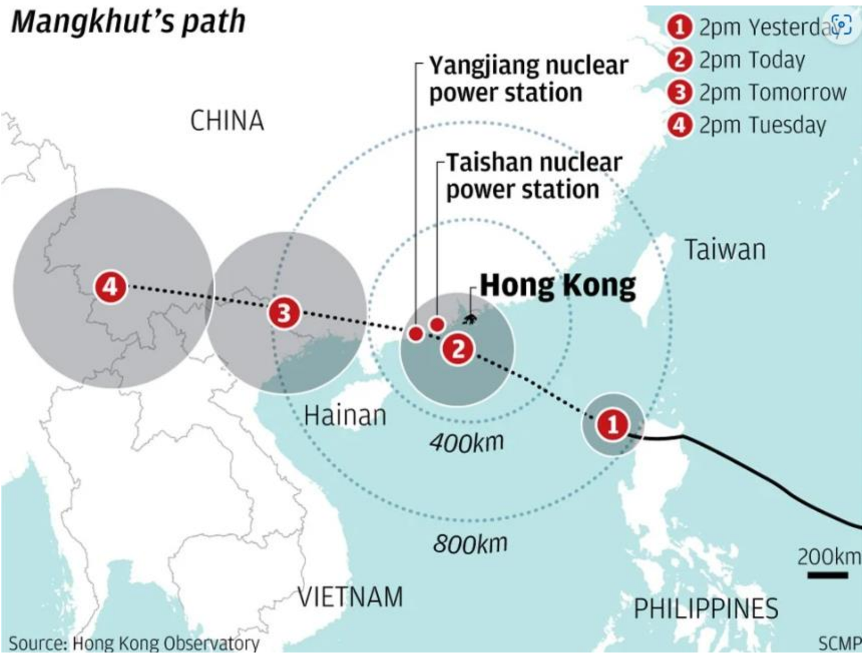

Figure 2.17 - Track of Typhoon Mangkhut in September 2018 [133].

Typhoon Mangkhut inflicted extensive damage in China and the Philippines. According to news accounts, there were at least 82 fatalities, 138 wounded, and two missing on the island of Luzon, as well as around 15,000 destroyed homes. At least 458 injuries were recorded in Hong Kong and 40 in Macao. There were at least six deaths and 4.64 million people impacted in the Chinese provinces of Guangdong, Guangxi, Hainan, GuiCDou, Hunan, and Yunnan (CMA, 2018).

A number of tidal stations experienced record-breaking storm surges (HKO, 2020c), including Quarry Bay Station (2.35 m) since 1954, Tai Po Kau Station (3.4 m) since 1962, and Tism Bei Tsui (2.75 m) since 1974.

As reported by local media, the increasing sea level and enormous waves pushed a substantial volume of overtopping (Figure 2.18a), generating a "small tsunami". Significant damage was incurred to the TKO Waterfront Park's promenades and amenities (Figure 2.18c). Several high-rise structures had electricity and water outages. Following Typhoon Mangkhut, a wave wall was built at the TKO Waterfront Park to mitigate the hazard of wave overtopping (Figure 2.18b).

Figure 2.18 - Photos of the Tseung Kwan O waterfront park: (top left) wave overtopping during Mangkhut (video snapshot: https://www.youtube.com/watch? v=fmViQCDc1FM); (bottom) damage to the promenade and waterfront facilities; (top right) wave wall built after Typhoon Mangkhut (modified from: https://www.devb.gov.hk/filemanager/en/content_1044/20200607_04.html). (Qiang *et al.*, 2021).

This study developed a flood analysis model that considers the combined effects of wave overtopping, high sea levels, and rainfall in order to investigate the propagation and retreat of flooding in coastal urban regions and to assess the risk to residents posed by multiple flooding triggers during powerful tropical cyclones. As an input discharge hydrograph, wave breaking is included in the model in a flexible manner. The model is used to replicate an instance of coastal flooding that occurred in Tseung Kwan O (TKO), Hong Kong, during Super Typhoon Mangkhut. The effects of engineering mitigation solutions, such as urban drainage facilities and a wave wall, are explored in depth, and the built environment is defined using LIDAR data with a high resolution.

To estimate the flooding in TKO during Typhoon Mangkhut, the town center area and the adjacent catchments are included in the model with a grid cell size of 5.0 m, which is fine enough to represent the features of urban amenities in detail. The total number of grid cells is 140,666. The elevation of each grid cell is derived from a digital topography model of Hong Kong based on aerial pictures captured between 2014 and 2015 (Available at DATA.GOV.HK).

For the sake of this dissertation, more information on how the numerical model works and how it was used for flood analysis model in a coastal urban area and overtopping discharge estimation can be found in (Qiang *et al*., 2021).

The first abstraction parameter that takes into consideration rainfall collection by vegetation and ground objects, the infiltration parameters, and the Manning's coefficient are determined according to local land cover types based on FLO-2D (2018) and Lumb (1965), which are presented in Table 2.8.

Within the study region, there are seven outfalls, all of which are situated near the coast and are susceptible to the fluctuating sea level. Drainage infrastructure is an essential component of urban infrastructure. To examine the efficacy of the drainage system in mitigating flood danger in response to different triggers, six simulations are run, as indicated in Table 2.9.

Table 2.8 - Parameters for the flood analysis model (Adapted from Qiang *et al*., 2021).

Parameter	Urban area	Vegetated land	References
Mannung's coefficient	0.04	0.4	FLO-2D (2018)
Initial abstraction (mm)	1.27	6.35	FLO-2D (2018) and Lumb (1965)
Hydraulic conductivity (mm/hour)	-	16	FLO-2D (2018) and Lumb (1965)
Porosity	-	0.44	Lumb (1965)
Suction (mm)	-	109.2	FLO-2D (2018) and Lumb (1965)
Initial saturation	-	0.74	Lumb (1965)
Soil depth (m)	-	20	Lumb (1965)

Table 2.9 - Simulation scenarios for different flooding triggers and drainage condition. (Qiang *et al*., 2021).

Scenario	Flooding triggers	Drainage condition
Baseline	Rainfall; high sea level; wave overtopping	Allow backflows at outfalls
1	Rainfall; high sea level; wave overtopping	Not allow backflows at outfalls
2	Rainfall; high sea level; wave overtopping	No drainage
3	Rainfall; high sea level	Allow backflows at outfalls
4	Rainfall; high sea level	Not allow backflows at outfalls
5	Rainfall; high sea level	No drainage

Figure 2.19 shows the simulated flood maps for the six scenarios. The flood extent (defined as the region with maximum flow depths higher than 0.15 m) decreases in the vicinity of Chin Shin Street when tidal control structures are implemented, indicating that tidal control structures prevent flooding in high sea

level scenarios. Because wave overtopping is disregarded in the study, the locations of flooding are spatially dispersed in situations when drainage infrastructure function (Scenarios 3 and 4).

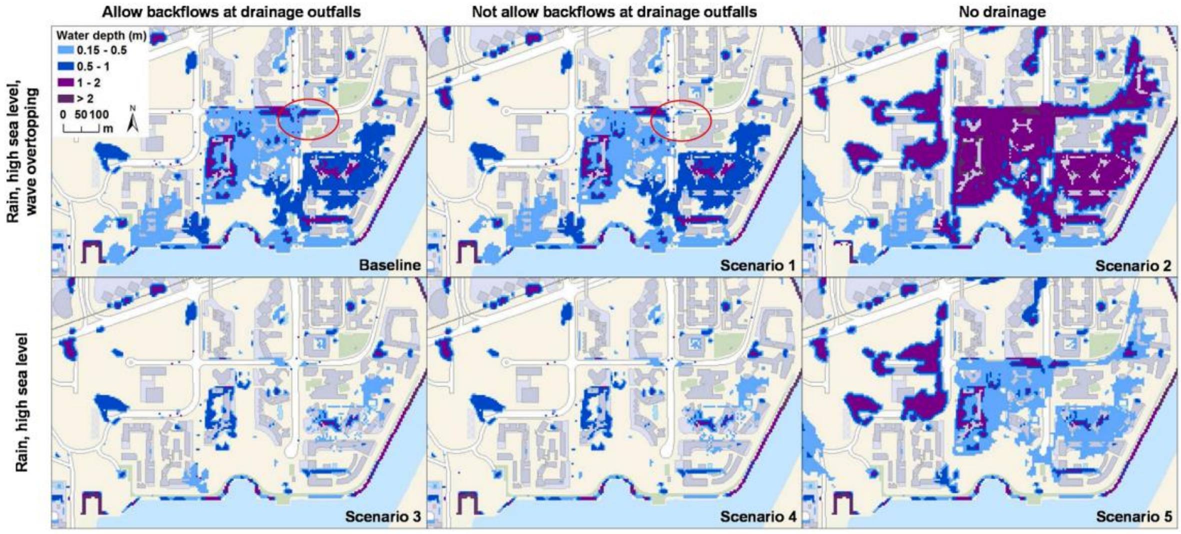

Figure 2.19 - Comparison of simulated maximum flow depths upon different flooding triggers and drainage conditions in Table 2.11 (Adapted from Qiang *et al*., 2021).

It was fortunate that the peak of the storm surge did not overlap with the high astronomical tide during Typhoon Mangkhut. The water level might be more severe if high tides and peak storm surges occur simultaneously, as occurred during Typhoon Hato in 2017. To evaluate the adverse combination, the recorded time series of storm surge is advanced 14 hours, the peak of storm surge and high tide are superimposed, and a synthetic sea level is formed (Figure 2.20b). The apex of the synthetic sea level curve is 4.19 m above Chart Datum, which is 0.54 m more than the highest sea level reported during Mangkhut. With the occurrence of wave overtopping during Mangkhut, the Civil Engineering and Development Department initiated a project to construct a 1.1-meter-tall wave wall along the TKO waterfront promenade. In this part, the simulated scenarios provided in Table 2.10 are used to evaluate the potential flooding situations resulting from an adverse combination of storm surge and astronomical tide, as well as the efficiency of the wave wall (Figure 2.21).

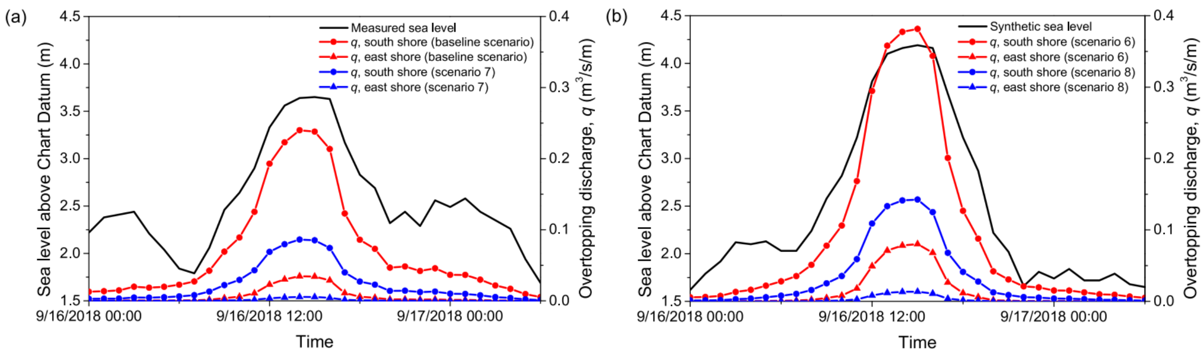

Figure 2.20 - Sea level and overtopping discharge for various storm surge, tide, and wave wall height combinations from Table 3: (a) sea level as observed; (b) sea level as anticipated (Qiang *et al*., 2021).

Table 2.10 - Simulation scenarios and areas of dangerous region for pedestrian upon different storm surge-tide combinations and wave wall heights (Qiang *et al*., 2021).

Scenario	Sea level	Wave wall	Area of dangerous region for pedestrian [m^2]
Baseline	Measured (3.65 m, Fig 12a)	No	1775
6	Synthetic (4.19 m, Fig 12b)	No	7950
7	Measured (3.65 m, Fig 12a)	Yes	300
8	Synthetic (4.19 m, Fig 12b)	Yes	375

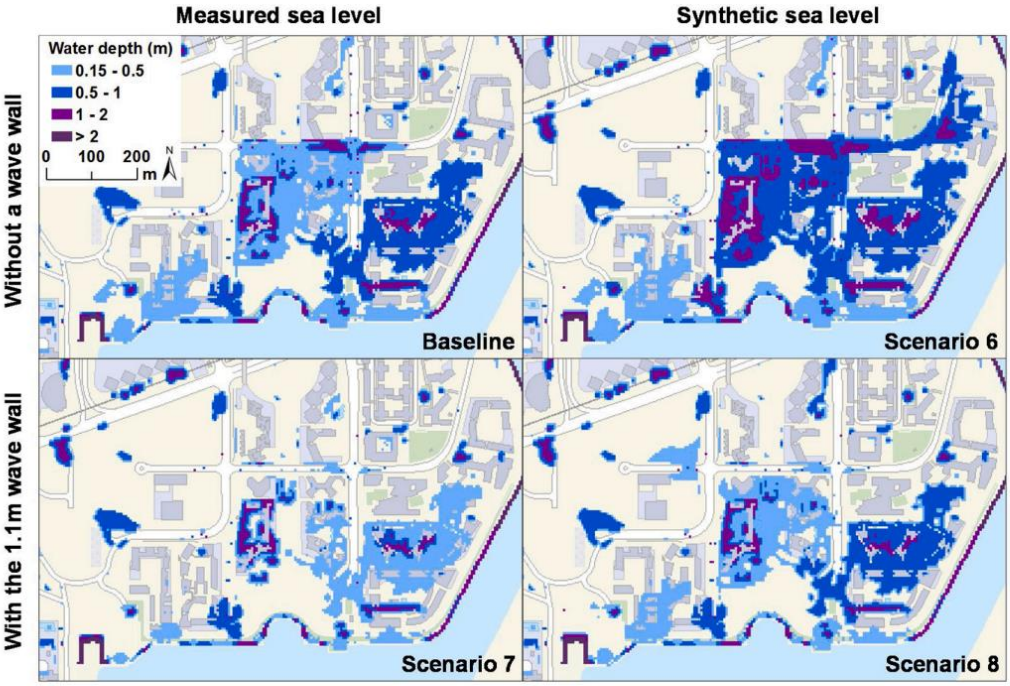

Figure 2.21 - Comparison of simulated maximum flow depths different combinations of storm surge, tide and wave wall height in Table 2.10.

In Scenarios 7 and 8, the decline in drainage effectiveness near the coast owing to the building of wave barriers is not accounted for, which may result in an underestimation of the severity of floods. Yet, with the completion of the wave wall, hazardous regions have almost disappeared in both sea level scenarios (Scenarios 7 and 8). Thus, the wave wall is deemed beneficial for ensuring the protection of local populations. Note that the stability of children in moving water is not taken into account.

The model accurately replicates the flooding conditions. The extensive flooding was caused mostly by wave overtopping, and neglecting the impact of waves would significantly understate the severity of the disaster.

2.5. CONCLUSIONS

Coastal engineers do consider climate change, but this must be strengthened, particularly in terms of mid- and long-term planning, and adaptation actions must be incorporated into system scale management schemes. Coastal engineers would benefit from training and preparation specific to climate change hazards and adaptation concerns. For the design and adaptation planning of structures, the widest range of potential future alterations must be considered. In some instances, available computational resources may be a limitation since they don't include other parameters that are important to analyse and predict the effects of climate change.

It can be easily observed that, from the reviewed studies from several authors, there are some uncertainties in the results obtained. This is mostly due to different models that were used since some of them disregard some important parameters of overtopping and some do not consider all phenomenon of wave breaking, or when it has an impact with the defence structure. Additionally, all proposed solutions to mitigate overtopping and floods in the coastal areas are based on predictions made by engineers, for example, the positioning of breakwater structures, their dimensions and their configurations. There is no literature available that shows or prove that optimization process of the coastal protection solutions has ever been done before using machine learning to predict and speed-up this process.

In the wave prediction study, the machine learning models have the capability to efficiently create the H_s field and its accompanying characteristic T_p. In the context of a 48-hour forecast, consisting of 16 simulations conducted at intervals of 3 hours, it was observed that the execution time for SWAN simulations on a single-core processor was 583 s. However, when utilizing 8 cores, the execution time reduced to 112 s. In contrast, the machine-learning approach, specifically for calculating the H_s field, required only 0.086 s, and for calculating the characteristic T_p, it took 0.034 s. Consequently, to calculate the characteristic T_p on ML (a total of 0.12 s on a single processor) is over 3 times (485,833%) faster than the running the full physics-based SWAN models.

In the prediction of morphological changes, the results of the study demonstrates that ANN is an effective instrument for predicting the evolution of beach profile. Due to the complexity and uncertainty associated with a physical comprehension of morphodynamics in the intertidal zone, the ANN results are more compelling than those obtained by mathematical models of the same region. In addition, an ANN model requires significantly less computational effort to construct. However, the application of ANN is restricted to historical training data, and it cannot be applied to hypothetical situations such as future port construction or extraordinary events not included in the training data.

The use of ML demonstrated to be effective in solving coastal engineering problems. It can be constructed by learning the correlations between the input and output variables, even in the absence of fundamental mathematical and physical knowledge pertinent to the extremely complex interactions and processes of coastal engineering. To implement such highly accurate models, the researchers must take a number of factors into consideration.

The result of the ML model was more consistent with the buoy observation values than the result of the SWAN model, and the ML model required 100 times less computation time than the SWAN model. Based on the findings of previous research, this demonstrates that the model's accuracy and reliability could be enhanced through proper data preprocessing.

In the first case study, in section 1, it was determined that littoral evolution projections are necessary for the creation of more effective planning strategies for coastal zones. Reduction in sediment supply to the coast and anthropogenic degradation of natural protection structures have been identified as the primary causes of coastal erosion and the resulting retreat of the littoral. Therefore, the evolution of the Portuguese littoral region will depend primarily on the direct consequence of human actions. It is believed that littoral evolution predictions are now required for the development of more effective planning strategies for coastal zones. Consequently, the study of vulnerability and risk in coastal areas is essential to the formulation of effective planning and management strategies, enabling for improved decision-making in areas where the risk is already present. Adaptation strategies must be implemented, taking into account the study of impacts and alternatives for mitigating social and economic costs and benefits of potential scenarios. These are imperative endeavours that should be encouraged and centred on long-term (decades to century-scale) objectives.

In section 2 of the first case study, the outcomes indicate that strategies aimed at mitigating the sediment deficit and constraining the coast's regressive trend are the solutions that resulted in a greater reduction in coastal erosion risk, resulting in the conclusion that substantial benefits can be obtained from artificial beach nourishments or bypass solutions to reduce coastal erosion risk. Due to population density and the presence of infrastructure, the urban areas of Barra, Costa Nova, and Vagueira stand out as being particularly susceptible to coastal erosion. The fact that the entire coastline has a uniform and low-level topography confers a high consequence classification on the entire study area. According to historical records of coastal erosion, virtually the entire span presents a high or extremely high risk of coastal erosion. The results indicate that strategies aimed at mitigating the sediment deficit and constraining the coast's regressive trend are the solutions that lead to a greater reduction in coastal erosion risk, leading to the conclusion that significant benefits can be derived from artificial beach nourishments or bypass solutions to reduce the coastal erosion risk. Coastal erosion risk assessments should take climate change into account. As a result of the forecasted increase in the number of cyclones over the current value, the examined scenarios result in a risk that is generally greater than that predicted by evaluating the current situation. This fact highlights the significance of conducting additional research to comprehend the characteristics of wave climate in climate change scenarios.

In the second case study, simulations of various drainage scenarios demonstrate that drainage facilities are also effective in mitigating flood hazards caused by wave overtopping, despite the fact that the drainage capacity is somewhat reduced by high sea levels, and that tidal control structures can help reduce the severity of floods.

3
CHARACTERIZATION OF THE CASE STUDY

3.1. LOCATION

Furadouro Beach is situated in the municipality of Ovar which has a total area of about 148 km^2 (DGT, 2013) and is situated on the northwest coast of Portugal. Its coastline extends around 15 km into the Atlantic Ocean and is mostly composed of sand. This municipality is integrated in the district of Aveiro and shares boundaries with the municipalities of Espinho and Murtosa, as well as the Atlantic Ocean, Figure 3.1. It is situated around 30 km south of Porto and 25 km north of Aveiro.

This beach is visited by bathers during the swimming season and sportsmen year-round. Summer and weekend sunshine attract many travellers. As a result, the whole central boulevard area and the waterfront are filled with pubs and restaurants, and in recent years, hostels have become accessible and old guesthouses have been rebuilt to accommodate visitors' consumption levels (Castro, 2015).

There are wooden paths to the south and north of the coastline so that visitors may access the guarded areas without harming the dunes and plants.

Figure 3.1 - Furadouro Beach (Google maps, 2023).

Furadouro beach is one of the coastal stretches in Portugal more severely affected by erosion (Gomes, 2010). Many coastline protection structures are now in place as a means of mitigating this issue. The beach is bounded by two groins, located north and south, and three longitudinal sea defences, located north and south of both groins, and between them, respectively (Figure 3.2).

Figure 3.2 - Coastal defense works at Furadouro Beach (Câmara Municipal de Ovar, 2012, adapted from Marques, 2021).

3.2. WAVE CONDITIONS, EVENTS AND MITIGATION MEASURES

3.2.1. SEDIMENTARY DYNAMICS

The wave climate of the Portuguese Northwest coast is dominated by north-westerly directions (almost 90% of recordings). Consequently, the majority of longitudinal sediment transport occurs in a north-south direction. In the last decades there has been a weakening of sedimentary sources (Veloso-Gomes, 2010) and a decrease in sediment flow from rivers to the shore.

In the Ovar municipality coastline, the decreased sediment supply from the Douro river is responsible for the majority of the sedimentary deficit, which is now estimated to be roughly 2×10^5 m^3/year (GTL, 2014). This is mostly attributable to the growing number of dams and the dredging of sand for construction and navigation channel (Coelho *et al.*, 2009). The coastal defence works constructed in urban areas north of Ovar also alter sediment dynamics, spreading sedimentary deficit problems to the south as a result of i) the retention of sediments by the groins; ii) the reduction of beach erodibility associated with the artificial nature of the coastline (Coelho *et al.*, 2016).

3.2.2. Storm events and Mitigation measures

In 1857, the first concerns with the sea's advancement were reported, resulting in the demolition of many cottages. Only in 1958, when tourism-oriented structures were constructed, was a 600 m long temporary wall constructed for the protection of the marginal. In order to reduce the problems associated with the sea's advance, between 1972 and 1974, a definitive coastal defence work was carried out that included the construction of a 9 m high wall and three groins, 350 m apart, with a length of approximately 200 m and a height of 5.5 m, with the northernmost groin eventually buried due to the high accumulation of sediment in that area (Reis, 2015).

Before the existing coastal interventions, there were several reconstructions and changes of the two groins owing to the devastation caused by the sea waves on the structures and the periphery and the buildings placed there, necessitating the adoption of safety-enhancing measures. Moreover, three attached defensive structures were constructed.

Coelho *et al*. (2015) identified five categories of occurrence: shoreline retreat (SR), overtopping (OV), dune system destruction (DD), damage to infrastructure (DI), and damage to coastal defence works (DC). Figure 3.4 and Figure 3.5 depict the frequency of occurrences by category and their temporal distribution, correspondingly. Furadouro beach has the largest number of damage incidents in the municipality of Ovar, and there has been a definite increased tendency in recent decades.

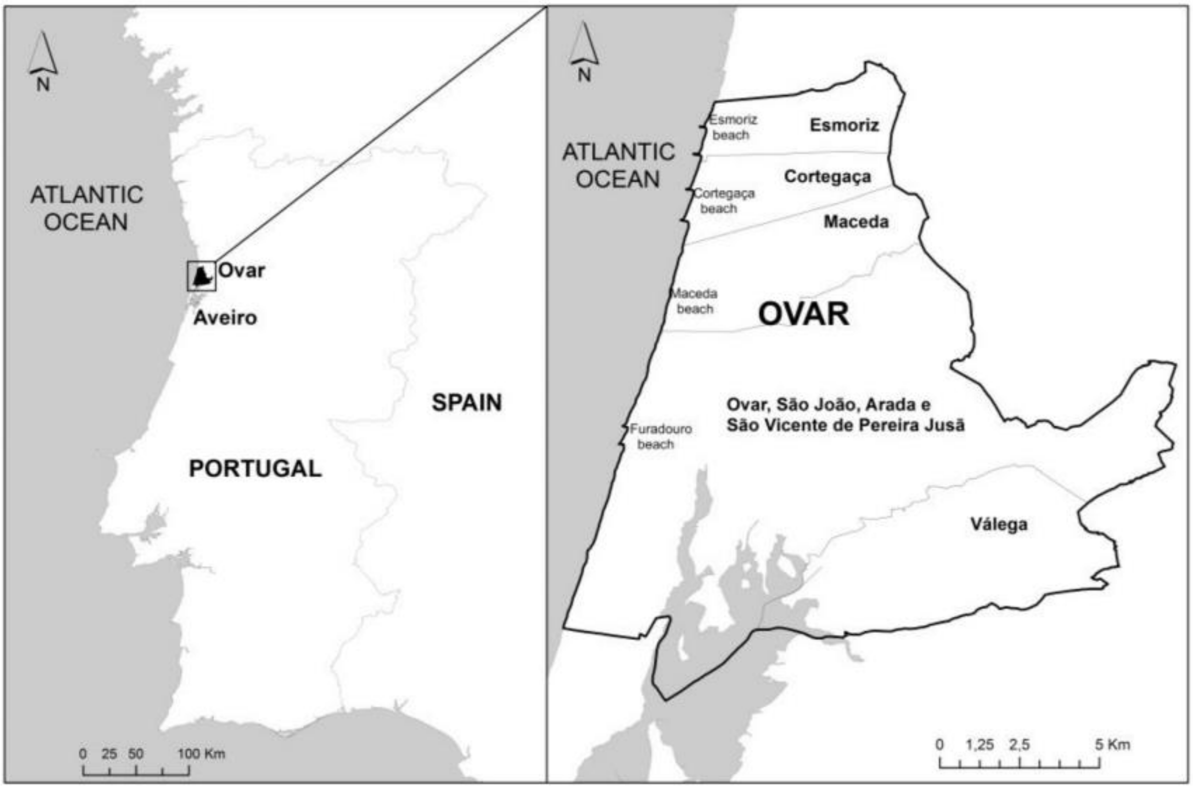

Figure 3.3 - Study area's location. Groins and longitudinal revetments are shown along the coastline (Cruz *et al*., 2015).

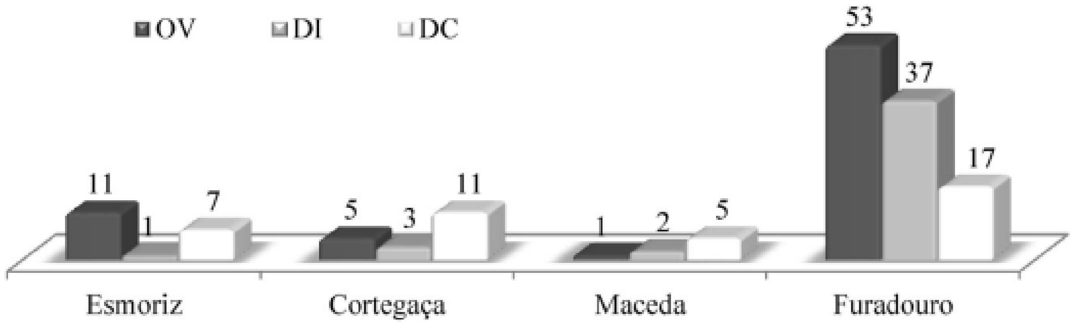

Figure 3.4 - Damage events registered between 1857 and 2015, distributed by type: overtopping (OV), damage to infrastructure (DI) and to coastal defense works (DC) (Cruz, 2015).

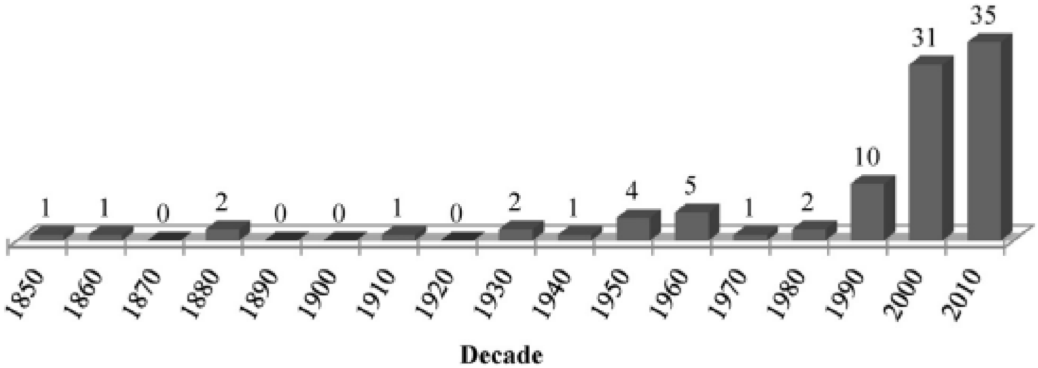

Figure 3.5 - Damage events occurrence by decade, registered at Ovar municipality littoral, between 1857 and 2015 (Cruz, 2015).

Between 1857 until 2010, Furadouro saw 19 occurrences of overtopping, the shoreline retreated between 400 and 500 m until 1971, 106 infrastructures (haylofts, residences, etc.) were demolished, there were two records of dune cordon destruction, and many coastal defence installations were damaged (Coelho *et al.*, 2015).

In 2014, the two biggest storm caused substantial damage, resulting in the partial destruction of groins and attaching structures, as well as the shoreline, wall, and buildings on the waterfront, and inland streets. Table 3.1 presents the storms that occurred since 2013.

Due to the emergency circumstances and as a precaution, these incidents have resulted in the repeated rebuilding of the coastal protection structures, often without a great degree of in-depth analysis, in order to lessen the potential repercussions of another storm.

The tremendous precariousness of the current solutions in face of the approaching sea and the sense of fear among inhabitants and merchants, who are on high alert every winter for the occurrence of overtopping, are well-known. Many measures to reconstruct the military buildings and the waterfront incur substantial expenses, which might be decreased using more efficient alternatives.

The last flooding was on February 1st, 2021. Figure 3.6 presents the pictures of Furadouro taken during the storms that hit in January and February of 2021, as well as pictures of the devastation that was caused by those storms. Sand in the dune cord south of the south groin has been removed, and the amount of sand removed has been so large that the geotubes (a previously implemented technique to decrease sand removal from the beach) became visible in this location due to recent sea action.

Table 3.1 - Occurrences related to the sea action between 2014 and 2021.

Event date	Consequences
Jan 2013	Flooding on the waterfront, deposition of sand on the public highway. [2]
Jan 2014	Overtopping on the revetments with flooding and formation of cracks. Deposition of sand on the public road. Damage to infrastructures, namely walls and beach supports. Flooding of houses and establishments. [3]
Oct 2015	Destruction of the Meia Praia bar, located between groins. [4]
Feb 2016	Waves of 5 to 6.5 m caused the waves to flood the streets. [5]
Fen 2017	Overtopping of the urban waterfront. [5]
Jan 2018	Flooding of the waterfront. Flooding and allocation of sediments on public roads. Displacement of marginal banks. The sediments that filled the geotubes were dragged offshore. [1,5]
Feb 2018	Creep/rubble on the embankment slope near the head of the south groin. Creep and groove on the slope of the longitudinal work adhering to lowering of the beach. [1]
Mar 2018	Overtopping of the waterfront. Dune scarping south of the southern groin. Retreat of the coastline with lowering of the beach in its surroundings with erosion on the back of the adhering longitudinal work. Rumbling in the longitudinal adherent work between groins. High sediment deficit on the beach. [1]
Apr 2018	Frequent and intense flooding of the waterfront. Collapse and rumblings in the works of coastal defense. High sediment deficit. [5]
Sep 2018	Lowering of the beach to a maximum height of 2 m. Dune scarping at a maximum height of 7 m. [1]
Nov 2018	Overtopping of the shore. Lowering the beach to a maximum height of 4 m. Rhombos in the adherent longitudinal work. [1]
Feb 2019	Overtopping of the waterfront. Damage to the infrastructure north of the north groin. [5]
Mar 2019	Dunes south of the southern groin falling. [1]
Sep 2019	Damaged geotube. [1]
Nov 2019	Frequent overtopping on the southern rockfill, allowing accentuated erosion in its back. [1]
Dec 2019	Flooding of the waterfront. Sediments on the pedestrian and roadway from the overtopping. Damage to coastal defense works. Relocation of bicycle parking structures in the area between groins. Beach lowering to the north at a maximum height of 3 m. [1,5]
Feb 2020	Overtopping on the waterfront. [1]
Oct 2020	Overtopping in the urban front. Damage to coastal defense works. [1]
Dec 2020	Intense overtopping on the waterfront. Projection of rockfill from the adhering longitudinal work on the waterfront. Some overflows reached the roofs of some buildings and forced the removal of vehicles from the public road. Flooding of the public road and restaurant buildings. Damage to coastal defense works. [5]
Feb 2021	Intense seepage over the waterfront. Damage to the coastal defense works. Dune destruction south of the south groin. Flooding of the public road. Sediments on the pedestrian and roadway from the overflows.[5]

1. Lima *et al*, 2021; 2. PCP, 2013; 3. Ferreira, 2014; 4. Redação / AR, 2015; 5. Câmara Municipal de Ovar, n.d.

Figure 3.6 - Erosion of dunes, overtopping into the streets, saltwater in the streets and flooding (Câmara Municipal de Ovar, 2021).

3.2.3. Local wave climate

The North Atlantic Oscillation (NAO) corresponds to a large-scale meridional oscillation of atmospheric mass between the Icelandic Low and the Azores High, exerting a strong influence on the storm tracks across the North Atlantic, and has a significant impact on the wave climate of the North coast of Portugal (Ramos *et al*., 2020). The NAO index may be either positive or negative, corresponding to a high- or low-pressure differential between the Azores High and the Icelandic Low. Thus, higher NAO values result in heavier winter storms crossing the Atlantic in a north-easterly direction, creating high wave regimes with a prominent north-westerly direction, which are mainly concentrated along the northern coast of Portugal. The NAO index is an excellent indicator for analyzing the regional wave conditions along the Portuguese coastline. The Hydrographic Institute (IH) has four wave buoys on the Portuguese mainland coast (Leixões, Nazaré, Sines and Faro), in this regard, the data collected by the offshore wave buoy of Port of Leixões due to its proximity to Furadouro (41.33ºN, 8.98ºW, and 83 m sea depth) were evaluated in terms of wave directionality and significant wave height (H_{m0}) from January 1, 2004 to December 31, 2018 (15 years). In general, the majority of incoming waves are concentrated in the fourth quadrant, and more specifically in a narrow band from WNW to NW. For the yearly scenario (Figure 3.7), the fourth sector concentrates up to 85% of incoming waves and focuses only on waves with substantial wave heights (more than 5 m).

In this context it is important to mention that, with a digitization interval of 0.78125 s, data is acquired and recorded in two ways: time series of 10 min designed for real-time processing and time series of 30 min for a posteriori analysis. Under normal circumstances, the delay between series is 3 h, but in stormy conditions, it is shorter than one min, during which the stormy state is confirmed (IH, 2021).

The IECTS 62600-101 model was used for the processing of the data acquired by the Leixões buoy and the characterisation of the region. Marine energy Wave, tidal and other water current converters-Part

101: Wave energy resource evaluation and characterization, which can estimate at least 10 years of sea state data, created with a minimum frequency of one data point every three hours (Marques, 2021).

Analyzing the data annually, it was concluded that in these recent years, *i.e.*, 2013, 2014 and 2018 were significantly energetic with values of mean yearly wave power up to 25 MWh/m, and with most of the energy concentrated in the range 1.5-5 m of Hs and 9-18 s of Tp. The years 2004, 2005, and 2007 had values of mean yearly wave power 12 MWh/m, centered in the region of 1.5-3 m of Hs and 9-14 s (Ramos *et al.*, 2020).

The astronomical tide, which is created by the gravitational pull between the Earth, sun, and moon, in association to a height of the tide that changes according to the location of these celestial bodies. The tides in Portugal are semi-diurnal, with two high tides and two low tides occurring per lunar day. The periodicity of the tides is known; hence it is feasible to forecast their records. The repercussions linked with this elevation vary with its magnitude and, in particular, the level of astronomical tide that occurs, being readily related with a larger risk when it happens during a high tide.

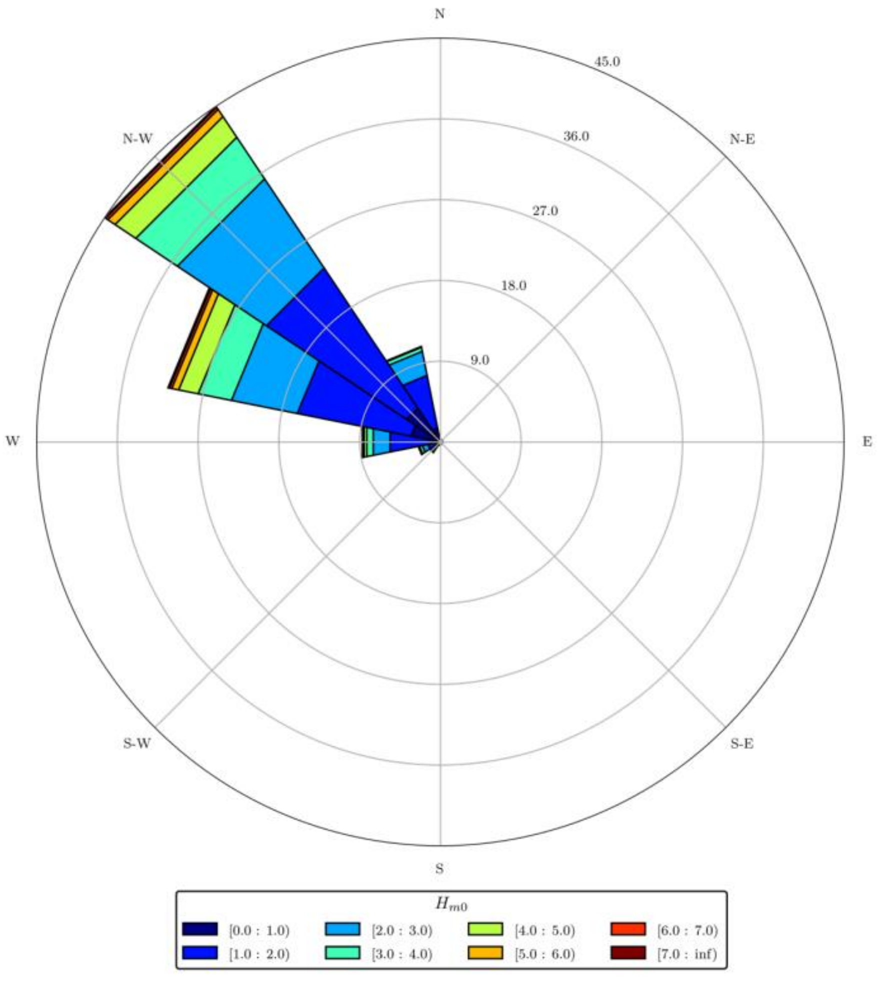

Figure 3.7 - Annual wave conditions (Leixões wave buoy). Adapted from Ramos *et al.*, 2020.

As boundary conditions, the sea wave parameters are derived from ECMWF (European Centre for Medium-Range Weather Forecasts), an organization that forecasts meteorological data and provides various air and sea-based data. Estimates of offshore waves in the study area (Furadouro beach) at 6h intervals from October 1, 1979, to August 31, 2015, including the significant wave height, the mean direction, and the mean period. There is a small increase in the average of the recorded values closer to the north when analyzing the summer and winter months, of 296.3º and a standard deviation of 9.7º. Table 3.2 indicates that during the winter and fall months, the mean direction of the records decreases to 285.6º, with a standard deviation of 60.8º.

Table 3.2 - Summary of the statistical analysis performed on the offshore wave regimes between 1980 – 2015 (Martins, 2016).

Winter	H_s [m]	T_m [s]	θ_m [º]
Average	2.49	10.1	285.6
Median	2.32	10.1	298.0
Fashion	1.73	10.8	300.0
Standard Deviation	1.02	1.8	60.8
Minimum	0.51	5.1	0.0
Maximum	9.82	16.7	360.0
Counting	26244	26244	26244

Summer	H_s [m]	T_m [s]	θ_m [º]
Average	1.60	8.0	296.3
Median	1.49	7.8	310.0
Fashion	1.36	7.1	315.0
Standard Deviation	0.36	1.5	69.7
Minimum	0.40	4.4	0.0
Maximum	5.84	14.5	360.0
Counting	26232	26232	26232

3.3. PREVIOUS STUDIES CARRIED OUT IN THE CASE STUDY AREA

This dissertation is the continuation of several other studies that were conducted throughout time and proposed different solutions to mitigate coastal erosion and flooding at Furadouro beach. Based on the collected literature, the following studies were carried:

Ramos (2011) s*tudied the rehabilitation of coastal defense structures* at Furadouro and Torreira The analysis of each study case was conducted on an initial approach to previous events, an understanding of the present situation and existing dynamics, and a comprehensive examination of potential methods to the settlement of coastal defense concerns. Owing to the requirement to validate some of the methodologies used, a study of the structures of the Furadouro beach using numerical modeling and SMC software (González and Medina, 2001) was also conducted.

Analysis of Coastal Flooding and Overtopping in Furadouro front of Furadouro (Municipality of Ovar, 2014).

In January 2014, between days 3 and 7, the storm Hercules (initially named Christine by the Institute of Meteorology of the University of Berlin) devastated several areas of the Portuguese coast, including the urban front of Furadouro (Sousa, 2015; Pinto *et al*., 2014). Maximum wave height values were recorded above normal, in the order of 14 m, as well as, long wave periods, with average values of 19 s and maximum of 27 s (Figure 3.8), associated with an average wave direction of Northwest (NW) and West-Northwest (WNW), according to data from the Leixões offshore buoy (Pinto *et al*., 2014). In addition, this period coincided with the period of high tides (New Moon). This led to a greater height and reach of the waves, including a great transmission of energy over the coastal zone, promoting overtopping, flooding and erosive processes (Pinto *et al*., 2014).

Storm Hércules was associated with significant damage, especially in the southern part of the Furadouro urban front. The Technical Report on the registration of occurrences on the coast, from the Central Hydrographic Regional Administration (ARH Centro), identified as main impacts the worsening of erosion processes, sediment deficit and strong retreat of the frontal dune cordon (especially in the areas below the groins and the adherent defense structures), considerable structural damage in coastal defense works, occurrences of overtopping, projection of sand, rock fragments and concrete on the public highway, flooding on the urban network, affectation/destruction of establishments, street furniture, beach access walkways, equipment and beach support facilities, among other material damage, such as vehicles as shown in Figure 3.9 (CMO, 2014; Pinto *et al*., 2014).

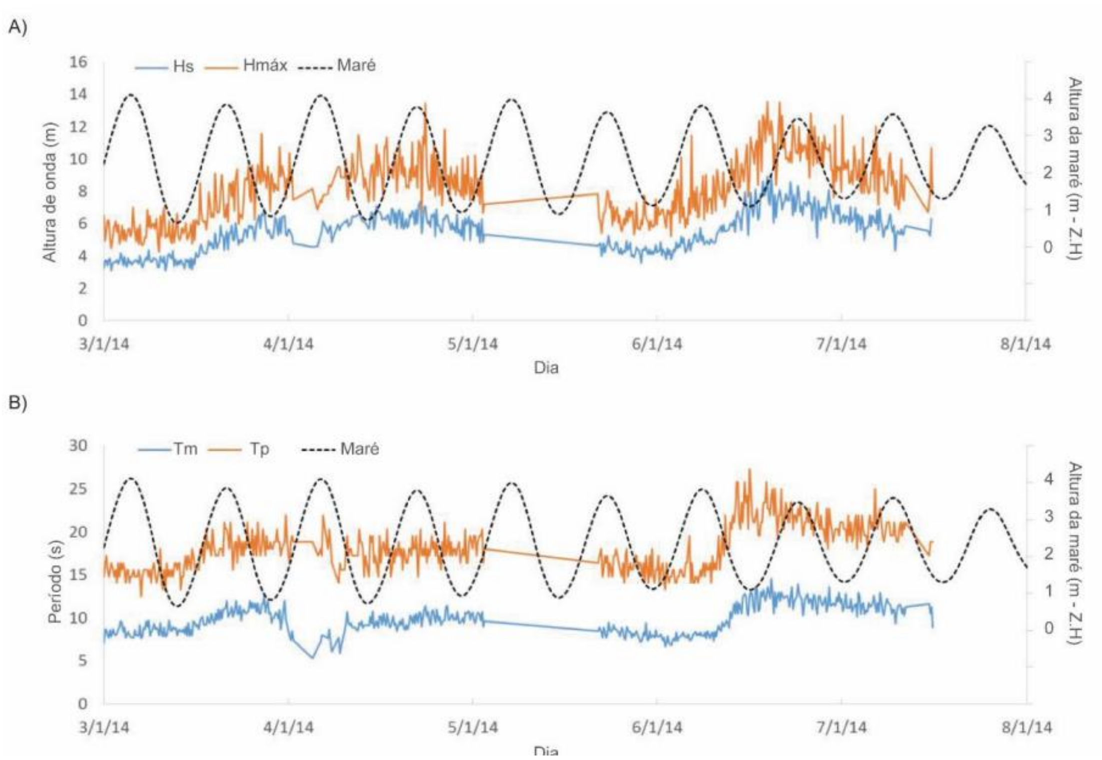

Figure 3.8 - Wave and tidal values during storm Hercules (January 2014) at the Leixões wave buoy: A) Significant (Hs) and maximum wave height (Hmax) and tidal values; B) Average (Tm) and peak (Tp) wave period (Pinto *et al*., 2014).

During the early morning of February 2, the average swell reached 5-6 meters, with the maximum height reaching 14-15 m, with tidal values of 4 m and wave periods around 18-19 s, with a predominant NW direction (Figure 3.10) (CMO, 2014).

The delimitation of the susceptible area comprised the marking and georeferencing of points where there is record that the water mass arrived, supported by the exhaustive analysis of photographic records and local reports, followed by the understanding of the factors that promoted the event and its progression.

Figure 3.9 - Pictures taken by residents: a) Coastal erosion and destruction of the access walkways to Furadouro North beach (DA-CMO, 2014); b) Coastal overtopping at Furadouro South waterfront (José Monteiro, 2014); c) Projection of wood, stone and sand from coastal overflows on the South Furadouro waterfront (RTP Notícias, 2014) and d) Rua de Álvares Cabral (Filipe Rilho, 2014).

The results in Figure 3.11a dictate that on January 6, 2014, water from overtopping flooded a total area of about 7 hectares, reaching the third row of building blocks of Furadouro (up to Avenida da República), which represents a maximum reach of about 260 m, taking into account the top of the adhering longitudinal structure. Already on February 2 of 2014, the flooded area was noticeably higher, especially in the northern zone, reaching 12 hectares of the study area. Likewise, the reach of water and debris was higher, reaching 340 m from the coastal front, namely to Raúl Brandão, located on the 4th block or street of the urbanized area (Figure 3.11b). Table 3.3 represents the hydrodynamic boundary values that were observed from the wave buoy of Leixões and the props just a few kilometers away from the beach of Furadouro, which was later used for the calibration of the model in this dissertation.

This increase, in a short period of time, is due to the fact that the January storm had left the Furadouro coastal system very weakened, that is, the drainage systems and the coastal protection mechanisms were unable to absorb the energy of the waves and the considerable volume of water coming from the overtopping, which promoted the amplification of the flood scenario in February (Pinto, 2022).

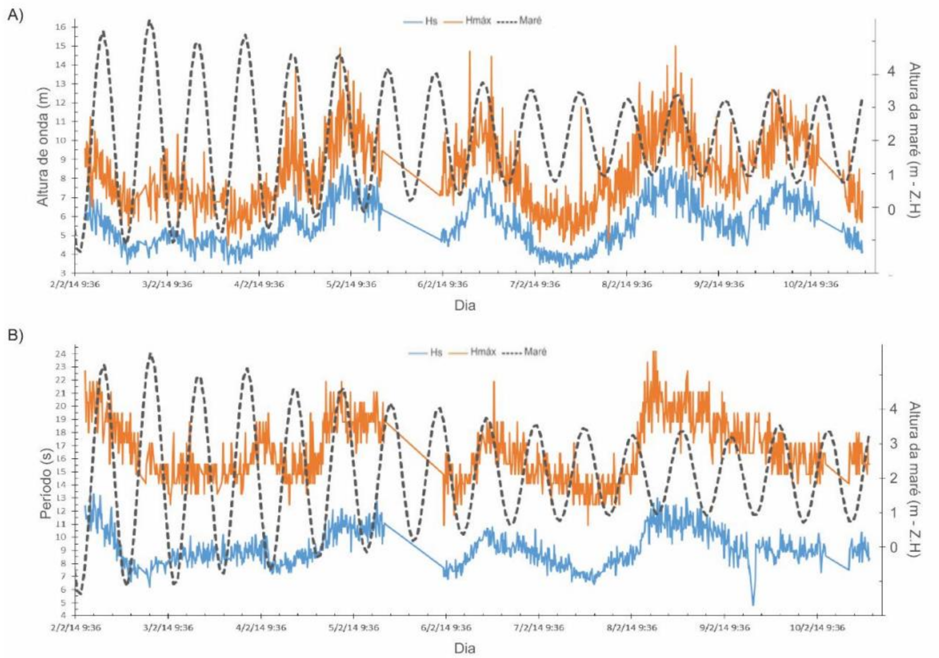

Figure 3.10 - Wave and tidal values during the February 2014 storm at the Leixões wave buoy: A) Significant (Hs) and maximum wave height (Hmax) and tidal values; B) Average (Tm) and peak (Tp) wave period (Pinto *et al.*, 2014).

Figure 3.11 - a) The storm event of the 6th of January and b) the storm event of the 2nd of February (Pinto, 2022).

Table 3.3 - Hydrodynamic boundary conditions (Pinto *et al.*, 2014).

	H_{s_Off} [m]	T_{p_Off} [s]	$Dir_{\_Off}$ [°]	H_{s_prop} [m]	T_{p_prop} [s]	$DIr_{\_prop}$ [°]	Tide [m]
2014 – 01 – 06	8.54	18.80	NW 288	7.27	18.97	NW 284	3.55
2014 – 02 – 02	7.21	19.23	NW 319	5.67	19.00	NW 299	4.00

Fonseca (2015) conducted further research in which he analyzed many possibilities, such as the formation of a groin field, the installation of a detached breakwater in various places, and the expansion of the southern groin.

Castro (2015) performed a *Study of a detached coastal protection work for furadouro urban front*. Using numerical modeling, this study aimed to contribute to a better understanding of the reaction of the Furadouro beach environment to the presence of coastal protection structures. MIKE software was used to model the current beach situation and two proposed solutions of one and two detached breakwaters, taking into account medium wave and storm conditions. The primary objectives of these solutions were to help mitigating adjacent beach erosion and reducing the marginal overtopping.

The analyzed results correspond to the output of three software modules: Hydrodynamic Module (in which the parameters deemed most relevant to the current study were evaluated, including: mean water level, and current velocity, whose values correspond to the mean values at depth), Spectral Wave Module (whose output data are: significant and maximum wave height, peak wave period, average wave direction, and wave power), and Sand Transport Module (which provides: significant and maximum wave height, peak wave period, average wave direction, and wave power). Furthermore, these findings pertain to the time instant at which the water level corresponds to the maximum high tide in the data studied - 3.85 m at the hydrographic zero (H.Z.) (1.85 m at the topographic zero (T.Z.)), which was deemed the least beneficial.

Two sea wave situations, medium and storm, were evaluated. The first one describes the medium wave conditions: significant height of 2.2 m, peak period of 11.4 s, and a northwesterly direction. The second one describes the storm conditions: significant height of 6 m, peak period of 14 s, and a westerly direction.

The selected structural solution corresponds to a 250 m long, 20 m wide detached breakwater, and two 150 m long, 20 m wide crowned breakwaters, Figure3.12.

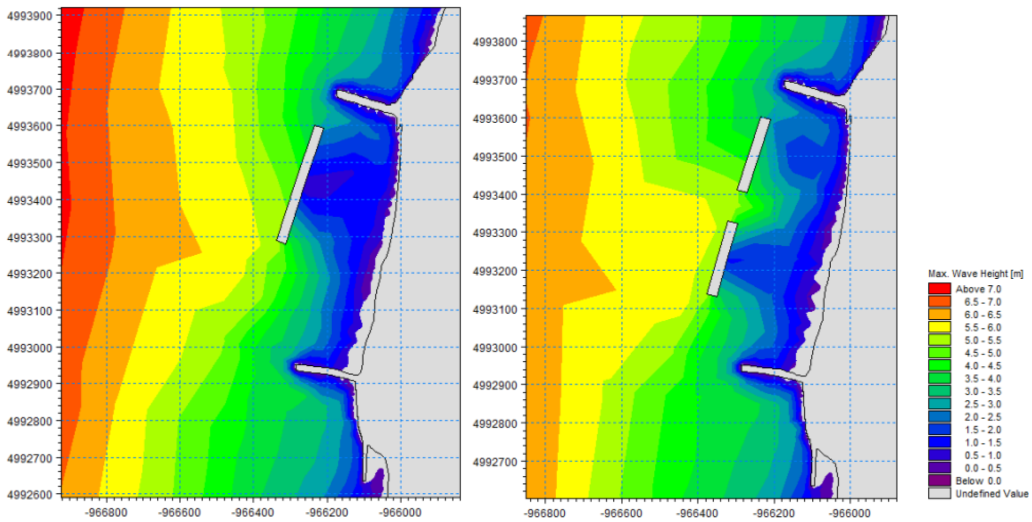

Figure 3.12 - Maximum wave height (Hs=6m; Tp=14s; West) Adapted form Castro, 2015.

It was concluded that the single detached breakwater greatly decreases both the wave height on the lower beach and the wave energy that reaches the coast between the groins. Yet, despite the fact that current speeds are similarly lower on the lower shore, the existence of this structure creates a channel of greater current speeds along the beach south of the north groin, which may impede bathing activities.

The concept of two detached breakwaters was the alternative approach offered. Relative to the preceding solution, it was discovered that the fall in wave height downstream is less pronounced. Due to the gap between the two breakwaters, erosion phenomena are also larger at mid-distance between the breakwaters.

Martins (2016) *evaluated of the hydrodynamics and the levels of overtopping at furadouro beach.* The empirical Mase formulae (Mase *et al*., 2013), the NN OVERTOPPING2 neural network (Coeveld *et al*., 2005), and SWASH numerical model were used to analyze the overtopping for the present circumstance (Zijlema *et al*., 2011). The planned coastal defence structure was a detached breakwater, as presented by Castro (2015). To analyze the overtopping in the presence of this structure, only the SWASH model was utilized since, unlike the other techniques, it can account for the variations in wave action caused by the presence of a physical obstruction.

In addition, the SWASH model was selected because it is a robust and efficient model with a wide range of applications and a faster simulation processing time than other equivalent models.

It was determined that the building of the breakwater would safeguard the land in the shadow zone of the structure by significantly reducing the frequency and severity of overtopping. In the area directly south of the north groin, the opening between the groin and the breakwater, close to the placement of structure 3, there was still the occurrence of overtopping, although with a lower frequency than those obtained for the scenario without breakwater.

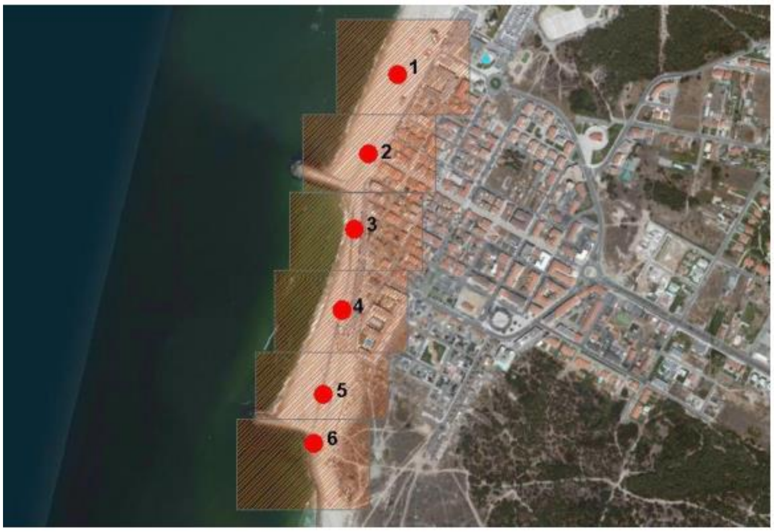

Figure 3.13 - Zones of influence of each structure for the risk calculation (ArcMap 10). Adapted from Martins, 2016.

Under the investigated wave regime, it was determined that the whole study region has a very high-risk level. However, the building of a detached breakwater markedly reduced this risk. In addition, it was determined that some factors (for example friction, smoothing, Iribarren number, current velocity and vertical layers) considered in the use of SWASH, which result in wave energy loss, were underestimated. Consequently, it was determined that the established coastline protection system must be optimized.

Marques (2021) *assessed solutions for reducing the risk overtopping at coastal urbanized fronts for different climate change scenarios.* The purpose of this study was to investigate present circumstances and evaluate a coastal defense option using numerical model. First, the XGBoost tool, which is based on machine learning methods, was used to conduct a simplified study of the present longitudinal defensive structures and various modifications to these structures in an effort to lower the overtopping flow. The SWASH numerical model also permitted the analysis of the effects of the average sea level rise on the urban front of Furadouro. This solution required a modification to the geometry of the northern groin. The proposed adjustment involves extending the current groin perpendicularly to the coastline by 40 m, so that the groin will have a total length of 160 m and transforming the groin's head into a Y-shape with 90 m to the north and 110 m to the south. 100° is the opening angle between the center of the groin and its northward and southern extension (Figure 3.14). Both numerical models were used to investigate various wave conditions, particularly storm surge conditions, since they are the most concerning.

As waves approach from the west, the region bordering the structure will be well shielded, whilst the area below the groin will be more exposed. In contrast, when the wave direction is NW, a considerable portion of the region downwind of the north groin will be shielded from direct swell, whilst the area upwind may be more exposed.

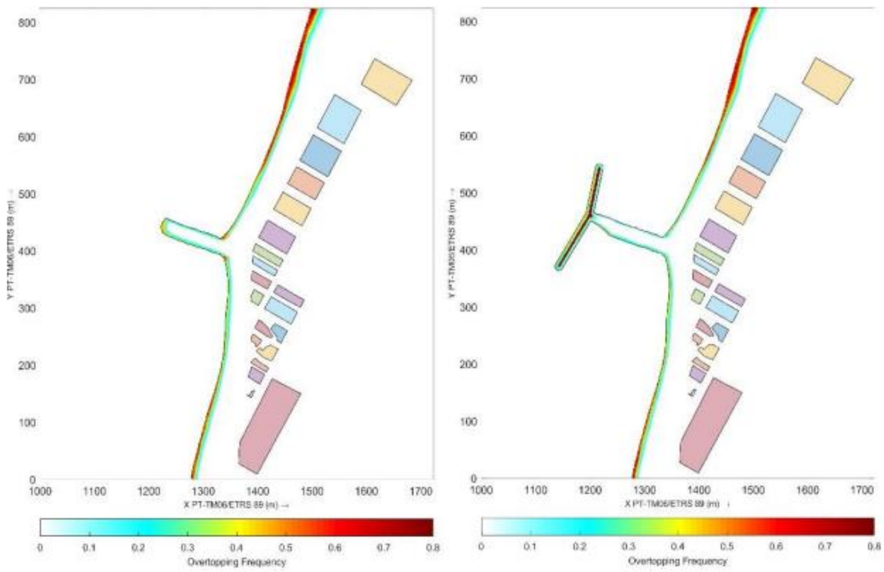

Figure 3.14 - Frequency with which a computational cell has water in the actual (left) and for the proposed solution (right) with Hs= 2 m and Tp= 16 s, W direction, adapted from Marques (2021).

In conclusion, when the mean sea level (MSL) rises, the adjustment to the groin head will not successfully protect the urban area of Furadouro, and the frequency and size of street flooding during storms at sea will remain high.

It was determined that application of some of the proposed measures would reduce the overtopping flow, with the most promising scenario involving the combination of three interventions (rearrangement of the rock-fill blocks, an increase of 0.5 m in the wall's crest, and the construction of an intermediate berm). For these arrangements, both in the northern structure and in the structure between groins, average overtopping flows are reduced by more than 50%.

With a 0.6 m increase in the MSL, neither the present structures nor the planned modification of the groin will be able to safeguard the urban area of Furadouro. In the future, both the frequency and severity of floods will likely grow (Marques, 2021).

3.4. Definition, Development and Preliminary design of new solutions

3.4.1. Combination of Different solutions from previous studies

Several studies were conducted (as already shown in the previous sections) to propose new solutions to mitigate overtopping (magnitude and frequency) in the urban area of Furadouro near the coastline. In this section, the solutions that were proposed in the previous works are combined to verify which combination resulting in best solution to prevent overtopping, Figure 3.15.

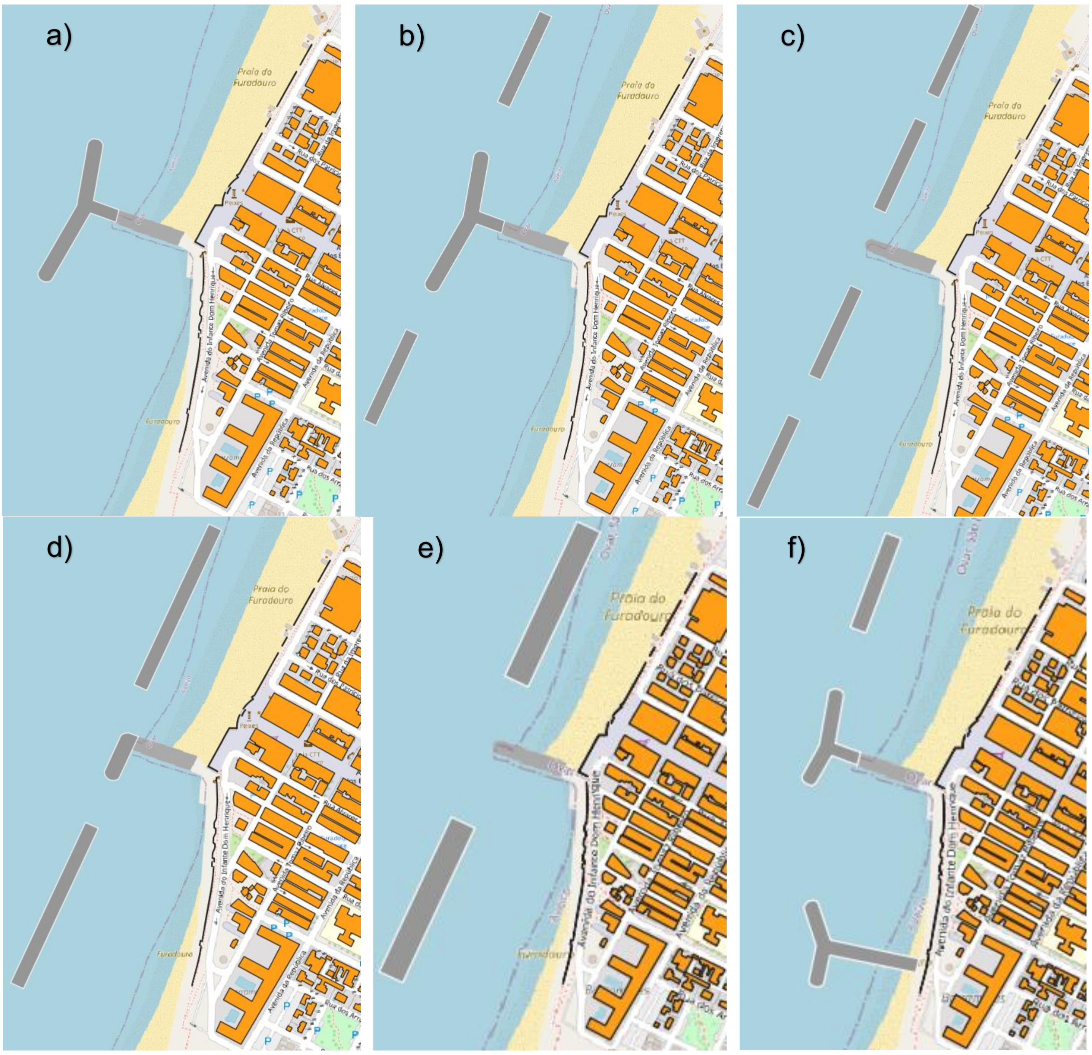

Figure 3.15 – Solutions to mitigate overtopping: a) extension of the groin head and its modification with the same dimensions that Marques (2021) used; b) the vertical breakwater structures with the dimensions of L = 150 m with W =20 and the crest of +4 m CD (Castro, 2015) are positioned on each side of the groin; c) the same structures used in b) are shown adding 2 structures on each side of the groin; d) configuration of the groin head with extension to the south of 50 m (Ramos, 2011) with structures of dimensions of L = 250 m, W = 20 m and the crest = +4 m CD (Martins, 2016); e) the structures of Ramos (2011) with the dimensions of L = 250 m, W = 38 m and crest of +4 m CD; f) modification of the north groin head with addition of the new emerged groin between the existing south and north groins with a crest of +6 m CD and the vertical breakwater structure on the north side with a crest of +4 m CD.

The effectiveness of groins depends on their extension and the spacing between them. In the study area, the spacing between the groins is 3 times the length of the groins, to increase the effectiveness of the groins it is suggested that the spacing between them be 1 or 2 time the length of the groin thus the addition of a groin between the existing ones, Figure 3.16.

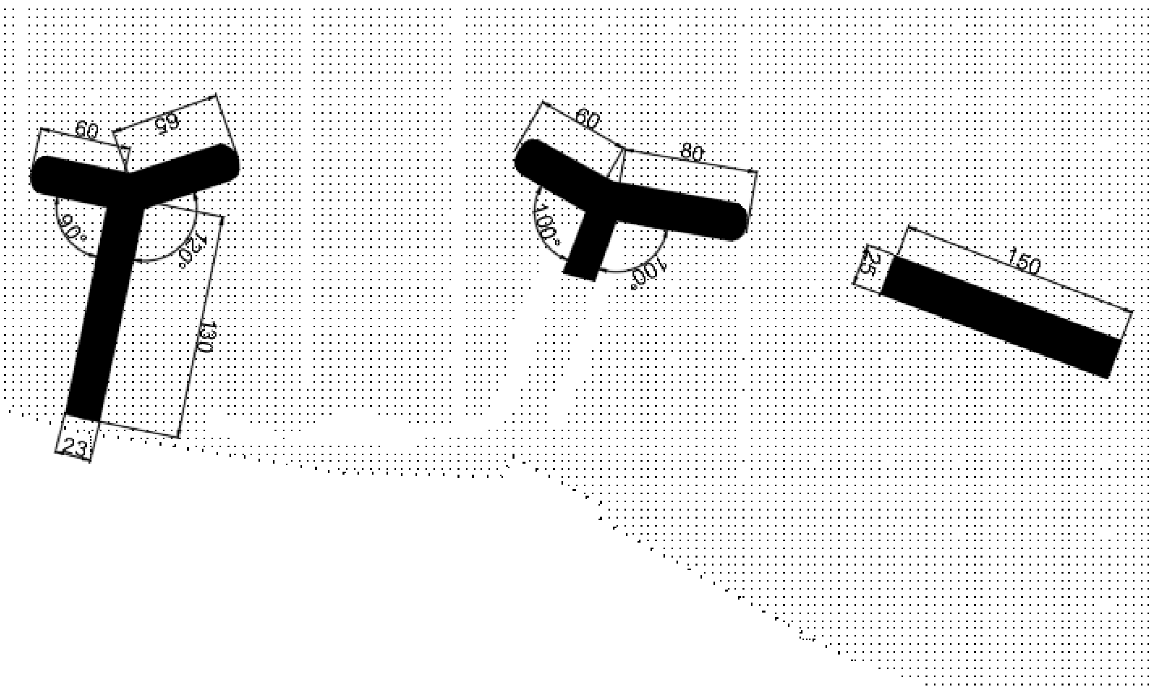

Figure 3.16 - Dimensions of the proposed breakwater structures.

3.4.2. Solutions prepared for machine learning

In the preparation of the dataset for the machine learning (ML), structures were positioned -75 m, 75 m, 170 m, 350 m and 700 m in from the north groin of the Furadouro beach. Vertical breakwater structures with the same crest elevation of +4 m (CD) and dimensions of 250 × 38 m are used for this purpose. It was decided to keep these dimensions and the crest elevation constant, as well as the number of structures used in each simulation, which is two structures per simulation, and alter only the locations and orientations of the structures. 20 simulations were prepared as data that would be used to train and generate a machine learning (ML) model. However, it was later concluded that the model requires more data to provide more accurate predictions. Since the model will still be required to split the available simulations into the training set and the testing set, an additional 17 simulations were added to the data, bringing the total to 37 simulations. During the validation of the models, initially, it was also discovered that the models still performed very poorly. As a result, the models were retrained with 20 additional simulations added to the dataset, for a total of 57 simulations. Figure 3.17 presents 4 different locations of structures related with distance from the head of the groin. The rest of the figures can be found in the Appendix D.

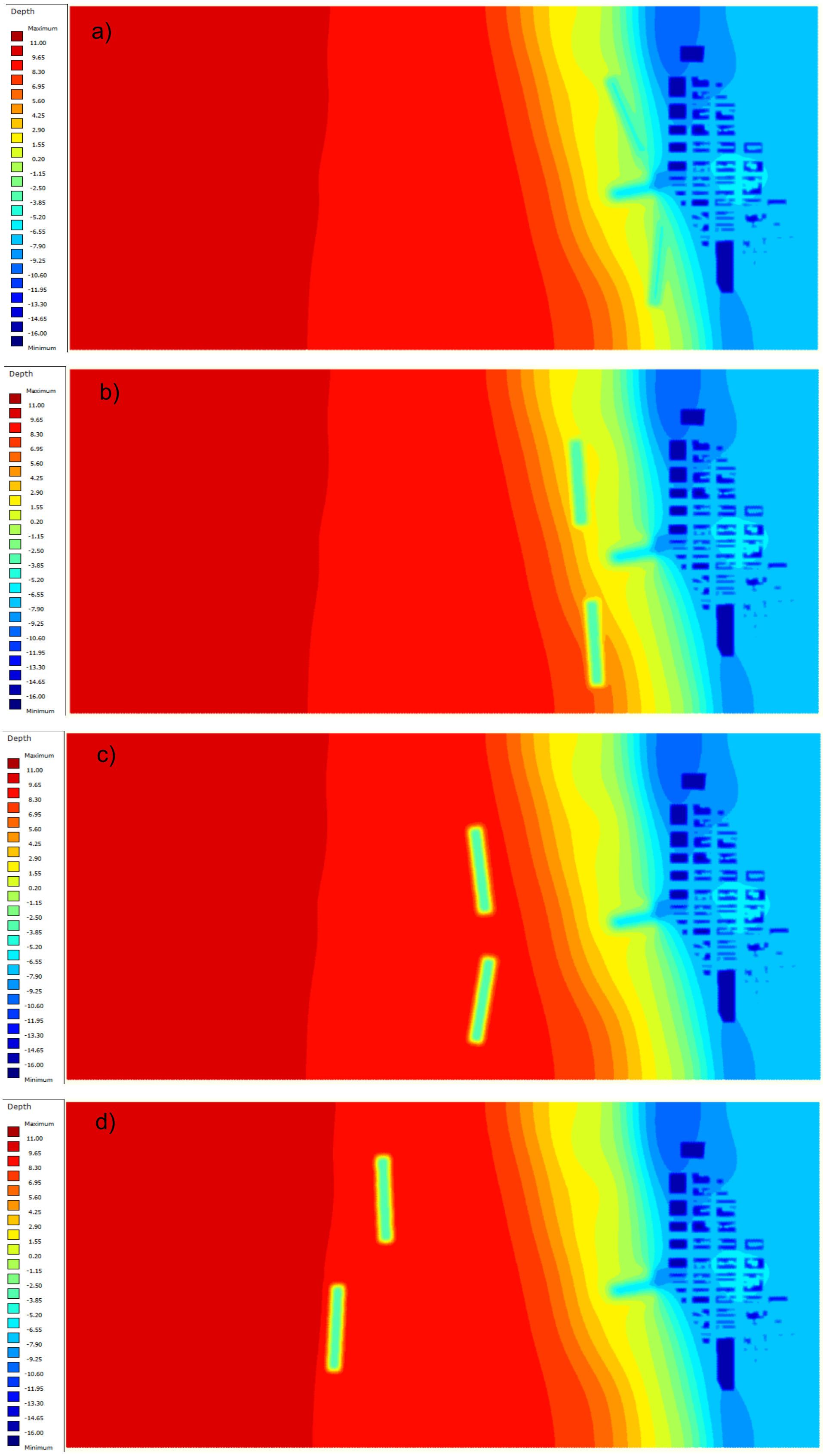

Figure 3.17 - 4 different positions of 2 vertical breakwater structures: a) positioned -75 m; b) positioned 75 m; c) positioned 350 m and d) positioned 700 m from the head of the groin.

4

NUMERICAL STUDY

4.1. HYDRODYNAMIC NUMERICAL MODEL

4.1.1. GENERAL DESCRIPTION OF THE SWASH MODEL

SWASH (Simulating Waves to Shore) was developed at the technical University of Delft by Stelling and Zijlema (2003), Stelling and Duinmeijer (2003), Zijlema and Stelling (2005, 2008), Smit *et al.* (2013), and Stelling (2020). It is a non-hydrostatic wave-flow model intended for estimating transformation of dispersive surface waves from coastal areas to the beach for analysing the surf zone and swash zone dynamics, wave propagation and agitation in ports and harbours, rapidly varied shallow water flows typically found in coastal flooding due to *e.g.*, tsunamis and flood waves, tides and storms.

4.1.1.1. Physics and boundary conditions

The open-source SWASH model was used to model in detail the characteristics of the waves generated in the proposed Artificial Surf Reef (ASR) (Zijlema *et al.*, 2011). SWASH is a free-surface, terrain-following, multi-dimensional, non-hydrostatic wave-flow simulation model designed to characterize unsteady, rotational flow and transport phenomena in coastal waters, propelled by waves, tides, buoyancy, and wind forces. It solves the continuity and momentum equations, as well as, optionally, the equations for conservative transport of salinity, temperature, and suspended load for both cohesive and non-cohesive sediment. In addition, the standard κ-ε turbulence model is utilised to calculate the vertical turbulent dispersion of momentum and the diffusion of salt, heat, and suspended sediment. The momentum equations are coupled to the transport equations via the baroclinic forcing term.

SWASH accounts for the following physical phenomena:

- Wave propagation, frequency dispersion, shoaling, refraction, and diffraction;
- Nonlinear wave-wave interactions (including surf beat and triads);
- Wave breaking;
- Depth-limited wave growth by wind;
- Moving shoreline;
- Bottom friction;
- Wave runup and rundown;
- Wave-current interaction;
- Wave-induced currents;
- Partial reflection and transmission;

- Tidal waves;
- Sub grid turbulence;
- Wave interaction with rubble mound structures;
- Wave interaction with floating objects;
- Vertical turbulent mixing;
- Wave damping induced by aquatic vegetation;
- Turbulence anisotropy;
- Space varying wind and atmospheric pressure;
- Rapidly varied flows bores and flood waves;
- Wind driven flows;
- Turbidity flows;
- Transport of suspended load for (non)cohesive sediment;
- Transport of tracer.

SWASH has been validated via a variety of analytical, laboratory, and field test scenarios. Zijlema *et al.* (2011) discovered a high level of concordance between predictions and observations. Concerning wave transformation in the surf zone, it has demonstrated that SWASH accurately accounts for the most important physical processes, including nonlinear shoaling, wave breaking, wave runup, and wave-driven currents (Smit *et al.*, 2013).

The governing equations are the nonlinear shallow water equations, which include non-hydrostatic pressure, and, optionally, the equations for the conservative transport of salt, temperature, and suspended material presented below. For the sake of simplicity, the governing equations are expressed in terms of the Cartesian coordinates *x* and *z* and time *t* for the vertical 2D plane. Hence, the mass and momentum conservation equations are as follows:

$$\frac{\partial u}{\partial x}+\frac{\partial w}{\partial z}=0 \tag{8}$$

$$\frac{\partial u}{\partial t}+\frac{\partial uu}{\partial x}+\frac{\partial wu}{\partial z}=-\frac{1}{\rho}\frac{\partial(p_h+p_{nh})}{\partial x}+\frac{\partial \tau_{xz}}{\partial z}+\frac{\partial \tau_{xx}}{\partial x} \tag{9}$$

$$\frac{\partial w}{\partial t}+\frac{\partial uw}{\partial x}+\frac{\partial ww}{\partial z}=-\frac{1}{\rho}\frac{\partial p_{nh}}{\partial z}+\frac{\partial \tau_{zz}}{\partial z}+\frac{\partial \tau_{zx}}{\partial x} \tag{10}$$

where g is the gravitational acceleration; $u(x, z,t)$ and $w(x, z,t)$ are the horizontal and vertical velocities, respectively; ρ is the water density, p_h and p_{nh} are the hydrostatic and non-hydrostatic pressure terms, respectively; and τ_{xx}, τ_{xz}, τ_{zz}, τ_{zx} represent the turbulent stresses, which are defined as follows:

$$\tau_{zx_i}=v_v\frac{\partial u_i}{\partial z} \tag{11}$$

$$\tau_{x_jz}=v_h\frac{\partial \omega}{\partial x_j} \tag{12}$$

$$\tau_{x_jx_i}=v_h\left(\frac{\partial u_i}{\partial x_j}+\frac{\partial u_j}{\partial x_i}\right) \tag{13}$$

$$\tau_{zz}=v_v\frac{\partial \omega}{\partial z} \tag{14}$$

where v_h and v_v are the turbulent viscosities related to the vertical and horizontal exchange of momentum. The water column is vertically restricted by the moving free-surface $\zeta(x,t)$ and stationary bottom $d(x)$ (measured positive downwards), defined relative to the still water level z_0. Furthermore, the hydrostatic pressure is explicitly expressed in terms of the free-surface level as:

$$p_h = \rho g(\zeta - z) \tag{15}$$

Consideration of the mass (or volume) balance for the whole water column yields the temporal evolution of the surface elevation:

$$\frac{\partial \zeta}{\partial t} + \frac{\partial}{\partial x}\int_{-d}^{\zeta} u\, dz = 0 \tag{16}$$

Mass and momentum conservation equations are solved for surface and bottom kinematic and dynamic boundary conditions. The kinematic boundary requirements stipulate that no particle may leave the surface or enter the (stationary) bottom:

$$w = \frac{\partial \zeta}{\partial t} + u\frac{\partial \zeta}{\partial x}\ at\ z = \zeta(x,t) \tag{17}$$

$$w = -u\frac{\partial d}{\partial x}\ at\ z = -d(x) \tag{18}$$

At the surface, the dynamic boundary condition is a constant pressure (zero atmospheric pressure, p_h = p_{nh} = 0) and the absence of surface tensions. Considering that bottom friction is crucial for low-frequency movements and wave run-up, a stress factor is introduced at the bottom boundary based on a quadratic friction law:

$$\tau_b = c_f\frac{U|U|}{h} \tag{19}$$

where U is the average depth of the stream, $h = d + \zeta$ is the water depth, and c_f is a dimensionless coefficient of friction. Several bottom roughness formulas (Manning, Chezy, and Colebrook-White) are incorporated in the model. It is important to note that the model's creators propose the Manning formulation since it provides the most accurate description of the wave dynamics in the surf zone.

$$c_f = \frac{n^2 g}{h^{1/3}} \tag{20}$$

where c_f is the coefficient of bottom friction and n is the Manning roughness coefficient, the value of which must be determined using a calibration technique.

Regular or irregular waves may be created at the outer open boundary (wave-maker) by providing a local velocity distribution u_b. To prevent reflections at this border, a weakly reflective condition is employed, allowing outgoing waves to traverse the whole boundary (Blayo and Debreu, 2005):

$$u_b = \pm\sqrt{\frac{g}{h}}(2\zeta_b - \zeta) \tag{21}$$

Where u_b is the inflow velocity at the boundary and ζ_b is the incident wave surface elevation signal.

In terms of the onshore boundary condition, SWASH offers two distinct methods. The usage of a shifting coastline boundary condition is necessary for the computation of wave runup and rundown. In circumstances when the onshore border is situated inside the pre-breaking zone, secondly, an absorption requirement may be enforced. Often, Sommerfeld's radiation condition is used, which permits (long) waves to traverse the outflow barrier without being reflected (Zijlema *et al.*, 2011). Last but not least, closed borders are regarded as solid walls and are hence entirely reflective.

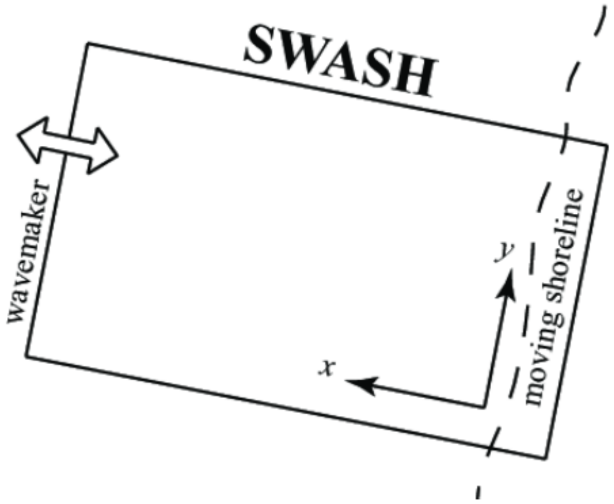

Figure 4.1 - Sketch of the computational domain in SWASH. Adapted from (Rinjsdorp, 2016).

SWASH provides the following specification of boundary conditions:

- wavemakers:
  - By use of Fourier series or time series, regular waves may be analysed;
  - irregular unidirectional waves by way of 1D spectrum. The spectrum may be produced from observations or by providing a parametric form (Pierson-Moskowitz, Jonswap or TMA) (Pierson-Moskowitz, Jonswap or TMA);
  - a spectrum of irregular multidirectional waves in two dimensions. The spectrum may be acquired from a SWAN run or by defining a parametric shape (Pierson-Moskowitz, Jonswap, or TMA), whilst the directional spreading can be described using the well-known cosine power or the directional standard deviation.
- absorbing-generating boundary conditions;
- velocity or discharge;
- Riemann invariants;
- full reflection at closed boundaries or solid walls;
- Sommerfeld or radiation condition;
- sponge layers;
- periodic boundaries.

Furthermore, the typical *k-ε* turbulence model is used to simulate the vertical turbulent dispersion of momentum and the diffusion of salt, heat, and sediment load. The transport equations are connected with the momentum equations through the baroclinic forcing component, while the density-salinity-temperature-sediment-density equation of state is used.

SWASH is limitless and is capable of capturing flow events with spatial sizes ranging from cm to km and temporal ranges ranging from seconds to hours. This model may also be used to determine the dynamics of wave transformation, buoyancy flow, and turbulent interchange of momentum, salinity, temperature, and suspended material in shallow seas, coastal waters, estuaries, reefs, rivers, and lakes.

It is important to note that SWASH is not a Boussinesq-type wave model. Conceptually, the solution includes the vertical structure of the flow. SWASH may be run in either depth-averaged mode or multilayered mode, in which the computational domain is partitioned into a predefined number of vertical terrain-following layers. SWASH enhances its frequency dispersion by increasing the number of layers, unlike Boussinesq-type wave models, which increase the order of derivatives of the dependent variables. Nevertheless, SWASH has no more than second-order spatial derivatives, but the applied finite difference approximations are only accurate to the second order in space and time. This is most likely the primary reason why SWASH is much more resilient and quicker than any other Boussinesq-type wave model. This method achieves excellent linear frequency dispersion up to kh 7 with two equidistant layers and a 1% inaccuracy in phase velocity (k and h are the wave number and water depth, respectively). In addition, SWASH lacks a numerical filter and a specific method for dissipating short-wave instabilities.

4.1.1.2. Wave breaking approximations.

When modelling depth-induced wave breaking, non-hydrostatic wave-flow models have significant limitations. The absence of processes such as overturning, air-entrainment, and wave-generated turbulence from the physics of these types of models contributes to this result. Non-hydrostatic models, on the other hand, account for the macro-scale effects of wave breaking (*i.e.*, the effect on the statistics of wave heights) by considering wave breaking as a discontinuity in the flow variables (breaking waves eventually evolve into a quasi-steady bore where the entire front face of the wave is turbulent, analogous to a hydraulic jump). Consequently, conservation of mass and momentum throughout the flow discontinuity is used to determine the wave energy dissipation in the surf zone.

However, when a limited number of vertical layers (1-3) is used in SWASH, the quantity of energy dissipation may be underestimated due to the approximation of the phase velocity at the breaking wavefront face (Smit *et al*., 2013). To avoid the aforementioned limitation, SWASH provides two options. On the one hand, the use of high vertical resolutions (10-20 layers) results in an accurate computation of the phase velocity at the breaking front, but at a significant cost increase. SWASH presents the so-called Hydrostatic Front Approach (HFA), which allows prescribing a hydrostatic pressure distribution (vertical accelerations are ignored) for grid points located in the front of a breaking wave (Smit *et al*., 2013). When the local surface steepness ($\partial_t\zeta$) exceeds a fraction (α) of the shallow water velocity, the grid points that must operate in the hydrostatic mode are determined:

$$\frac{\partial\zeta}{\partial t} > a\sqrt{gh} \tag{22}$$

A grid point only becomes non-hydrostatic again if the crest of the wave has passed, which occurs when:

$$\frac{\partial\zeta}{\partial t} < 0 \tag{23}$$

To represent the persistence of wave breaking, grid points, neighboring the ones that have been labelled hydrostatic, will be considered for hydrostatic computation if the local steepness ($\partial_t\zeta$) exceeds a smaller fraction (β) of the shallow water celerity:

$$\frac{\partial\zeta}{\partial t} > \beta\sqrt{gh} \quad where\, \beta < \alpha \tag{24}$$

According to Smit (Smit *et al*., 2013), α = 0.6 and β = 0.3 provide the best results for a broad variety of wave conditions.

4.1.1.3. Computations

In a cartesian or spherical coordinate system, SWASH calculations may be performed on a normal grid, an orthogonal curvilinear grid, or a triangular mesh.

SWASH runs may be executed serially, *i.e.*, one SWASH program on a single processor, or in parallel, *i.e.*, one SWASH program on several processors utilizing a MPI interface.

4.1.1.4. Output quantities

SWASH provides the following output quantities (ASCII or binary MATLAB files containing tables and maps):

- Surface elevation;
- Depth-averaged velocity magnitude and direction;
- Vorticity;
- Layer-averaged velocity magnitude and direction;
- Discharges;
- Friction velocity;
- Vertical distribution of horizontal velocity;
- Vertical runup height;
- Pressure at bottom;
- Velocity in z-direction or relative to sigma plane;
- Turbulence quantities (k, ε and ν_t);
- Time-averaged velocities (*e.g.*, undertow);
- Wave-induced setup;
- Significant wave height;
- Time-averaged turbulence quantities;
- Layer-averaged pressure;
- Transport constituents (salt, heat, and suspended sediment);
- Time-averaged transport constituents;
- Vertical distribution of pressure;
- Maximum horizontal runup or inundation depth;
- Hydrodynamic loads acting on a moored ship;
- Non-hydrostatic pressure.

4.1.1.5. Limitations

At present, SWASH does not account for:

- hot starting (temporary_limit);
- unstructured mesh computations in parallel using MPI (temporary_limit).

4.1.2. IMPLEMENTATION OF SWASH MODEL

In this section, the most important steps of SWASH model implementation for the study area of Furadouro are described.

4.1.2.1. Bathymetric dataset

A collection of data was utilized to create the bathymetry to be employed in the SWASH numerical model, including the cartography given by the Municipality of Ovar and the topographic hydrographic survey (LTH) data from the Coastal Zone Monitoring Program of Continental Portugal - COSMO.

The cartography was produced on the basis of an aero photographic survey resulting from a flight carried out in 1999. The Portuguese Geographic Institute checked and validated the cartography (in accordance with Order no. 23915/2005, of November 23, Diário da República 2nd series) produced, which is based on the Hayford-Gauss Datum 73 and is altimetrically referenced to topographic zero (Câmara Municipal Ovar City Council, 2021). The LTH obtained for the Espinho-Furadouro stretch has a resolution of 0.3 m and is the result of the combination of various data acquisition techniques: aero photogrammetric survey, GNSS survey GNSS survey, interpolation of missing areas, single beam survey and multibeam survey, the survey was conducted in June 2019 and is georeferenced to the ETRS89/PT-TM06 coordinate system, using the Cascais Datum (1938) as the altimetric referential, that is, the hydrographic zero, which is 2 m below the topographic zero. The survey falls within the criteria specified by Commission Regulation (EU) No. 1312/2014 of December 10 modifying Commission Regulation (EU) No. 1089/2010 of November 23, 2010 (COSMO, 2020).

To join the cartographic data with the LTH data Marques. (2021) adjusted the two referential using AutoCAD, the altimetric referential and the planimetric referential, by subtracting 2 m from the z coordinate of the points, and the planimetric referential was corrected by converting the referential from ETRS89/PTTM06 to Datum 73 Hayford-Gauss.

Delft 3D toolboxes Delft3D-RGFGRID was used to generate the grid and Delft3D-QUICKIN for the bathymetry interpolation and smoothing. Because Delft3D does not recognize identical coordinates with different heights, the vertical walls in Figure 4 2 were designed in AutoCAD with a very slight slope to avoid having identical coordinates with different heights. The coordinates were exported to an Excel file, inserted in an “.xyz” file, and then integrated into Delft 3D for smoothening and interpolation. To enable the model to recognize the structures, the bathymetry was extruded using polygons with the shape of the buildings up to a height of -18 m. Due to the fact that the grid consisted of 2 × 2 cells, it was challenging for Delft 3D to depict the 1 m vertical wall along the coast; however, the wall could be identified by its porosity layer and height. After generating the ".dep" file from Delft 3D, MATLAB scripts were used to generate the “.bot” file depicted in Figure 4.3.

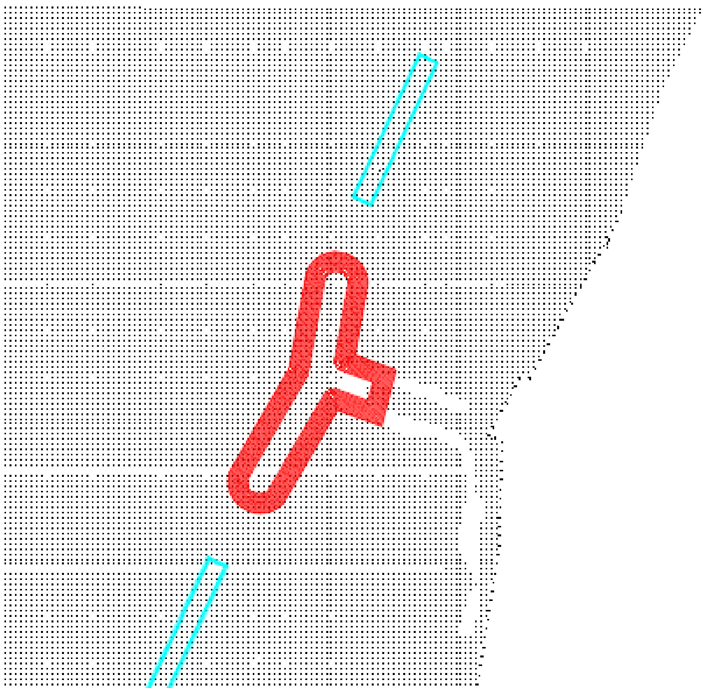

Figure 4 2 - Groin’s head and vertical breakwater structures designed on AutoCAD.

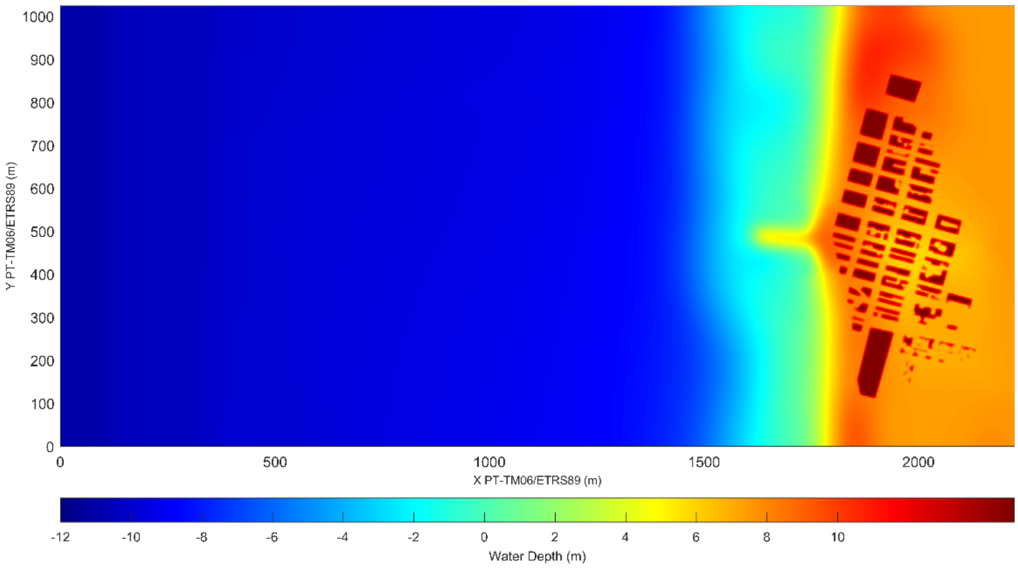

Figure 4.3 - The bottom file generated using a MATLAB script.

4.1.2.2. Computational Grid

A uniform regular grid is used to discretize the computational domain. The grid resolution is calculated using the formulae that depend on the wavelength, λ, at the domain's wavemaker border. Furthermore, it is advised that 50 to 100 grid cells be used per wavelength (SWASH User Manual, 2020).

$$\lambda^2 = \frac{g}{2\pi} T^2 \tanh\left(2\pi \frac{h}{\lambda}\right) \tag{25}$$

$$Grid_{Size_T} = \frac{\lambda_T}{NumGridCells} \tag{26}$$

After applying the two equations, it was determined that a 2 × 2 m grid should be utilized. As the wave directions for this case study originate from the northwest (dominant), the west boundary was selected as the wavemaker for all directions and simulations. If it is necessary to alter the wave direction, only the bathymetry will be rotated using MATLAB scripts. Table 4.1 displays the primary characteristics of the computational grids for incoming waves for the first simulations that were performed. Then, later, the grid was extended on the North and South boundaries by 100 m and on the West by 500 m and rotated for the calibration. This was due to some instabilities that were observed in the first simulations.

Table 4.1 - Main characteristics of the computational grids.

Orientation	W	W	NW 284°	NW 299°
Status	Initial	Extended	Extended	Extended
Resolution in X direction [m]	2	2	2	2
Resolution in Y direction [m]	2	2	2	2
No. Grid Cell in X direction	861	1111	1111	1111
No. Grid Cell in Y direction	412	512	512	512
Length in X direction [m]	1722	2222	2222	2222
Length in Y direction [m]	824	1024	1024	1024

Regarding the vertical definition of the computational grid, the linear frequency dispersion determines the number of layers. In particular, the number of vertical strata is determined by the dimensionless depth (*kh*). In general, the greater the value of *kh*, the greater the number of layers required. However, the value of *kh* obtained (having the wave characteristics as Hs = 5.67 m, Tp = 19 s, k = 0.0313 with water depth of 15 m) was 0469 and according to SWASH manual (2020) if the value is less than 0.5, only 1 vertical layer is used.

4.1.2.3. Grain Size

According to research done on the Portuguese coast between the port of Aveiro and Mira beach, about 30 km from Furadouro beach, the observed values of the average mean grain size at the study location fall within the range of 0.39 to 0.57 mm (Silva *et al*., 2009). In this work, however, the values in Table 4.2, from a previous study conducted by (Marques, 2021), will be used and later tested with combination of other parameters for the calibration of the model.

Table 4.2 - Recommended values for the grain size of porous structures. Based on Komen (2019).

	Water Area	Land Area	Vertical wall	RMB
Grain Size (m)	0.002	0.002	0.001	0.500

4.1.2.4. Roughness

As waves propagate in shallow water, the wave-bottom interaction becomes significant owing to the loss of energy caused by friction with the bottom. According to Johnson and Kofoed-Hansen (2000), the dissipation coefficient is influenced by hydrodynamic and sediment conditions. Thus, it is important to characterize bottom friction as friction coefficient, friction factor, Nikuradse roughness, or d_{50} sand sediment size.

The friction coefficient may be retrieved from a .rgh file for Manning or Chezy formulas or Nikuradse roughness height. Nevertheless, numerical investigations have shown that the Manning formula represents wave dynamics in the surf zone more accurately than alternative friction formulas (SWASH Team 2020), hence it will be used in this study.

Marques (2021) considered various values of the Manning coefficient: the value 0 $m^{1/3}/s$ was used offshore (in the sea), the maximum value in buildings and on the rubble mound structures was roughly 0.045 $m^{1/3}$ /s.

In the study of Martins (2016), a constant horizontal turbulence value of 0.01 m/s and a Manning's roughness coefficient of 0.03 $m^{-1/3}$ s are used to account for adhering structures with a greater roughness and the high irregularity seen in the bottoms. Table 4.3 shows the values that are recommended based on Komen (2019) study and the SWASH manual. In this dissertation, these values will be tested as a starting point and later during the calibration of the model, other values will be used.

Table 4.3 - Recommended values for the grain size of porous structures (Komen, 2019).

	Clean Sand	Rock masses	Sand & Alternate Rocks	RMB
Manning Coefficient	0.02	0.05	0.03	0.06

4.1.2.5. Porosity

The value of the volumetric porosity ranges between 0 and 1. For rubble mound breakwaters, a porosity value of 0.45 is commonly used. A low number (0.1) should be considered as impenetrable, comparable to walls and dams. Additionally, relative structure heights may be set such that both submerged and emergent breakwaters are permitted. Values of porosity smaller than one indicate the presence of porous structures. The number 1 denotes water points (SWASH Team 2020).

In the study of Marques (2021), the porosity grid was first used according to Table 4.4. However, since the simulation was unstable therefore unrealistic, it was decided to assume that only the buildings (which are more reflecting) had a porosity of 0.1 and the rest of the region had a porosity of 1.

Pérez (2014) investigated breakwater overtopping using the SWASH model. When the porosity is applied to the whole structure, the author discovered that there is almost 100% transmission with a negligible effect of the structure on the propagation of ocean waves. By adding a layer of porosity to an impermeable breakwater, as determined by bathymetry, the existence of the breakwater had significant impacts; nonetheless, the model depicts a high dissipation of energy in the wave's contact with the structure, which is not a good representation of reality. Therefore, Pérez (2014) found that SWASH was unable to appropriately simulate the presence of a structure with porosity, and that this command should be enhanced since it is a numerical model that is still under development. Nevertheless, Van Mierlo (2014) performed studies including the application of various porosities to a harbor breakwater and the remaining computational mesh.

The purpose of the research was to examine the influence of the breakwater on the wave height and period beneath the structure by comparing the findings to those of a previously conducted physical test. Van Mierlo (2014) stated that the SWASH findings were an excellent approximation of the actual test results, hence the model was able to mimic the effect of the breakwater on the sea turbulence. The settings used were:

- A breakwater modeled as a porous structure with a height equal to four times the depth of the water;
- There are two vertical layers;
- Modeling concrete walls as porous structures with a porosity of 0.1% and a particle size of 0.1 mm;
- Gravel slopes and the breakwater are modeled as porous structures with a 40% porosity and a stone diameter range of 22 to 150 mm, but no bottom friction is accounted for.

Both the roughness and the porosity are very sensitive parameters that can significantly affect the results of the simulations. Several studies were conducted apart from the ones already mentioned above that show and conclude that the SWASH model needs to be calibrated using the results from physical model tests and other models to ensure realistic and good results. These two parameters will always be different and sometimes one of them is not considered depending on the study area (type of simulation) or adjustments need to be made to other parameters that are related to these two. For instance, studies show that porosity is related to turbulent friction loss (β) Pérez (2014) and roughness coefficient shows that certain correlations exist between the apparent friction coefficient and the two dimensionless variables of relative crest freeboard, R_c/H_{m0}, and wave steepness, S_{op}, CDang *et al.* (2020). In this dissertation, for the starting point of simulations, the values of Marques (2021) were considered together with the values recommended by the (SWASH manual 2020), Table 4.4.

Table 4.4 - Volumetric porosity values for different conditions. Values based on Komen (2019) and the SWASH manual.

	Porosity	Reflection Coefficient
Water area	1.00	0
Land area	0.01-0.25	0.99-0.65
Vertical wall	0.01	0.99
RMB	0.45	0.36-0.52

4.1.2.6. Model initial and boundary conditions

For the model's initial conditions (zero velocity and spatially constant water level), a cold start was used. Regarding the boundary conditions, a wave generation boundary was applied to the western boundary, with the sea wave conditions specified according to the JONSWAP spectrum (γ = 3.3), *i.e.*, the data referring to significant wave height, peak wave period, wave direction, and directional dispersion. The WEAK command was applied to this boundary in order to make it nonreflective.

4.1.2.7. Model sponge layers and physics

Sponge layers are very effective in absorbing wave energy at open boundaries where waves are supposed to leave the computational domain freely, therefore they prevent reflections at open boundaries. SWASH manual (2020) recommends a sponge layer of 1 to 3 typical wave lengths. Therefore, based on the hydrodynamic boundary conditions that are used in this dissertation, a minimum sponge layer of 200 m will be necessary. However, since the simulations were not stable and sometimes crashing with an error message *"terminating error: INSTABLE: water level is too far below the bottom level! ** Massage Please reduce the time step!"* Taking as reference other studies dealing with SWASH, this problem is solved by smoothing the bathymetry several times or by ensuring that the bottom level where waves are generated is flat *i.e.*, has a constant elevation. For this work, it was noticed that when the sponge layer is reduced, the simulations would run successfully. For instance, when the sponge layer is placed on the north and south boundaries with a width of 50 or 100 m after extending the grid size together with 200 m of width on the east boundary most of the simulations crashed. However, when the sponge layer of 10 m and sometimes 50 to 100 m is used only on the east boundary, the simulations would run successfully. For this reason, for all simulations a sponge layer of 10 m was applied only on the East boundary of the grid and other borders will be considered, by default, in the model as closed borders, which may induce some reflection to occur.
Regarding the model physics, The BREAking command was also applied so that SWASH assumed wave breaking and a horizontal viscosity according to the Smagorinsky model, with a value of 0.1 was considered.

4.1.2.8. Model discretization, bottom cell, computation time and time integration

The discretization of the conservation of the quantity of motion was applied according to the MUSCL limit. Analogously, for the conservation of the quantity of momentum, a MUSCL limit was applied in the command concerning the indication of the discretization type for the water depth at the velocity points of the horizontal and vertical components of the water particles.

The command that considers the non-hydrostatic pressure is the NONHYDrostatic command, and the Keller-Box scheme was applied, with the ILU preconditioner. The lowest level should be calculated at the center of the cell with the maximum of the four surrounding corner points.

Finally, in the SWASH numerical model for the time discretization the TIMEI METH command was applied, limiting the number of Courant to a minimum value of 0.05 and a maximum value of 0.3. As initial condition, water particles were considered to be at rest *i.e.*, the water level was assumed still and the velocity of the horizontal and vertical components of the water particles equal to zero. A total simulation time of 40 minutes was adopted, with a time discretization of 0.01 s, and this total time is only counted after 30 minutes, so that the simulation stabilizes and more reliable values are obtained.

The simulations were run on a cluster of computers since, due to the grid size, it was discovered that running a 40-min simulation on a local or personal computer with installed RAM of 16.0 GB (15.9 GB usable) and a processor of Intel(R) Core(TM) i7-6700HQ CPU @ 2.60GHz was impossible, as it required approximately five hours to complete only 12% of the simulation. The Inductiva API made it possible to conduct 38 simulations in a single day, with the first group of simulations (20 solutions) completing in 5 to 6 hours, which was 1,000 times faster than on a local computer. Whereby, during the first simulations, the machine with - Intel Core i9-12900K (released in Q4 2021, 12th gen., 5.2 GHz, 16 cores, 24 threads, 64 GB) was used and for the dataset Google Cloud Machines Intel Cascade Lake (Intel® Xeon® Gold 6253CL Processor, C2-Machine series with 15 cores, 120 Gb and 3.1 GHz) was used.

Inductiva API is a Python module that simplifies simulation and optimization at scale by facilitating access to computational capacity (to accelerate simulations with GPU and CPU) and a library of pre-defined simulation use cases. It can be utilized to execute open-source simulation packages from different fields such as Coastal dynamics (*e.g.*, SWASH and Xbeach), Fluid dynamics (*e.g.*, DualSPHysics, SPlisHSPlasH, OpenFOAM) and Molecular dynamics (*e.g.*, GROMACS).

4.1.2.9. Model outputs

It was determined that, as a result of the simulations, the following data should be obtained: the water level, the significant wave height, and the run-up height at the coordinate points with a time interval of 30 s, beginning to record data after 5 s of the start of the simulation.

In order to analyze the obtained data, a new MATLAB routine was created from the SWASH Manual. Thus, it was possible to acquire a map that, when combined with the initial bathymetry, allowed the efficacy of coastal protection structures and the extent of overtopping to be evaluated. Using the run-up height data, maps of flooded areas were generated using MATLAB scripts. With the data obtained from SWASH, it was possible to generate videos illustrating the evolution of the overtopping over the course of the simulation.

4.2. Numerical model validation and Preliminary simulations

4.2.1. Simulations before validating the model

Due to the fact that the SWASH model version used by Marques (2021) was version 6.01, it was necessary to verify if the version 9.01 used in this dissertation produces the same results as version 6.01, as some of the simulations that will be performed will be run in a cluster of computers that use the older version, while others will be run in Inductiva API, which uses the latest version. The main differences between these 2 versions are that version 9.01 supports:

- Internal wave generation for rectilinear non-uniform grid;
- Time series of translation/rotation of rigid bodies and PTO power as output quantities are added;
- Optional inclusion of floating rigid bodies with six degree of freedom motions and fluid-structure interaction (FSI) coupling.

The conditions in Table 4.5 were applied in conjunction with the grid layers shown in Table 4.6. After running simulations with and without the groins head modification, as done by Marques (2021), it was determined that the newest version of SWASH is capable of producing similar results to the older version. However, it was observed that the newest version represents the dry land based on elevation values whereas colors are used to represent the water depth, making it difficult to observe and analyze the inundated area during the simulation on the screen. Appendix B provides, for the purposes of this dissertation, some results acquired during these simulations and while investigating the effect of various combinations of grid layers on breakwater structures.

Table 4.5 – Test conditions.

Test	Orientation [°]	H_s [m]	T_p [s]	Tide [m]
T1	West	2	16	4.2
T2	West	3	16	4.2
T3	West	5	16	4.2

Table 4.6 – Grid layers.

	Particle size [m]	Roughness [$m^{-1/3}s$]	Porosity [-]
Buildings	0.001	0.08	0.01
Walls	0.001	0.045	1
Ocean sand	0.002	0.02	1
Dry land	0.002	0.06	1
RMB and Groins	0.5	0.06	1

4.2.2. Numerical model validation

Several simulations conducted in the preceding section have led to the conclusion that the simulation results were unstable and, therefore, not realistic. Consequently, a careful calibration and validation procedure of the model was required to ensure that the results obtained are accurate. For this purpose, data from the 2014 storm event (section 3.3) were utilized. To calibrate the model, Table 3.3 (which represents hydrodynamic boundary conditions measured by a buoy located a few kilometers from the coast of Furadouro beach) was used in conjunction with Table 4.7, which depicts the various grid layers that were employed. Some simulations are illustrated in Appendix C.

Table 4.7 - Different layers of grids.

	Particle size [m]	Roughness [$m^{-1/3}s$]			Porosity [-]	
Buildings	0.001	0.08	0.08	0.08	0.01	0.01
Walls	0.001	0.045	0.012 [3]	0.016 [3]	1	0.01
Ocean sand	0.002	0.02	0.019	0.019	1	1
Dry land	0.002	0.06	0.04 [4]	0.05	1	0.1 [1]
RNB and Goins	0.5	0.06	0.036 [5]	0.045	1	0.45 [2]

1. Most of the area is impermeable because of pavements, roads, buildings etc.
2. Recommended by SWASH Manual
3. Concrete finished with float. (Suzuki, *et al.*, 2018)
4. Clean, winding, some pools and shoals. (Suzuki *et al.*, 2018)
5. Dry rubble or riprap (0.036) and rocky beds (0.045). (Suzuki *et al.*, 2018)

Figure 4.4 depicts the streets that are primarily affected by flooding after overtopping. These streets are used by the overtopping water to reach the fourth building blocks. The simulation was run smoothly and successfully after multiple simulations using different combinations of layers (porosity, particle size, and roughness) and using only one test condition of NW 299°. Figure 4.5 depicts the flooded area, and Table 4.8 lists the roughness grid layer employed.

During the tests of several simulations, it was discovered that, in addition to the values of porosity, particle size, and roughness, one of the factors affecting the results of the flooded area was the method of smoothening the bathymetry. For instance, if the buildings are placed on the bathymetry and smoothening is applied to both the buildings and the bathymetry, the ground level is raised by a few centimeters and the sides of the buildings are lowered. This minor elevation of the ground level affects the depiction of the inundated area because it obstructs the flow of floodwater. Therefore, the bathymetry was first refined, followed by the deployment and smoothing of the structures using polygons.

After obtaining an inundated area analogous to Figure 3.11 of the 2014 storm event, it was essential to determine whether the inundated area obtained from this simulation is the same as the one mentioned in section 3 (12 hectares). To calculate the flooded area, it was necessary to first compute the maximum dry area that can be achieved, which is the area behind the adhered vertical wall as shown in Figure 4.6, which is 44.2158 ha, and the dry area of 34.3552 ha obtained from Figure 4.5 (using a MATLAB script in which the dry cells are counted and multiplied by 4 because the grid size is 2 by 2 m). The difference of these dry areas gives the flooded area of 9.8606 ha, note that the obtained inundated area does not include the area of the buildings which when it is added could give 12 ha.

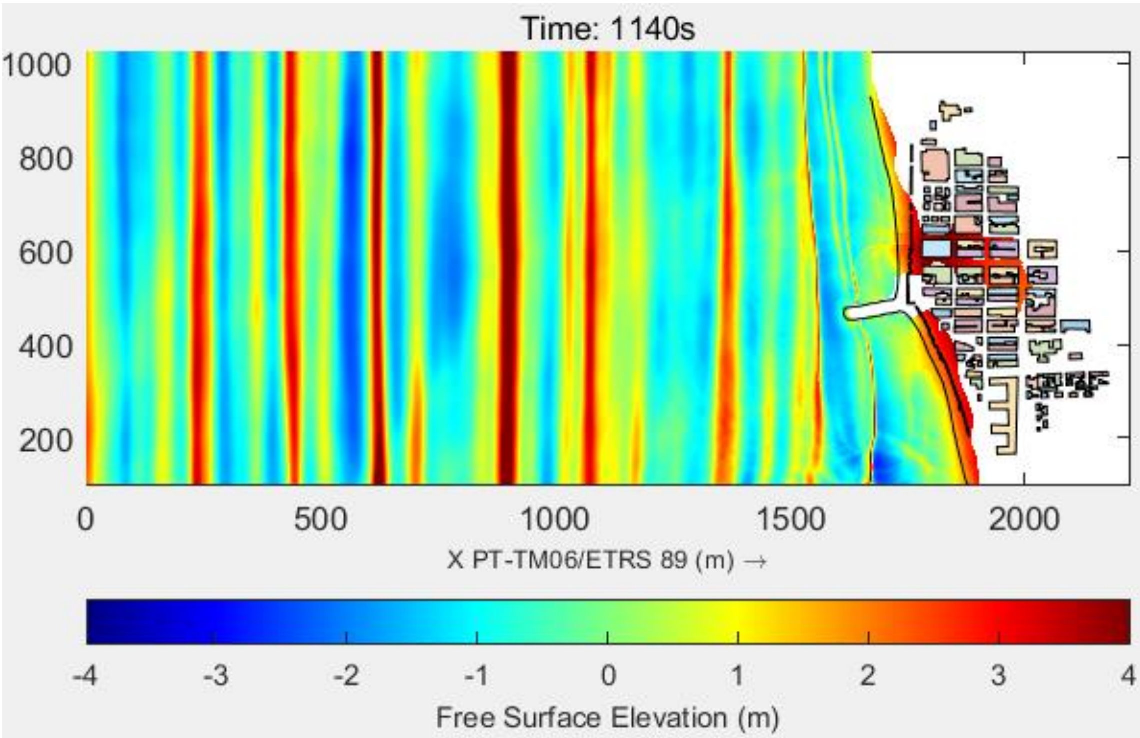

Figure 4.4 – The snapshot of the video at time =1140s that was obtained from the results of the simulation.

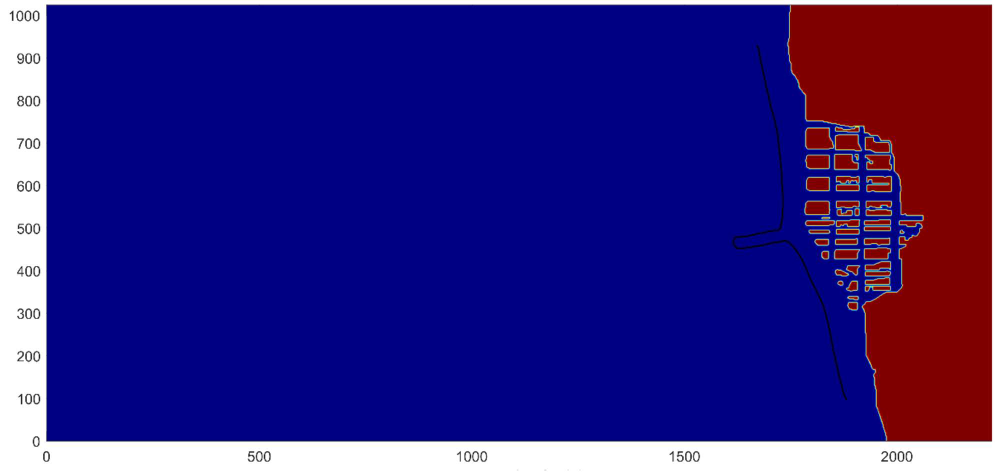

Figure 4.5 - Flooded area obtained for the test condition of NW 299°.

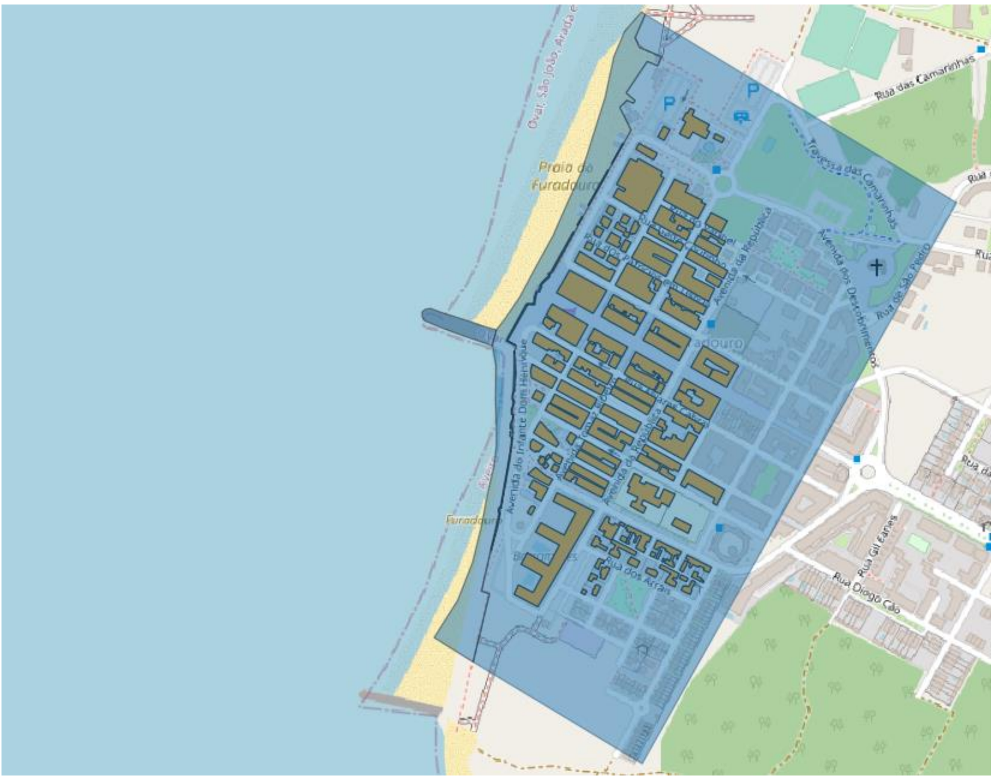

Figure 4.6 - Maximum dry area that can be obtained behind the vertical wall.

Table 4.8 - Roughness layer used.

	Roughness [$m^{-1/3}s$]
Buildings	0.08
Walls	0.012
Ocean sand	0.019
Dry land	0.04
RMB and Groins	0.045

4.2.3. Test conditions

The definition of a perimeter prone to coastal flooding is a complex endeavor, not only due to the variety of methods, but also due to the need to understand the area under study by analyzing oceanographic and morphological characteristics, historical occurrences, and urban typicity.

To determine the maximum area susceptible to coastal overtopping and flooding, it was first necessary to identify the extreme event that resulted in the largest known floodable area, at least within the last century. This was accomplished through the development of an occurrence and damage database, which also permitted the estimation of the likelihood of occurrence and intensity of this process. Thus, the events of January 6 and February 2, 2014, were defined (Table 4.9), emphasizing the significance of mentioning the two incidents together because, despite being separate, they have a strong causal relationship.

Table 4.9 - The test conditions.

Date	H_{s_prop} [m]	T_{p_prop} [s]	Direction [°]	Tide [m]
2014-01-06	7.27	18.97	NW 284	3.55
2014-02-02	5.67	19.00	NW 299	4.00

4.2.4. Preliminary simulations

Figure 4.7 to Figure 4.12 presents the results obtained after the simulation of the 12 solutions proposed in the previous section (3.4). The simulations were conducted for both wave directions of NW 284° and NW 299°.

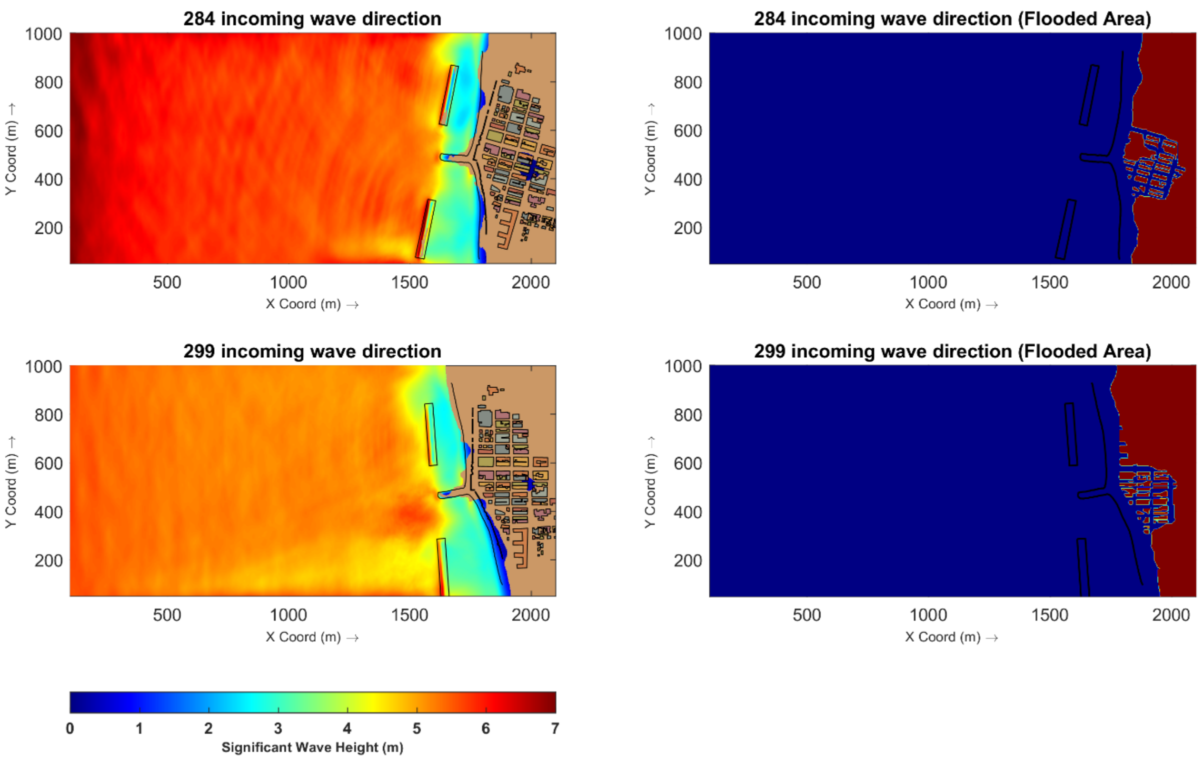

Figure 4.7 - Results of the proposed solution from Castro (2015).

In Figure 4.7, the reflection of waves due to the breakwater structures can be observed, diffraction and refraction as waves approach the shoreline and interact with structures can be observed clearly for both directions of incoming waves. Refraction is more pronounced on the southern part of the domain due to the steeper slope and greater elevation differences between the northern and southern parts of the bathymetry. Regarding the flooded area, it can be seen that in the NW 299° direction, the area on the south side of the groin is not protected by the structures, whereas in the NW 284° direction, the flooded area transfers to the centre behind the groin. In both instances, the flood's extension reached the third row of buildings.

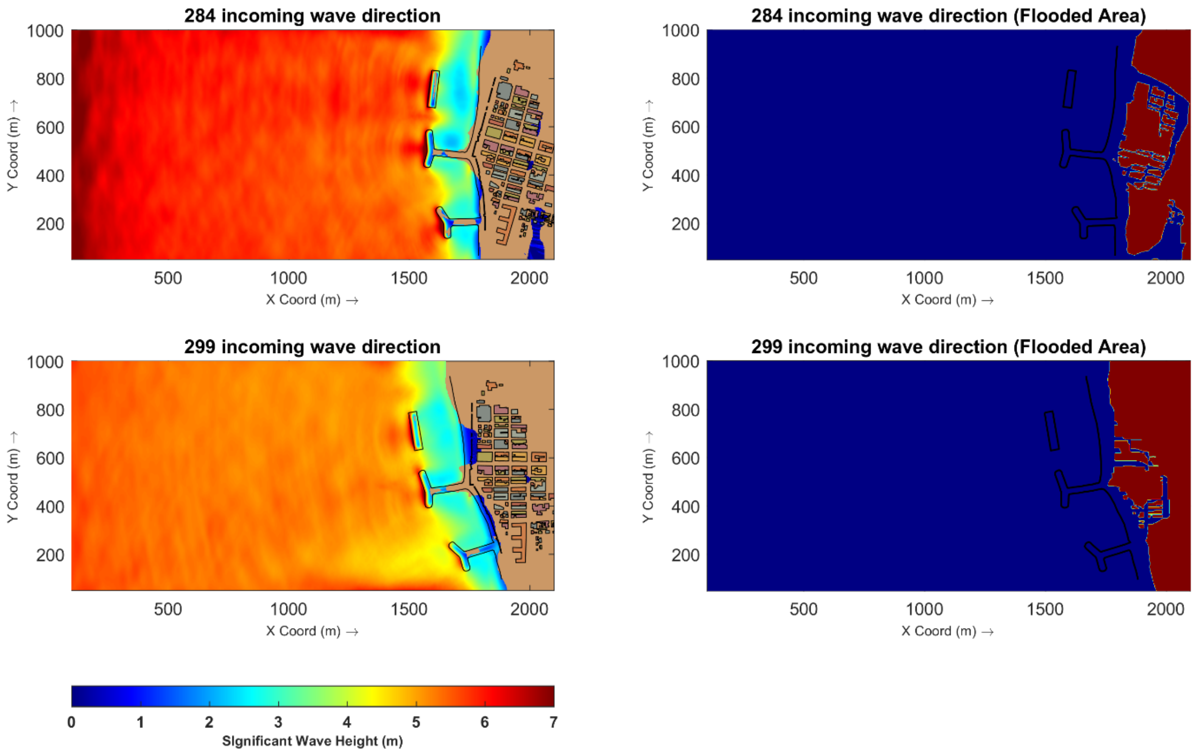

Figure 4.8 - Results of the proposed solution.

Compared to the previous results, modification of the groin's head was able to protect the central area behind the groin in Figure 4.8. As much as the head of the groin reduced the impact of waves on the centred area in both incoming wave directions, the area was still impacted by inundation caused by waves that were able to propagate between the groins' heads. Therefore, the vertical breakwater must be extended to be effective against NW 284° incoming waves in order to secure the northern part of the urbanized area.

For wave direction NW 299°, the solution required the use of vertical breakwaters in the north, as the modification of the groin proposed by Marques (2021) presented in Figure 4.9 appears to be very effective only at dissipating wave energy and preventing a significant amount of overtopping in the south and central areas of the region. Observing the flooded area of NW 284, one can conclude that the majority of streets were flooded by water flowing from the north overtopping, while the water flowing from the centre overtopping reached the third row of buildings through one street located on the north side of the groin.

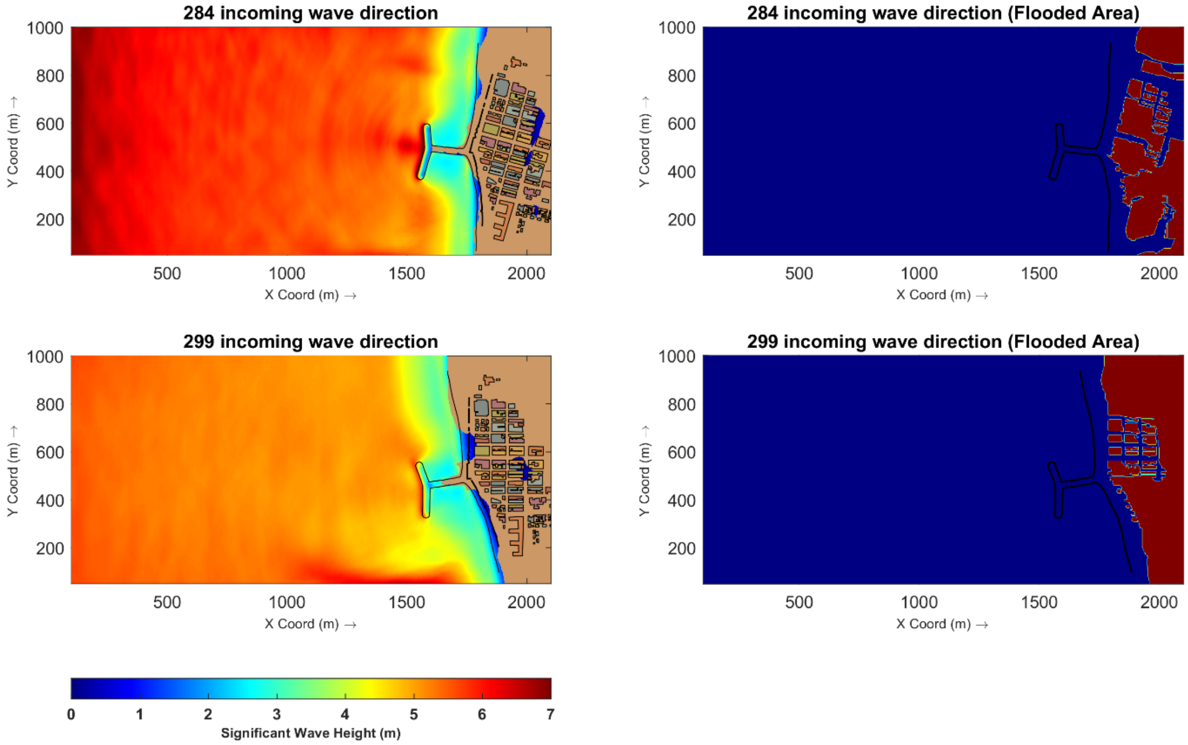

Figure 4.9 - Results of the proposed solution from Marques (2021).

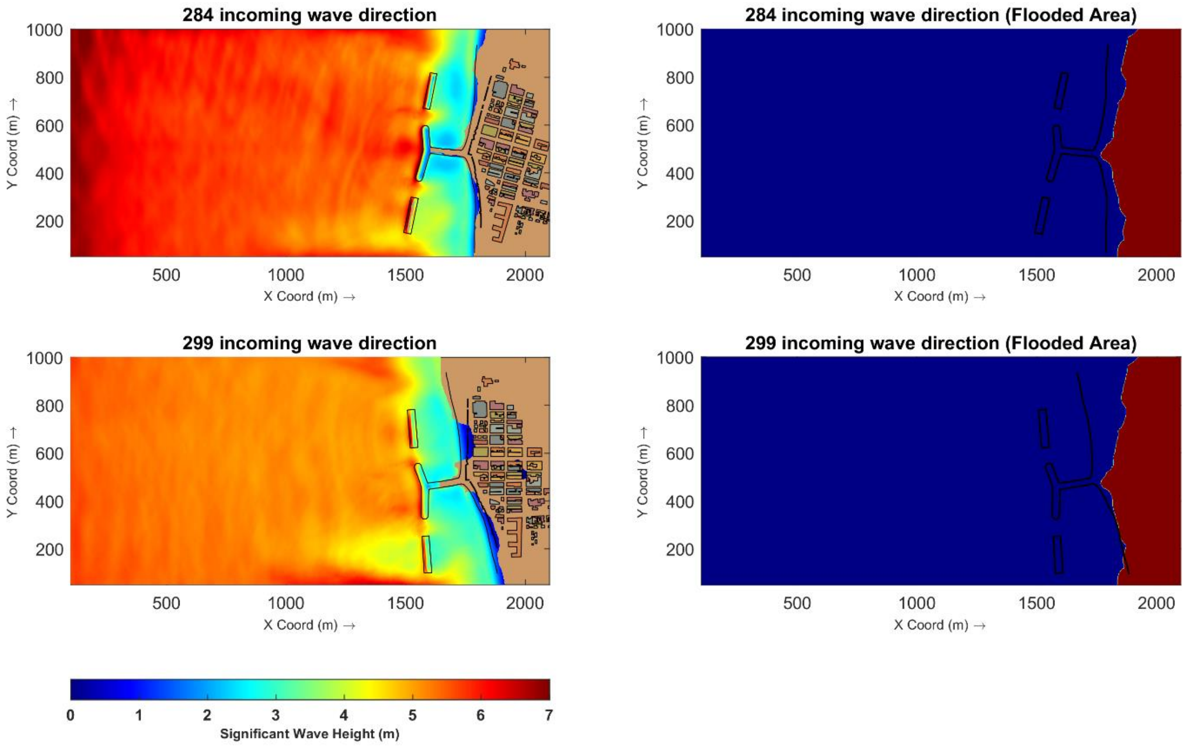

Figure 4.10 - Results of the proposed solution from Marques (2021) and Castro (2015).

In the previous analysis of Figure 4.9, it was suggested to add the vertical breakwater on the north side of the groin with the same configuration of the groin's head proposed by Marques (2021). However, as shown in Figure 4.10 for wave direction of NW 299°, the results indicate that the structure is still incapable of reducing the overtopping on the north side of the area, as waves still propagated between the north vertical breakwater structure and the north arm of the groin. Regarding the south side of the groin, both the south hand of the groin and the vertical breakwater structure appear to be effective, as they were able to dissipate wave energy and reduce the overtopping and consequently the inundated area by a significant amount.

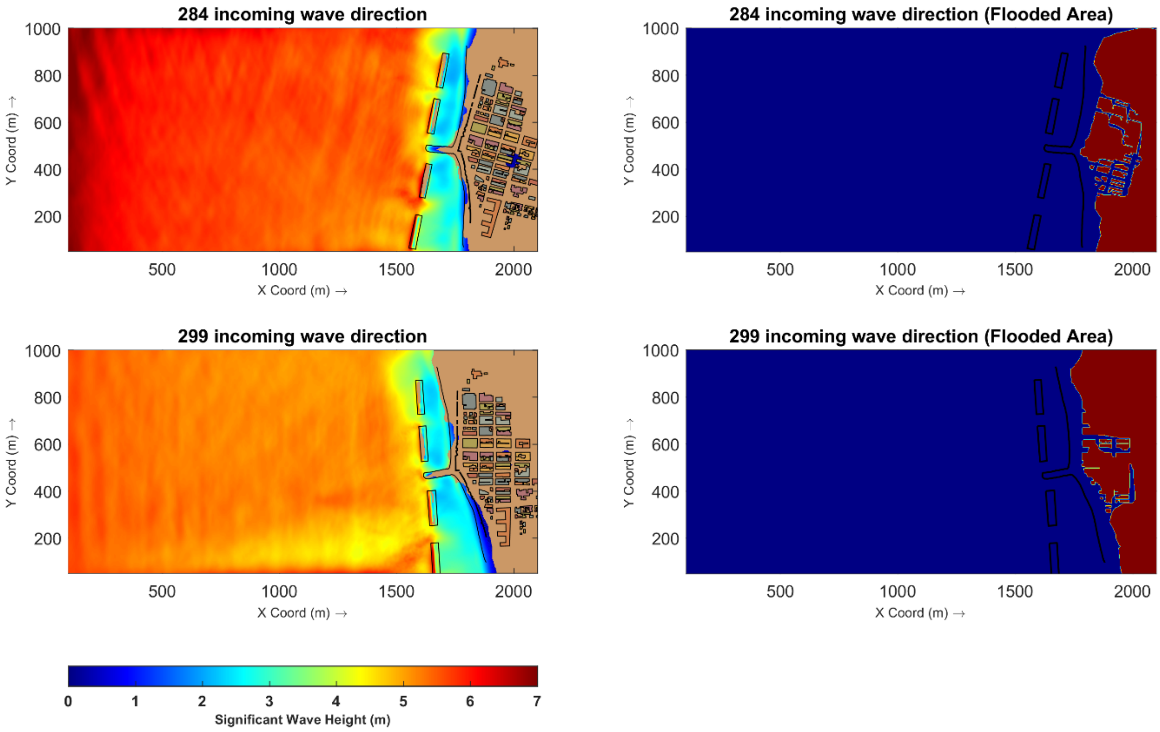

Figure 4.11 - Results of the proposed solution from Castro (2015).

On the basis of these results and previous ones, it can be concluded that the solution proposed by Marques (2021), extending and modifying the groin's head, appears to be the optimal one for protecting the southern region close to or behind the groin. For this solution presented in Figure 4.11, it can be concluded that the deployment of vertical breakwater structures alone is insufficient; the solution should be combined with Marques' proposal.

The area on the north side of the groin is protected from both incoming wave orientations for the first time in all of the previously analyzed solutions (Figure 4.12). Furthermore, the percentage of inundated area has been significantly lowered. Therefore, it can be concluded that the area to the north of the groin required thicker vertical breakwater structures because the vertical breakwater structures proposed by Ramos were 38 m thick, which is 14 m thicker than the breakwater structures proposed by the other tested solutions.

Moreover, in all simulations, extreme significant wave heights and instabilities are observed at the south boundary of the grid. As already mentioned earlier, the sponge layers could not be introduced to absorb these waves and prevent reflection on the north and the south boundaries since the simulations were crashing even after the extension of the grid on these boundaries. It is concluded that the results of this solution have a major effect in the area of interest, *i.e.*, the area that is close to the groin.

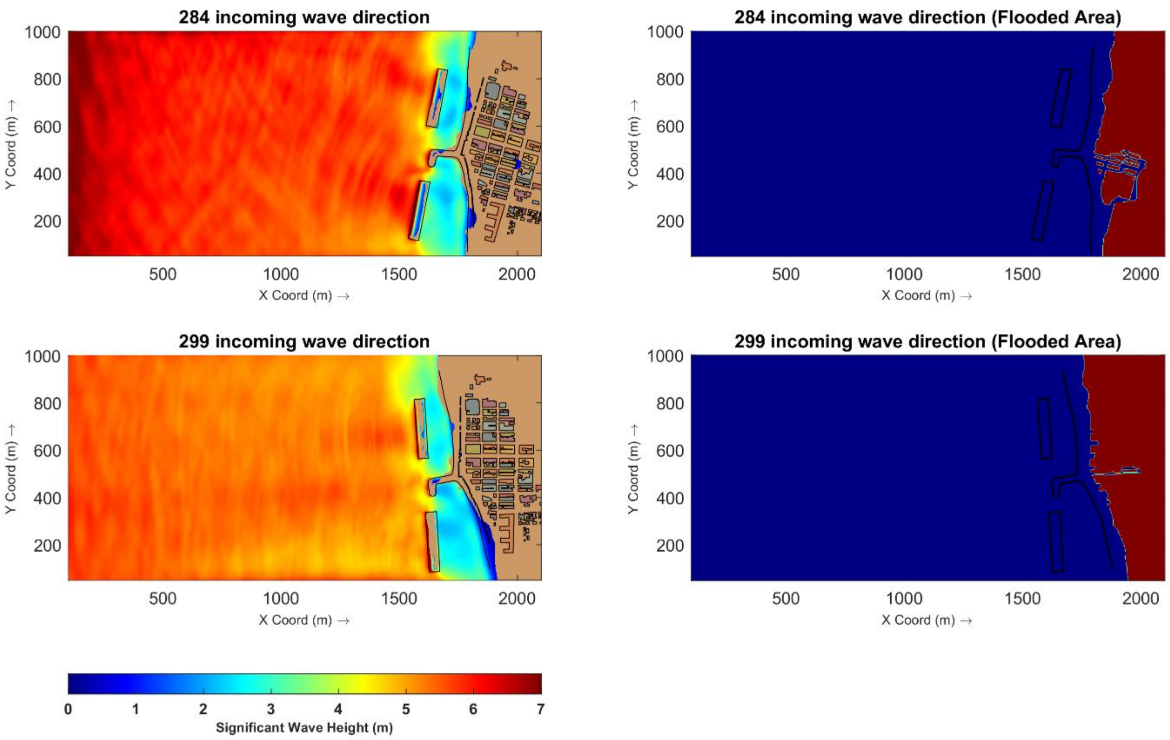

Figure 4.12 - Results of the proposed solution, groin's head modification by Ramos (2011) with the vertical breakwater structures of Martines (2015).

4.3. HYDRODYNAMIC SIMULATIONS, ANALYSIS AND DISCUSSION OF RESULTS

Figure 4.13 presents the results of 4 simulation that were obtained from different solutions introduced in section 3.4.2. To simplify the input features for the ML algorithm, only the income wave direction of NW 299° (conditions shown in Table 4.9) was used and the dimensions of the structures were kept constant. The other 53 simulation results are presented in the Appendix E.

LEGEND:

Dry area
Flooded area
Vertical breakwater structures
The shoreline

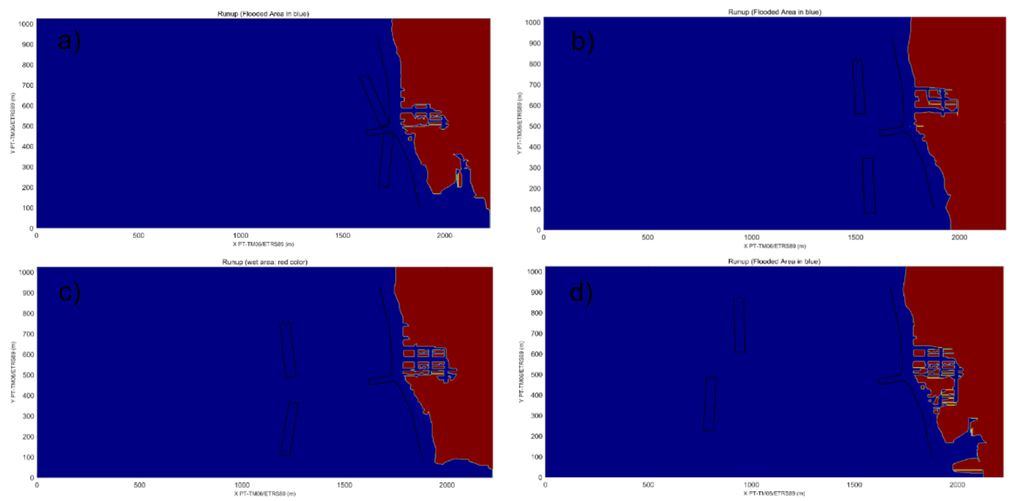

Figure 4.13 - The results of 4 solutions.

The results indicate that structures located 75 m from the groin (solution b) were the most effective of the 4 solutions, followed by structures located 350 m from the head of the groin (solution c). Clearly, the structures of solution d) are insufficient to safeguard the coastal zone's central and southern regions. Solution a) demonstrates that even when structures are positioned -75 m from the head of the groin and operate as revetment walls, they are insufficient to protect the study area. Other results can be seen in Appendix E in order to comprehend and be persuaded of which location combinations provide the best results in terms of reducing the overtopping and, consequently, the inundated area.

4.4. APPLICATION OF MACHINE LEARNING

4.4.1. INTRODUCTION

A machine learning project involves a number of steps shown below:

i. **Import the data:** this data is often coming as a csv file.
ii. **Clean the data:** this includes tasks such as removing duplicated data because such data will cause the model to learn incorrect patterns in the data, resulting in an incorrect output. Additionally, the data must be cleaned by removing or modifying irrelevant and insufficient data, depending on the type of data used. This phase can also entail data normalisation if performed manually.
iii. **Split the data into Training and Test sets:** this means the data needs to be separated into two segments one for training the model and the other for testing it to make sure that the model produces the right results.
iv. **Create a Model:** this entails selecting an algorithm to analyse the data, such as neural networks and decision trees. Each model has advantages and disadvantages in terms of accuracy and performance, so the algorithm chosen depends on the type of problem to be solved and the input data. It is not necessary to programme this algorithm explicitly because libraries can provide it.
v. **Train the Model:** the model looks for the pattern in the data.
vi. **Make predictions:** here the test set is used to ask the model to make predictions.
vii. **Evaluate and improve:** in the majority of cases, it is highly probable that the predictions will be inaccurate, therefore, it is necessary to evaluate and measure the accuracy of the predictions before returning to the model to either select a different algorithm that will produce more accurate results for the type of problem being solved or to fine-tune the parameters of the model, as each algorithm has parameters and hyperparameters that can be modified to optimize the accuracy.

Examples of parameters are:

- Weights (w);
- Bias (b).

Examples of hyperparameters are:

- The learning rate (α);
- Number of iterations of gradient descent;
- Number of hidden layers;
- Number of hidden unites or notes;
- Choice of activation functions;
- Momentum term;
- Mini-batch size;
- Regularizations;
- Choice of an optimizer;

- Metrics.

Applied deep learning is a highly empirical process, which necessitates trial and error to determine what works. For instance, various values of the learning rate *versus* the number of iterations (epochs) can be tested to determine which yields the lowest cost.

4.4.2. PREPARATION OF DATA

To create and train the ML model, data was extracted from 37 simulations that were conducted in section 4.3.

The data contains 8 input features as follows, also illustrate in Figure 4.14:

- The distance from the reference line behind the shoreline to the location of the North vertical breakwater (VBW) structure measured parallel to the wave direction from West;
- The distance from the reference line behind the shoreline to the location of the South VBW structure measured the same way as the previous one;
- The orientation to the North VBW structure measured clockwise from the West;
- The orientation of the South VBW structure measured clockwise from the West;
- The x and y coordinates from the centre point of the North VBW structure;
- The x and y coordinates from the center point of the South VBW structure.

In this case, the only output variable will be the dry area. Since the inundated area from SWASH includes the entire offshore area and not just the dry area that is inundated during the simulation, it was easy to measure and calculate the dry area from the urbanized area of Furadouro. Therefore, if the dry area is large, this will mean less overtopping and consequently less inundated area. This indicates that the solution with the largest dry area among the 37 simulations conducted is the most effective one to prevent flooding and overtopping in Furadouro coastal front.

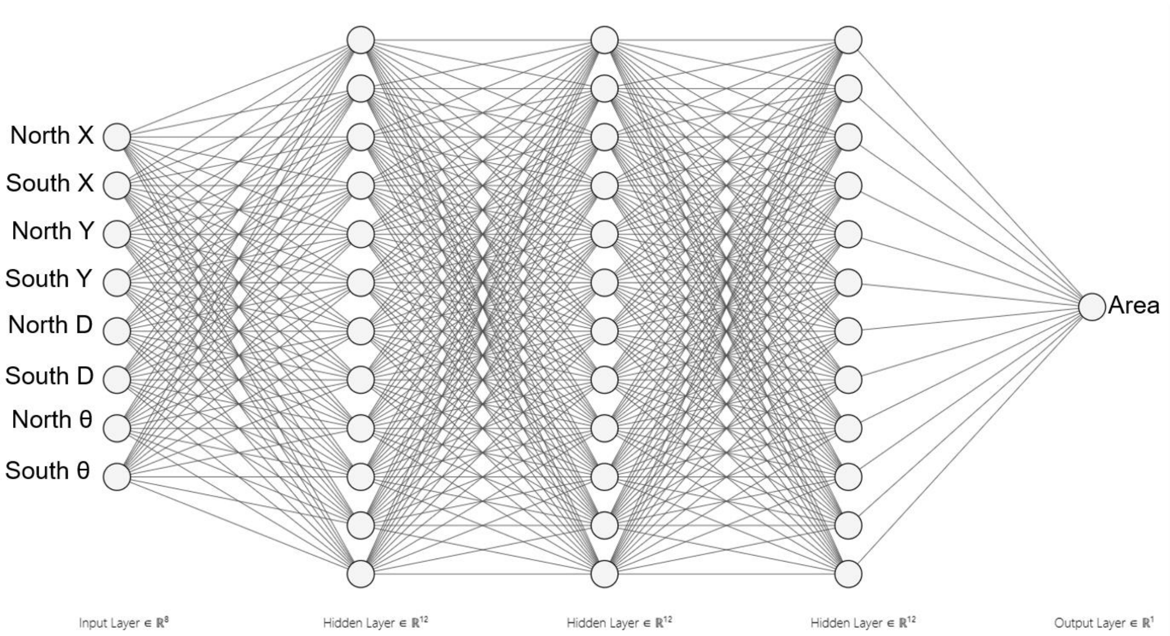

Figure 4.14 - A typical neuron network used.

It was ultimately necessary to normalize the dataset in order to facilitate ML's ability to learn more quickly and accomplish rapid convergence. For this purpose, the columns with x and y coordinates were normalized so that they fell within the range [0-1] because their values were significantly larger compared to the rest of the data values, which would lead to undesirable oscillations during the optimization process. In order to achieve this, the following formula was used:

$$\text{Min-max normalization: } x' = \frac{x - x_{min}}{x_{max} - x_{min}} \quad (27)$$

However, it was later determined that it was difficult for the model to learn from the dataset with that type of normalization because the MSE was significant. As a result, a different normalization strategy was applied, which consisted of limiting all values in the dataset to two digits before the comma (by dividing the columns with 100s by 10 and the one with 1000s by 100); after this, the MSE value decreased for all ML models that were trained. Therefore, it was decided to utilize the second normalized data for the remaining model training.

4.4.2. Model setup

In this dissertation, the Artificial Neural Network (ANN) is used. ANN is a paradigm of learning and autonomic processing that was inspired by brain function. It is a network of neurons that cooperate to produce a stimulus output. Engineers, mathematicians, physicists, computer scientists, and neuroscientists collaborated to create them as a field of study within Artificial Intelligence (Bishop, 1995). The primary elements of an ANN are:

- The synapses or connection links that provide the weights (W_i) and are usually designed to minimize error in a training data set;
- One function adds the input of each of values weighted using Eq (5), and;
- An activation function that applies $N \rightarrow y = h(N)$.

The primary components of an ANN are its architecture, learning algorithm, and activation function, while the method for determining the weights is known as the learning or training method. The activation functions of a neuron transform input data into output (Fausett, 1994).

In ANN applications, back propagation (BP) is a common learning algorithm. It employs the error gradient back propagation (BP) algorithm. This training algorithm is a method for distributing errors in order to find the optimal fit or minimum error. After the data has passed through the network in a forward direction and the network has predicted an output, the back propagation algorithm redistributes the error associated with this output and adjusts the weights accordingly. Several iterations are conducted in order to minimize the defect. The term "epoch" refers to a complete cycle. Each neuronal connection is assigned a synaptic weight that represents the potency of the connection (Govindaraju, 2000). Traditional BP employs a gradient descent algorithm to determine network weights.

4.4.3. Training the NN models

4.4.3.1. Model training type one

First Criteria

During the model training process, it was observed that the mean squared error (MSE) is dependent on the quality of data used. Initially, 20 simulations were used for model training, but it was determined that the data was insufficient because the MSE was significantly larger than anticipated (the MSE value should at least be less than 1); consequently, 17 additional simulations were added to balance the data, *i.e.*, to support the solutions with unique orientation and position of structures. After this, a decrease in MSE was observed.

The MSE is not only affected by the data, but also by hyperparameters, such as the number of hidden layers and the number of neurons. Sometimes, when both are increased, the accuracy increases as well, but an excessive increase can result in a less accurate prediction. One can determine the optimal combination of the two through trial and error. Controlling hyperparameters such as the learning rate, momentum, batch size, the number of iterations (epochs), and by choosing the right loss functions, and the right optimizer for the model, can further reduce the MSE.

In this study, 96 model trainings were conducted using a number of hidden layers between 3 and 6, with and without a normalization layer, 12 and 20 neurons, and batch sizes. If the trained model produced promising results, the training was repeated with a different learning rate. The regression loss functions were the optimal choice for the data used and for the desired output; consequently, various loss functions were analyzed. Adam was used as the optimizer, and since the dataset contained both large negative and positive values, it was initially decided to use LeakyRelu, which has the ability to retain some of the negative values that flow into it (see Figure 4.15). This offers a slightly higher degree of flexibility to the model using it. However, it was discovered during training that the benefits of LeakyReLU are inconsistent, so ReLU was used instead, which will consider all negative values as zero. A linear transfer function was used with back propagation (BP) learning for the output layer. Mean squared error was used as a metric, and 5000 epochs were executed for each model's training. To split the input data, 80% of the data was used for training and 20% for testing, or X_Train: (30, 8) and X_Test: (7, 8).

Table 4.10 depicts the manner in which 96 model trainings were conducted, taking into account three loss functions: Log cosh, mean squared error, and mean square logarithmic error (MSLE). Three indicators were used to select the most promising and accurate models: the metric function of mean squared error, which is used to evaluate a model's performance, the mean squared error between the true values and the predicted values (Eq 28), and the mean absolute percentage error (Eq 29). After training the models, the models with the lowest values of indicators were saved to be validated with different datasets. The models that were saved are shown in

Table 4.11 using an optimizer of Adam, where A represents the Model number, B the number of hidden layers C, a normalized layer is or not present, D the number of neurons, E the loss function, F the learning rate, G batch size, H: the mean squared error of the training set, I is the mean squared error of the test set, and J the mean absolute percentage error,

$$MSE = \frac{1}{n}\sum_{i=1}^{n}(y_i - \hat{y}_i)^2 \qquad (28)$$

where y_i is the true value, $\hat{y}_i$ is the predicted value and *n* number of data being analyzed.

$$MAPE = \frac{100\%}{n}\sum_{t=1}^{n}\left|\frac{A_t - F_t}{A_t}\right| \qquad (29)$$

where A_t is the actual value and F_t the forecast value. Their difference is divided by the actual value A_t. The absolute value of this ratio is summed for every forecasted point in time and divided by the number of fitted points n.

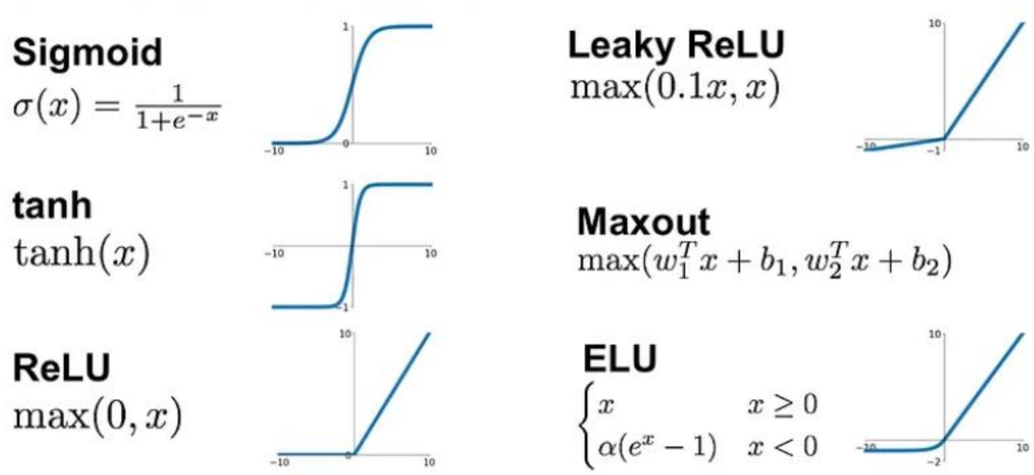

Figure 4.15 - Different activation function graphs [134].

Table 4.10 - 96 options for model training.

Loss function	Hidden layers	Normalized layer	Neurons	Optimizer	Learning rate	Batch size
Log Cosh	3	Yes and No	12 and 20	Adam	0.001	5 and 29
	4	Yes and No	12 and 20	Adam	0.001	5 and 29
	5	Yes and No	12 and 20	Adam	0.001	5 and 29
	6	Yes and No	12 and 20	Adam	0.001	5 and 29
MSE	3	Yes and No	12 and 20	Adam	0.001	5 and 29
	4	Yes and No	12 and 20	Adam	0.001	5 and 29
	5	Yes and No	12 and 20	Adam	0.001	5 and 29
	6	Yes and No	12 and 20	Adam	0.001	5 and 29
MSLE	3	Yes and No	12 and 20	Adam	0.001	5 and 29
	4	Yes and No	12 and 20	Adam	0.001	5 and 29
	5	Yes and No	12 and 20	Adam	0.001	5 and 29
	6	Yes and No	12 and 20	Adam	0.001	5 and 29

Table 4.11 - ML Models saved after training.

A	B	C	D	E	F	G	H	I	J
1	5	Yes	20	MSLE	0.001	5	0.6462	0.3919	1.6595
2	3	No	20	MSE	0.001	5	0.2198	0.4938	1.7459
3	6	Yes	20	MSE	0.001	5	0.7515	0.9924	2.2189
4	6	No	20	Log Cosh	0.001	29	0.4658	0.3203	1.3600
5	6	No	12	Log Cosh	0.001	29	0.7118	0.9521	2.2668
6	3	Yes	20	Log Cosh	0.001	29	0.8465	0.1956	1.0651
7	3	Yes	12	Log Cosh	0.001	29	0.9190	0.5130	1.8171
8	6	Yes	20	Log Cosh	0.001	29	0.8244	0.4075	1.7893
9	6	Yes	12	Log Cosh	0.001	29	0.9626	0.6847	2.0684
10	3	No	12	Log Cosh	0.001	5	0.2347	0.5035	1.8723
11	5	Yes	12	Log Cosh	0.0005	29	0.6361	0.4942	1.5997
12	5	Yes	12	Log Cosh	0.001	29	0.6622	0.8388	1.8279
13	5	No	12	Log Cosh	0.001	29	0.1464	0.2428	0.9323

Figure 4.16 represents the test results of 4 models that were selected from
Table 4.11 (model 2, 4, 10 and 13) after training these models. The test set which is 20% of the dataset was used to test the models' predictions. It is important to note that these models were trained using a dataset with a total of 37 samples.

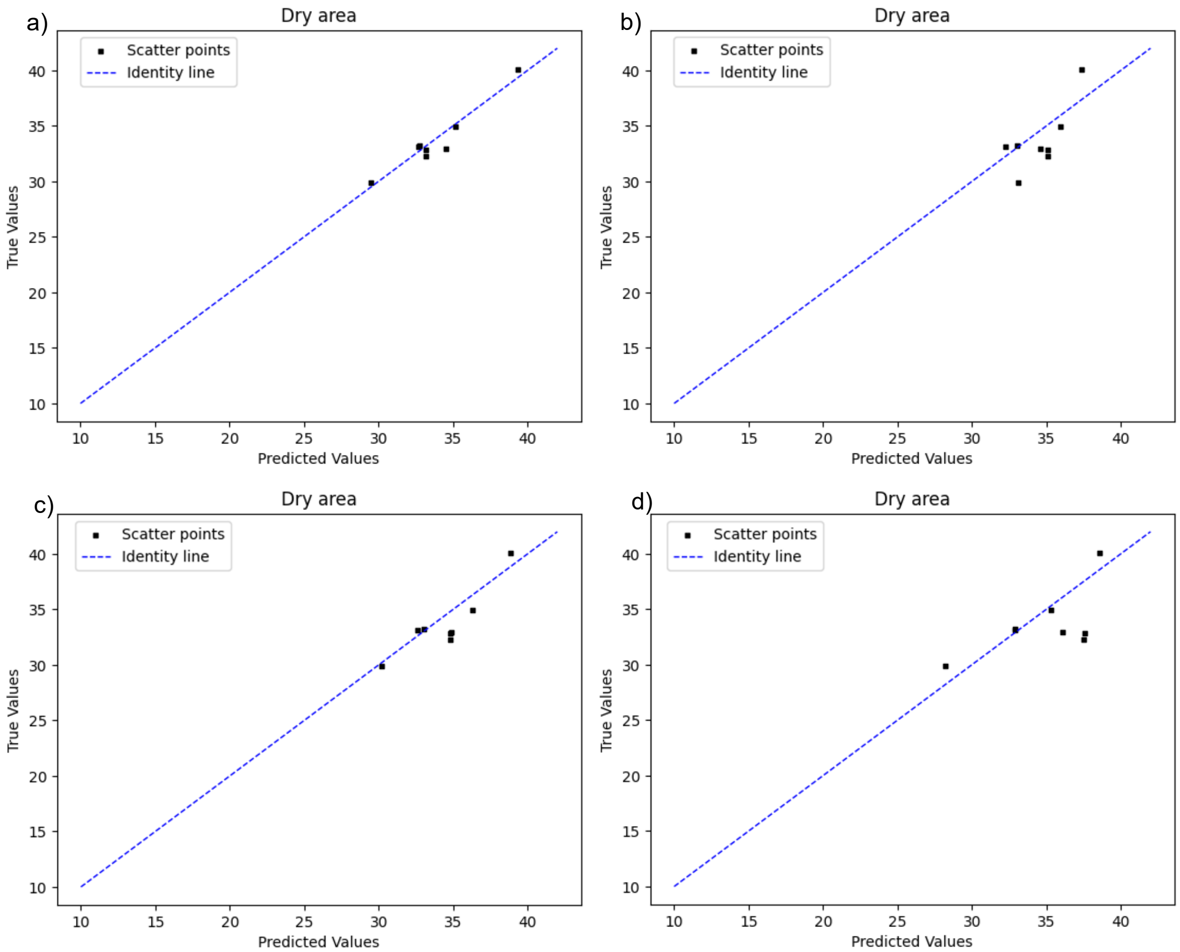

Figure 4.16 – Comparison of predicted values with "true" values: a) results from model 2 with MSE of 9.2604, b) model 4 with MSE of 10.3289, c) model 10 with MSE of 9.7347 and d) model 13 with MSE of 26.2797.

Second Criteria

Some of the previous models were performing well (with MSE less than 0.5), however, it was discovered during model validation that the results were not sufficiently good (with MSE greater than 1) with MSE of model 2, 4, 10 and 13 being 9.2604, 10.3289, 9.7347 and 26.2797. As a result, it was necessary to add 20 more samples, bringing the total to 57 samples, as explained in the previous sections. With this new data set, new models were generated. The first difference between the previous model and the one presented in this subsection is that the area used from the dataset to train the model is the flooded area instead of the dry area, because the values of the flooded area are smaller than those of the dry area, allowing the model to learn more quickly. The second distinction was the method used to construct the model, *i.e.*, the method to determine the number of neurons to use and which optimizer or activation function to employ. In previous models, hyperparameters were arbitrarily selected, and various combinations were tested to determine which hyperparameter combination yields the best model. In this subsection, instead of manually training each model individually as shown in Table 4.10

from the previous subsection, the grid search cross validation method was used to determine the optimal combination of hyperparameters. This method scans the data and configures the optimal parameters for a given model. The grid search parameters defined for this purpose are listed in Table 4.12 below. Only the number of hidden layers (1 and 3) and loss functions (Log Cosh and mean squared error) were already specified. Figure 4.17 illustrates a typical example of a neuron network, while
Table 4.13 lists the trained models obtained from gridsearchCV with an Activation function of ReLU and number of epochs of 3000 for all models. Figure 4.18 depicts the results of the models' predictions.

Table 4.12 - Grid search parameters.

Parameters				
Activation function	ReLU	LeakyReLU	tanh	Linear
Optimizer	Stochastic gradient descent (SGD)		Adam	
Neurons	12	15	20	25
Batch size	5	10	45	
Epochs	1000	3000	5000	
Leaning rate	0.0005	0.001	0.005	0.01

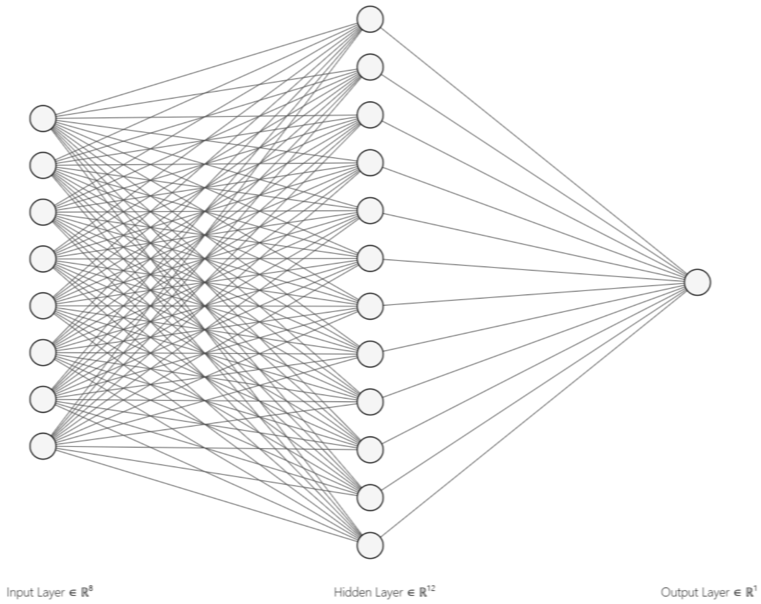

Figure 4.17 - Example of a neuron network used.

Table 4.13 - Trained models.

Loss	Layer	Neurons	Optimizer	Batch size	Learn rate	MSE (Test)	MAPE
Log Cosh	1	20	SGD	10	0.0005	0.3773	1.8467
	3	20	SGD	45	0.01	0.5131	0.5298
MSE	1	12	Adam	10	0.01	0.4777	0.8406
	1	12	Adam	10	0.01	0.3943	1.0211

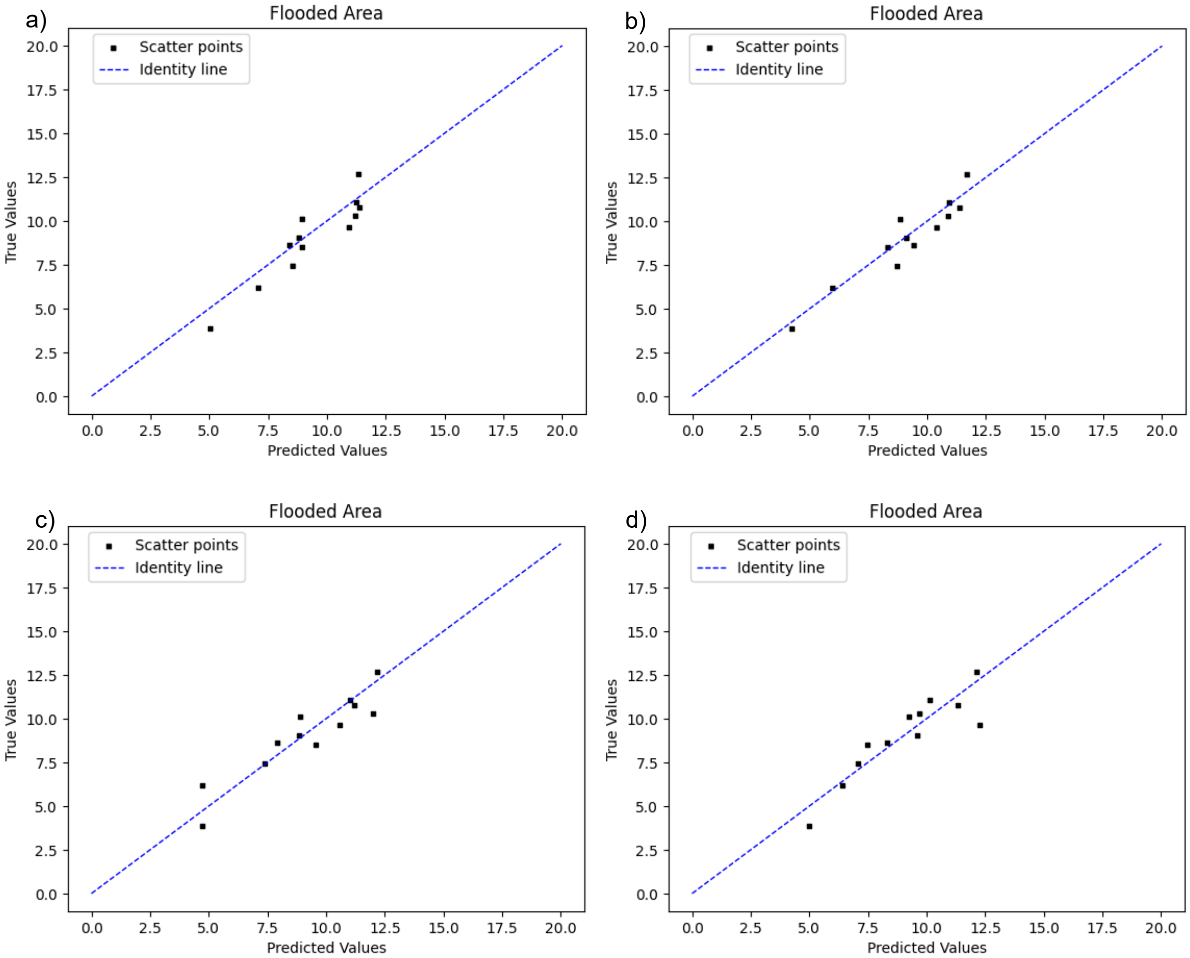

Figure 4.18 – Comparison of predicted values and the “true” values: the results of the first model with one hidden layer using loss function of log cosh (a), Model with 3 hidden layers (b), first model in the rows of MSE loss function (c), the second model using MSE loss function, the uses one hidden layer and also includes the normalization layer (d).

4.4.3.2. Model training type two

Machine learning was incorporated into this work so that it could be used to predict the positions of structures that would provide a certain level of protection against coastal inundation. However, this is not attainable with the models already presented before. Those models only help to predict the flooded area that could be obtained when structures are positioned at different locations, with a given orientations. This could be considered as part of the solutions for accelerating the process of determining the inundated area when one proposes the location and orientation of breakwater structures. In fact, with this approach, it would not be necessary to perform the simulation of the proposed structures (assuming the same wave boundary conditions and study region that were used to train the model) in order to define the inundated area that corresponds to the position and orientation of structures. In other words, simulations that previously required four hours to determine how much area will be inundated when vertical breakwater structures are deployed can now be completed in a matter of seconds using machine learning.

However, the goal here is to provide the model with the inundated area that is intended to be attained to ensure safety in the region, *i.e.*, the area with the least amount of overtopping and flooding. For this reason, a distinct Neural Network was required in which the output of ANN type two becomes the input and the input becomes the output, so that the input layer consists of three neurons for the inundated area, the orientation of the north structure, and the orientation of the south structure. The output layer, on the other hand, will have 4 neurons for the x and y coordinates of both structures on the north and south, as depicted in Figure 4.19. The distances from the shore will be disregarded, as it will be simple to measure the distance from the shoreline to the structures' positions if one knows their coordinates. Using the same methodology as ANN type 2 to generate new models, Table 4.14 shows the 2 trained and validated models (where an activation function of ReLU and Adam optimizer were used with number of epochs equal to 5000). Figure 4.20 depicts the results of the test dataset predictions for X and Y coordinates as a scatterplot.

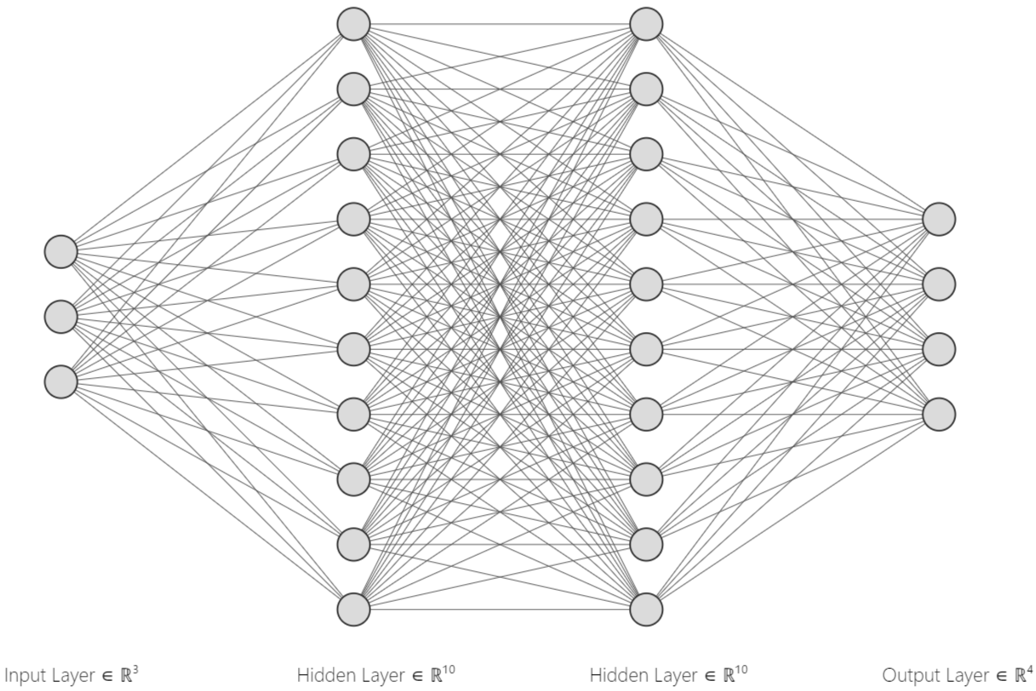

Figure 4.19 - Example of a neuron network used in this subsection.

Table 4.14 - Trained models for ANN machine learning type two.

Loss	Layer	Neurons	Batch size	Learn rate	MSE	MAPE
MSE	2	30	10	0.01	0.0612	0.1110
	2	25	5	0.01	0.0396	0.0946

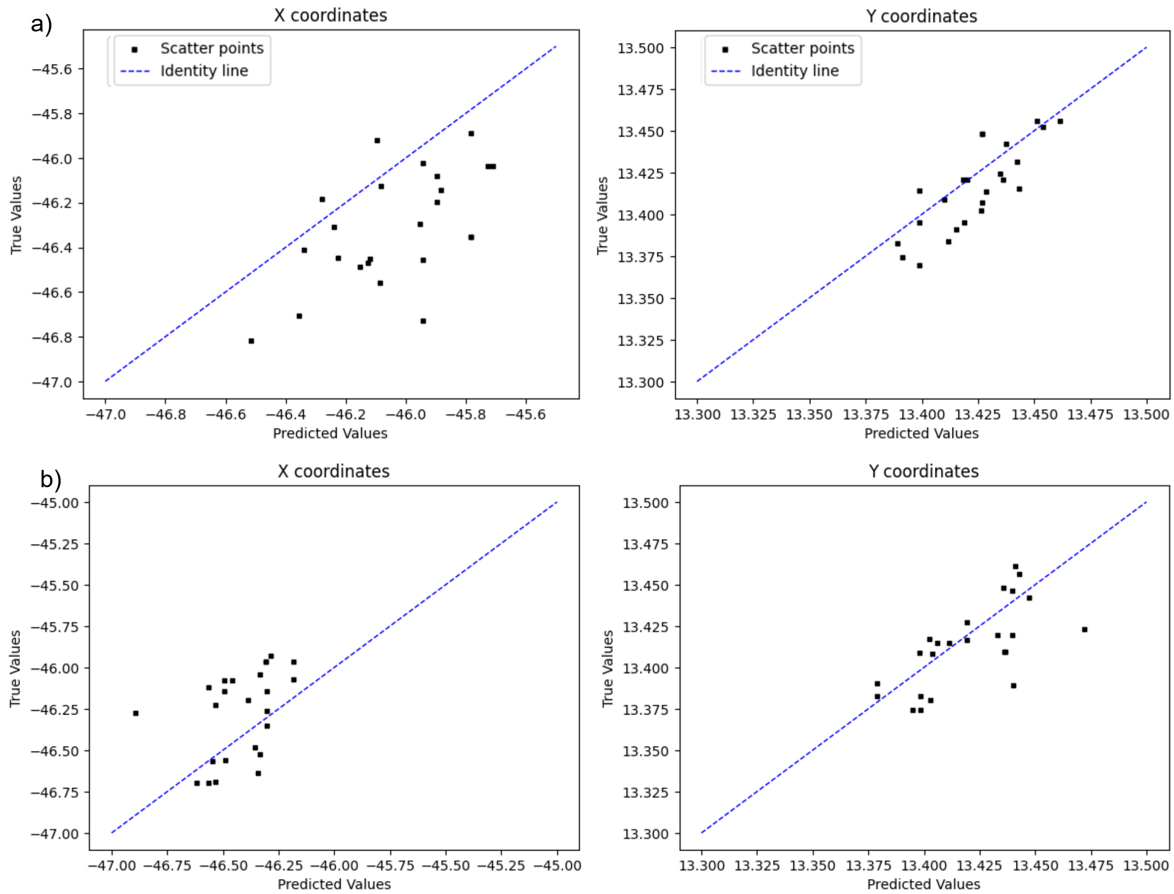

Figure 4.20 - Model test results for X and Y coordinates; the first model in Table 4.14 (a) and the second model in the table (b).

4.4.4. Validation of the NN models

To validate the models, 6 simulations were conducted in SWASH with the intention of generating datasets that were entirely distinct from those used to train and evaluate the models. Figure 4.21 to Figure 4.22 present the scatter plots of the predicted inundated areas and of the X and Y coordinates, followed by a conclusion and interpretation of the results.

4.4.4.1. Model training type one

Figure 4.21 presents the validation results of the trained models in

Table 4.13. The values of the indicators are, for a) RMS = 11.8628 and MAPE = 20.3216%, b) RMS = 1.2533 and MAPE = 8.8160%, c) RMS = 5.2607 and MAPE = 20.3647% and finally d) RMS = 20.2700 and MAPE = 37.4842%.

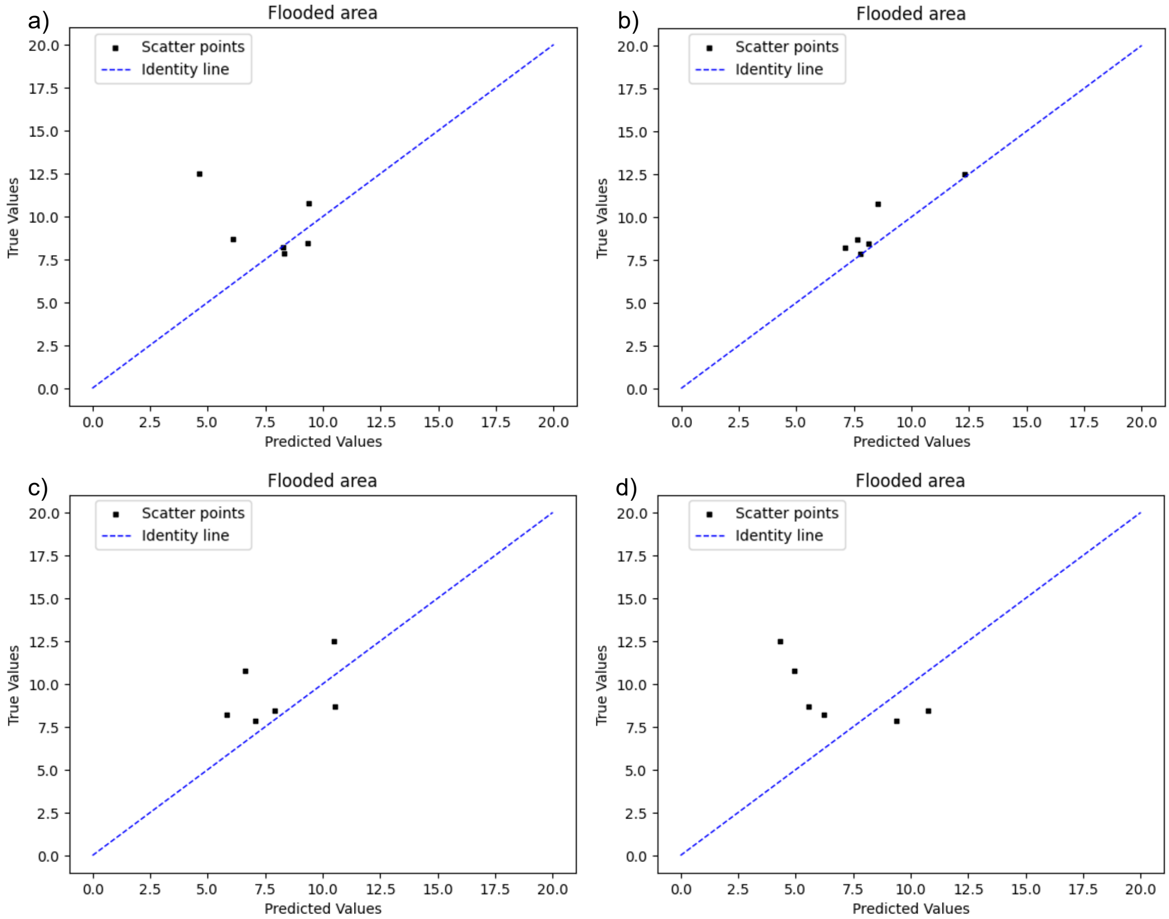

Figure 4.21 - Validation results of ANN machine learning type one.

Based on the validation results, the model with the greatest performance among the trained models is model 2 from

Table 4.13 with three hidden layers, as shown in Figure 4.21 b). Aside from tuning the model's hyperparameters, the performance of the model also depends on the type of data used, that is, the type of normalisation performed and whether the data is balanced or not. For instance, if the data is imbalanced in this case, it could mean that there are more samples in the data with structures near shore (within the range of 300 m) and fewer samples with structures far from shore (beyond 300 m, based on the grid size that was used, the structures could be located up to 1 500 m away from shore). In general, this would indicate that inadequate data was utilized to train the machine learning model, which is the case in this instance.

4.4.4.2. Model training type two

Figure 4.22 represents the validation results of the 2 models that were trained from Table 4.14. a) represents model 1 with RMS of 0.1014 and MAPE of 0.5231% and b) represents model 2 with RMS of 0.0307 and MAPE of 0.3705%. The analysis was done using the same dataset (from

Table 4.13) of the 6 samples that was used to validate the previous models.

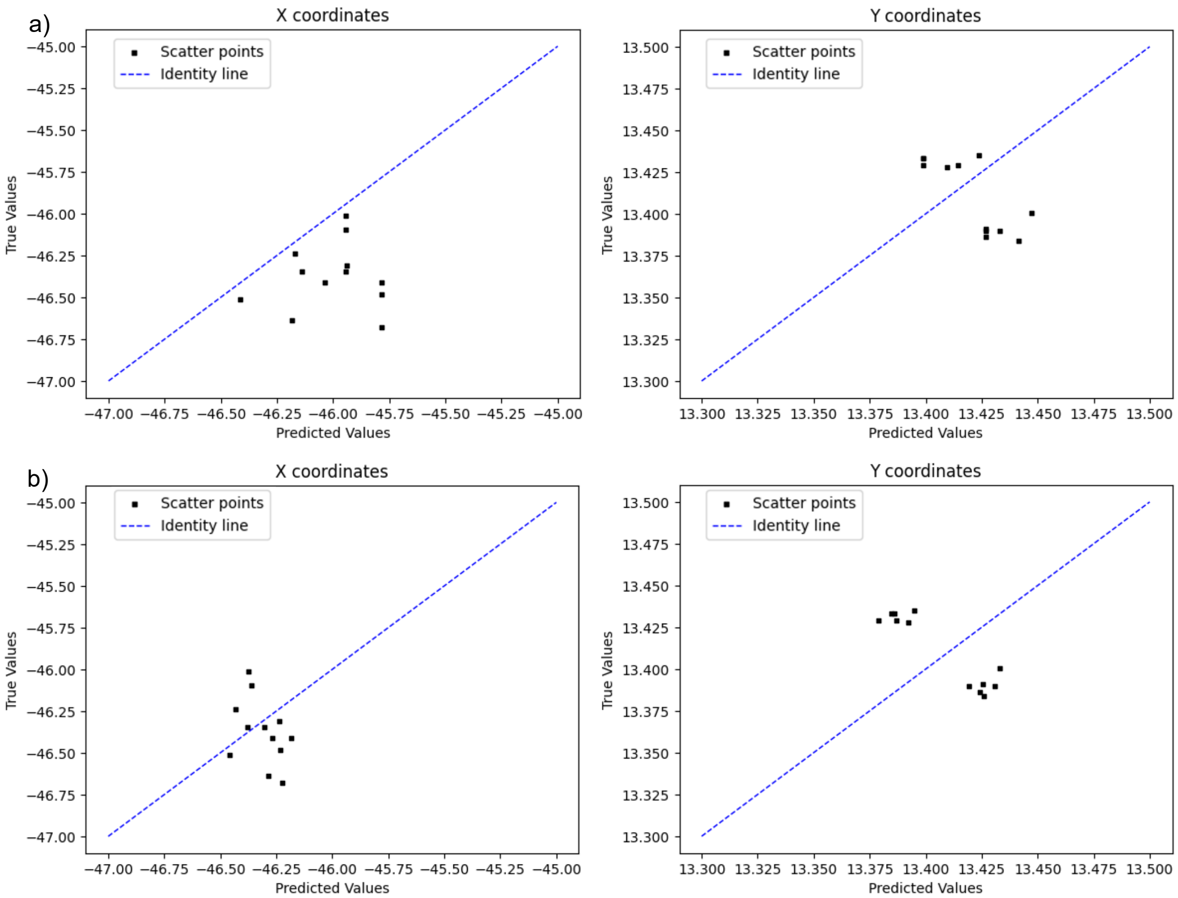

Figure 4.22 - Validation results of 2 ML models.

It is evident from the results that the models are functioning inadequately. The first reason for this poor performance may be related to the fact that the model's performance was already poor from the training and test results, so it was to be expected that the model would produce less accurate results. Secondly, the dataset used to validate the models is completely different from the one used to train them, that is, the samples in the validation dataset consist of structures with unique orientation and location. It follows that for this form of NN with four outputs, more data is required to train the model than for NN with a single output, as the results for this network were more precise. The method used to normalize the data for NN type 1 may not be appropriate for this NN with 4 outputs, on the other hand, it is conceivable that the machine learning algorithm used for this objective may not be suitable for attaining the desired outcomes.

4.4.5. Considering other ML algorithms

With this approach, a dataset with 75 samples (Table F1 in the Appendix F) was used to train the models, several algorithms which were already explained in section 2.3 were considered depending on their performance. There were two types of normalized datasets that were used as shown by Table F2 and Table F3 in the Appendix F.

4.4.5.1. Model training type one

In this subsection, the objective of the models is the same as the one in subsection 4.4.3.1, where the model will have 8 input features and only one output as the flooded area. 10 ML algorithms were used and their results are presented in Figure 4.23 to Figure 4.32 and Table 4.15 using 4 regression metrics.

- Linear regression model

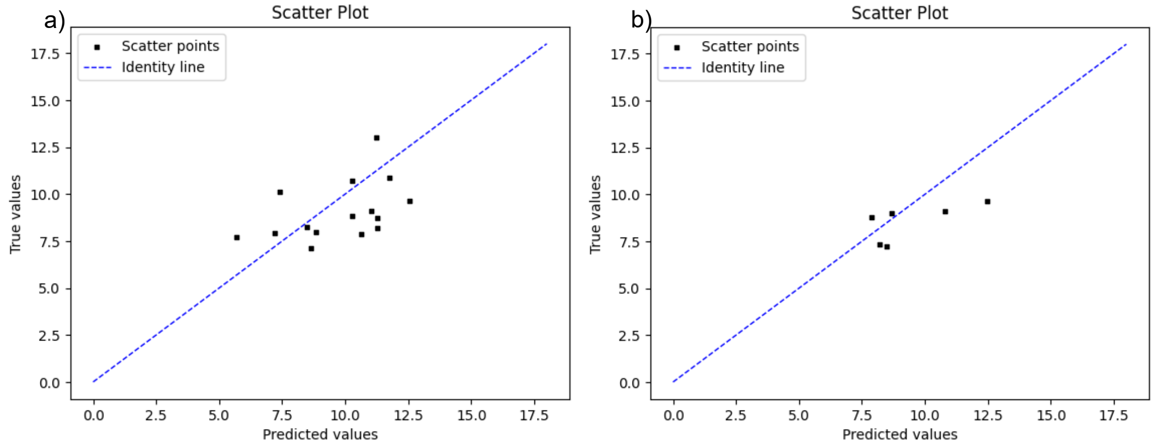

Figure 4.23 – Comparison of “True” values and Predicted values from the Linear regression model: the results of the test set (a) and of the model validation (b).

- Ridge regression model

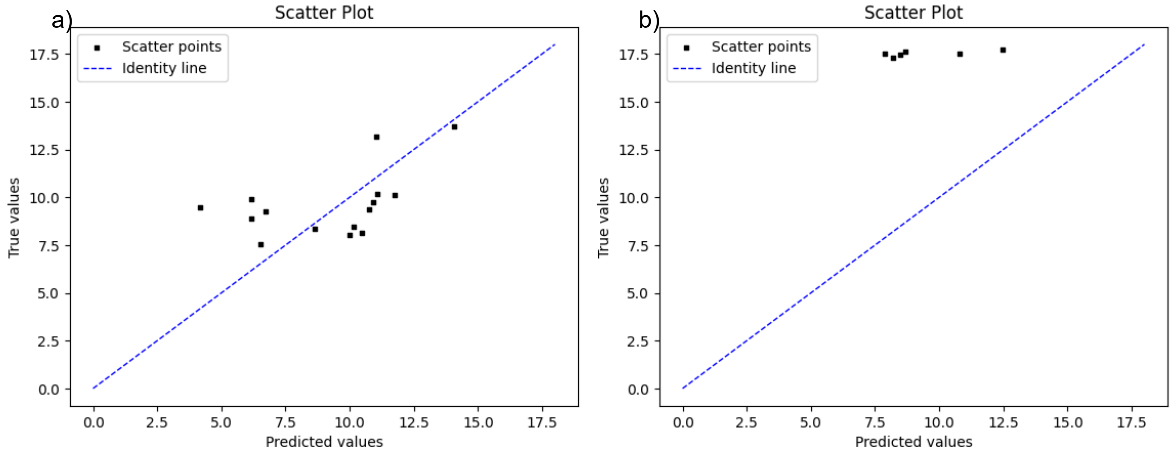

Figure 4.24 - Comparison of “True” values and Predicted values from the Ridge regression linear model: the results of the test set (a) and of the model validation (b).

- Lasso linear model

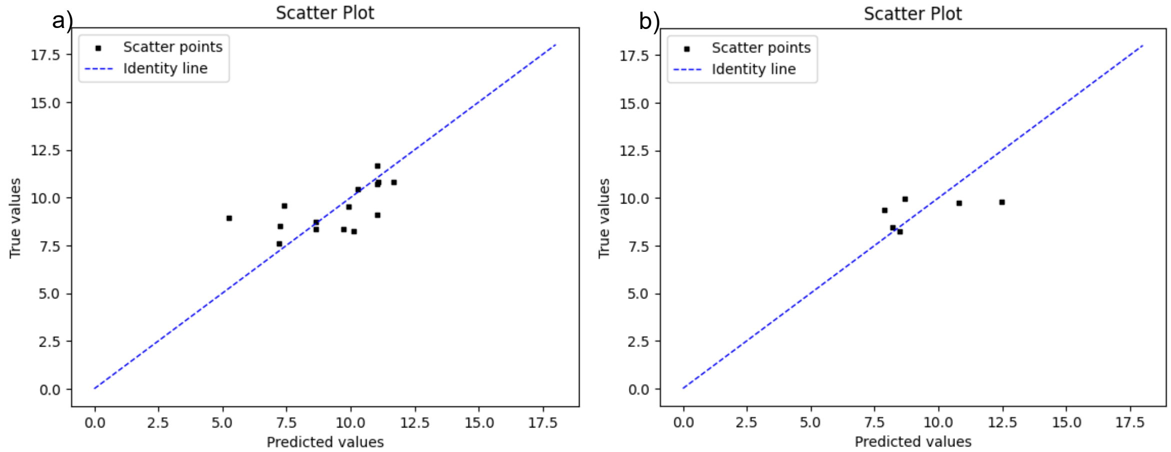

Figure 4.25 - Comparison of “True” values and Predicted values from the Lasso linear model: the results of the test set (a) and of the model validation (b).

- Decision Trees regression model

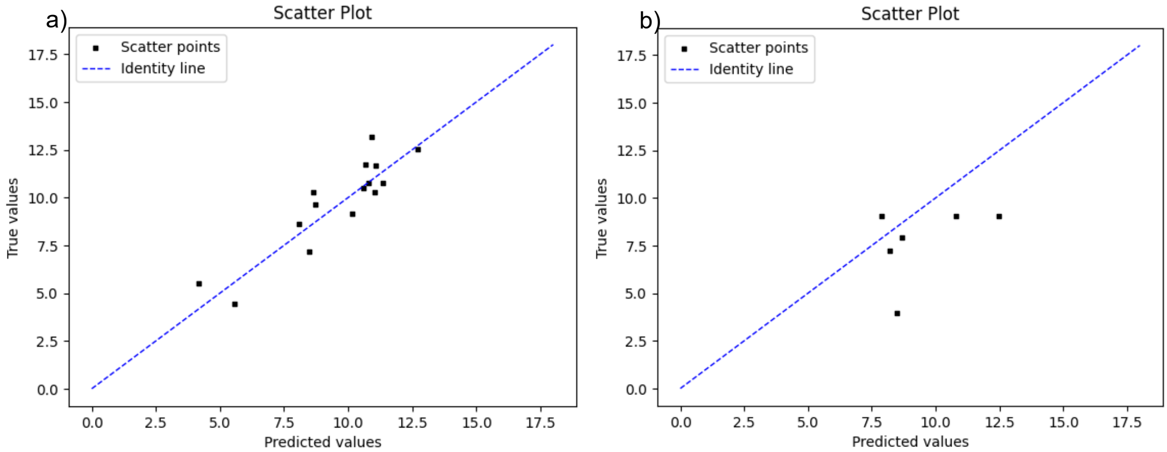

Figure 4.26 - Comparison of “True” values and Predicted values from the Decision Tree regression model: the results of the test set (a) and of the model validation (b).

- Random Forest regression model

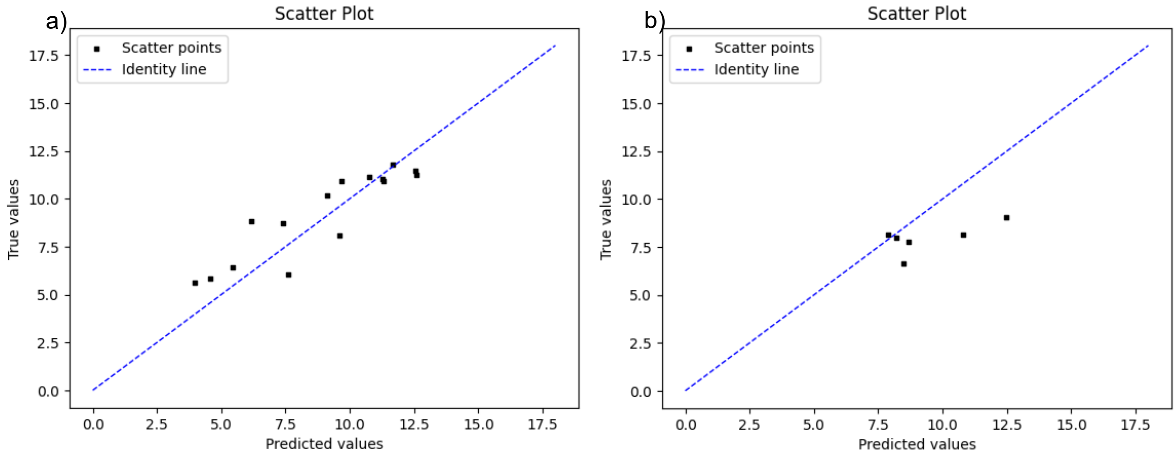

Figure 4.27 - Comparison of “True” values and Predicted values from the Random Forest regression model: the results of the test set (a) and of the model validation (b).

- Gradient Boosting regression model

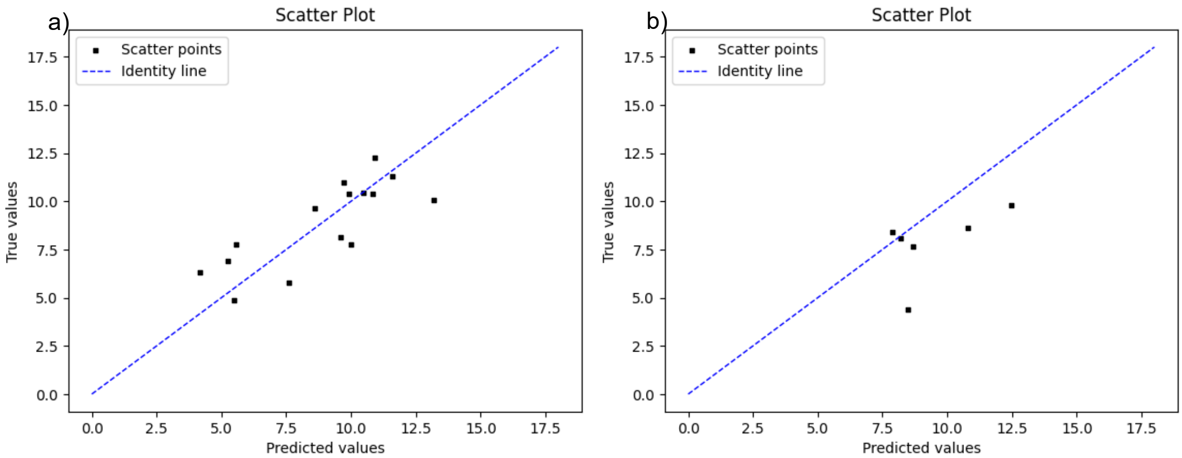

Figure 4.28 - Comparison of “True” values and Predicted values from the Gradient Boosting regression model: the results of the test set (a) and of the model validation (b).

- Linear Support Vector regression model

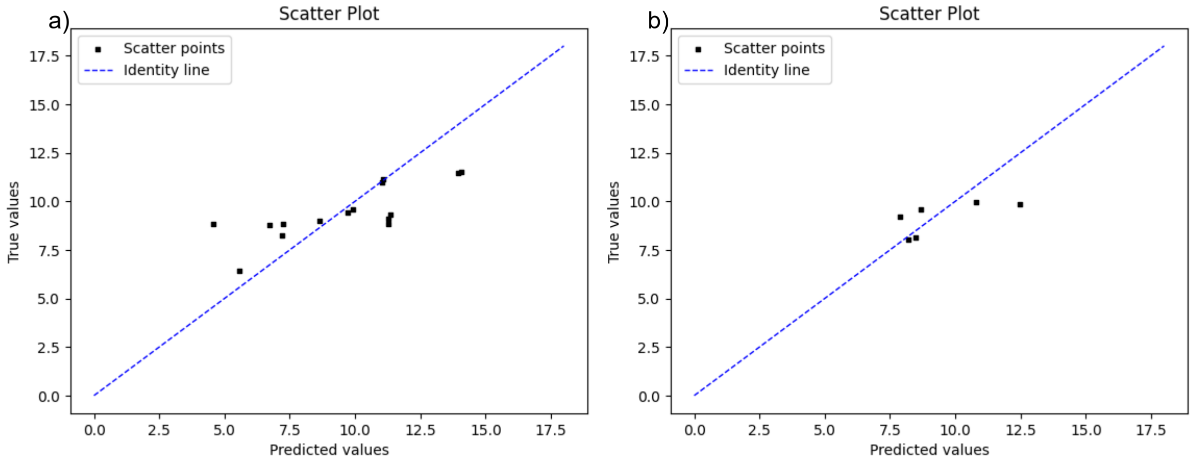

Figure 4.29 - Comparison of “True” values and Predicted values from the Linear Support Vector regression model: the results of the test set (a) and of the model validation (b).

- Polynomial Support Vector regression model

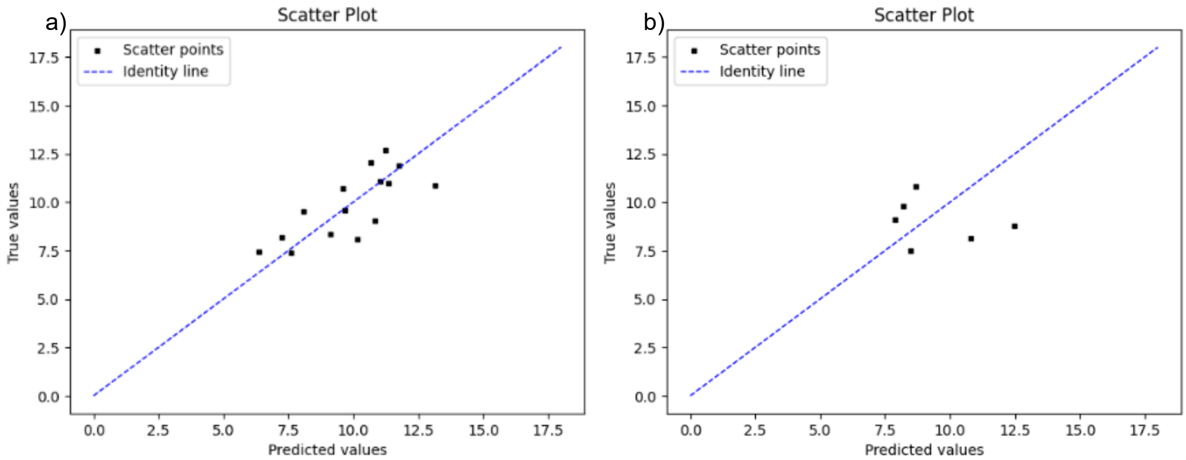

Figure 4.30 - Comparison of “True” values and Predicted values from the Polynomial Support Vector regression model: the results of the test set (a) and of the model validation (b).

- Radial basis function Support Vector Regression model

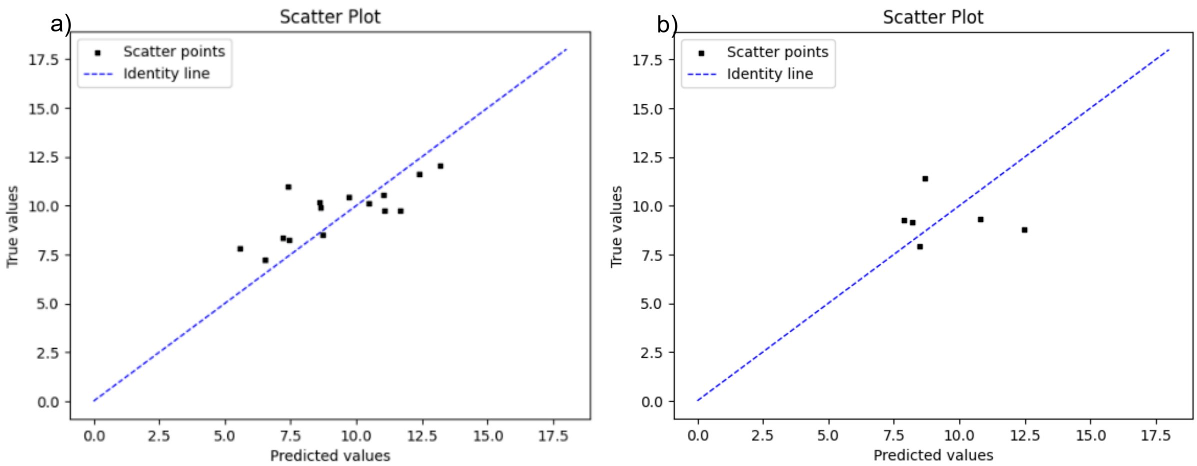

Figure 4.31 - Comparison of “True” values and Predicted values from the Radial Basis Function regression model: the results of the test set (a) and of the model validation (b).

- Artificial Neural Network model

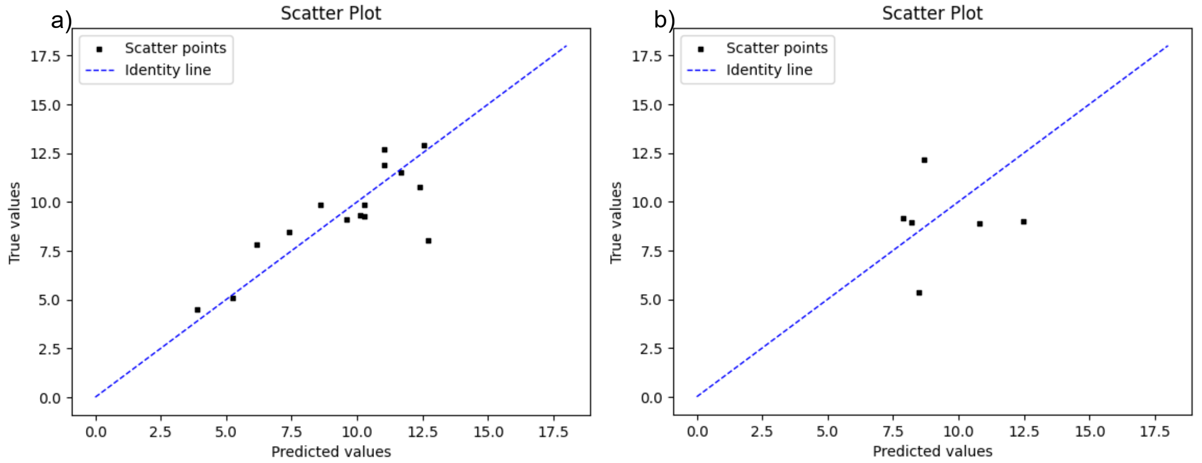

Figure 4.32 - Comparison of "True" values and Predicted values from the Artificial Neural Network regression model: the results of the test set (a) and of the model validation (b).

Table 4.15 – Regression metrics to measure and indicate the performance of each model (model training type 1).

Models	Performance	R^2	MSE	MAE	MAPE
Linear	Model	-0.3592	9.7878	2.3109	0.3095
	Test	-0.0644	3.8348	1.7316	0.1811
	Validation	0.1367	2.3745	1.3193	0.1325
Ridge Linear	Model	0.1734	5.2225	1.8294	0.2505
	Test	0.2142	5.4032	1.9478	0.2771
	Validation	-23.8232	68.2768	8.1114	0.9125
Lasso Linear	Model	0.0772	6.3006	2.0691	0..2894
	Test	0.3802	2.0452	1.0421	0.1334
	Validation	0.2531	2.0545	1.1700	0.1187
Decision Trees	Model	0.2512	4.8643	1.5641	0.1865
	Test	0.7664	1.1447	0.8970	0.1098
	Validation	-1.2864	6.2888	2.0865	0.2197
Random Forest	Model	0.4151	3.6058	1.5397	0.1947
	Test	0.7870	1.6669	1.1228	0.1594
	Validation	-0.3965	3.8412	1.5553	0.1510
Gradient Boosting	Model	0.5327	2.7913	1.2884	0.1590
	Test	0.6215	2.5024	1.3402	0.1783
	Validation	-0.7879	4.9176	1.77512	0.1815
SVR Linear	Model	0.0087	5.7818	1.9432	0.2751
	Test	0.5163	3.6824	1.5148	0.1894
	Validation	0.3793	1.7073	1.0291	0.1032
SVR RBF	Model	0.1521	4.6516	1.7128	0.2299
	Test	0.5502	2.1677	1.2139	0.1465
	Validation	-0.6106	4.4301	1.8007	0.1845
SVR Polynomial	Model	0.3239	4.9203	1.8349	0.2395
	Test	0.5356	1.5376	1.0146	0.1048
	Validation	-0.8488	5.0850	2.0583	0.2104
Neural Network	Model	0.5910	2.1408	1.1364	0.1114
	Test	0.6614	2.3683	1.1142	0.1183
	Validation	-1.4137	6.6388	2.3347	0.2467

4.4.5.2. Model training type two

In this subsection, the objective of the models is the same as the one in subsection 4.4.3.2, where the model will have 3 input features and 4 outputs as the X and Y coordinates of the south and north vertical breakwater structures. Only 5 ML algorithms were used in this subsection and their results are presented in Figure 4.33 to Figure 4. 42 and in Table 4.16.

- Linear regression model

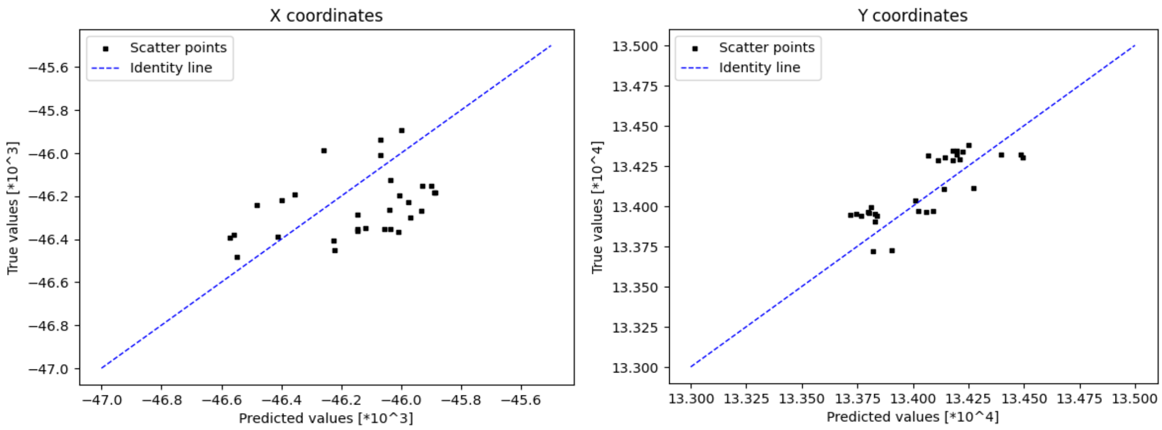

Figure 4.33 - Linear regression model: the results of the test set.

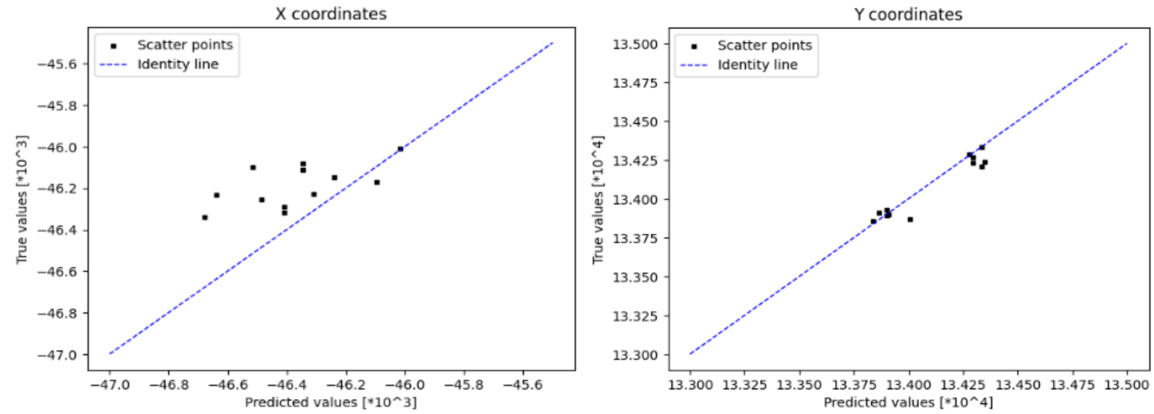

Figure 4.34 - Linear regression model: the results of the model validation.

- Ridge regression model

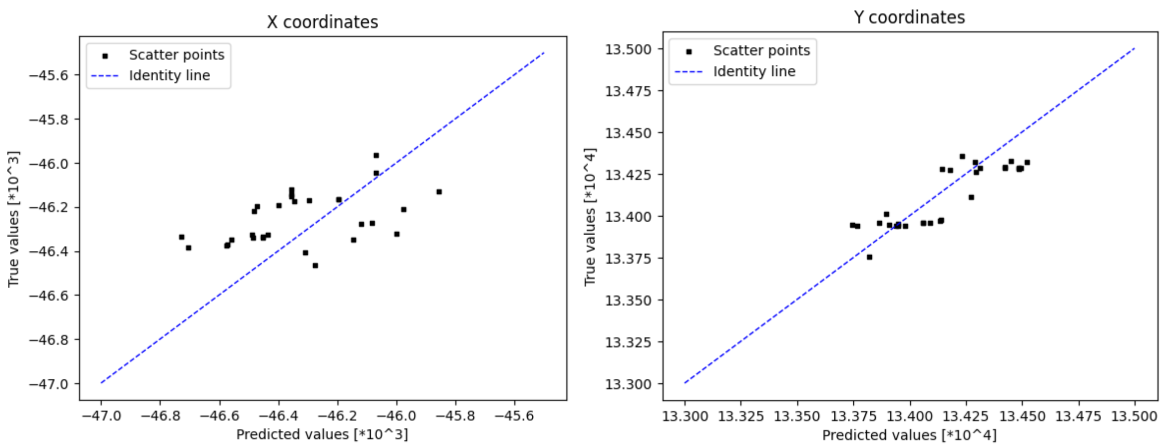

Figure 4.35 - Ridge regression model: the results of the test set.

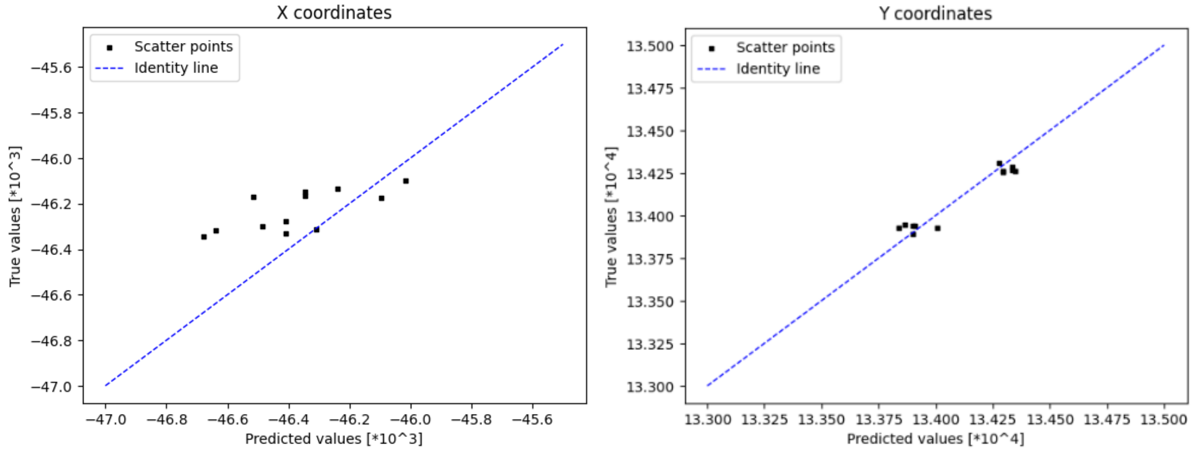

Figure 4.36 - Ridge regression model: the results of the model validation.

- Decision Trees model

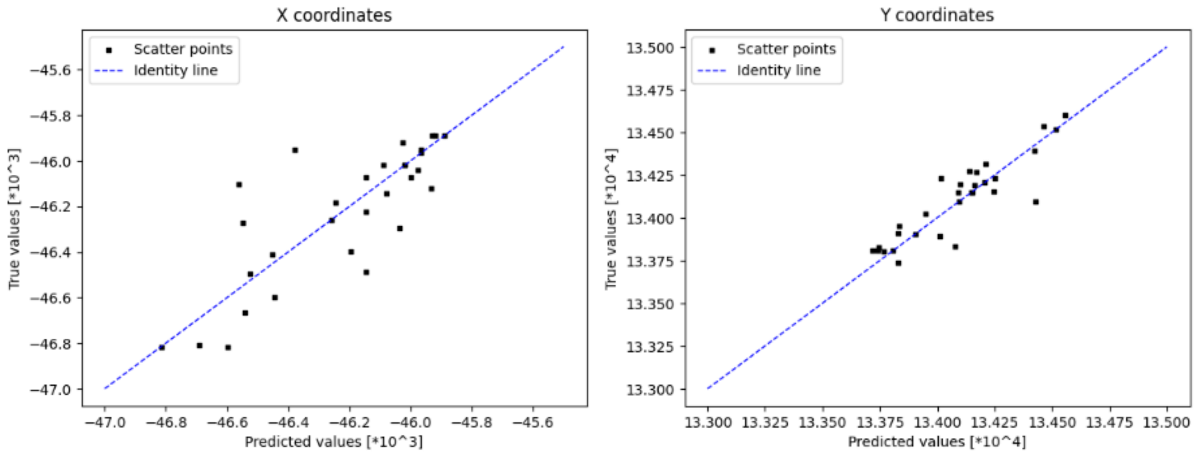

Figure 4.37 - Decision Tree model: the results of the test set.

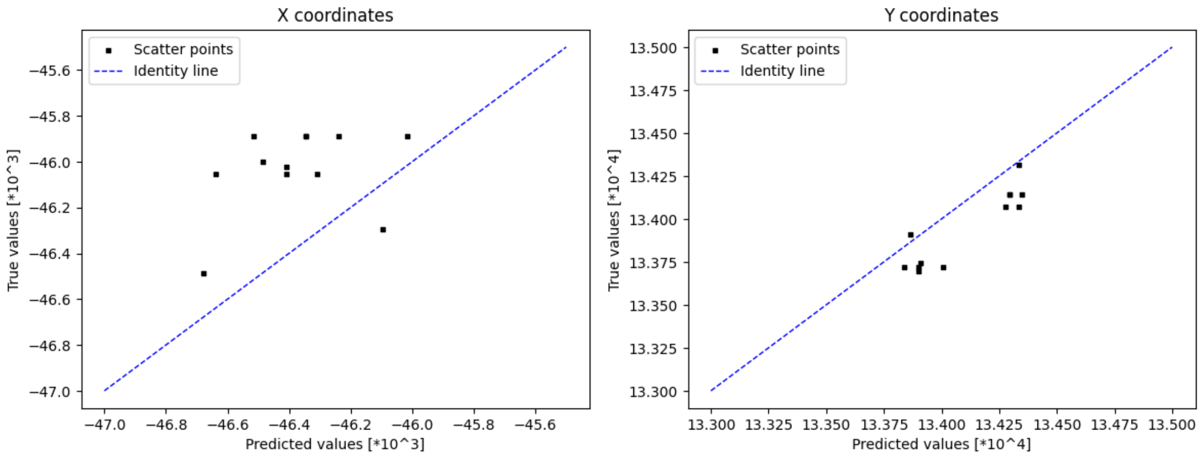

Figure 4.38 - Decision Tree model: the results of the model validation.

- Random Forest model

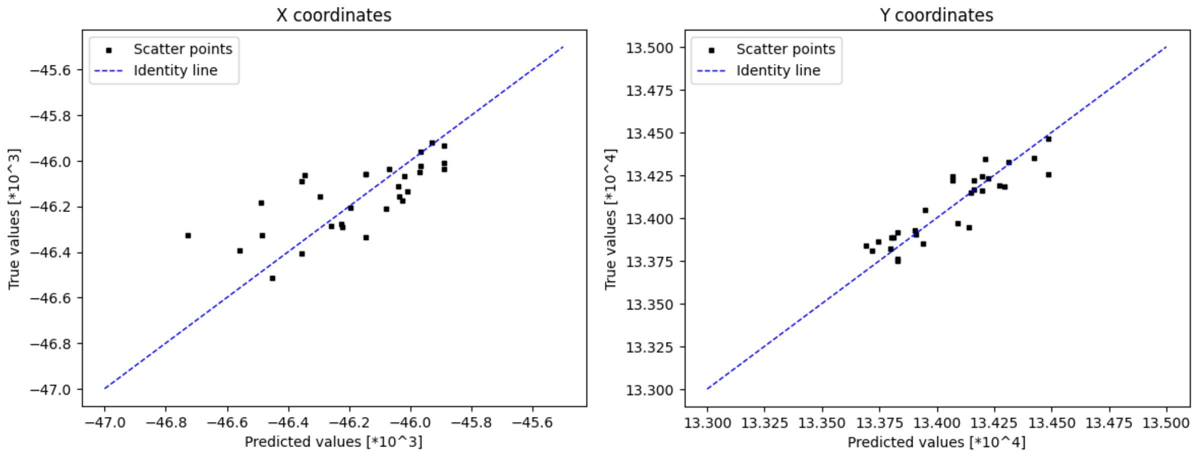

Figure 4.39 - Random Forest model: the results of the test set.

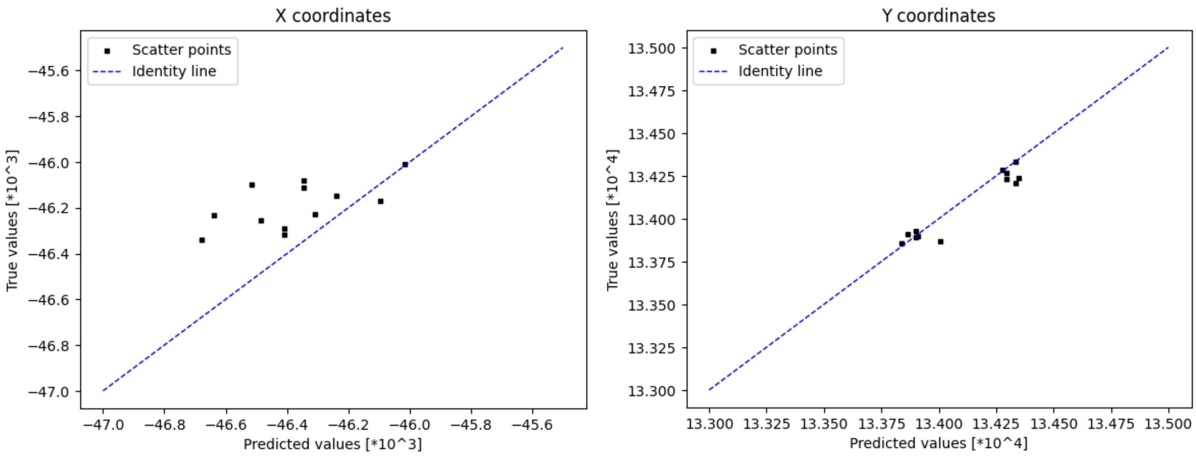

Figure 4.40 - Random Forest model: the results of the model validation.

- Artificial Neural network

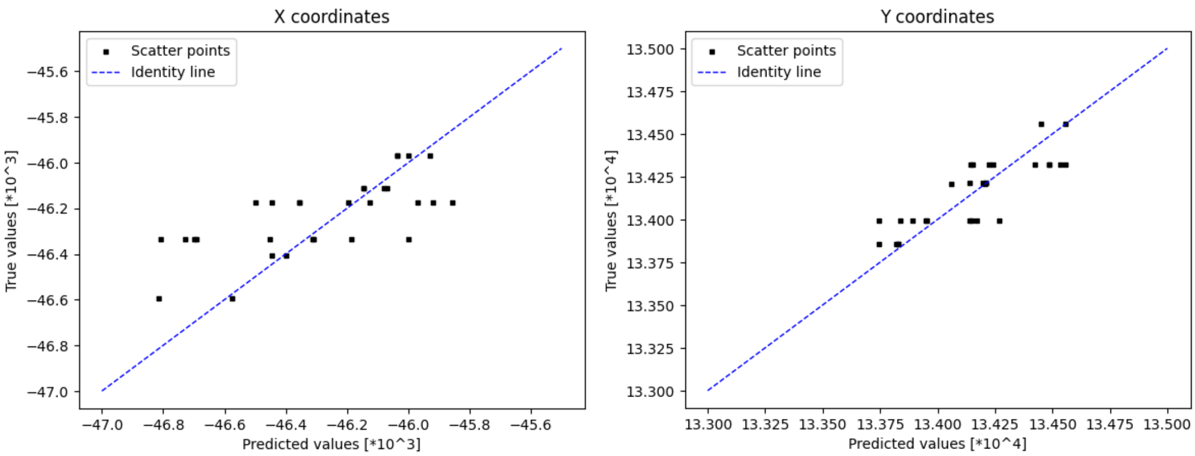

Figure 4. 41 - ANN model: the results of the test set.

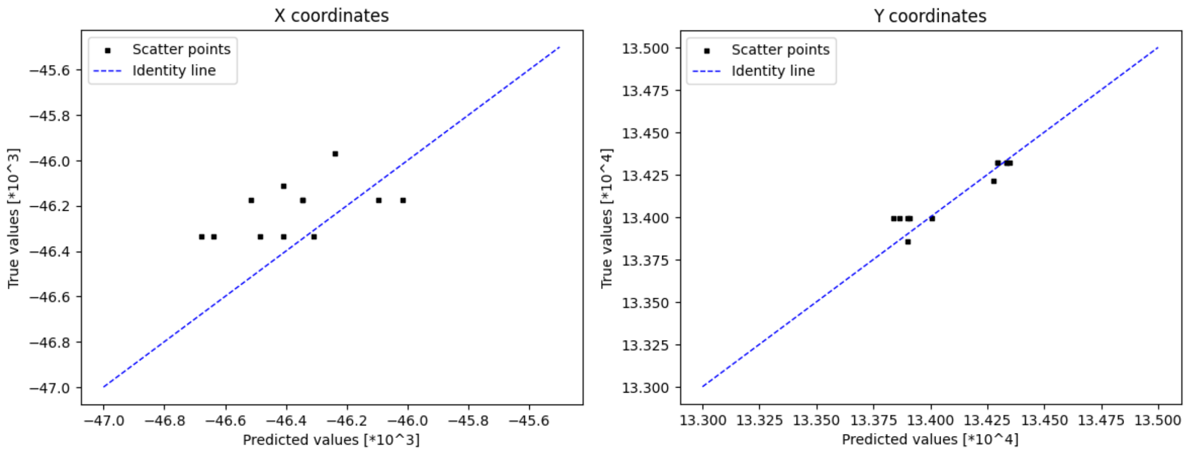

Figure 4. 42 - ANN model: the results of the model validation.

Table 4.16 - Regression metrics to measure and indicate the performance of each model (model training type 2).

Models	Performance	R^2	MSE	MAE	MAPE
Linear	Model	-0.3329	0.0409	0.1341	0.1210
	Test	-0.4719	0.0255	0.1111	0.1136
	Validation	-1.0365	0.0175	0.0809	0.0617
Ridge Linear	Model	-0.1505	0.0356	0.1273	0.1150
	Test	-0.1451	0.0208	0.0981	0.0844
	Validation	-1.4247	0.0205	0.0882	0.0659
Decision Trees	Model	-0.6564	0.0524	0.1278	0.1169
	Test	0.5094	0.0146	0.0622	0.0557
	Validation	-18.2385	0.0811	0.1948	0.1537
Random Forest	Model	0.1687	0.0302	0.0988	0..0881
	Test	0.3921	0.0112	0.0623	0.0576
	Validation	-2.7592	0.0282	0.1007	0.0731
Neural Network	Model	-0.0409	0.0289	0.1074	0.0969
	Test	0.3309	0.0219	0.0834	0.0729
	Validation	-1.5145	0.0254	0.1024	0.0782

4.4.6. Conclusions

The coefficient of determination, denoted as R^2, represents the percentage of data points that fall inside the regression line. Ranging between 1 and 0, a value of 1 signifies optimal results, while a value of 0 suggests inadequate outcomes. Any number below zero signifies a very poor performance of the model. The last 3 metrics used exhibit a range from 0 to infinity, depending on the values present in the data. A value of 0 corresponds to the best result.

The results obtained in Model training type one, which focused only on predicting the flooded area, indicate that the Lasso and SVR linear regressors provide the most promising predictive performance based on the R^2 metric. Notably, both models exhibit the absence of negative values. The Lasso model demonstrates a performance of 7% on the training set, 38% on the test set, and 25% on the unseen data. This suggests that although the model attempted to generalize the sample, it encountered difficulty in learning the underlying pattern due to the limited amount of available data. Similar behaviour is observed in the SVR model. In contrast, certain models such as Random Forest and Gradient Boosting regressor exhibit superior performance on both the training and test sets, as evidenced by Table 4.15. Nevertheless, these models demonstrate inadequate predictive capabilities when applied to an unseen dataset that differs significantly from the test dataset. Based on the observed phenomenon of the model's superior performance on the tests compared to the training data, it can be inferred that the model was exhibiting an amount of generalization. However, it is evident that the model was also experiencing overfitting, although in an unspecified manner.

In the model training type two, it has been noticed that using alternative techniques with larger datasets yielded significantly improved predictive outcomes compared to the artificial neural network (ANN) used in section 4.4.3.2, which was trained on a smaller dataset. It is evident that the Y coordinates exhibit superior predictive performance in all models, as compared to the X coordinates. The R^2 metric shown in Table 4.16 indicates that the models exhibit unsatisfactory performance, as they have a limited ability to generalize and provide accurate predictions. In order to enhance the performance and predictive capabilities of the models, it is important to get a larger volume of data and conduct a comprehensive examination of parameter tuning.

5
CONCLUSIONS AND FUTURE DEVELOMPEMENTS

5.1. CONCLUSIONS

This dissertation aimed to analyze the current conditions of the Furadouro coastal front, map the flooded area in space and time for different scenarios, and assess the effectiveness of new measures aimed at reducing overtopping along this stretch of coastline using a CFD numerical model-SWASH and machine learning tools.

From the literature review that was conducted for this dissertation, it was concluded that:

- Strategies aiming to mitigate the sediment deficit and constrain the coast's regressive trend are the solutions that lead to a greater reduction in coastal erosion risk, leading to the conclusion that substantial benefits can be derived from artificial beach nourishments or bypass solutions to reduce coastal erosion risk;
- Due to the complexity and uncertainty associated with the physical understanding of morphological dynamics at the shore, ML models may be a more effective instrument than the traditional numerical model for predicting changes in the beach profile at the same locations. However, the ML models are only applicable to previous measurement data; it cannot easily be applied to climates or structures not depicted in the training data. Therefore, a research project incorporating numerical models and machine learning is necessary (or field measurements);
- The simulation of various drainage scenarios demonstrate that drainage facilities are also effective in mitigating flood hazards caused by wave overtopping, despite the fact that the drainage capacity is somewhat reduced by high sea levels, and that tidal control structures can help reduce the severity of floods;
- Due to emergency circumstances and as a precaution, the incidents in the Furadouro coastal front have resulted in the repeated rebuilding of the coastal protection structures, frequently without a great deal of in-depth analysis, in order to mitigate the potential effects of future storms. As a result, the incorporation of ML maybe a significant contribution to assess in detail several alternative solutions because it reduces the time required to perform simulations.

For the work conducted in this dissertation:

- It was necessary to validate the selected numerical model to ensure that the results obtained were reliable and plausible. To this end, various porosity and roughness values were evaluated in an effort to replicate the inundated area from the February 2014 flood event. The SWASH model has been demonstrated to be capable of accurately mapping the flooded area. In addition, the numerical model was utilized to generate flooded areas for 57 different coastal protection interventions that were used to train and generate the ML models;

- During the preparation of data by running simulations, it was found that the vertical breakwater structures proposed by Ramos (2015) with dimensions of 38 by 250 m were the most effective structures due to their ability to significantly reduce overtopping. Consequently, these dimensions were utilized for the remaining simulations;
- Furthermore, when structures are located between 75 and 200 m from the north groin's head and are oriented appropriately (perpendicular to the incoming wave, or at a maximum angle of 20º), a significant reduction in flooding is attained;
- Concerning the incorporation of machine learning, two distinct approaches were considered, and models were developed for each one. The first approach has one output and eight inputs. Four NN models and ten other models were trained using this type of approach, and the performance of Decision Tree and RF on the test set were the best of all with 76% and 78% accuracy from R^2 score. However, only one NN model (from the models with 57 samples) and 3 other models (Linear regression, Lasso and Linnear Support Vector) were able to make better predictions during validation since they are the only models with positive R^2 score. With the models that produced the most accurate predictions, it was possible to propose the positions of vertical breakwater structures, and alternates to use the model to predict the flooded area in a matter of seconds, without the need to run SWASH simulations, which can take anywhere from 3 to 5 hours (assuming the same hydrodynamic boundary conditions that were used to train the models are used);
- The second type of approach had 3 input features and 4 outputs. 2 NN models were tested, but the models did not perform well (although their MSE was less than 1, 0.061 and 0.039, the models were underfitting). As a result, the validation results were very poor with MSE being 0.1014 which is greater than before. It is presumed that this is due to the normalization method that works perfectly for the first type of NN but not for the second type. Secondly, the dataset used to validate the models is entirely distinct from the one used to train them. The samples in the validation dataset are comprised of structures with unique orientations and locations. It follows that for this form of NN with four outputs, more training data is required than for NN with a single output, as the results for this network were more accurate. The procedure used to normalize data for the second approach might not be suitable, Consequently, an additional 19 samples were included in the existing set of 57 samples. Subsequently, five machine-learning techniques were used to train and evaluate the models. Notably, the Random Forest approach exhibited the most promising outcomes in comparison to the other models as it is the only model with positive values for R^2 score both on the model performance and testing;
- In general, the ML models proved to be effective for solving coastal engineering issues. In the absence of foundational mathematical and physical knowledge relevant to the extraordinarily complex interactions and processes of coastal engineering, the ML model can be constructed by understanding the correlations between the input and output variables. To implement such highly precise models, researchers must take a number of factors into account, and more data is needed to improve precision.

5.2. FUTURE DEVELOPMENTS

- The adoption of a more current bathymetry that fully considers the study area, without the need to manually combine data from different surveys, and a survey of the structures and beach profile, would result in a more accurate approximation of what is found in the study area;
- A different approach is needed to design and deploy structures on the bathymetry because when using Delft-3D toolboxes, points with the same location but different elevations are invalid, resulting in less precision with respect to the dimensions of the structures. When smoothing is applied, consequently, the precise geometry of the structures is destroyed. This leads to a less accurate simulation, which may result in unstable and unrealistic results if precautions are not taken;
- The SWASH numerical model has a large number of commands that permit the execution of very diverse simulations. This Master's dissertation had a very brief development period for the evaluation and in-depth examination of the various possibilities. Such as the use of varying bottom porosity and structures, the use and study of various momentum conservation systems, a better definition of the energy dissipation parameters, the use of layers, and the definition of a finer and larger mesh;
- The study of combinations of different wave regimes and tide levels for the study area would be important applications for future work, allowing for better results, better solution proposals, and a better description of their influence on the SWASH model;
- It is necessary to generate more datasets to balance the data, to try different normalization techniques so that the ML model has a high accuracy score, and to conduct an economic analysis in order to obtain a viable solution in terms of construction costs; for instance, structures located in deep waters are penalized as well as those that are very close to the shore;
- Sometimes, the presence of vertical breakwater structures results in a channel with faster current velocities along the coastline, which can hinder swimming. Therefore, current velocities must be considered when proposing solutions, lest one attempts to solve one problem by causing another to become worse (like erosion);
- In conclusion, the analysis of overtopping in the urban area of Furadouro under current conditions and for a broader range of potential solutions with multiple scenarios of mean sea level rise and wave condition changes should be studied.

BIBLIOGRAPHIC REFERENCES

[1] Abel, N., Gorddard, R., Harman, B., Leitch, A., Langridge, J., Ryan, A., 2011. *Sea level rise, coastal development and planned retreat: Analytical framework, governance principles and an Australian case study*. Environ. Sci. Policy 14, 279–288. doi: 10.1016/j.envsci.2010.12.002

[2] Ahmad, H., 2019. Machine learning applications in oceanography. Aquatic Research, 2(3), 161-169. https://doi.org/10.3153/AR19014

[3] Almar, R., Ranasinghe, R., Bergsma, E. W. J., Diaz, H., Melet, A., Papa, F., 2021. *A global analysis of extreme coastal water levels with implications for potential coastal overtopping*. Nat. Commun. 12:3775. doi: 10.1038/s41467- 021-24008-9

[4] André, C., Boulet, D., Rey-Valette, H., and Rulleau, B., 2016. *Protection by hard defence structures or relocation of assets exposed to coastal risks: Contributions and drawbacks of cost-benefit analysis for long-term adaptation choices to climate change*. Ocean Coastal Management. 134, 173–182. doi: 10.1016/j. ocecoaman.2016.10.003

[5] Anguelovski, I., Shi, L., Chu, E., Gallagher, D., Goh, K., Lamb, Z., 2016. *Equity impacts of urban land use planning for climate adaptation: critical perspectives from the global North and South*. J. Plan. Educ. Res. 36, 333–348. doi: 10.1177/0739456X16645166

[6] APA, 2020. COSMOS (https://cosmo.apambiente.pt/).

[7] Apollonio, C., Bruno, M. F., Iemmolo, G., Molfetta, M. G., & Pellicani, R., 2020. *Flood Risk Evaluation in Ungauged Coastal Areas: The Case Study of Ippocampo (Southern Italy)*. Water*, Vol.12, 12*(5), pp.1466, https://doi.org/10.3390/W12051466

[8] Atlantic Network for Coastal Risk Management (ANCORIM), 2010. *Riscos costeiros: para melhor os compreender e lhes fazer face*. Espanha.

[9] Bishop, C.M., 1995. Neural Networks for Pattern Recognition. Oxford university press.

[10] Bongarts Lebbe, T., Rey-Valette, H., Chaumillon, É., Camus, G., Almar, R., Cazenave A., Claudet J., Rocle N., Meur-Férec C., Viard F., Mercier D., Dupuy C., Ménard F., Rossel B-A., Mullineaux L., Sicre M-A., Zivian A., Gaill F and Euzen A., 2021. *Designing Coastal Adaptation Strategies to Tackle Sea Level Rise*. Front. Mar. Sci. 8:740602. doi: 10.3389/fmars.2021.740602

[11] Boser, B., Guyon, I., Vapnik, V., 1992. *A training algorithm for optimal margin classifiers. Proceedings of the 5th Annual Workshop on Computational Learning Theory* – COLT'92.

[12] Burcharth, H. F; Lykke Andersen, T; & Lara, J. L., 2014. *Upgrade of coastal defence structures against increased loadings caused by climate change: A first methodological approach*. Coastal Engineering, *87*, pp.112–121, https://doi.org/10.1016/J.COASTALENG.2013.12.006

[13] Cardona, F., 2015. *Avaliação do risco de erosão, galgamento e inundação costeira em áreas artificiais de Portugal continental - Adaptation strategies for different risk scenarios (relocation, accommodation and protection)*. Master's Thesis in Environmental Engineering, FCT, Universidade Nova de Lisboa

[14] Castro, J., 2015. *Study of a detached coastal protection work for Furadouro urban front*. Integrated Master Thesis, Department of Civil Engineering, Faculty of Engineering, University of Porto, Porto, Portugal, 127p.

[15] CDang, N; CDang, Q; Wang, K. H; Zou, G; Jiang, X; Yang, A; & Li, Y., 2020. *Numerical Simulation of Wave Overtopping on Breakwater with an Armor Layer of Accropode Using SWASH Model*. Water*, 12*(2), pp.386, https://doi.org/10.3390/W12020386

[16] CMA (China Meteorological Administration), 2018. In: ESCAP/WMO Typhoon Committee 13th Integrated Workshop. Chiang Mai, Thailand.

[17] CMO., 2014. *Estado das obras de engenharia costeira a 28 de janeiro de 2014 - Resumo técnico da Divisão de Ambiente*. Câmara Municipal de Ovar.

[18] CMO., 2014. *Ocorrências de 1 a 2 de fevereiro de 2014 - Relatório intercalar da Divisão de Ambiente*. Câmara Municipal de Ovar.

[19] Coelho, C., 2005. *Riscos de exposição de frentes urbanas para diferentes intervenções de defesa costeira (Exposure risk of urban waterfronts, for different coastal defense interventions)*. University of Aveiro, Portugal, Aveiro (Ph.D. dissertation, 404 pp.)

[20] Coelho, C., Conceição, T., Ribeiro, B., 2009ª. *Coastal erosion due to anthropogenic impacts on sediment transport in Douro river—Portugal*. In: Mizuguchi, M., Sato, S. (Eds.), Proceedings of Coastal Dynamics 2009. World Scientifc, pp 1–15, Tokyo, Japan

[21] Coelho, C., Lima, M., Veloso-Gomes, F., 2013. *Relationship between cross-shore active profile and one-line shoreline evolution models performance*. In: Conley, D.C., Masselink, G., Russell, P.E., O'Hare, T.J. (eds.), Proceedings 12th International Coastal Symposium, Journal of Coastal Research, Special Issue No. 65, pp. 2107-2112

[22] Coelho, C., Silva, R., Veloso-Gomes, F., Taveira-Pinto, F., 2009. *Potential impacts of climate change on NW Portuguese coastal zones*. ICES J. Mar. Sci. 66 (7), 1497–1507.

[23] Coelho, C., Taveira-Pinto, F., Veloso-Gomes, F., 2004. *Coastal evolution and coastal works in the southern part of Aveiro lagoon inlet, Portugal*. Proceedings of the 29th International Conference on Coastal Engineering (Lisbon, Portugal), pp. 3914–3926.

[24] Coelho, C., Veloso-Gomes, F., Silva, R., 2007. *Shoreline coastal evolution model: two Portuguese case studies.* In: Smith, J.M. (Ed.), Coastal Engineering 2006, Proceedings of the 30th International Conference (San Diego, California), pp. 3430–3771.

[25] Coelho, C; Cruz, T., Roebeling, P., 2016. *Longitudinal revetments to mitigate overtopping and flooding: Effectiveness, costs and benefits*. Ocean & Coastal Management, 134, pp93-102, http://dx.doi.org/10.1016/j.ocecoaman.2016.09.022

[26] Coelho, C; Silva, R., Veloso Gomes, F., Taveira Pinto. T., 2006. *Avaliação de Riscos. Modelos de previsão da evolução da configuração costeira*. 1ª Jornadas de Hidráulica, Recursos Hídricos e Ambiente. FEUP, Porto.

[27] Cruz, T., 2015. *An alise custo-benefício de obras longitudinais aderentes. Master thesis*. Aveiro University, p. 140 (in Portuguese).

[28] Dawarakish, G.S., Rakshith, S., & Natesan, U., 2013. *Review on Applications of Neural Network in Coastal Engineering*. Artificial Intelligent Systems and Machine Learning, 5(7), 324–331.

[29] DGT, 2013. *Areas das freguesias, municípios, distritos e ilhas da carta administrativa oficial de Portugal*. (CAOP), Instituto Geogr afico Portugues, Lisboa, Portugal. ^ http://www.dgterritorio.pt/ficheiros/cadastro/caop/caop_download/caop_2013_0/areasfregmundistcaop2013_2.

[30] Elsayed, S. M; & Oumeraci, H., 2018. *Modelling and mitigation of storm-induced saltwater intrusion: Improvement of the resilience of coastal aquifers against marine floods by subsurface drainage*. Environmental Modelling & Software, *100*, pp.252–277, https://doi.org/10.1016/J.ENVSOFT.2017.11.030

[31] Fausett, L., 1994. *Fundamentals of neural networks: architectures, algorithms, and applications*. Prentice-Hall, Inc.

[32] Feng, X., Ma, G., Su, S., Huang, C., Boswell, M. K., & Xue, P., 2020. *A multi-layer perceptron approach for accelerated wave forecasting in Lake Michigan*. Ocean Engineering, 211, 107526. https://doi.org/10.1016/j.oceaneng.2020.107526

[33] Fernandéz-Fernandéz S, Baptista P, Bernardes C, Silva P, Fontán-Bouzas Á, Lópes-Olmedilla L, Ferreira C., 2019. *Variação da Linha de Costa em Praias Arenosas: Aveiro (Portugal)*. IX Congresso sobre Planeamento e Gestão das Zonas Costeiras dos Países de Expressão Portuguesa, Lisbon, Portugal (in Portuguese)

[34] Ferreira, A. M; Coelho, C; Narra, P., 2021. *Coastal erosion risk assessment to discuss mitigation strategies: Barra-Vagueira, Portugal*. Natural Hazards, 105, pp.1069–1107, https://doi.org/10.1007/s11069-020-04349-2

[35] Ferreira, J.C., Cardona, F.S., Jóia Santos, C., Tenedório, J.A., 2021. *Hazards, Vulnerability, and Risk Analysis on Wave Overtopping and Coastal Flooding in Low-Lying Coastal Areas: The Case of Costa da Caparica, Portugal*. Water, 13, 237, https://doi.org/10.3390/w13020237

[36] FLO-2D, 2018. *FLO-2D Pro Version: Two-dimensional Flood Routing Model Storm Drain Manual*. FLO-2D Software, Inc., Nutrioso, Arizona.

[37] Fonseca, D. F., 2015. *Modelação da evolução da costa do Furadouro (Aveiro)*. Dissertação de Mestrado em Engenharia Civil, IST da Universidade de Lisboa.

[38] Foti, E., Musumeci, R. E., & Stagnitti, M., 2020. *Coastal defence techniques and climate change: a review*. Rendiconti Lincei, *31*(1), pp123–138, https://doi.org/10.1007/S12210-020-00877-Y/FIGURES/8

[39] GeoInfo Map, 2020. (Accessed December, 2020). https://www.map.gov.hk/.

[40] Gervais, M., Balouin, Y., & Belon, R., 2012. *Morphological response and coastal dynamics associated with major storm events along the Gulf of Lions Coastline, France*. Geomorphology, pp.*143–144*, pp.69–80, https://doi.org/10.1016/J.GEOMORPH.2011.07.035

[41] Goldstein, E.B., Coco, G., & Plant, N.G., 2019. *A Review of Machine Learning Applications to Coastal Sediment Transport and Morphodynamics*. Earth-Science Reviews, 194, 97–108. https://doi.org/10.1016/j.earscirev.2019.04.022

[42] González, M., Medina, R., 2001. On the application of static equilibrium bay formulations to natural and man-made beaches. Coast. Eng. 43, 209–225.

[43] Govindaraju, R.S., 2000. *Artificial neural network in hydrology. II: hydrologic application, ASCE task committee application of artificial neural networks in hydrology*. J. Hydrol. Eng. 5, 124–137

[44] GTL, 2014. *Gestao da zona costeira - o desa ~ fio da mudança, Relatorio do Grupo de Trabalho do Litoral*. http://www.apambiente.pt/_zdata/DESTAQUES/2015/GTL_ Relatorio Final_20150416.pdf.

[45] Guimaraes, T., 2017. *Evaluation of the damage progression and study of wave overtopping in rubble mound structures*. Integrated Master Thesis, Department of Civil Engineering, Faculty of Engineering, University of Porto, Porto, Portugal, 164p.

[46] Haasnoot, M., Lawrence, J., and Magnan, A. K., 2021. *Pathways to coastal retreat*. Science 372:1287. doi: 10.1126/science.abi6594

[47] Hakeem, K. J; & Henrik, K. H., 2000. *Influence of Bottom Friction on Sea Surface Roughness and Its Impact on Shallow Water Wind Wave Modeling*. Journal of physical oceanography, Hydraulic Institute (DHI), Agern Alle´ 5, DK-2970, Hørsholm, Denmark.

[48] Hallegatte, S., 2009. *Strategies to adapt to an uncertain climate change*. Global environmental change, 19(2), pp.240-247.

[49] Hashemi, M.R., Ghadampour, Z., & Neill, S.P., 2010. *Using an Artifi cial Neural Network to Model Seasonal Changes in Beach Profi les*. Ocean Engineering, 37(14–15), 1345–1356. https://doi.org/10.1016/j.oceaneng.2010.07.004

[50] Henderson, C. S., Fiedler, J. W., Merrifield, M. A., Guza, R. T., & Young, A. P., 2022. *Phase resolving runup and overtopping field validation of SWASH*. Coastal Engineering, *175*, https://doi.org/10.1016/J.COASTALENG.2022.104128

[51] Hinkel, J., Nicholls, R. J., Tol, R. S. J., Wang, Z. B., Hamilton, J. M., Boot, G., et al., 2013. *A global analysis of erosion of sandy beaches and sea-level rise*: An application of DIVA. Glob. Planet. Change 111, 150–158. doi: 10.1016/j. gloplacha.2013.09.002

[52] HKO (Hong Kong Observatory), *2020a. Typhoons Necessitating the Issuing of the Hurricane Signal No.10. Hong Kong Special Administration Region*: Hong Kong Observatory (Accessed December, 2020). https://www.hko.gov.hk/en/informtc/historical_tc/no10_reporte.htm.

[53] HKO, 2020b. *Climate Change in Hong Kong-mean Sea Level. Hong Kong Special Administration Region*: Hong Kong Observatory (Accessed December, 2020. https:// www.hko.gov.hk/en/climate_change/obs_hk_sea_level.htm.

[54] HKO, 2020c. *Storm Surge Records in Hong Kong During the Passage of Tropical Cyclones*. Hong Kong Special Administration Region: Hong Kong Observatory (Accessed December, 2020. https://www.hko.gov.hk/en/wservice/tsheet/pms/stormsurgedb.htm.

[55] IPCC, 2012. In: Field, C.B., et al. (Eds.), *Managing the Risks of Extreme Events and Disasters to Advance Climate Change Adaptation. A Special Report of Working Groups I and II of the Intergovernmental Panel on Climate Change*. Cambridge University Press, Cambridge, UK, and New York, USA, p. 582.

[56] IPCC, 2014. *Climate Change 2014 Synthesis Report. Synthesis Report, Geneva: The Intergovernmental Panel on Climate Change*. The Core Writing Team, Rajendra K. Pachauri e Leo Meyer.

[57] ISO 31000, 2018. *Risk management* – guidelines. www.iso.org/obp/ui#iso:std: iso:31000:ed-2:v1:en.

[58] James, S.C., CDang, Y., & O'Donncha, F., 2018. *A Machine Learning Framework to Forecast Wave Conditions*. Coastal Engineering, 137, 1–10. https://doi.org/10.1016/j.coastaleng.2018.03.004

[59] Johnson, H.K., and Kofoed-Hansen, H., 2000. *Influence of bottom friction on sea surface roughness and its impact on shallow water wind wave modeling*. Journal of physical oceanography, 30(7), pp.1743-1756.

[60] Kankal, M., & Yuksek, O., 2012. *Artificial Neural Network Approach for Assessing Harbor Tranquility: The Case of Trabzon Yacht Harbor, Turkey*. Applied Ocean Research, 38, 23– 31. https://doi.org/10.1016/j.apor.2012.05.009.

[61] Kim, T., & Lee, W-D., 2022. *Review on Applications of Machine Learning in Coastal and Ocean Engineering*. Journal of Ocean Engineering and Technology, 36(6), 194-210. https://doi.org/10.26748/KSOE.2022.007

[62] Komen, R., 2019. *Simulating wave penetration in an inlet using the numerical models SWAN and SWASH: Dimensioning of an inlet and the comparison of two numerical models*.

[63] Lamy, A., Rodrigues, A., 2001. *Furadouro: a land with past and with future*. Comissão de Melhoramento do Furadouro, Ovar

[64] Li, Y., CDou, W. H., & Shen, P., 2023. *Flood risk assessment of loss of life for a coastal city under the compound effect of storm surge and rainfall*. Urban Climate, *47*, 101396, https://doi.org/10.1016/J.UCLIM.2022.101396

[65] Lira, C., Silva, A., Taborda, R., Andrade, C., 2016. *Coastline evolution of portuguese low-lying sandy coast in the last 50 years: an integrated approach*. Earth Syst Sci Data Discuss 8(1):265–278. https://doi. org/10.5194/essd-2016-5

[66] Liu T, Wang Z, Zeng J, Wang J., 2021. *Machine-learning-based models to predict shear transfer strength of concrete joints*. Eng Struct, 249:113253.

[67] Liu, Y., Esan, O. C., Pan, Z., & An, L., 2021. *Machine Learning for Advanced Energy Materials*. Energy and AI, 3, 100049. https://doi.org/10.1016/j.egyai.2021.100049

[68] Lumb, P., 1965. *The residual soils of Hong Kong*. Geotechnique 15 (2), 180–194.

[69] Luo, Q. R., Xu, H., & Bai, L. H., 2022. *Prediction of significant wave height in hurricane area of the Atlantic Ocean using the Bi-LSTM with attention model: Significant wave height prediction using the Bi-LSTM with attention model*. Ocean Engineering, *266*, https://doi.org/10.1016/J.OCEANENG.2022.112747

[70] M Li, M., Wu, W., Wang, J., Che, Z., Xie, Y., 2017. *Simulating and mapping the risk of surge floods in multiple typhoon scenarios: a case study of Yuhuan County, CDejiang Province, China*. Stoch Environ Res Risk Assess, 13, pp.645-659, DOI 10.1007/s00477-016-1238-2

[71] Manz, A., Zózimo, A. C; & Garzon, J. L., 2022. *Application of SWASH to Compute Wave Overtopping in Ericeira Harbour for Operational Purposes*. Journal of Marine Science and Engineering*,* *10*(12), pp.1881, https://doi.org/10.3390/JMSE10121881

[72] Marques, M., 2021. *Assessment of solutions for reducing the risk of saltwater seepage at fronts urbanized coastal areas for different climate change scenarios*. Integrated Master Thesis, Department of Chemical Engineering, Faculty of Engineering, University of Porto, Porto, Portugal, 139p.

[73] Martins, A., 2016. *Evaluation of the hydrodynamics and the levels of overtopping at Furadouro beach*. Integrated Master Thesis, Department of Civil Engineering, Faculty of Engineering, University of Porto, Porto, Portugal, 164p.

[74] McGinlay, J., Jones, N., Clark, J., and Maguire-Rajpaul, V. A., 2021. *Retreating coastline, retreating government? Managing sea level rise in an age of austerity*. Ocean Coast. Manage. 204:105458. doi: 10.1016/j.ocecoaman.2020.105458

[75] Mellink, B. A., 2012. *Numerical and experimental research of wave interaction with a porous breakwater*. Master thesis, Department of Hydraulic Engineering, Faculty of Civil Engineering and Geosciences, Delft University of Technology, Delft, Netherlands, https://doi.org/10.4121/UUID:A66190CA-5A88-4CC2-A4B8-401B21EB77C0

[76] Mesuras, T., 2018. *Estratégia de Adaptação de frentes urbanas ao risco de galgamentos e inundações costeiras – O Caso de Estudo do Furadouro (Ovar)*. Dissertação de Mestrado em Engenharia do Ambiente, FCT da Universidade Nova de Lisboa.

[77] Müller, A. C., & Guido, S., 2016. *Introduction to machine learning with Python: a guide for data scientists*. " O'Reilly Media, Inc.". http://bit.ly/intro-machine-learning-python.

[78] Narra P., 2018. *CERA: GIS-Based Assessment of Coastal Erosion Risk*. Aveiro University, Ph.D. Thesis, Aveiro University, p 262

[79] Narra P., Coelho C., Sancho F., 2019. *Multicriteria GIS-based estimation of coastal erosion risk: implementation to Aveiro sandy*. Coast ocean and coastal management. Elsevier, Portugal, p 19

[80] Oliveira, M., 2013. *"Retirada planeada" de áreas edificadas em zonas costeiras de elevado risco*. Dissertação Mestrado em Engenharia Civil, FEUP

[81] Pereira, C; Coelho, C., 2013. *Mapping erosion risk under different scenarios of climate change for Aveiro coast, Portugal*. Nat Hazards, Vol.69, pp. 1033–1050, DOI 10.1007/s11069-013-0748-1.

[82] Pérez, M. S., 2014. *Overtopping over a real rubble mound breakwater calculated with SWASH.* Master thesis, Department of Hydraulic Engineering, Faculty of Civil Engineering and Geosciences, Delft University of Technology, Delft, Netherlands.

[83] Peterson, J.A., Ebel, R.E., & O'Keefee, D.H., 1978. *[23] Dual-wavelength stopped-flow spectrophotometric measurement of NADPH-cytochrome P-450 reductase*. In Methods in Enzymology (Vol. 52, pp. 221-226). Academic Press.

[84] Pinto, C., Rodrigues, A., Costa, C., Lima, J., 2014. *Record of occurrences on the coast -.Storm from January 3 to 7, 2014*. Technical Report of the Portuguese Agency for the Environment. 123 pp. DOI: 10.13140/RG.2.2.22310.73288.

[85] Pinto, I. M. P., 2022. *Overtopping and coastal flooding at the urban front of Furadouro,* Master thesis, Faculdade de Letras da Universidade do Porto.

[86] Pranzini, E., 2018. *Shore protection in Italy: From hard to soft engineering … and back*. Ocean & Coastal Management, *156*, pp.43–57, https://doi.org/10.1016/J.OCECOAMAN.2017.04.018

[87] PROCIV, 2010. *Caderno técnico PROCIV 15: Riscos Costeiros – Estratégias de prevenção, mitigação e proteção, no âmbito do planeamento de emergência e do ordenamento do território*. Autoridade Nacional de Proteção Civil (ANPC).

[88] Qiang, Y., He, J., Xiao, T., Lu, W., Li, J., & CDang, L., 2021. *Coastal town flooding upon compound rainfall-wave overtopping-storm surge during extreme tropical cyclones in Hong Kong*. Journal of Hydrology: Regional Studies, *37*, 100890, https://doi.org/10.1016/J.EJRH.2021.100890

[89] Ramos, T., 2011. *Study of the rehabilitation of coastal defense structures - Case studies from Mindelo, Norte do Furadouro and Torreira*. Master's Thesis, Faculty of Engineering, University of Porto.

[90] Ramos, V., Cabral, T., Rosa-Santos, P., and Taveira-Pinto, F., 2020. *Advanced and high-resolution numerical modeling ofwave energy resource*: Port of Leixões. Faculdade de Engenharia da Universidade do Porto, Deliverable 5.5 PORTOS - Towards Energy Self Sufficiency.

[91] Ranasinghe, R., & Jongejan, R., 2018. *Climate change, coasts and coastal risk*. Journal of Marine Science and Engineering, *6*(4), https://doi.org/10.3390/JMSE6040141

[92] Reis, A.R., 2015. *Dichotomy between fishing area and bathing area*: Espinho, Esmoriz and Furadouro.

[93] Rita, A., 2016. *Nonlinear and non-hydrostatic modelling of surface waves on rapidly varying backgrounds-Model*. Master Thesis, Instituto Superior Técnico, Lisbon, 74p

[94] Robeiro, N., 2019. *Evaluation of overtopping rubble mound breakwaters using numerical modelling*. Integrated Master Thesis, Department of Civil Engineering, Faculty of Engineering, University of Porto, Porto, Portugal, 164p.

[95] Roebelinga, P; Eliab, E; Coelhoc, C; Alvesd, T., 2018. *Efficiency in the design of coastal erosion adaptation strategies: An environmental-economic modelling approach*. Ocean and Coastal Management, 160, pp.175-184, https://doi.org/10.1016/j.ocecoaman.2017.10.027

[96] Salehi, H., & Burgueño, R., 2018. *Emerging Artificial Intelligence Methods in Structural Engineering*. Engineering Structures, 171, 170–189. https://doi.org/10.1016/j.engstruct.2018.05.084

[97] Santos, F., Lopes, A., Moniz, G., Ramos, L., Taborda, R., 2014. *Gestão da Zona Costeira – O Desafo da Mudança. Relatório do Grupo de Trabalho do Litoral*, p 237 (in Portuguese)

[98] See, J., and Wilmsen, B., 2020. *Just adaptation? Generating new vulnerabilities and shaping adaptive capacities through the politics of climate-related resettlement in a Philippine coastal city*. Glob. Environ. Change 65:102188. doi: 10.1016/j. gloenvcha.2020.102188

[99] Shukla, P.R., Skea, J., Calvo Buendia, E., Masson-Delmotte, V., Pörtner, H.O., Roberts, D.C., Zhai, P., Slade, R., Connors, S., Van Diemen, R. and Ferrat, M., 2019. *IPCC, 2019: Climate Change and Land: an IPCC special report on climate change, desertification, land degradation, sustainable land management, food security, and greenhouse gas fluxes in terrestrial ecosystems*.

[100] Silva, R., Baptista, P., Veloso-Gomes, F., Coelho, C. and Taveira-Pinto, F., 2009. *Sediment grain size variation on a coastal stretch facing the North Atlantic (NW Portugal)*. Journal of coastal research, pp.762-766.

[101] Smit, P., Zijlema, M., Stelling, G., 2013. *Depth-induced wave breaking in a non-hydrostatic, nearshore wave model*. Coastal Engineering, pp. 1-16.

[102] Sousa, D., 2015. *Avaliação dos efeitos dos temporais de 2013/2014 nas infraestruturas e equipamentos do litoral de Vila Nova de Gaia. Dissertação de Mestrado*. Faculdade de Letras da Universidade do Porto

[103] Stelling, G., Zijlema, M., 2003. *An accurate and efficient finite-difference algorithm for non-hydrostatic free-surface flow with application to wave propagation*. Int. J. Numer. Meth. Fluids 43, 1–23.

[104] Stelling, G.S., Duinmeijer, S.P.A., 2003. *A staggered conservative scheme for every Froude number in rapidly varied shallow water flows*. Int. J. Numer. Meth. Fluids 43, 1329–1354.

[105] Suzuki, T., Altomare, C., De Roo, S., Vanneste, D., Mostaert, F., 2018. *Manning's roughness coefficient in SWASH: Application to overtopping calculation*. Version 2.0. FHR Reports, 17_026_1. Flanders Hydraulics Research: Antwerp.

[106] Suzuki, T., Altomare, C., Veale, W., Verwaest, T., Trouw, K., Troch, P., & Zijlema, M., 2017. *Efficient and robust wave overtopping estimation for impermeable coastal structures in shallow foreshores using SWASH*. Coastal Engineering, *122*, pp.108–123, https://doi.org/10.1016/J.COASTALENG.2017.01.009

[107] Suzuki, T., Altomare, C., Willems, M., & Dan, S., 2023. *Non-Hydrostatic Modelling of Coastal Flooding in Port Environments.* Journal of Marine Science and Engineering, *11*(3), pp.575, https://doi.org/10.3390/JMSE11030575

[108] SWSAH User Manual version 7.01, 2020. Delft University of Technology.

[109] Thai, H. T., 2022. *Machine learning for structural engineering: A state-of-the-art review*. In Structures (Vol. 38, pp. 448-491). Elsevier, https://doi.org/10.1016/j.istruc.2022.02.003.

[110] The SWASH team. *SWASH User Manual version 3.14A*. (2016). 31p

[111] The SWASH team. *SWASH User Manual version 6.01*. (2016). 148p

[112] Toimil, A., Losada, I.J., Nicholls, R.J., Dalrymple, R.A. and Stive, M.J., 2020. *Addressing the challenges of climate change risks and adaptation in coastal areas: A review*. Coastal Engineering, 156, p.103611.

[113] Van den Bos, J., Verhagen, H. J., Zijlema, M., & Mellink, B., 2014. *Towards a practical application of numerical models to predict wave-structure interaction: an initial validation.* Coastal Engineering.

[114] Van der Meer, J.W., Allsop, N.W.H., Bruce, T., De Rouck, J., Kortenhaus, A., Pullen, T., Schüttrumpf, H., Troch, P., Zanuttigh, B., 2018. *Manual on wave overtopping of sea defences and related structures*. EurOtop (overtopping-manual.com).

[115] Van Mierlo, F. A. J. M., 2014. *Numerical modelling of wave penetration in ports*. Master thesis, Department of Hydraulic Engineering, Faculty of Civil Engineering and Geosciences, Delft University of Technology, Delft, Netherlands, https://repository.tudelft.nl/islandora/object/uuid%3A36fa7a19-5e59-41c6-91bd-05ebc8da0752

[116] van Rijn, L. C., 2013. *Design of hard coastal structures against erosion*. (Site1 (leovanrijn-sediment.com)). Accessed April 03, 2023

[117] Vanneste, D.F., Altomare, C., Suzuki, T., Troch, P. and Verwaest, T., 2014. *Comparison of numerical models for wave overtopping and impact on a sea wall*. Coast. Eng. Proc, 1(5).

[118] Vapnik V., 1995. *The nature of statistical learning theory*. Springer.

[119] Veloso Gomes, F., 2010. *Situação crítica na marginal a norte do esporão norte da praia do Furadouro*. Protocolo FEUP/INAG, Porto.

[120] Veloso-Gomes, F., Oliveira, M., 2013. *Retirada Planeada de Áreas Edificadas em Zonas Costeiras em Risco. VII Congresso sobre o Planeamento e Gestão das Zonas Costeiras dos Países de Expressão Portuguesa*, Maputo, Moçambique.

[121] Ye, J; Shan, J; CDou, H; & Yan, N., 2021. *Numerical modelling of the wave interaction with revetment breakwater built on reclaimed coral reef islands in the South China Sea Experimental verification*. Ocean Engineering, *235*, 109325, https://doi.org/10.1016/J.OCEANENG.2021.109325

[122] Zijlema, M., Stelling, G., & Smit, P., 2011. *SWASH: An operational public domain code for simulating wave fields and rapidly varied flows in coastal waters*. Coastal Engineering, *58*(10), pp.992–1012, https://doi.org/10.1016/J.COASTALENG.2011.05.015

[123] Zijlema, M., Stelling, G.S., 2005. *Further experiences with computing non-hydrostatic free-surface flows involving water waves*. Int. J. Numer. Meth. Fluids 48, 169–197.

[124] Zijlema, M., Stelling, G.S., 2008. *Efficient computation of surf zone waves using the nonlinear shallow water equations with non-hydrostatic pressure*. Coastal Engineering. 55, 780–790.

[125] *Manning roughness coefficient*. (n.d.). Retrieved March 21, 2023, from https://serc.carleton.edu/details/images/9159.html

[126] *Manning's n Values*. (n.d.). Retrieved March 21, 2023, from https://www.fsl.orst.edu/geowater/FX3/help/8_Hydraulic_Reference/Mannings_n_Tables.htm

[127] https://censos.ine.pt/xportal/xmain?xpgid=censos21_produtos&xpid=CENSOS21&xlang=pt

[128] Estatísticas de Portugal www.ine.pt

[129] IH (2021). Hydrographic Institute. (https://www.hidrografico.pt/#). Accessed May 03, 2023.

[130] Environmental impacts of shore-parallel breakwaters along Nagahama and Ohgata, District of Joetsu, Japan - ScienceDirect (Retrieved March 2023)

[131] https://www.researchgate.net/figure/Variation-in-design-type-of-seawalls_fig9_216584246 (Retrieved March 2023)

[132] Overview of a Neural Network's Learning Process | by Rukshan Pramoditha | Data Science 365 | Medium (Retrieved March 2023)

[133] Typhoon Mangkhut: Two nuclear power plants on China's Guangdong coast in path of storm | South China Morning Post (scmp.com). (Retrieved April 2023)

[134] Introduction to Different Activation Functions for Deep Learning | by Shruti Jadon | Medium

[135] Support Vector Machine: Regression | by Beny Maulana Achsan | IT Paragon | Medium (Retrieved July 2023)

[136] Random Forest Interview Questions | Random Forest Questions (analyticsvidhya.com) (Retrieved July 2023)

APPENDIX A

```
$***************************** HEADING *********************************
PROJECT  'W_I2m16s' '1'
$***************************** MODEL INPUT ****************************
SET level=4.00 nor=90.00 depmin=0.01 maxerr=3
$**************************** MODEL MODE ******************************
MODE DYNAMIC TWODimensional
$**************************** MODEL COORD *****************************
COORDINATES CARTESIAN
$**************************** MODEL CGRID *****************************
CGRID REG 0 0 0 2222 1024 1111 512
$********************* MODEL VERTICAL LAYERS **************************
VERT 1
$*************************** MODEL BOTTOM *****************************
INPGRID BOTTOM 0 0 0 1111 512 2 2
READINP BOTTOM 1.0 'Maria_Str.bot' 5 0 FREE
$*************************** MODEL FRICTION ***************************
INPGRID FRICTION 0 0 0 1111 512 2 2
READINP FRICTION 1.0 'My_Rgh_Maria_Str.rgh' 5 0 FREE
$******************** MODEL INITIAL CONDITIONS ************************
INITIAL ZERO
$******************** MODEL BOUNDARY CONDITIONS ***********************
BOU SHAP JON 3.3 SIG PEAK DSPR DEGREES
BOU SIDE W CCW BTYPE WEAK CON SPECT 5.67 19.0 0.0 0.0
$************************ MODEL SPONGE LAYERS *************************
SPONgelayer E 10
$*************************** MODEL PHYSICS ****************************
BREaking
VISC H SMAG 0.1
$************************** MODEL FRICTION ****************************
FRICtion MANNing
$******************** MODEL DISCRETISATION ****************************
NONHYDROSTATIC BOX PREC ILU
DISCRET UPW MUS
DISCRET CORRDEP MUS
$******************** MODEL BOTCEL ****************************
BOTCEL MAX
$********************* MODEL TIME INTEGRATION *************************
TIMEI METH EXPL cfllow=0.05  cflhig=0.3
$********************* MODEL QUAMTITY OUTPUTS *************************
QUANTITY XP excv=-999.0
QUANTITY YP excv=-999.0
QUANTITY DIST excv=-999.0
QUANTITY DEPTH excv=-999.0
QUANTITY BOTLEV excv=-999.0
QUANTITY WATLEV excv=-999.0
QUANTITY VEL excv=-999.0
QUANTITY BRKP excv=-999.0
QUANTITY HRUN excv=-999.0
QUANTITY HSIG excv=-999.0 DUR 30 MIN
QUANTITY HRMS excv=-999.0 DUR 30 MIN
QUANTITY SETUP excv=-999.0 DUR 30 MIN
QUANTITY MVEL excv=-999.0 DUR 30 MIN
$********************* MODEL OUTPUT COMPGRID *************************
BLOCK 'COMPGRID' NOHEAD 'ts_map_grd.mat' LAY 3 XP YP WATL BOTLEV HSIG HRMS HRUN OUTPUT 000005.000 30.0 SEC
$********************* MODEL OUTPUT COMPGRID ****************
BLOCK 'COMPGRID' NOHEAD 'av_map_grd.mat' LAY 3 XP YP HSIG HRUN HRMS WATL BOTLEV
$************************** MODEL TESTS ********************************
TEST itest=1 itrace=0
$************************** MODEL COMPUTE ****************************
COMPUTE 000000.000 0.01 SEC 004000.000
STOP
```

Figure A1 – Typical input file used for SWASH simulations.

APPENDIX B

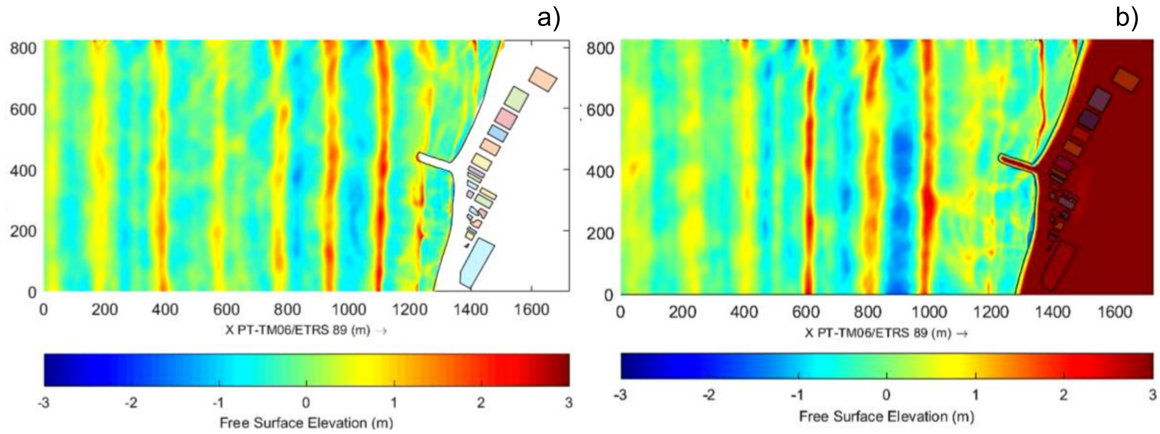

Figure B1 – Comparison of SWASH results for Hs 2 and Tp 16: a) results for SWASH version 6.01 and 7; b) the results for SWASH version 9.01.

Figure B2 - 2 cross-sections to analyze influence of the parameters for wave breaking when interacting with the structure, section 1 on the north side of the groin and section 2 on the south side.

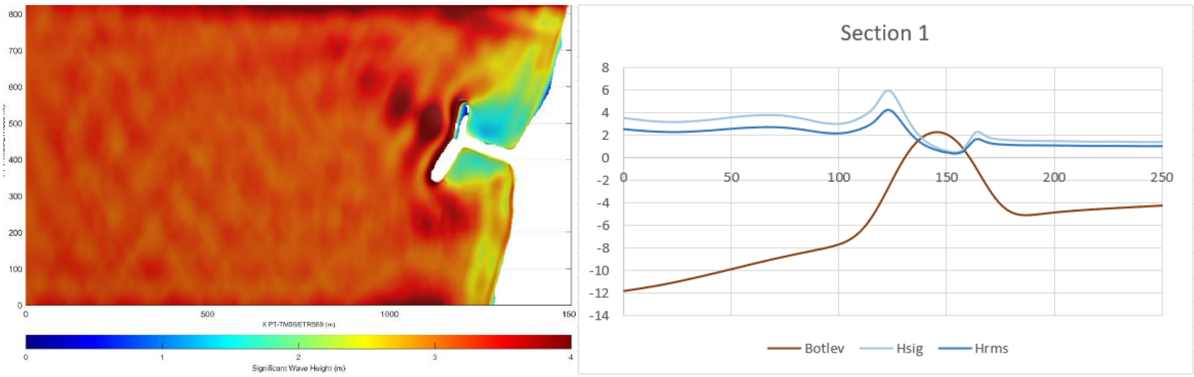

Figure B3 - Hs 3 m and Tp 16 with only bottom grid.

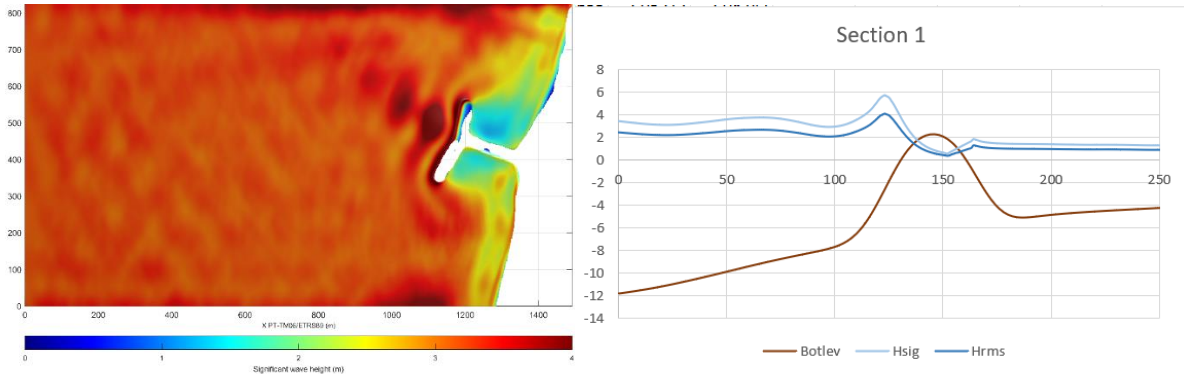

Figure B4 - Hs 3 m and Tp 16 with roughness, porosity and particles size values used by Marques (2021).

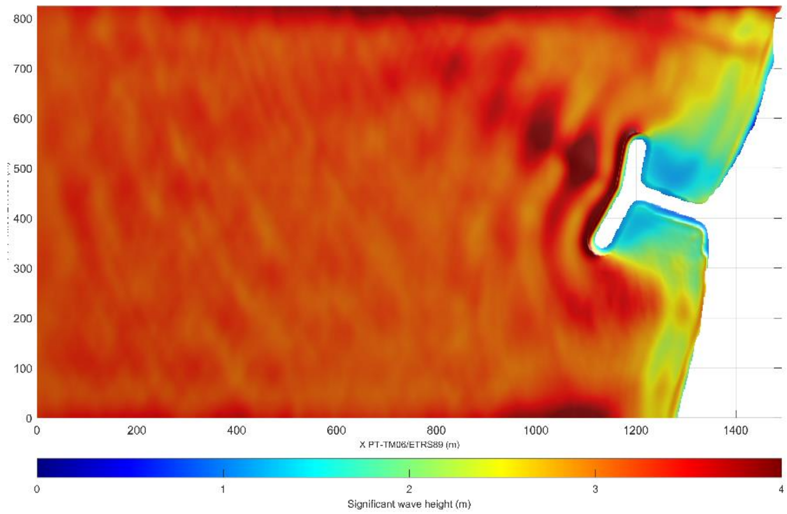

Figure B5 - Hs 3 m and Tp 16 with second column of roughness from Table 4.7 with porosity and particles size values used by Marques (2021).

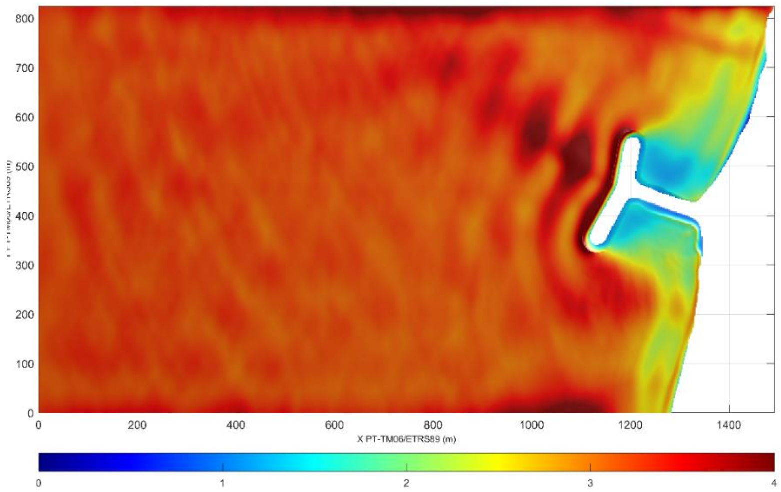

Figure B6 - Hs 3 m and Tp 16 with third column of roughness from Table 4.7 with porosity and particles size values used by Marques (2021).

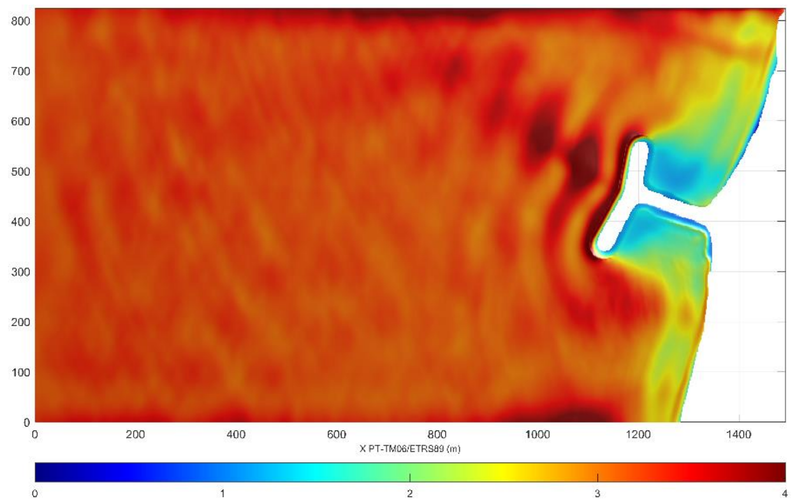

Figure B7 - Hs 3 m and Tp 16 with only with porosity and particles size values used by Marques (2021).

Figure B8 – Cross-section to analyze influence of the parameters on the vertical breakwater.

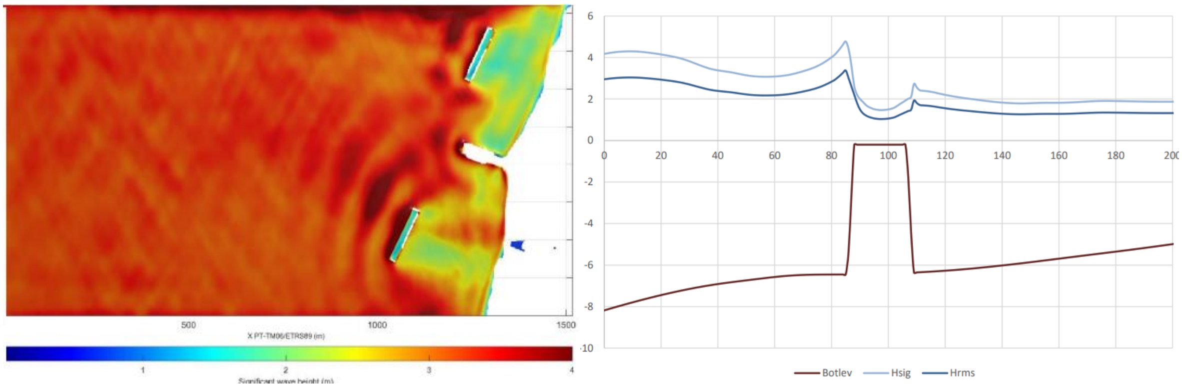

Figure B9 - Hs 3 m and Tp 16 with only bottom grid, in this simulation, the breakwater crest elevation was at 0 m (CD).

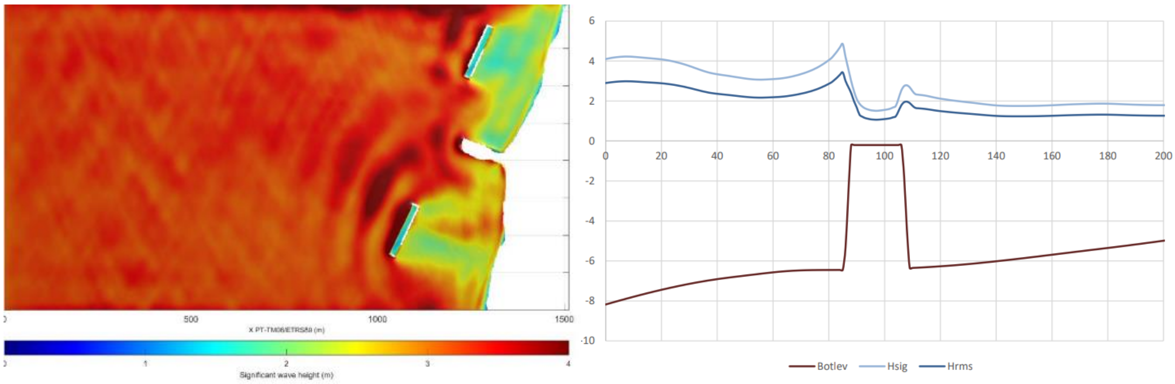

Figure B10 - Hs 3 m and Tp 16 with roughness, porosity and particles size values used by Marques (2021).

These simulations revealed that sometimes it is sufficient to use the bottom grid layer to represent the structures, since the SWASH manual also recommends that breakwater structures can be represented without modifying the bathymetry. For instance, the breakwater structure can be represented by the porosity and particle size layers in addition to the grid layer of structure height. It was observed that when all of these grids are used concurrently and depending on the values shown in Table 4.8, the model exhibits some instabilities near the breakwater structures, both the rubble mound and vertical breakwater structures; consequently, the curves that represent the H_s and H_{rms} were not obtained in the sections where these layers are used concurrently or in a combination that is not suitable for the model because some values were -999.

APPENDIX C

Test 1

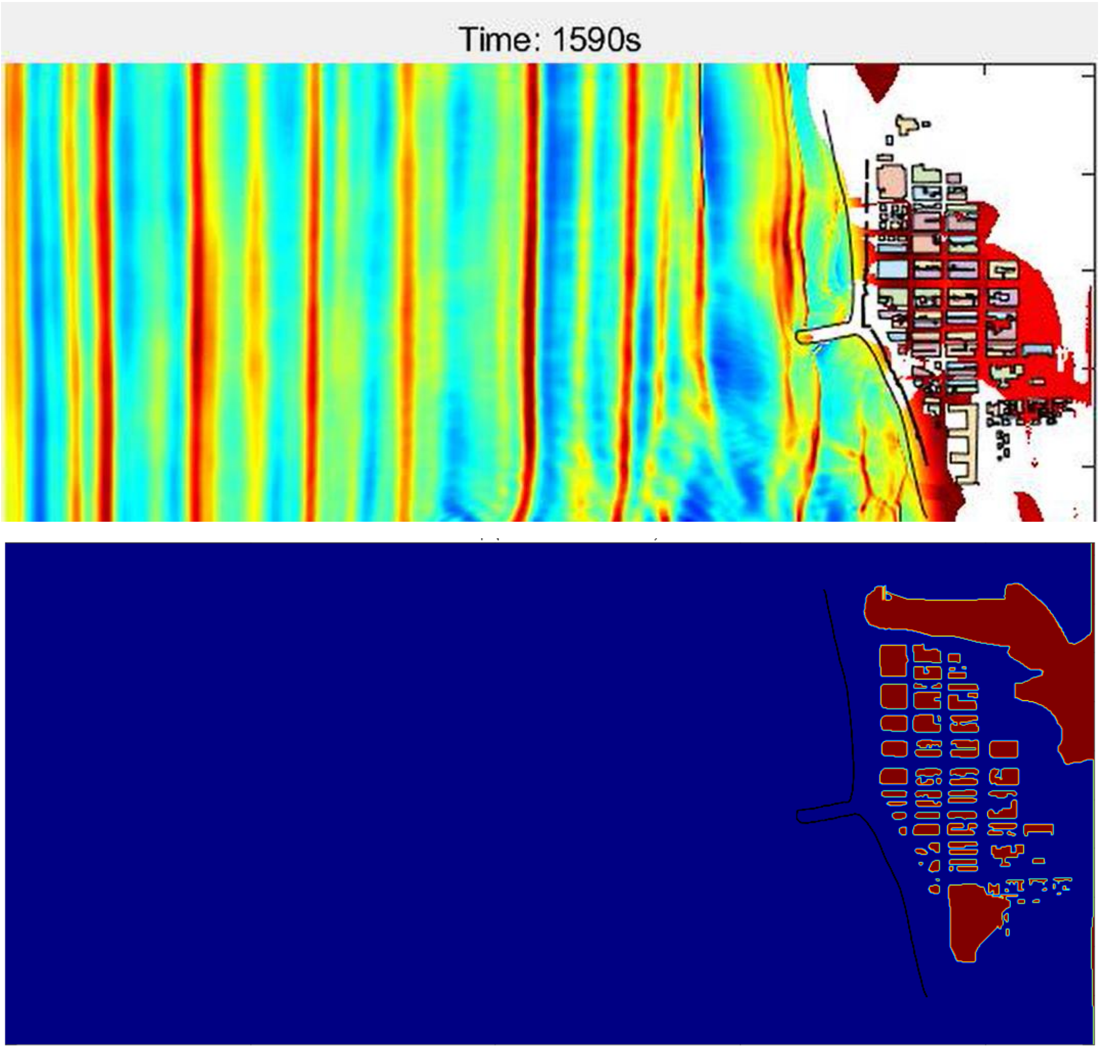

Figure C1 - Snapshot showing the propagation of the flood water in the urbanized area of Furadouro and the total flooded area, for this results the gird layer in Table C1 was used.

Table C1 - Roughness layer used.

	Roughness [$m^{-1/3}s$]
Buildings	0.01
Walls	0.01
Ocean sand	0.01
Dry land	0.01
RMB and Groins	0.01

Test 2

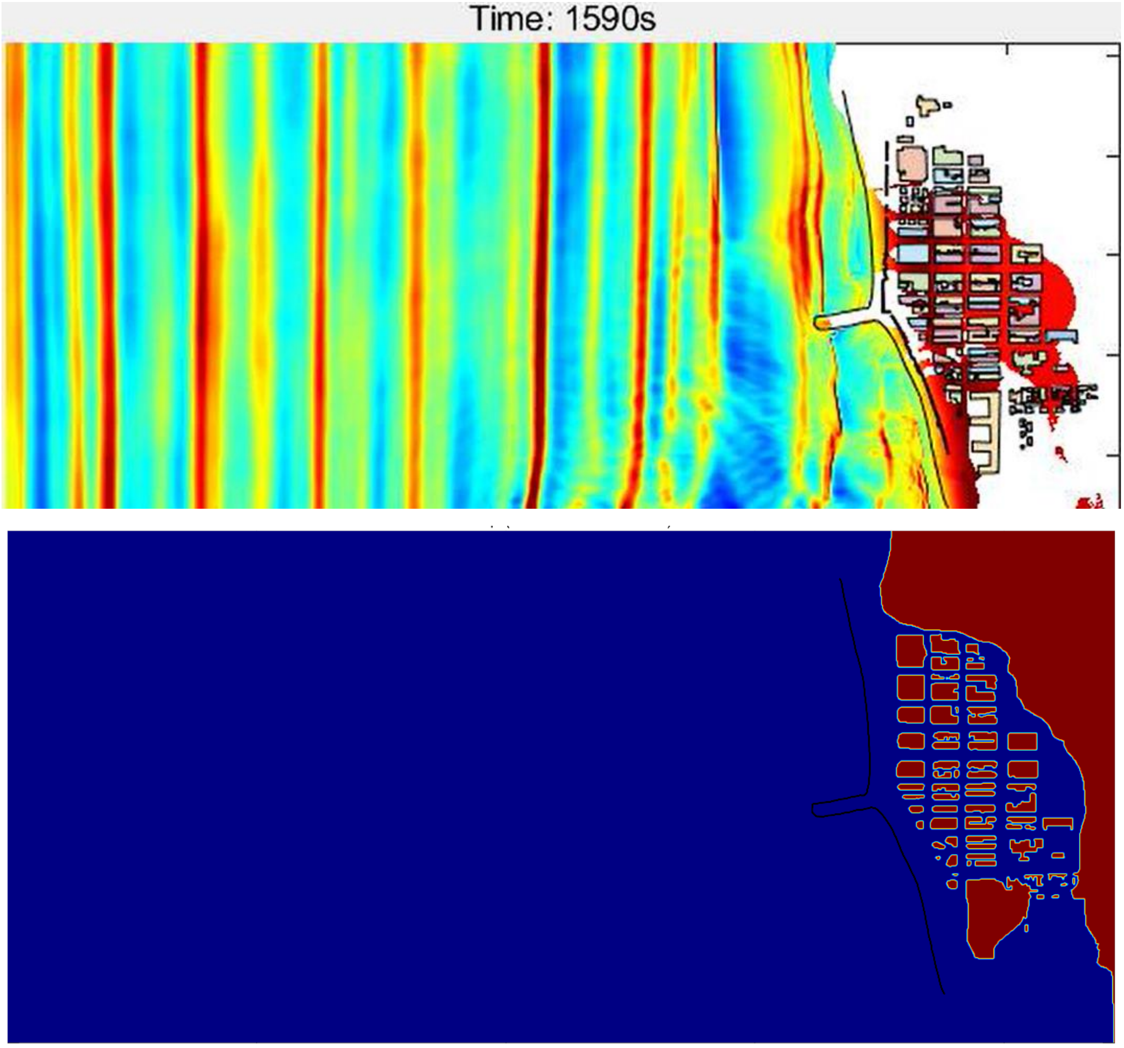

Figure C2 - Snapshot showing the propagation of the flood water in the urbanized area of Furadouro and the total flooded area, for this results the gird layer in Table C2 was used.

Table C2 - Roughness layer used.

	Roughness [$m^{-1/3}s$]
Buildings	0.015
Walls	0.015
Ocean sand	0.015
Dry land	0.015
RMB and Groins	0.015

Test 3

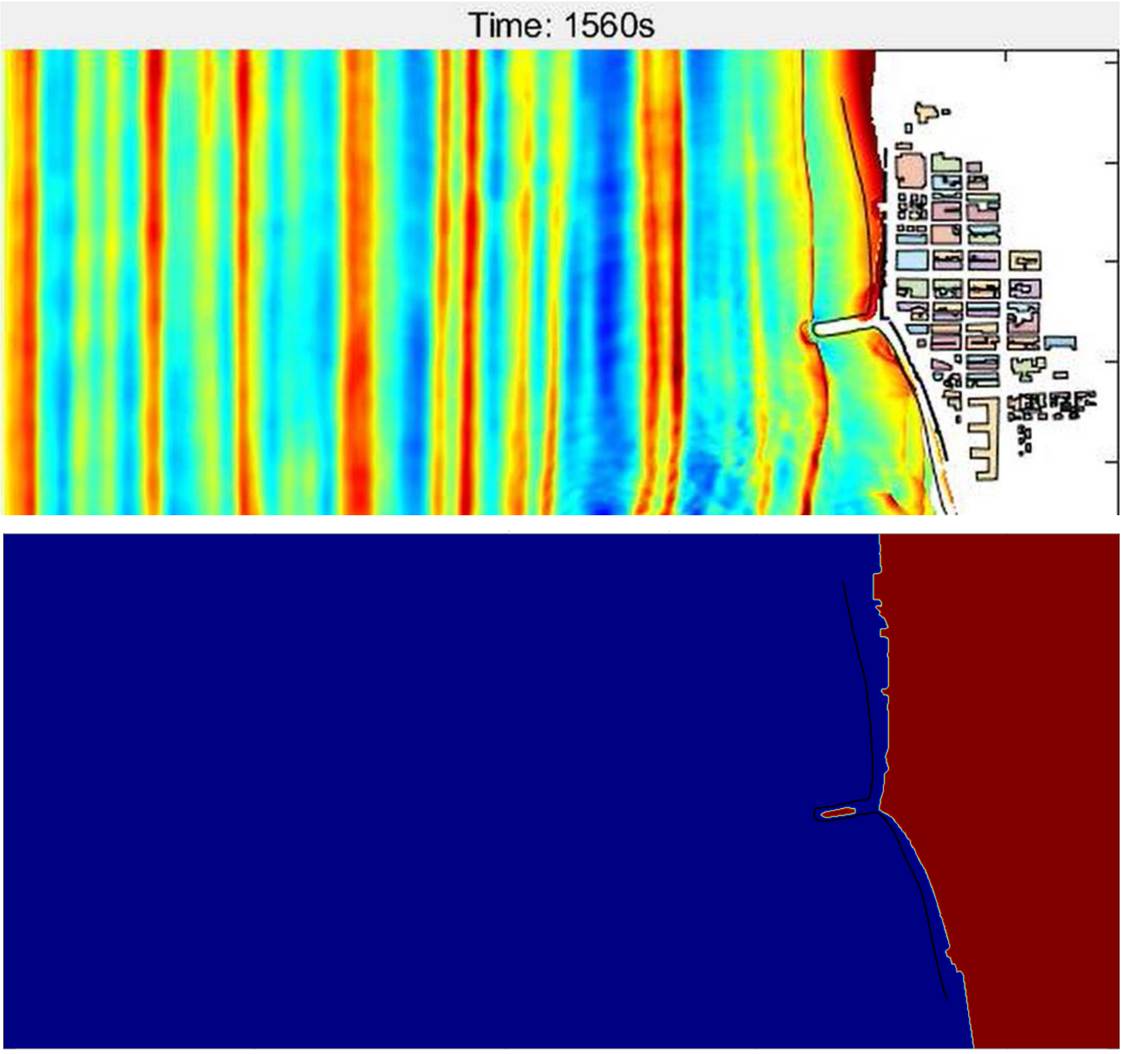

Figure C3 - Snapshot showing the propagation of the flood water in the urbanized area of Furadouro and the total flooded area, for this results the gird layers in Table C3 were used.

Table C3 – Porosity and Particle size layers used.

	P_Size [m]	Porosity [-]
Buildings	0.001	0.01
Walls	0.001	0.01
Ocean sand	0.002	1.00
Dry land	0.002	0.10
RMB and Groins	0.500	0.45

Test 4

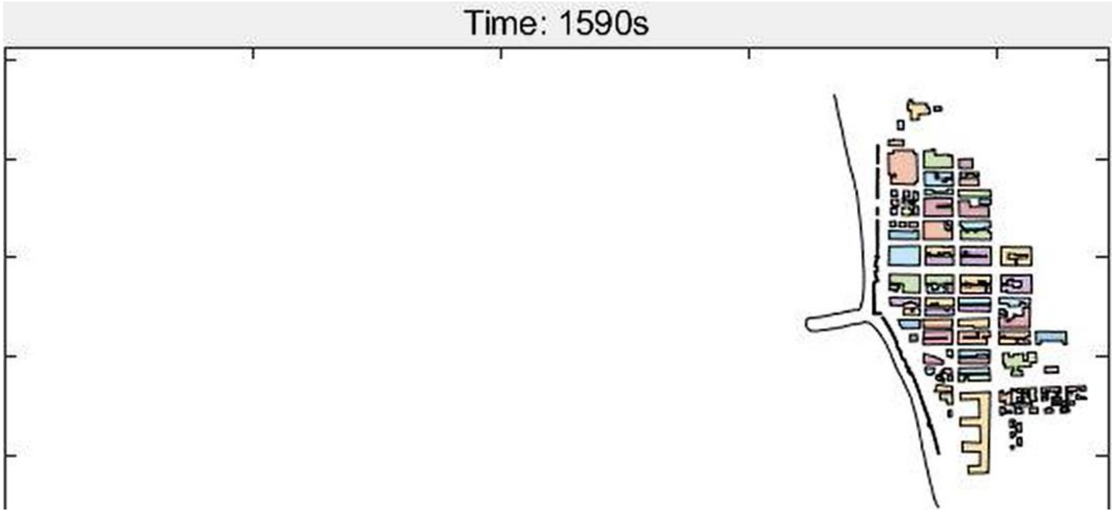

Figure C4 - Snapshot showing the propagation of flood in the urbanized area of Furadouro and the total flooded area, for this results the gird layers in Table C4 were used. However, the simulation crash, as already explained in the Appendix B, in most cases the simulations crashes or become unstable when all grid layers are used at the same time.

Table C4 – Roughness, Porosity and Particle size layers used.

	P_Size [m]	Roughness [$m^{-1/3}s$]	Porosity [-]
Buildings	0.001	0.08	0.01
Walls	0.001	0.012	0.01
Ocean sand	0.002	0.019	1.00
Dry land	0.002	0.04	0.10
RMB and Groins	0.500	0.045	0.45

APPENDIX D

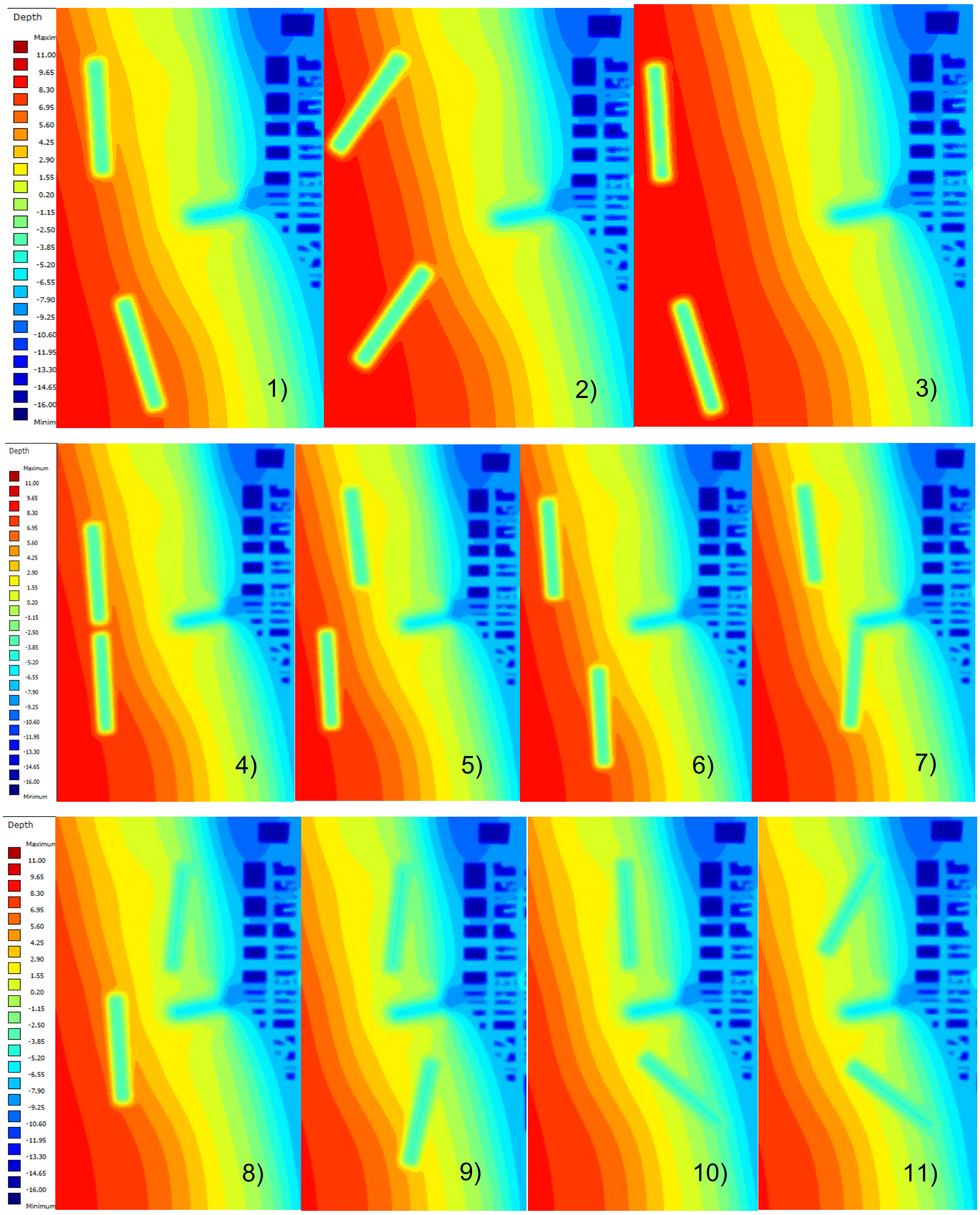
Depth
Maximum
11.00
9.65
8.30
6.95
5.60
4.25
2.90
1.55
0.20
-1.15
-2.50
-3.85
-5.20
-6.55
-7.90
-9.25
-10.60
-11.95
-13.30
-14.65
-16.00
Minimum
1)
2)
3)
4)
5)
6)
7)
8)
9)
10)
11)

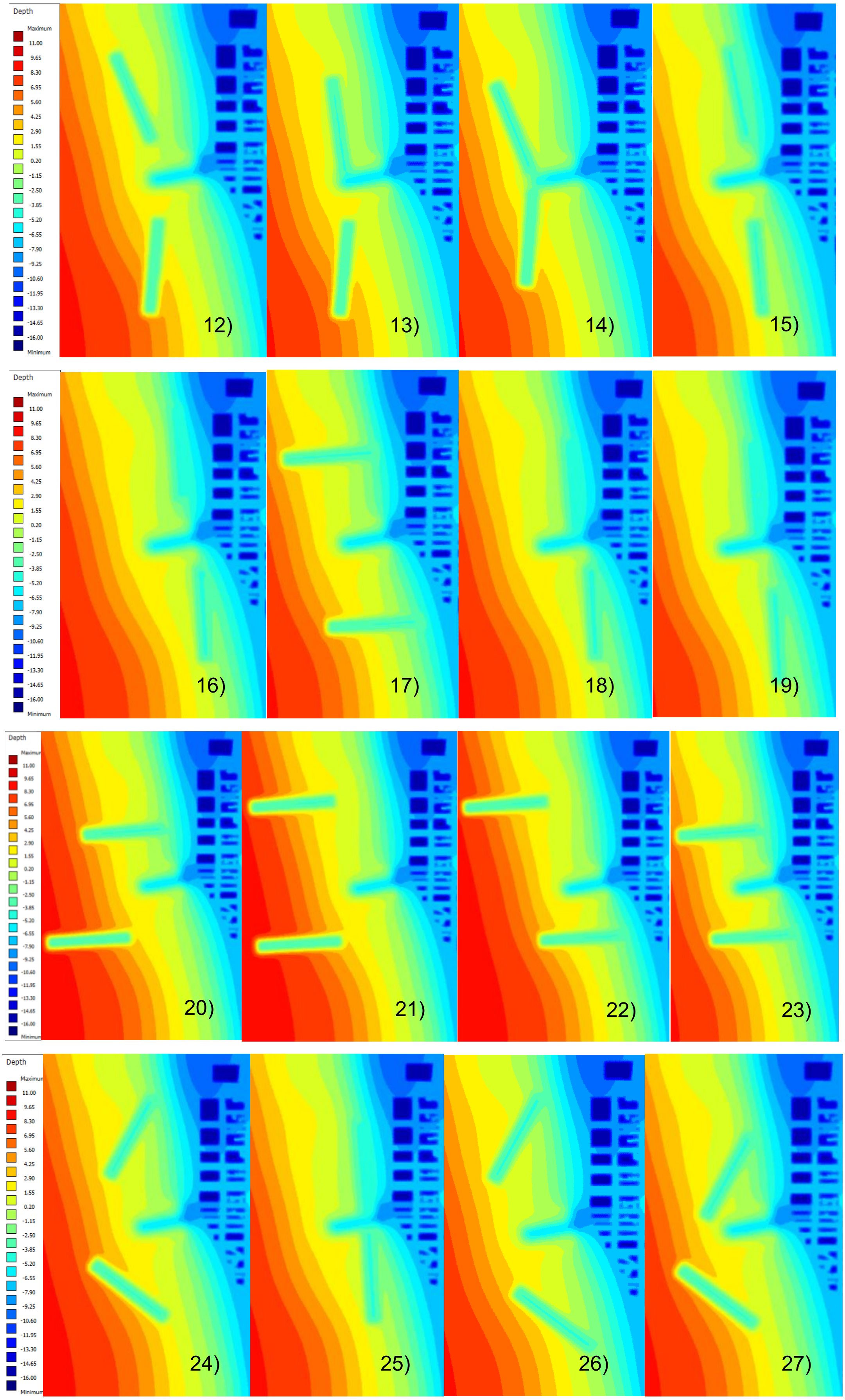
Depth
Maximum
11.00
9.65
8.30
6.95
5.60
4.25
2.90
1.55
0.20
-1.15
-2.50
-3.85
-5.20
-6.55
-7.90
-9.25
-10.60
-11.95
-13.30
-14.65
-16.00
Minimum
12)
13)
14)
15)
16)
17)
18)
19)
20)
21)
22)
23)
24)
25)
26)
27)

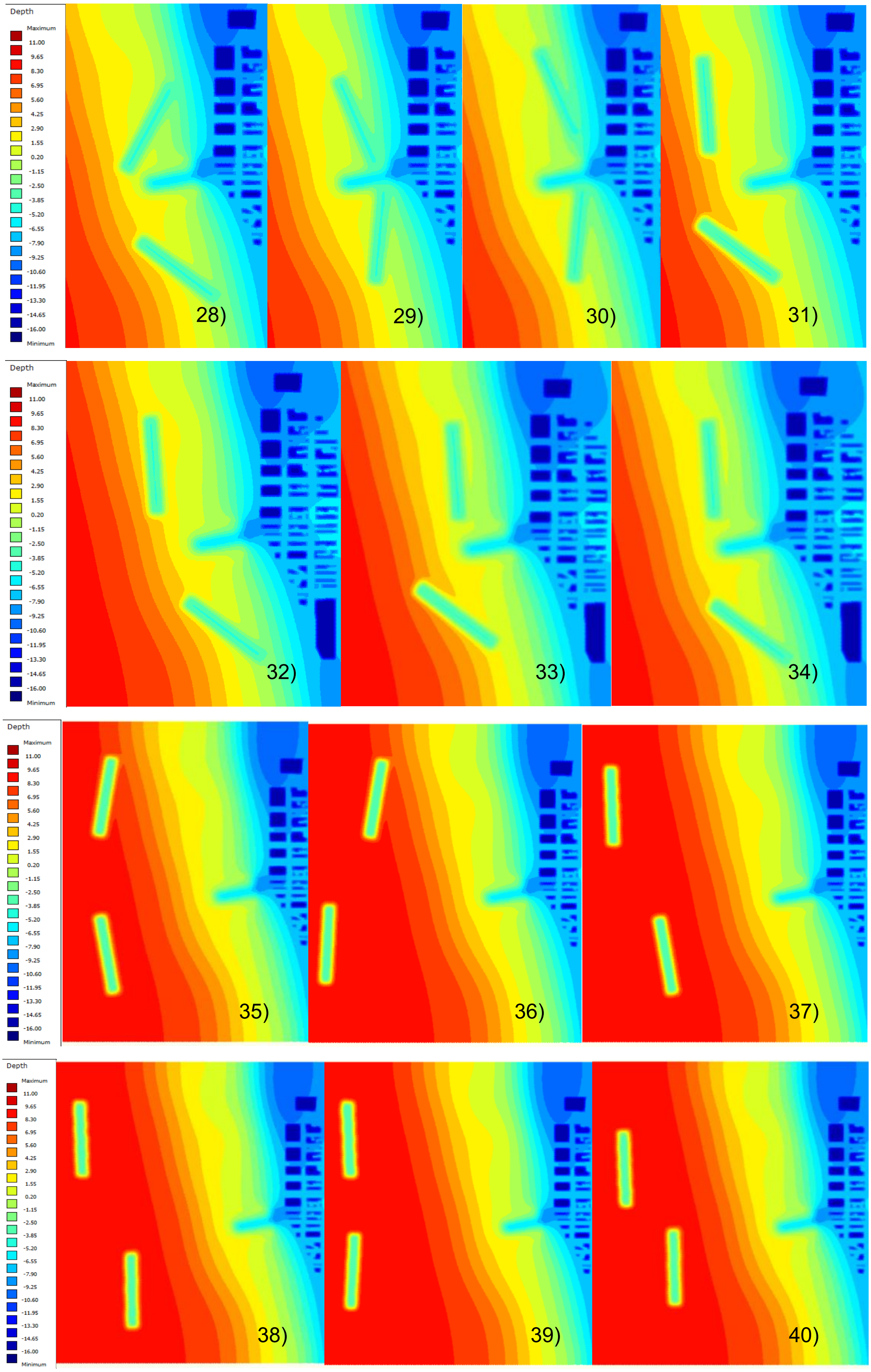
Depth
Maximum
11.00
9.65
8.30
6.95
5.60
4.25
2.90
1.55
0.20
-1.15
-2.50
-3.85
-5.20
-6.55
-7.90
-9.25
-10.60
-11.95
-13.30
-14.65
-16.00
Minimum
28)
29)
30)
31)
32)
33)
34)
35)
36)
37)
38)
39)
40)

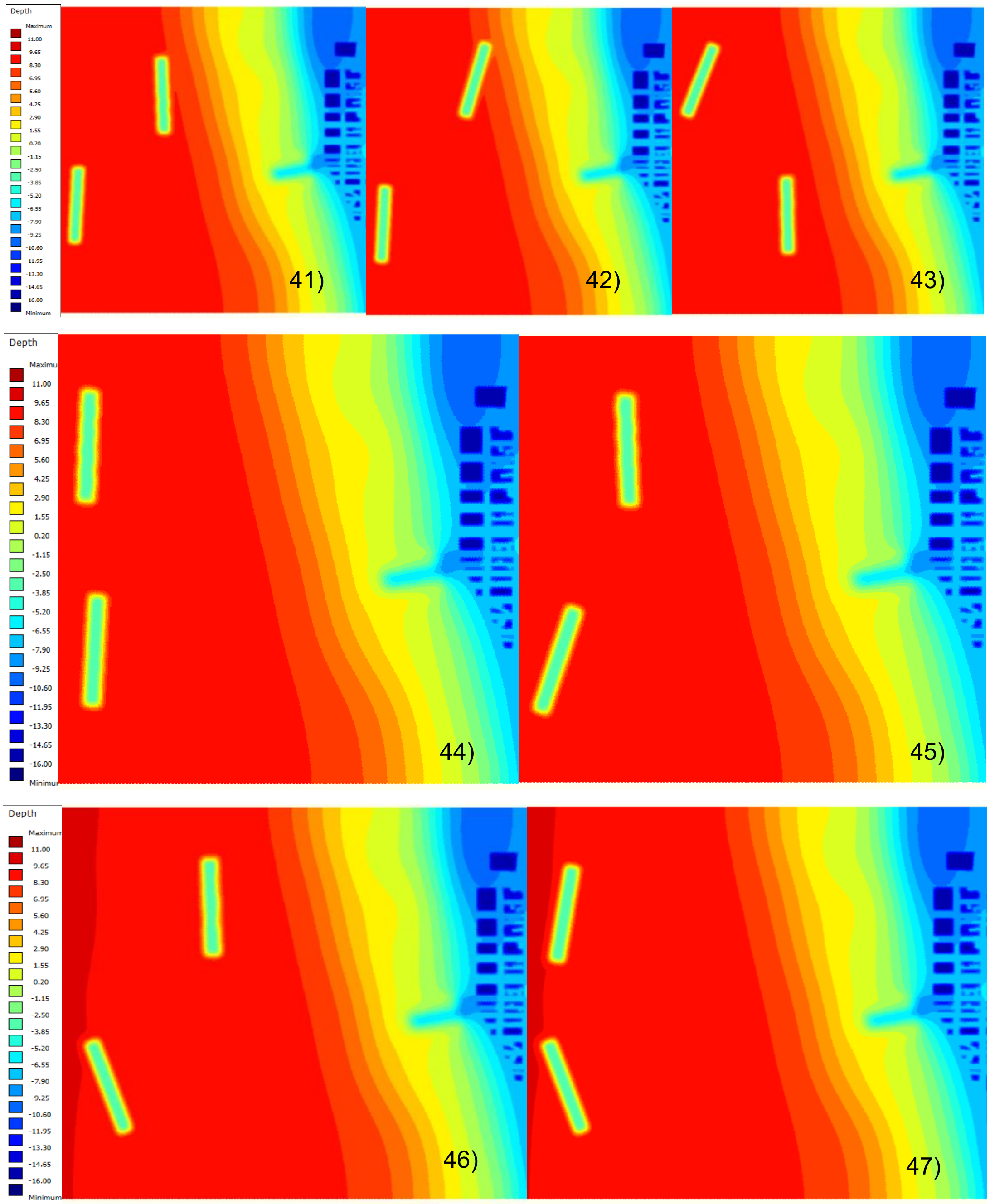
Depth
Maximum
11.00
9.65
8.30
6.95
5.60
4.25
2.90
1.55
0.20
-1.15
-2.50
-3.85
-5.20
-6.55
-7.90
-9.25
-10.60
-11.95
-13.30
-14.65
-16.00
Minimum
41)
42)
43)
44)
45)
46)
47)

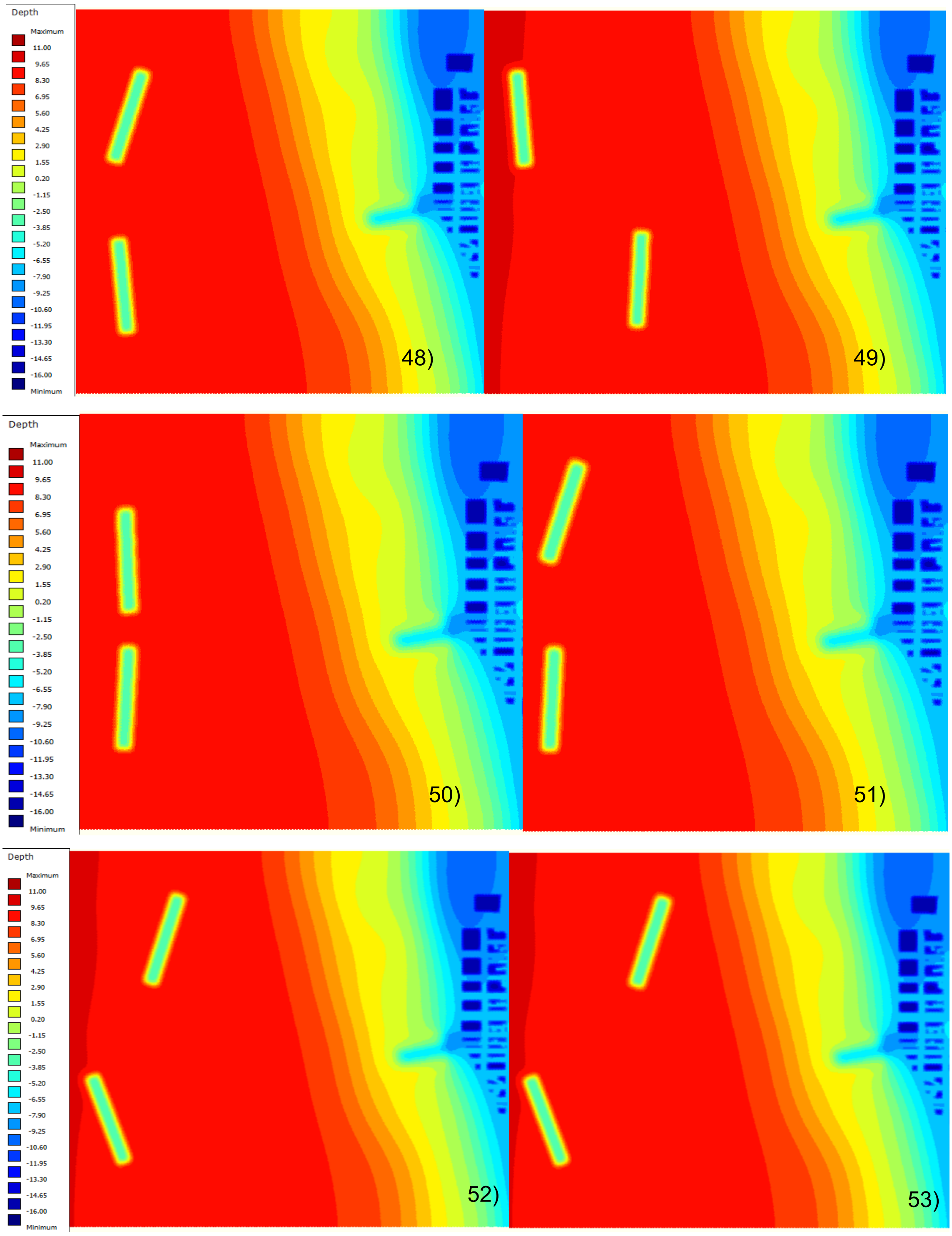
Depth
Maximum
11.00
9.65
8.30
6.95
5.60
4.25
2.90
1.55
0.20
-1.15
-2.50
-3.85
-5.20
-6.55
-7.90
-9.25
-10.60
-11.95
-13.30
-14.65
-16.00
Minimum
48)
49)
50)
51)
52)
53)

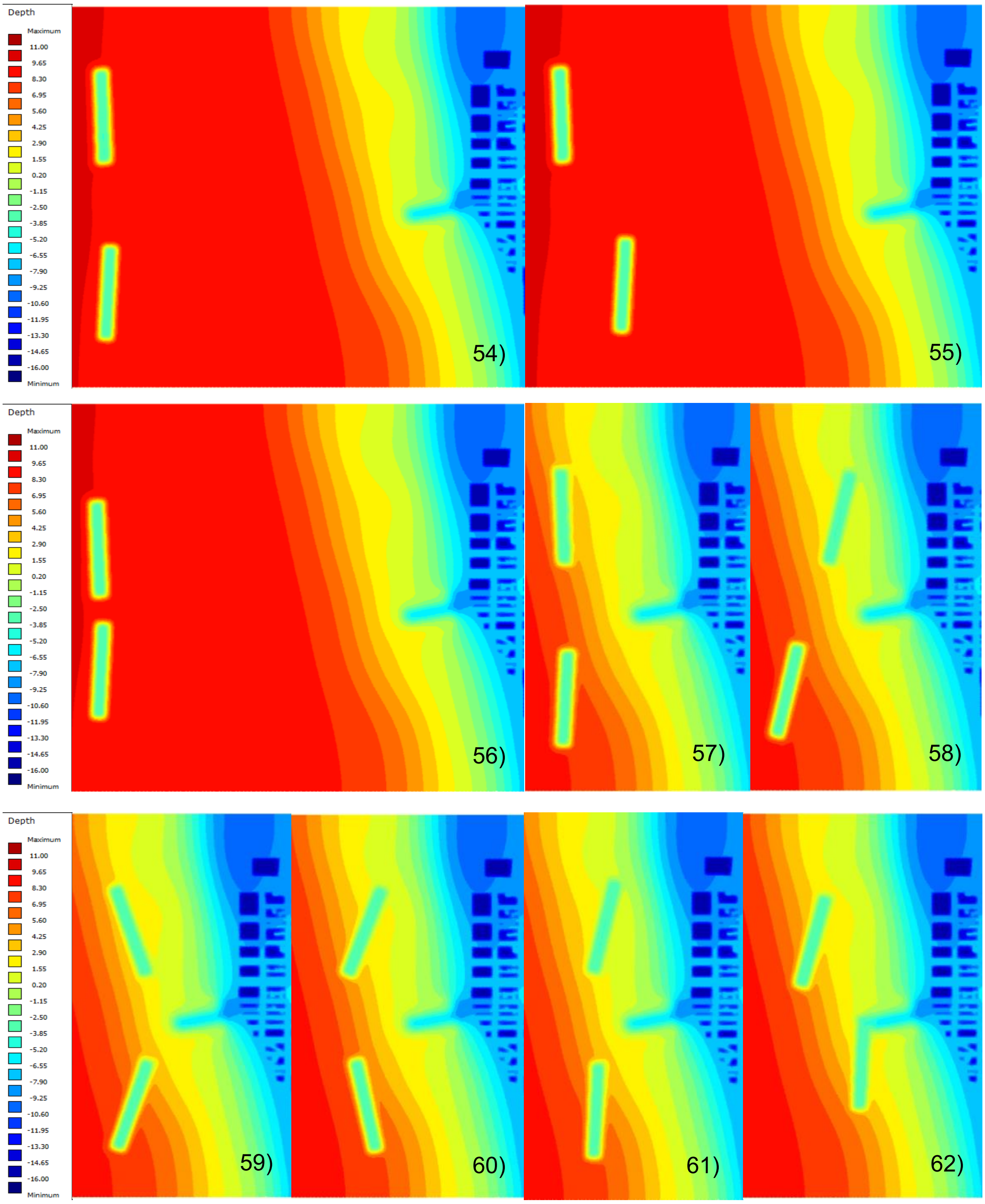
Depth
Maximum
11.00
9.65
8.30
6.95
5.60
4.25
2.90
1.55
0.20
-1.15
-2.50
-3.85
-5.20
-6.55
-7.90
-9.25
-10.60
-11.95
-13.30
-14.65
-16.00
Minimum
54)
55)
56)
57)
58)
59)
60)
61)
62)

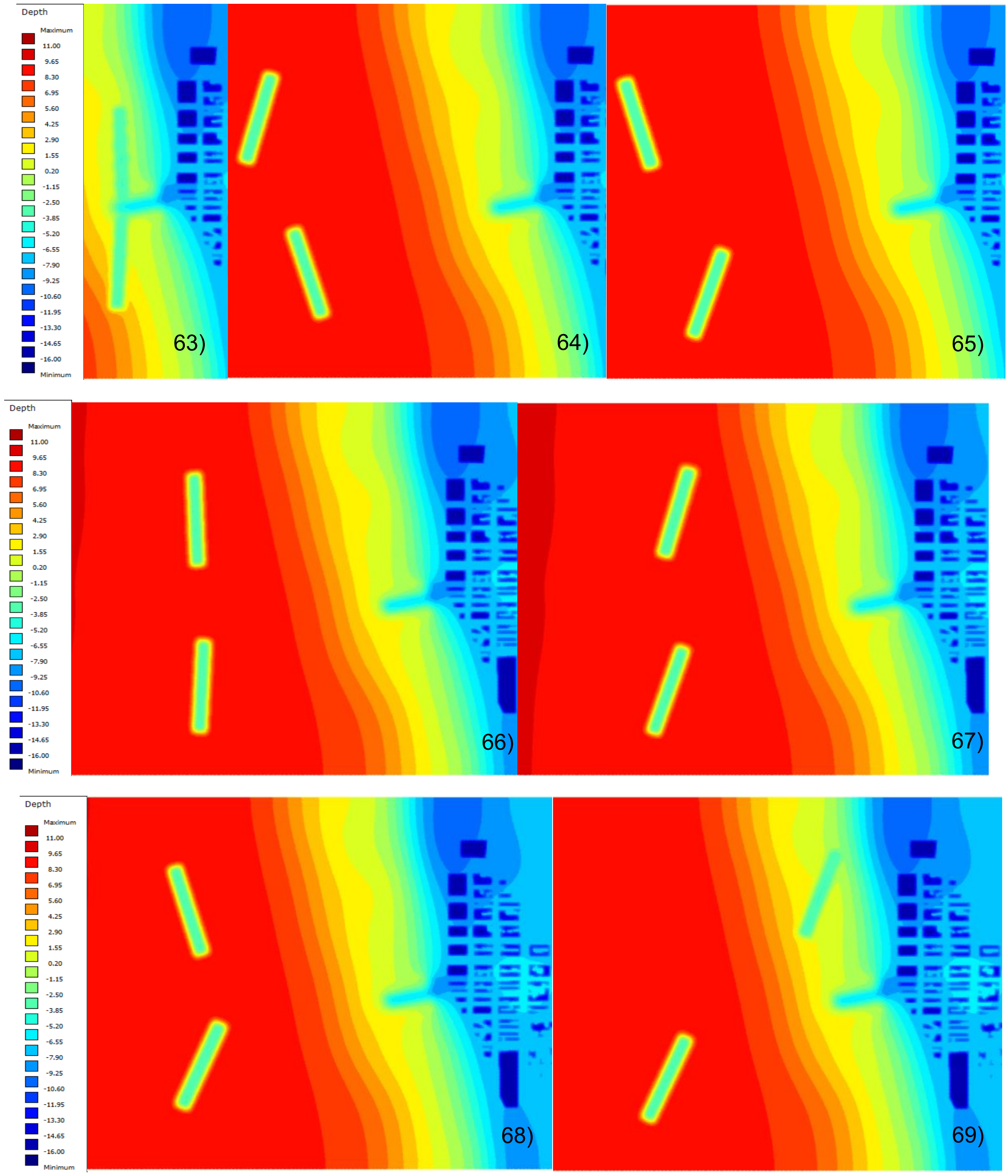
Depth
Maximum
11.00
9.65
8.30
6.95
5.60
4.25
2.90
1.55
0.20
-1.15
-2.50
-3.85
-5.20
-6.55
-7.90
-9.25
-10.60
-11.95
-13.30
-14.65
-16.00
Minimum
63)
64)
65)
66)
67)
68)
69)

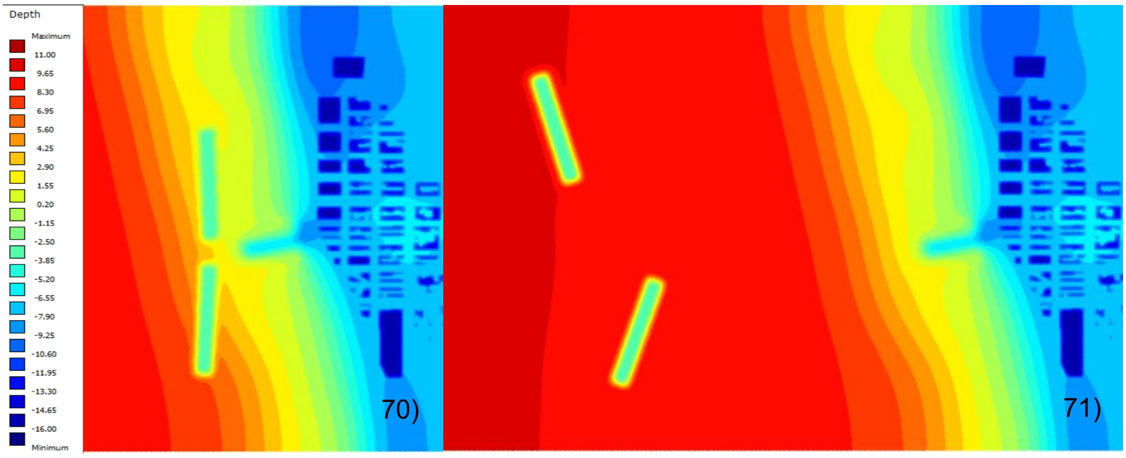

Figure D.1 – 75 simulations that were prepared for machine learning (the other 4 in section 4.3).

APPENDIX E

LEGEND:

- Dry area
- Flooded area
- Vertical breakwater structures
- The shoreline

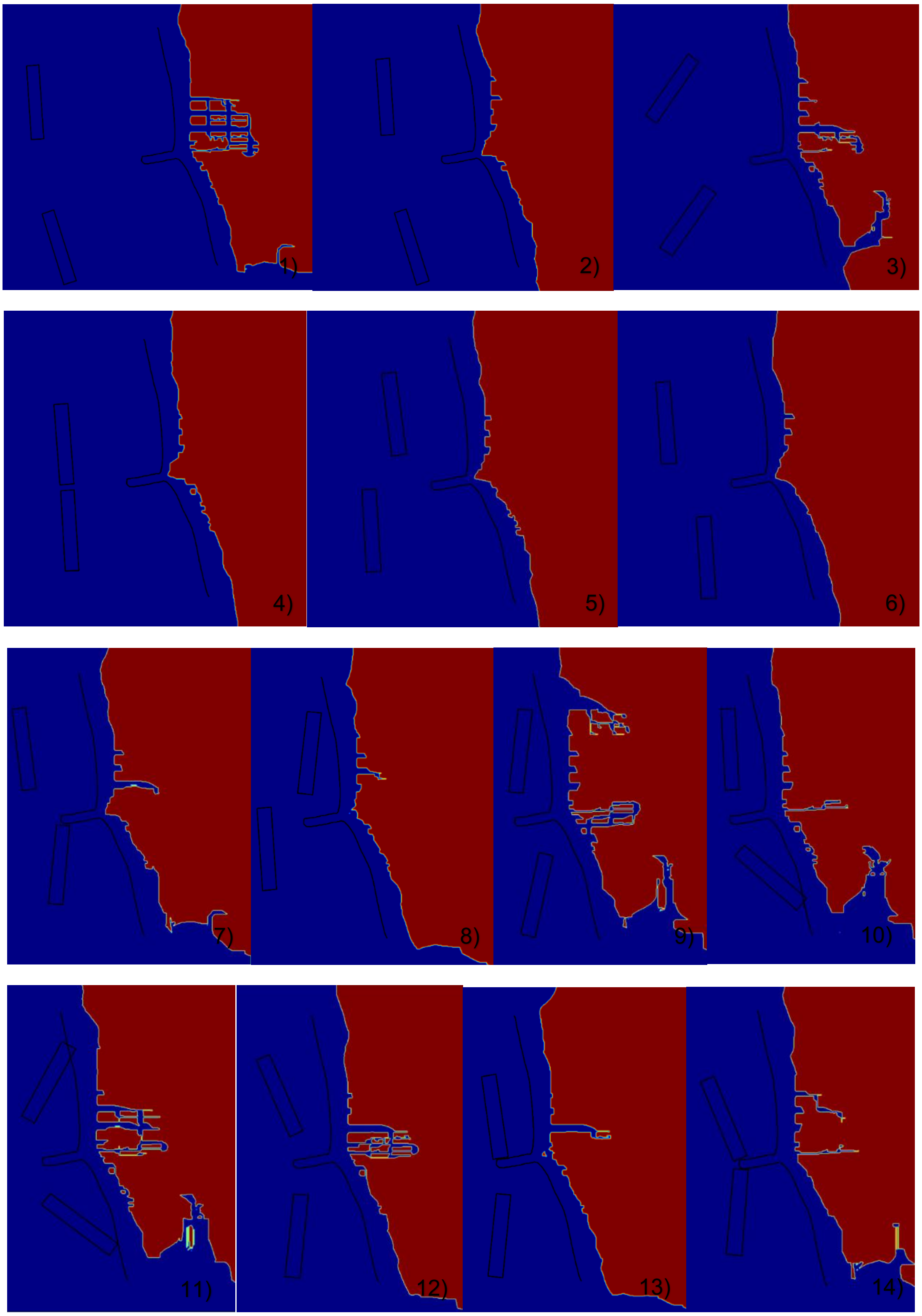

LEGEND:

Dry area

Flooded area

Vertical breakwater structures

The shoreline

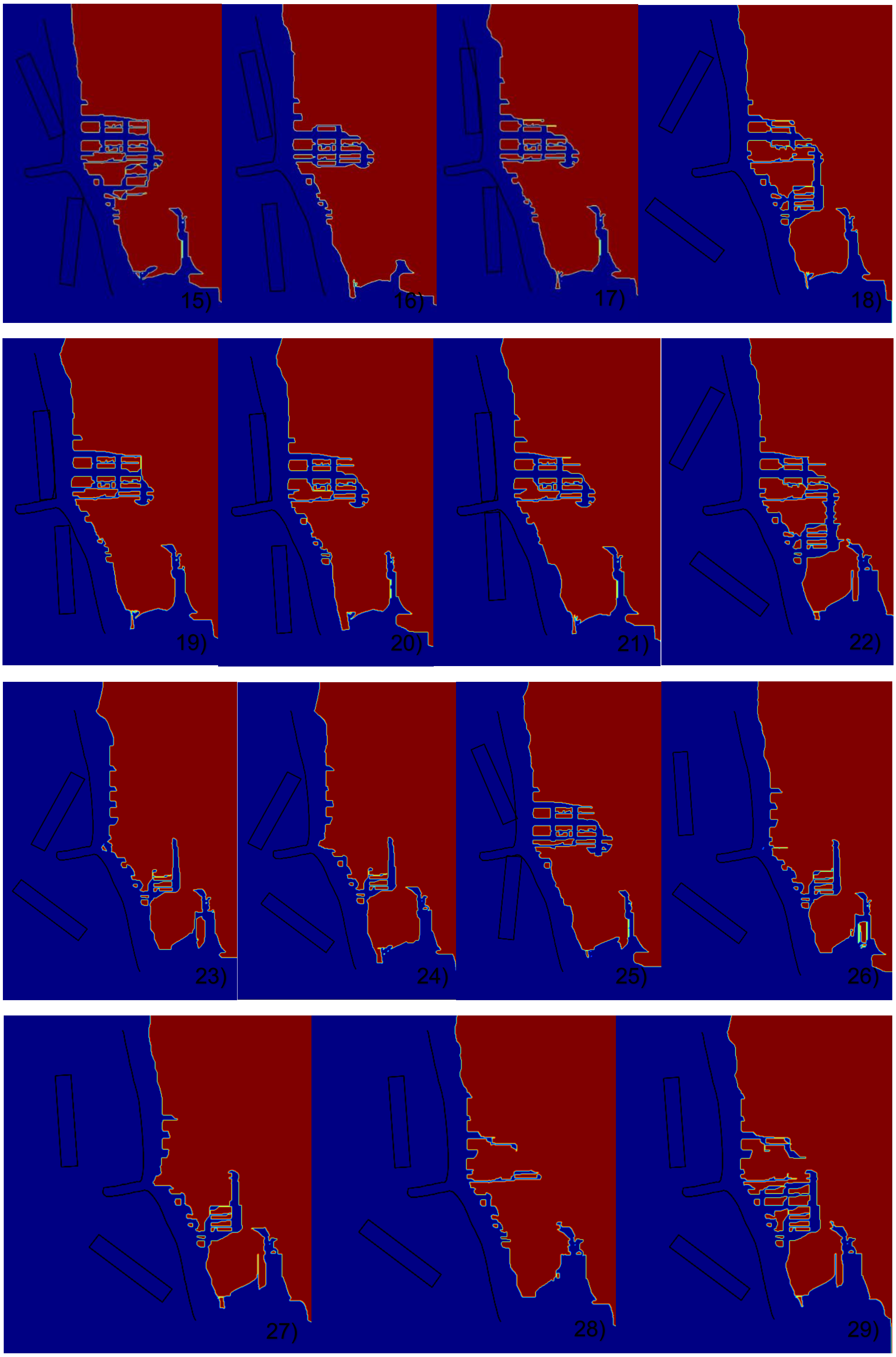

LEGEND:

Dry area

Flooded area

Vertical breakwater structures

The shoreline

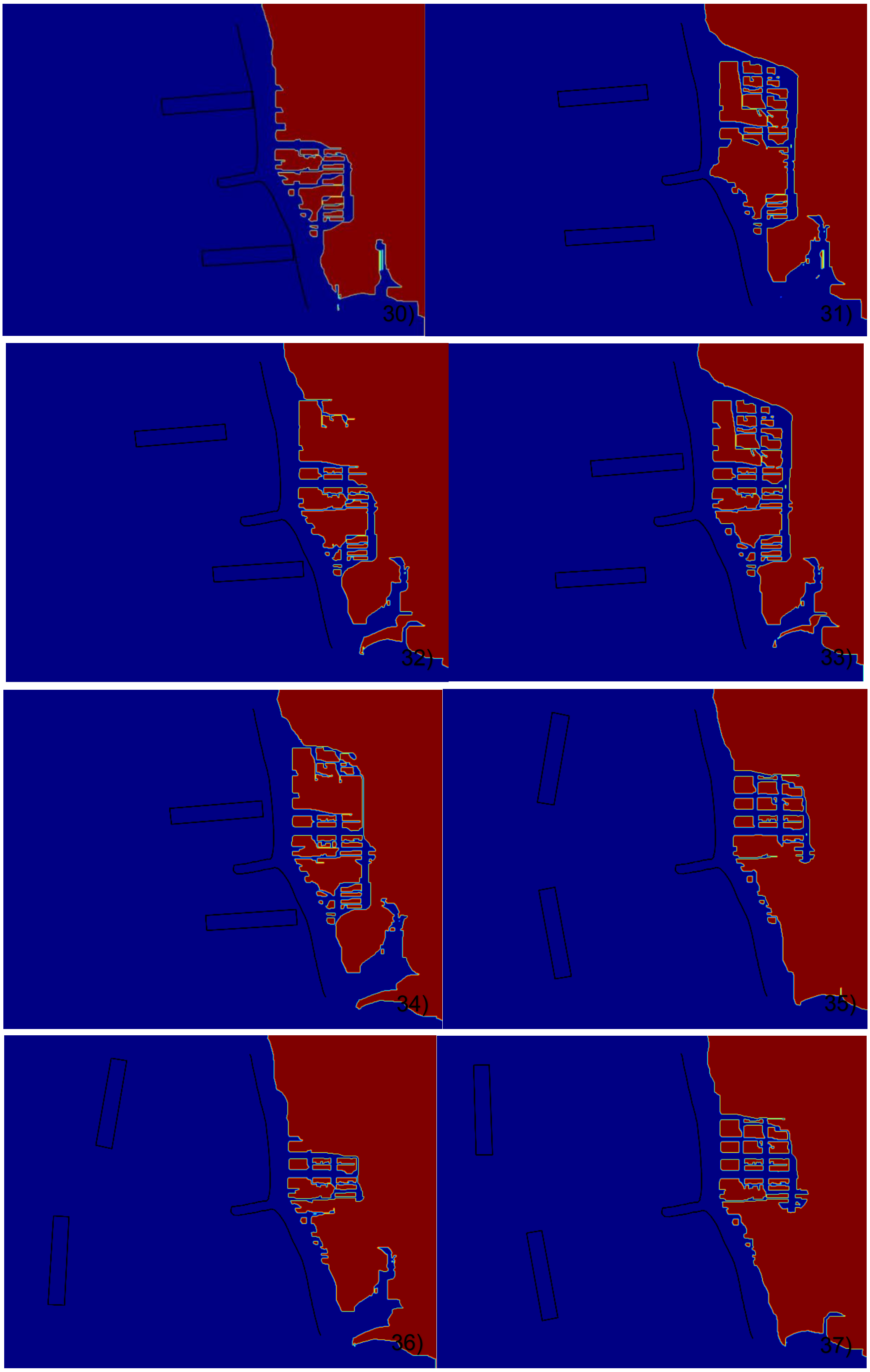

LEGEND:

Dry area

Flooded area

Vertical breakwater structures

The shoreline

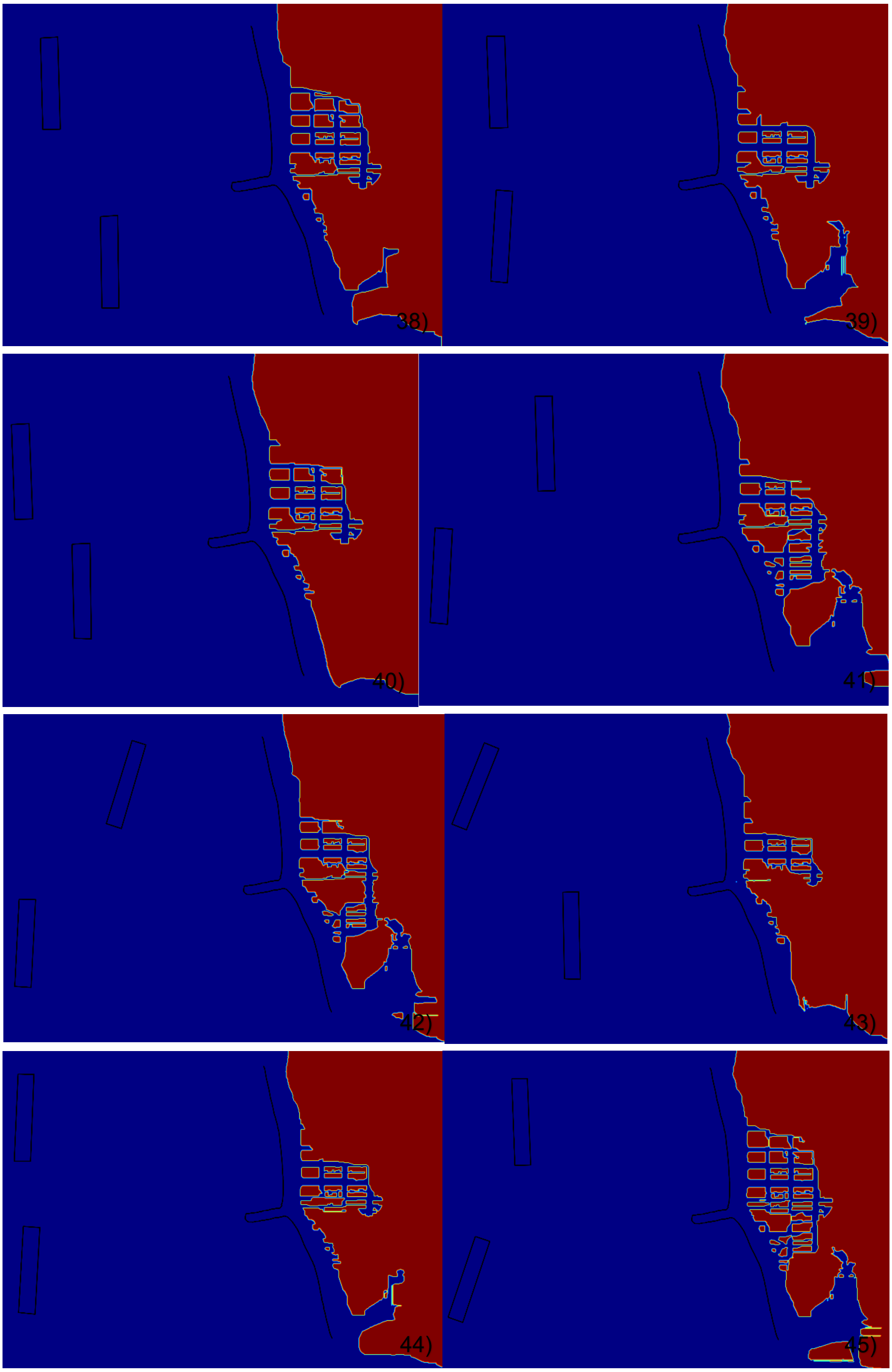

LEGEND:

- Dry area
- Flooded area
- Vertical breakwater structures
- The shoreline

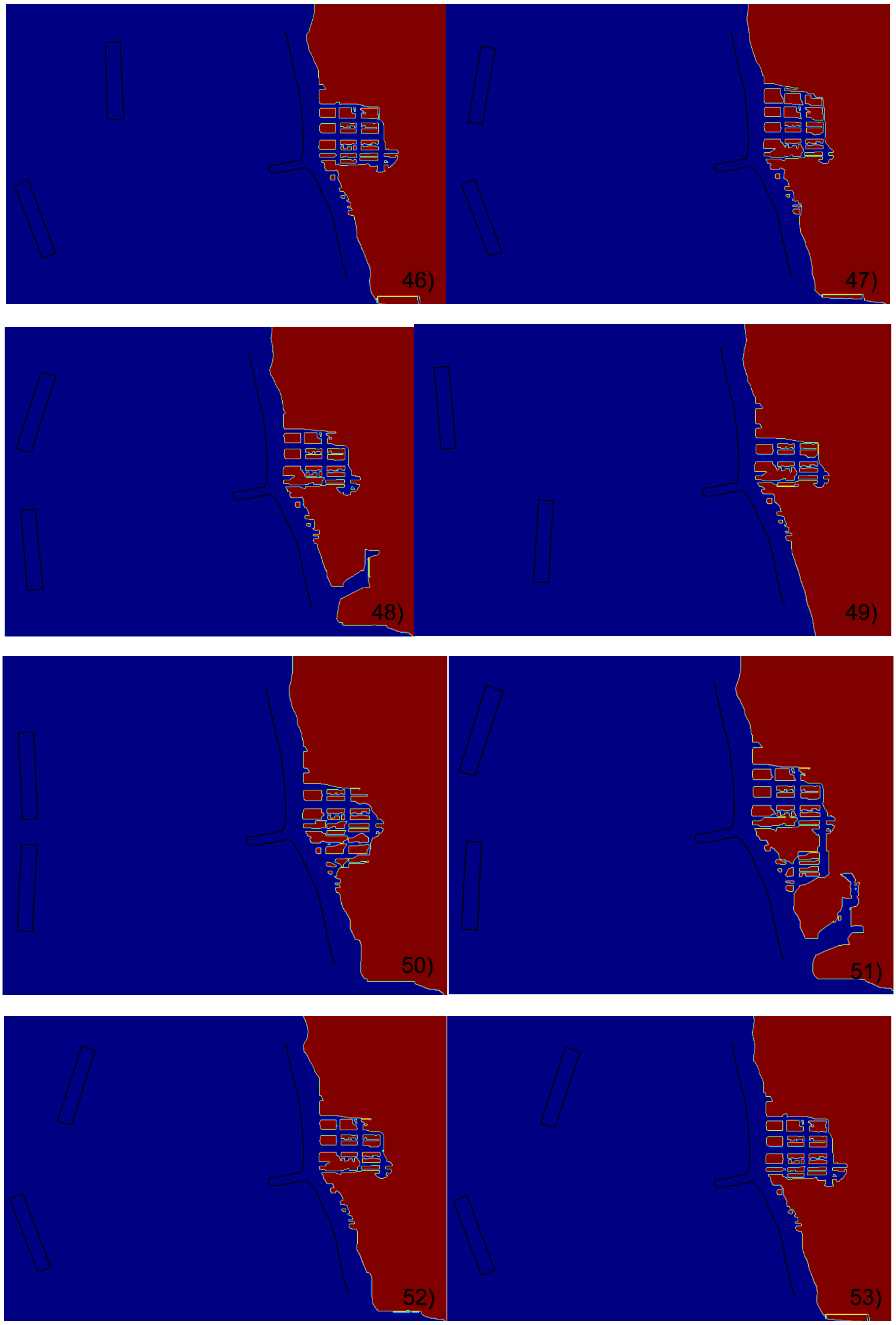

LEGEND:

- Dry area
- Flooded area
- Vertical breakwater structures
- The shoreline

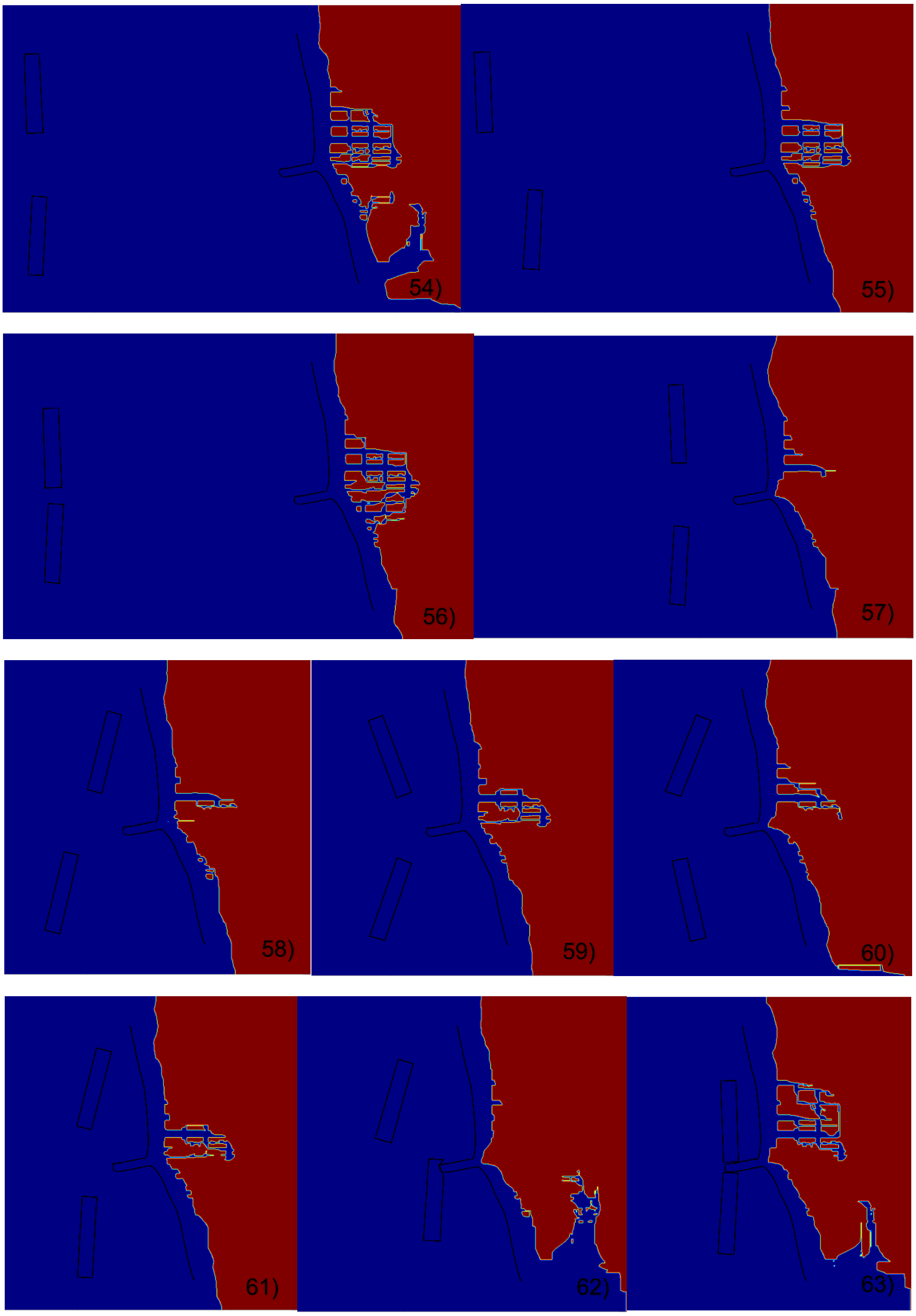

LEGEND:

Dry area

Flooded area

Vertical breakwater structures

The shoreline

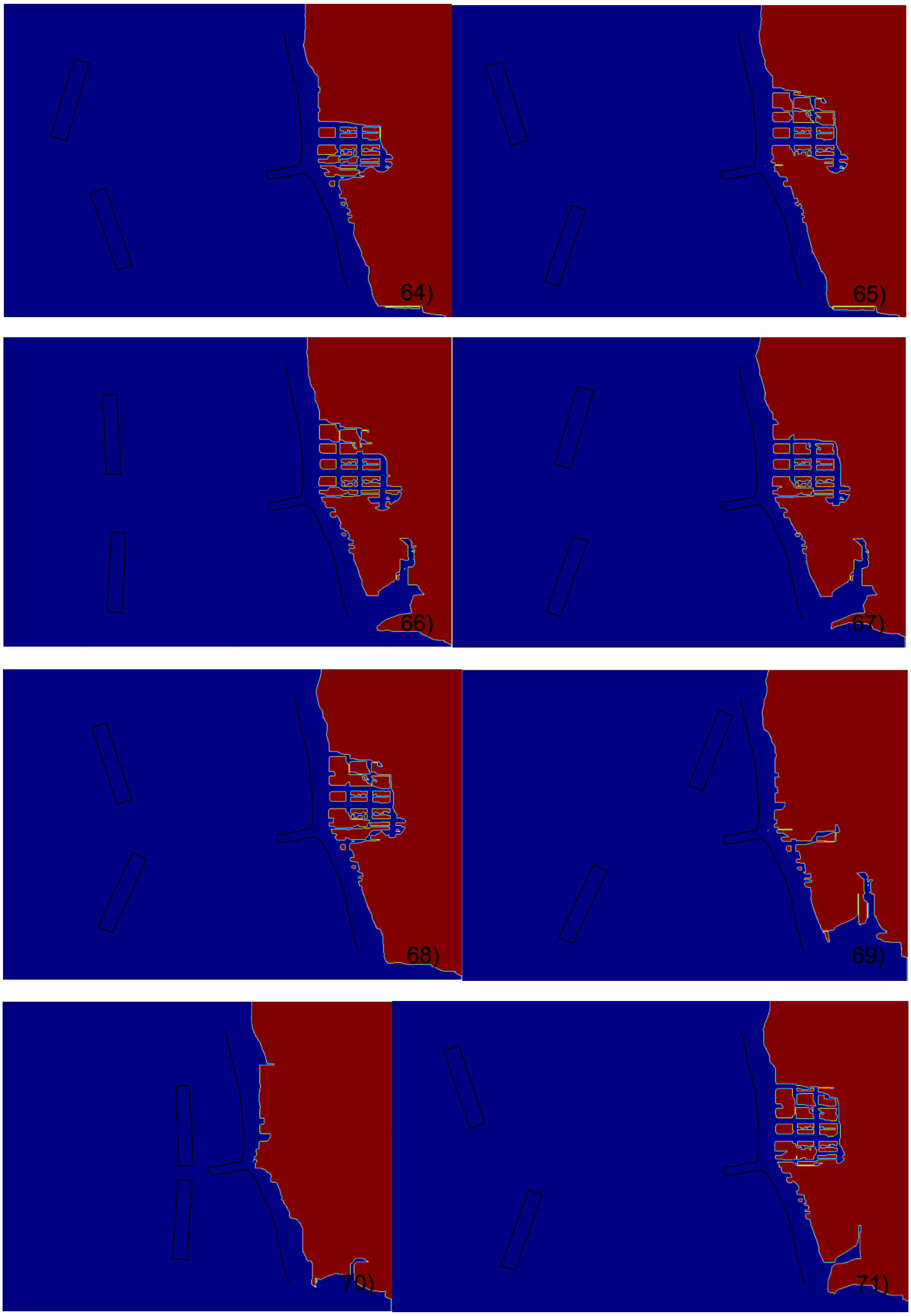

Figure E.1 – 75 simulation results (the other 4 in section 4.3).

As the structures are brought closer to the shore, *i.e.*, when they are placed about 170 and 75 m away from the groin's head, a significant reduction of inundation is achieved. This is clearly illustrated by the results of configurations 2); 4); 5) and 6) in Figure E1. On the other hand, structures that are located about 700 m or 350 m from the groin are not able to protect the central area of the coastal front behind the groin although sometimes they are able to reduce the wave energy on the north and south parts of the area and consequently reduce overtopping.

Figures E.1 30) to 34) clearly illustrate that the structures cannot be positioned parallel to the wave direction because as can be seen, they are not effective.

The results also illustrate that when the vertical breakwater structures are place on the shoreline or very close to the shoreline, acting as revetment walls, Figure E.1 15) to 25), the solutions will not be as effective as the ones of the structures located 75 or 170 m away from the groin's head.

APPENDIX F

Table F1 - The data used to train the Machine learning models (the coordinates, distances and orientations extracted from AutoCAD, and areas from the results of SWASH simulations using MATLAB scripts).

Solution	Area	S_Dist	N_Dist	S_Ort	N_Ort	S_X_cood	S_Y_cood	N_X_cood	N_Y_cood
1	19.2356	352.80	294.70	116	115	-46225.0	133803.7	-46040.1	134198.7
2	18.6846	430.10	381.00	143	147	-46274.7	133894.0	-46120.0	134233.7
3	20.0510	449.00	394.90	113	114	-46309.9	133838.7	-46125.0	134243.7
4	17.4522	643.40	582.70	113	114	-46484.9	133908.7	-46294.9	134313.7
5	17.5682	256.10	230.60	125	95	-46120.0	133838.7	-46005.1	134113.7
6	18.2914	273.00	293.10	131	116	-46035.1	133853.7	-46130.0	134213.7
7	19.9030	442.00	294.60	116	116	-46274.9	133933.7	-46040.1	134198.7
8	17.6708	657.60	626.20	125	95	-46489.9	133938.7	-46344.9	134293.7
9	20.0052	353.20	394.20	116	116	-46225.0	133803.7	-46130.0	134243.7
10	19.7126	442.50	403.90	116	116	-46279.9	133923.7	-46160.0	134173.7
11	16.4652	110.30	100.50	116	115	-46000.0	133743.7	-45855.1	134143.7
12	16.4618	175.40	200.30	27	26	-46070.1	133738.7	-45950.1	134188.7
13	16.1106	142.40	145.70	65	147	-46035.1	133743.7	-45900.1	134178.7
14	16.1996	121.00	126.90	125	95	-46020.1	133718.7	-45890.1	134148.7
15	18.6154	258.40	223.30	125	95	-46145.0	133768.7	-45975.0	134178.7
16	18.9122	258.40	195.60	125	111	-46145.0	133768.7	-45975.1	134098.7
17	17.1196	155.20	115.00	113	107	-46055.1	133718.7	-45888.1	134143.7
18	16.3240	196.70	156.60	131	125	-46090.1	133738.7	-45920.1	134153.7
19	16.6418	124.50	172.40	69	115	-46015.1	133743.7	-45930.1	134168.7
20	18.9054	359.60	156.60	115	125	-46185.0	133953.7	-45920.1	134153.7
21	16.3182	116.60	100.50	116	115	-46000.0	133743.7	-45889.9	134068.6
22	16.5902	116.60	100.50	116	115	-46024.8	133693.6	-45889.9	134068.6
23	16.6102	135.50	100.50	116	115	-46010.1	133798.7	-45889.9	134068.6
24	15.0148	414.00	344.79	27	26	-46259.9	133903.7	-46070.1	134273.7
25	16.3778	199.60	344.79	27	26	-46070.1	133818.7	-46070.1	134273.7
26	14.9464	414.00	234.50	27	26	-46259.9	133903.7	-46000.1	134138.7
27	15.7984	199.60	234.50	27	26	-46070.1	133818.7	-46000.1	134138.7
28	16.1474	279.64	184.65	65	147	-46145.0	133828.7	-45930.1	134198.7
29	15.4072	185.90	184.65	65	147	-46080.1	133743.7	-45930.1	134198.7
30	16.4476	279.64	182.10	65	147	-46145.0	133828.7	-45965.1	134093.7
31	16.5306	185.90	182.10	65	147	-46080.1	133743.7	-45965.1	134093.7
32	16.3414	148.76	147.50	125	95	-46020.1	133808.7	-45930.1	134088.7
33	16.3402	148.76	126.95	125	95	-46020.1	133808.7	-45890.1	134148.7
34	16.8390	279.64	286.50	65	115	-46145.0	133828.7	-46035.1	134208.7
35	16.4612	185.90	286.50	65	115	-46080.1	133743.7	-46035.1	134208.7
36	16.4780	279.64	203.59	65	115	-46145.0	133828.7	-45965.1	134163.7
37	15.6910	185.90	203.59	65	115	-46080.1	133743.7	-45965.1	134163.7
38	34.8364	619.80	519.40	109	116	-46453.6	133950.8	-46196.3	134421.4
39	34.3080	777.30	519.40	122	116	-46559.3	134088.6	-46196.3	134421.4
40	33.8052	619.80	697.50	109	117	-46436.9	133978.5	-46354.3	134484.6
41	33.8632	627.80	697.50	118	117	-46453.6	133950.8	-46354.3	134484.6
42	33.1260	777.30	697.50	122	117	-46559.3	134088.6	-46354.3	134484.6

43	35.2388	610.20	713.10	118	117	-46413.1	134023.5	-46398.3	134394.9
44	30.8020	920.50	547.00	122	117	-46667.9	134198.8	-46236.8	134381.0
45	31.4224	935.30	519.30	122	136	-46698.0	134150.2	-46196.2	134421.4
46	35.4812	610.40	815.70	118	141	-46413.1	134023.5	-46449.5	134557.7
47	35.3256	935.30	852.50	122	122	-46698.0	134150.2	-46484.7	134564.7
48	31.2816	962.80	696.80	138	116	-46728.5	134140.9	-46354.3	134484.6
49	36.0572	1071.80	678.20	98	137	-46817.3	134204.9	-46332.3	134493.5
50	36.5172	1071.80	979.30	98	129	-46817.3	134204.9	-46599.8	134599.6
51	35.3364	935.50	826.00	114	137	-46703.5	134133.9	-46470.8	134522.6
52	37.6176	781.90	1017.90	122	115	-46566.5	134081.3	-46635.1	134609.7
53	35.8988	936.00	862.40	122	117	-46692.4	134170.6	-46525.7	134464.4
54	33.6784	936.00	811.80	122	137	-46692.4	134170.6	-46445.3	134558.7
55	34.3664	1083.10	856.60	122	117	-46808.9	134269.9	-46497.7	134534.7
56	36.5576	1071.80	811.80	98	137	-46816.3	134204.9	-46445.3	134558.7
57	33.9932	1095.16	1010.12	122	117	-46849.2	134177.5	-46630.4	134599.7
58	37.4412	934.7	1010.12	122	117	-46706.8	134120.2	-46630.6	134599.7
59	36.7896	1078.54	1018.93	122	117	-46815.2	134232.9	-46664.9	134516.3
60	39.538	455.91	363.13	122	117	-46308.5	133866.7	-46081.6	134289.9
61	38.7192	467.56	230.39	132	135	-46312.3	133890.9	-45969.6	134224.1
62	38.4188	384.69	293.39	138	100	-46247.2	133835.3	-46026.5	134243.9
63	38.286	384.69	293.39	107	141	-46247.2	133835.3	-46023.4	134242.3
64	38.5172	354.03	230.39	122	135	-46224.2	133810.9	-45969.6	134224.1
65	33.3192	260.49	325.49	122	135	-46106.4	133887.6	-46061.8	134232.5
66	32.6276	241.34	173.02	122	117	-46103.7	133835.3	-45953.1	134095.7
67	36.784	780.32	829.75	101	136	-46571.7	134059.9	-46483.2	134495.7
68	36.7284	780.32	893.86	139	101	-46599.7	134015.1	-46541.1	134514.9
69	33.386	780.32	704.53	122	117	-46561.2	134077.1	-46379.2	134428.5
70	33.4828	780.32	667.01	139	117	-46599.7	134015.1	-46341.1	134432.5
71	35.364	780.32	731.66	143	102	-46574.9	134061.8	-46399.0	134451.7
72	34.0668	741.69	203.04	144	141	-46548.0	134009.6	-45934.8	134248.3
73	36.3684	343.98	273.36	122	117	-46195.2	133871.0	-46039.6	134139.5
74	34.2384	941.5	1036.94	138	102	-46592.5	134603.6	-46650.4	134622.9
75	38.3968	780.34	973.2	101	136	-46571.7	134059.9	-46712.9	134122.5

Table F2 - Normalized data used for Model training type one (only part of the 75 samples).

S_Dist	N_Dist	S_Ort	N_Ort	S_X_cood	S_Y_cood	N_X_cood	N_Y_cood	Area
35.28	29.47	11.6	11.5	-46.225	13.38037	-46.0401	13.41987	5.5021
43.01	38.1	14.3	14.7	-46.2747	13.3894	-46.12	13.42337	6.6041
44.9	39.49	11.3	11.4	-46.31	13.38387	-46.125	13.42437	3.8713
64.34	58.27	11.3	11.4	-46.4849	13.39087	-46.295	13.43137	9.0689
25.61	23.06	12.5	9.5	-46.12	13.38387	-46.0051	13.41137	8.8369

Table F3 - Normalized data used for Model training type two (only part of the 75 samples).

Area	S_Orientation	N_Orientation	S_X_cood	S_Y_cood	N_X_cood	N_Y_cood
5.5021	11.6	11.5	-1.225	0.380369	-1.04006	0.41987
6.6041	14.3	14.7	-1.27473	0.389401	-1.12003	0.423371
3.8713	11.3	11.4	-1.30996	0.383869	-1.12503	0.424371
9.0689	11.3	11.4	-1.4849	0.39087	-1.29496	0.431372
8.8369	12.5	9.5	-1.12003	0.383869	-1.00507	0.41137